Technische Universität München

Max-Planck-Institut für Physik

Investigation of Properties of Novel Silicon Pixel Assemblies Employing Thin n-in-p Sensors and 3D-Integration

Philipp Weigell

Vollständiger Abdruck der von der Fakultät für Physik der Technischen Universität München zur Erlangung des akademischen Grades eines

Doktors der Naturwissenschaften

genehmigten Dissertation.

Vorsitzender: Univ.-Prof. Dr. Martin Beneke
Prüfer der Dissertation:
1. Hon.-Prof. Dr. Siegfried Bethke
2. Univ.-Prof. Dr. Stephan Paul

Die Dissertation wurde am 20.12.2012 bei der Technischen Universität München eingereicht und durch die Fakultät für Physik am 15.01.2013 angenommen.

Abstract

Until the end of the 2020 decade the LHC programme will be defining the high energy frontier of particle physics. During this time, three upgrade steps of the accelerator are currently planned to further increase the luminosity and energy reach. In the course of these upgrades the specifications of several parts of the current LHC detectors will be exceeded. Especially, the innermost tracking detectors are challenged by the increasing track densities and the radiation damage. This thesis focuses on the implications for the ATLAS experiment. Here, around 2021/2, after having collected an integrated luminosity of around $300\,\mathrm{fb}^{-1}$, the silicon and gas detector components of the inner tracker will reach the end of their lifetime and will need to be replaced to ensure sufficient performance for continued running—especially if the luminosity is raised to about $5 \cdot 10^{35}\,\mathrm{cm}^{-2}\mathrm{s}^{-1}$ as currently planned. An all silicon inner detector is foreseen to be installed. This upgrade demands cost effective pixel assemblies with a minimal material budget, a larger active area fraction as compared to the current detectors, and a higher granularity. Furthermore, the assemblies must be able to withstand received fluences up to $2 \cdot 10^{16}\,\mathrm{n_{eq}/cm^2}$.

A new pixel assembly concept answering the challenges posed by the high instantaneous luminosities is investigated in this thesis. It employs five novel technologies, namely n-in-p pixel sensors, thin pixel sensors, slim edges with or without implanted sensor sides, and 3D-integration incorporating a new interconnection technology, named Solid Liquid InterDiffusion (SLID) as well as Inter-Chip-Vias (ICVs).

n-in-p sensors are cost-effective, since they only need patterned processing on one side. Their performance before and after irradiation is investigated and compared to results obtained with currently used n-in-n sensors. Reducing the thickness of the sensors lowers the amount of multiple scattering within the tracking system and leads to higher charge collection efficiencies after irradiation. Devices with thicknesses between $75\,\mu\mathrm{m}$ and $150\,\mu\mathrm{m}$ are investigated before and after irradiation with different experimental approaches, namely radioactive sources, beam tests, and laser measurements. The obtained results are compared to those gathered for devices using the currently widely used thickness of $285\,\mu\mathrm{m}$. By implanting the sides of the sensors, the distance between the last active pixel implant and the edge can be considerably reduced, allowing for a compact module concept. In this thesis several steps are discussed to reduce this distance from 1.1 mm down to $50\,\mu\mathrm{m}$. Subsequently, the performance of the different implementations is investigated. The SLID interconnections offer the possibility to stack sensors and several layers of read-out electronics as well as a reduced minimal pitch and eventually a lower cost. In combination with ICVs it paves the way to 3D-integrated pixel assemblies. These can be further optimised in terms of the active area, thanks to a reduced footprint of the read-out chip. Furthermore, it enables the use of specialised processes for the analogue and digital parts of the read-out chip in the different layers. First assemblies employing SLID interconnections were built and the properties of the interconnection are discussed. Finally, etching of ICVs was started and the present status is reviewed.

Keywords: ATLAS, Pixel detector, HL-LHC, n-in-p, Thin sensors, 3D-integration, Radiation damage

Zusammenfassung

Das LHC-Programm wird bis Ende der 2020er-Jahre Vorreiter in der Hochenergiephysik sein. Bis dahin sind derzeit drei Ausbau- und Erweiterungstufen des Beschleunigers geplant, die den Luminositäts- und Energiebereich erweitern. Im Zuge dieser Erweiterungen werden die Spezifikationen vieler Teile der LHC-Detektoren überschritten werden. Insbesondere die innersten Spurdetektoren werden durch die erhöhten Spurdichten und entstehenden Strahlenschäden beansprucht. In dieser Dissertation liegt der Schwerpunkt auf den Auswirkungen für das ATLAS-Experiment. Um 2020/1, nachdem um $300\,\mathrm{fb}^{-1}$ integrierte Luminosität gesammelt sein wird, erreichen die Silizium- und Gas-Detektoren des inneren Spurdetektors das Ende ihrer Lebenszeit und müssen ersetzt werden. Dadurch soll eine ausreichende Leistung für die weitere Laufzeit gewährleistet werden – insbesondere, wenn, wie derzeit geplant, die Luminosität auf näherungsweise $5 \cdot 10^{35}\,\mathrm{cm}^{-2}\mathrm{s}^{-1}$ angehoben wird. Hierbei ist vorgesehen, einen rein auf Silizium basierten Detektor einzusetzen. Für diesen Ausbau werden, verglichen mit den derzeitigen Detektoren, kostengünstige Pixelmodule mit minimalem Materialeinsatz, einem größeren aktiven Flächenanteil und einer höheren Granularität benötigt. Des Weiteren müssen die Module Strahlendosen bis zu $2 \cdot 10^{16}\,\mathrm{n_{eq}/cm^2}$ standhalten können.

Als Lösung für die sich aus der hohen instantanen Luminosität ergebenden Anforderungen wird in dieser Dissertation ein neues Pixelmodulkonzept erforscht. Dabei kommen fünf neue Technologien zum Einsatz: n-in-p-Pixelsensoren, dünne Sensoren, schmale Randzonen sowohl mit als auch ohne implantierte Sensorseiten sowie 3D-Integration. Die 3D-Integration setzt sich zusammen aus einer neuen Verbindungstechnologie, genannt Solid Liquid InterDiffusion (SLID), und Inter-Chip-Vias (ICVs).

n-in-p-Sensoren sind kostengünstig, da sie nur auf einer Seite strukturiert prozessiert werden müssen. Ihre Eigenschaften vor und nach Bestrahlung werden erforscht und mit Ergebnissen der derzeit verwendeten n-in-n-Sensoren verglichen. Die verringerte Sensordicke reduziert Vielfachstreuung im Spurdetektorsystem und führt zu höheren Ladungssammlungseffizienzen nach Bestrahlung. Sensoren mit Dicken zwischen $75\,\mu\mathrm{m}$ und $150\,\mu\mathrm{m}$ werden vor und nach Bestrahlung mit verschieden experimentellen Ansätzen erforscht, z. B. mit Strahltests, Messungen mit radioaktiven Quellen und Lasern. Zum Vergleich werden Ergebnisse für Sensoren mit der heute gebräuchlichen Sensordicke von $285\,\mu\mathrm{m}$ herangezogen. Durch Implantieren der Sensorseiten, kann der Abstand zwischen dem letzten aktiven Pixelimplantat und der Kante d_{edge} entscheidend verkleinert werden und damit das Pxielmodul kompakter gemacht werden. In dieser Dissertation, werden verschiedne Schritte vorgestellt, die es ermöglichen, d_{edge} von 1,1 mm auf $50\,\mu\mathrm{m}$ zu verkleinern. Anschließend wird die Eignung der verschiedenen Ansätze untersucht. Die SLID-Verbindungen ermöglichen neben der Schichtung von Sensoren- und mehrerer Ausleseelektroniklagen eine erhöte Granularität und sind günstiger. In Kombination mit ICVs ebnet dies den Weg für 3D-integrierte Pixelmodule. Dank des reduzierten Flächenbedarfs der Auslese, verbessert sich der aktive Flächenanteil dieser Pixelmodule weiter. Weiter ermöglichen sie die Nutzung spezieller Prozesse für analoge und digitale Bereiche in den verschiedenen Lagen der Ausleseelektronik. Erste Module mit SLID-Verbindungen wurden hergestellt und die Eigenschaften der Verbindung werden besprochen. Schlussendlich wurde das Ätzen von ICVs gestartet und der aktuelle Stand wird dargestellt.

Schlagwörter: ATLAS, Pixeldetektor, HL-LHC, n-in-p, dünne Sensoren, 3D-Integration, Strahlenschäden

Für Eva

Contents

Overview

A novel pixel assembly concept for high energy physics experiments at high luminosity hadron colliders is investigated. It incorporates five new technologies, namely n-in-p sensors, thin sensors, slim edges with or without implanted sensor sides, and 3D-integration incorporating a new interconnection technology, named Solid Liquid InterDiffusion (SLID) as well as Inter-Chip-Via (ICVs).

Chapter 1: After a physics motivation the LHC and the ATLAS detector as well as their upgrade roadmaps are discussed together with the resulting challenges and requirements on the individual detector parts. In the last section the investigated assembly concept is introduced as an answer to the challenges posed to the pixel part of the inner tracking detector.

Chapter 2: An introduction into semiconductor physics is given up to the level of detail needed for the investigations presented in the following chapters. Especially, the effects of radiation damage for silicon sensors are highlighted.

Chapter 3: Novel n-in-p pixel detectors are assessed in terms of operational performance before and after irradiation. In addition, their properties are compared to the currently used n-in-n pixel detectors.

Chapter 4: Thin strip and pixel detectors are investigated and their operational requirements are determined with a focus on quantities that are most relevant for high energy physics experiments as for example the collected charge to threshold ratio and the hit efficiency.

Chapter 5: The reach of the SLID interconnection technique is discussed along results derived from pixel assemblies interconnected with SLID. Afterwards, the present status of the ICVs is discussed.

Chapter 6: A summary of the key results obtained for all assembly concept ingredients is given, followed by an outlook.

Throughout this thesis natural units $c = \hbar = 1$ are used.

1 Upgrade Plans for the Large Hadron Collider and the ATLAS Detector

The Large Hadron Collider (LHC) [1, 2], based at the Conseil Européen pour la Recherche Nucléaire (CERN) [3], is the only presently running particle accelerator complex at the high energy frontier of particle physics. Furthermore, the centre of mass (cms) energy of the colliding protons will exceed the cms energy of its predecessor Tevatron [4] by an order of magnitude after reaching the design value of $\sqrt{s} = 14\,\text{TeV}$. In its second operation mode, lead ions are collided at $\sqrt{s} = 1.15\,\text{PeV}$ corresponding to a factor of 30 in energy when compared to its competitor the Relativistic Heavy Ion Collider (RHIC) [5, 6] at the Brookhaven National Laboratory [7].

Around the LHC ring four major experiments—ATLAS[1] [8], CMS[2] [9], ALICE[3] [10], and LHCb[4] [11]—as well as several smaller experiments are located, which have different physics scopes. ATLAS and CMS are large general purpose experiments designed to capture as many physics signatures as possible. The ALICE collaboration investigates mainly heavy ion physics and LHCb is designed for physics processes involving bottom quarks.

In this chapter first the high energy physics reach and limitations of the LHC will be discussed, followed by a discussion of the needed and planned measures to push the limits further in the future (Sections 1.1 and 1.2). In Section 1.3 first the layout and performance of the ATLAS detector will be discussed. Second, an overview of the requirements and plans for the future operation of ATLAS is given, with a special emphasis on the innermost tracking system. The last section introduces the novel pixel detector assembly concept investigated in this thesis as an answer to the challenges discussed in Section 1.3.

1.1 Physics Motivation

As a proton-proton collider the LHC opens access to physics processes in a wide energy range simultaneously and thus is an exploratory machine. It is hoped that it will help answering fundamental questions of physics: Which mechanism gives rise to the masses of massive elementary particles? What is the nature of dark matter? Why is there more matter than antimatter in the universe? Are there further or even more fundamental symmetries realised in nature?

1.1.1 Higgs Mechanism

Over the last decades, the description of the elementary matter constituents and their interactions, the Standard Model (SM) of particle physics [12–14], was tested to an overwhelming precision. The latest step in the successful history was marked by the announcement that

[1] A Toroidal LHC ApparatuS
[2] Compact Muon Solenoid
[3] A Large Ion Collider Experiment
[4] Large Hadron Collider beauty

a new boson with a mass around 126 GeV was observed [15, 16], which might be the Higgs boson—i. e. the boson predicted in the most favoured explanation of the electroweak symmetry breaking [17–22]. The next step is to demonstrate that this new boson is indeed the long sought Higgs boson. While the ultimate proof or disproof as well as precision measurements will be done at a future muon or electron collider with significantly lower background rates and well defined initial states, already at the LHC the spin and CP eigenstates will be determinable; especially if the statistics is increased further and additional rare channels become accessible. Furthermore, with a largely increased statistics triple couplings of the Higgs boson are expected to become visible [23].

1.1.2 Supersymmetry

If the existence of the Higgs boson is confirmed, the resulting quadratic divergence [24–28] of its renormalised mass within the SM is the next open question to be addressed. One of the most elegant solutions to this divergence is offered by a supersymmetric extension of the SM [29–37], where the contributions of the Higgs superpartners lead to a cancellation. This new symmetry between bosons and fermions predicts superpartners for all particles in the SM. Additionally, some of these particles could be the appropriate answer to the fundamental questions raised above. For example the lightest supersymmetric particle is a dark matter candidate, if its decay into non supersymmetric particles is forbidden, as it is the case in so-called R-parity [28, 38–41] conserving supersymmetric theory implementations. The first indications for the realisation of this symmetry in nature are expected from the supersymmetric partners of the top quark and the neutrino, the stop-quark and the neutralino. They can be probed up to 1 TeV or 0.5 TeV respectively over the currently planned lifetime of the LHC, if the upgrade schedule planned and described in the following is met. If they manifest themselves at lower masses, their spin and coupling structure becomes accessible [23] for the LHC experiments.

1.1.3 Further Beyond the Standard Model

Beyond supersymmetric extensions of the SM and the Higgs-Boson, an overwhelming number of theoretical models predict new particles and/or phenomena in the reach of the LHC. Often these models predict cascade-like decay patterns, which would manifest themselves in resonances in the dilepton- or top-antitop-spectra. Crucial for these searches is the highest statistic available.

However, being an exploratory machine, the most exiting results will be the unexpected ones pointing the direction for deeper insights.

1.2 From LHC to HL-LHC

Among the physics processes outlined above many are rare and thus demand besides refined analyses high statistics. This is delivered by the LHC and its planned upgraded version, the High Luminosity-Large Hadron Collider (HL-LHC) introduced in this section.

1.2.1 The LHC Accelerator Complex

The LHC is only the last joint, within a chain of accelerators which forms the LHC accelerator complex [42]. It is illustrated together with its interconnections with other CERN accelerators in Figure 1.1. As mentioned above, the LHC is operated as proton and as ion collider. Depending on the mode either the LINear ACcelerator (LINAC) 2 or the LINAC 3 is employed.

Protons from ionised H_2 are accelerated in bunches within the LINAC 2 up to an energy of 50 MeV before they are injected to the Booster, which they leave with an energy of 1.4 GeV. The accelerating steps within the Proton Synchrotron (PS) and the Super Proton Synchrotron (SPS) increase the energy further to 26 GeV and 450 GeV respectively. From here the proton bunches are injected in two opposing directions into the LHC. There they are first accelerated to the final energy, then squeezed in phase space and eventually collided at the experiments. In each collision about 20 protons out of the 10^{11} protons per bunch undergo a hard interaction [43].

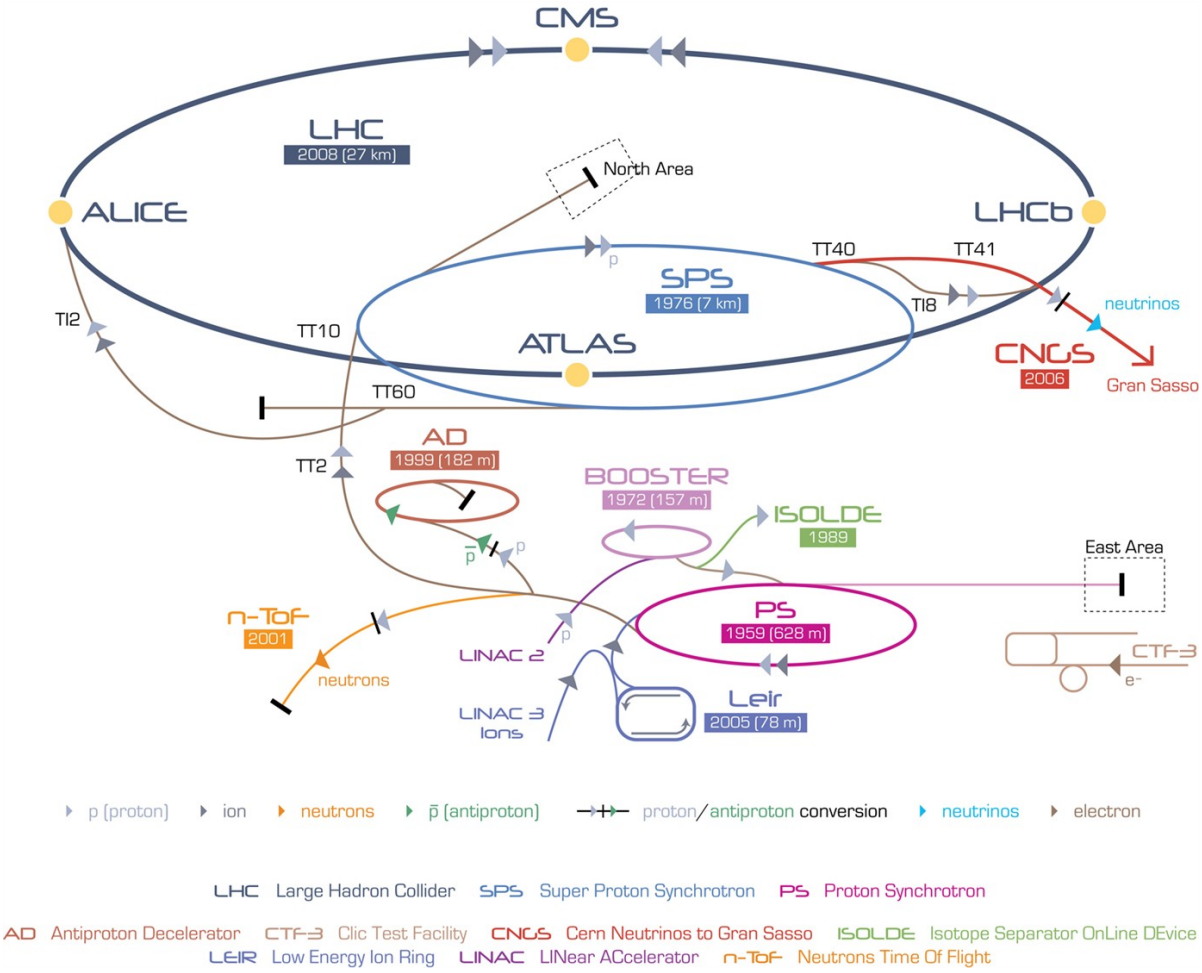

Figure 1.1: The LHC accelerator complex and its embedding into the CERN accelerators [44].

During heavy ion operation, stripped lead ions ($^{208}Pb^{54+}$) are accelerated in the LINAC 3 up to an energy of 4.2 MeV/u, from where they are injected into the Low Energy Ion Ring (LEIR) for further acceleration up to 14.8 MeV/u. After leaving the subsequent PS with an energy of 4.26 GeV/u the ions are fully stripped to $^{208}Pb^{82+}$ and injected into the SPS, which accelerates them further to 177 GeV/u before injecting two counter-rotating beams into the LHC for further acceleration, squeezing, and eventually collision.

Both operation modes can also be combined such that, lead ions are collided with protons.

1.2.2 Luminosity

For a given physics process with a cross section σ_{process} the number of events N_{event} occurring is given by [1, 45]:

$$N_{\text{event}} = L\sigma_{\text{process}} \tag{1.1}$$

where L is the luminosity. It measures the beam intensity I per colliding area A of an accelerator. With the assumption of Gaussian beam profiles, L can be expressed as:

$$L = \frac{I}{A} = \frac{N_{\text{b}}^2 n_{\text{b}} f_{\text{rev}} \gamma}{4\pi \epsilon_{\text{n}} \beta^*} \tag{1.2}$$

where N_{b} is the number of particles per bunch, n_{b} the number of bunches per beam, f_{rev} the revolution frequency, and γ the Lorentz factor. The two parameters ϵ_{n} and β^* are a measure for the beam geometry or quality; the first, the normalised transverse beam emittance, corresponds to the transverse phase-space ellipse of a bunch and the latter—the beta function at the Interaction Point (IP) [46]—accounts for the amplitude modulation of the bunch during collision.

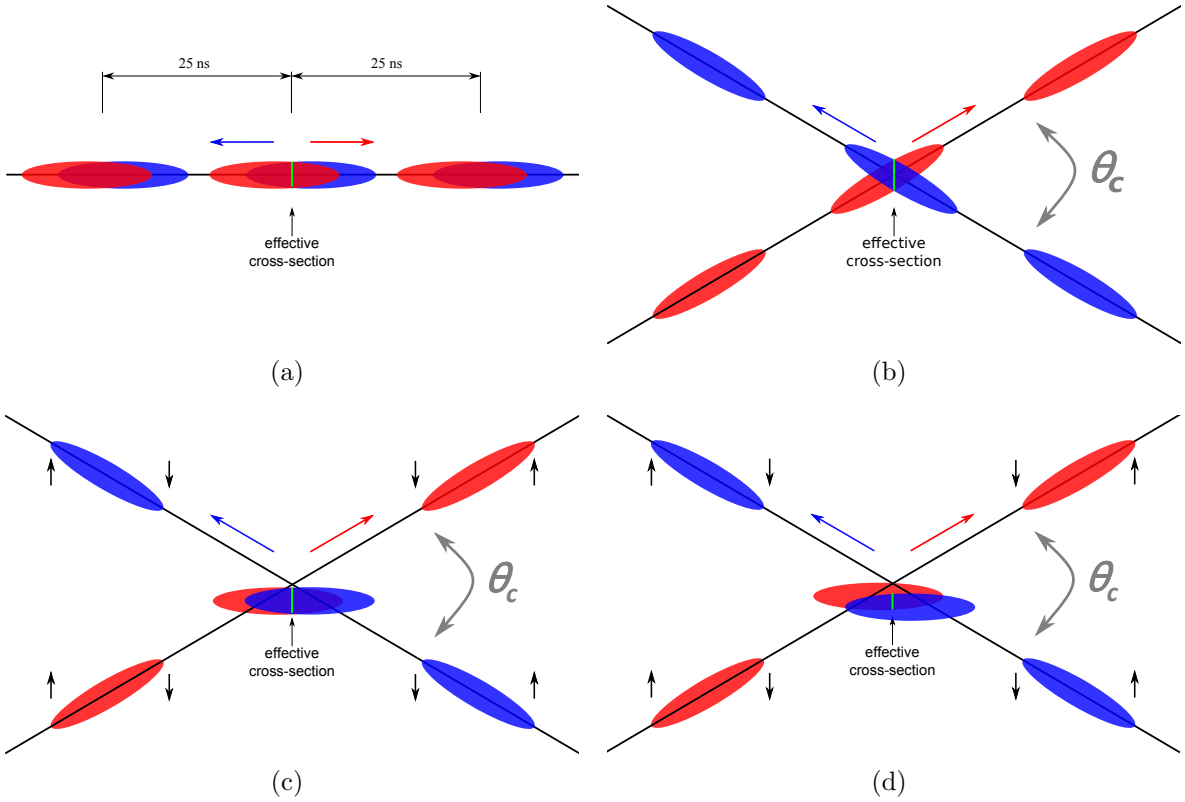

Figure 1.2: Illustrations of bunch collision schemes at the IP. (a) illustrates the head-on collision case, (b) the case with a small crossing angle θ_{c}. The HL-LHC scenarios using crab cavities are illustrated in (c) without and (d) with luminosity levelling.

Since the bunches are only separated by 25 ns multiple interactions would occur at different positions in the detector, see Figure 1.2(a). Thus, the beams are collided with a small crossing angle θ_{c}, see Figure 1.2(b), and the geometric luminosity reduction factor at the IP F has to be

taken into account. Assuming that β^* is greater or equal than the Root Mean Square (RMS) of the bunch lenght σ_z it is defined as:

$$F = \frac{1}{\sqrt{1 + \left(\frac{\theta_c \sigma_z}{2\sigma^*}\right)^2}} \tag{1.3}$$

with σ^* denoting the transverse RMS beam size at the IP. The total peak luminosity is then given by

$$L_{\text{peak}} = LF \tag{1.4}$$

Table 1.1 gives an overview of the typical current and nominal design values for the beam parameters of the LHC.

Table 1.1: Current average (Oct. 2012) and nominal design beam parameters of the LHC in proton operation mode. The current values are always given at the IP of the ATLAS experiment. Additional the current planing for HL-LHC is given. For the pile-up estimation the inelastic p-p cross-section is used [47].

Parameter Name	Symbol [Unit]	Current [48, 49]	Design [43]	HL-LHC [50]	
Bunch Spacing	[ns]	50	25	25	50
Number of bunches	n_b	1374	2808	2808	1404
Number of particles/bunch	N_b [10^{11}]	1.6	1.15	2.0	3.3
Revolution frequency	f_{rev} [kHz]	11.245	11.245	11.245	11.245
Normalised emittance	ϵ_n [μm]	2.4	3.75	2.5	3
Beta function at the IP	β^* [m]	0.6	0.55	0.15	0.15
Crossing angle	θ_c [μrad]	290	300	420	520
RMS bunch length	σ_z [cm]	≥ 9	7.55	7.55	7.55
RMS beam size at the IP	σ^* [μm]	19	16.7	13.6	10.0
L levelling factor		1	1	2.5	5
Pile-up	$\langle\mu\rangle$	19.5	19	140	140
Peak Luminostity	L_{peak} [$10^{34}\,\text{cm}^{-2}\text{s}^{-1}$]	0.7	1.0	5.3	7.6
Energy	$\sqrt{s}$ [TeV]	8	14	14	14

1.2.3 Current Performance

In March 2010 the first physics run at an energy of 3.5 TeV per beam was started at the LHC and the machine delivered 5.6 fb^{-1} until the end of 2011, while steadily increasing the peak luminosity. During the winter shutdown the beam energy was slightly increased to 4 TeV and 23.3 fb^{-1} have been delivered in 2012. The delivered and the recorded luminosity for the years 2010–2012 are summarised in Figure 1.3 for the ATLAS experiment. Following a steep learning curve the LHC is operated meanwhile with many parameters close to its nominal values, see Table 1.1. For some parameters as N_b and ϵ_n, it even exceeds the nominal specifications. One critical point is the beam energy, which cannot be raised further until the interconnections of the dipole magnets are improved. Their in part too high resistance when compared to specifications lead to a technical failure in 2008, delaying the start of the LHC by almost two years. Another key area for further improvement will be the reduction of the bunch spacing from 50 ns to 25 ns

since this allows to reduce the number of simultaneous hard interactions per bunch crossing, the so-called pile-up μ, while increasing the peak luminosity and thus helps to reduce systematic uncertainties in the high energy physics measurements conducted by the collaborations.

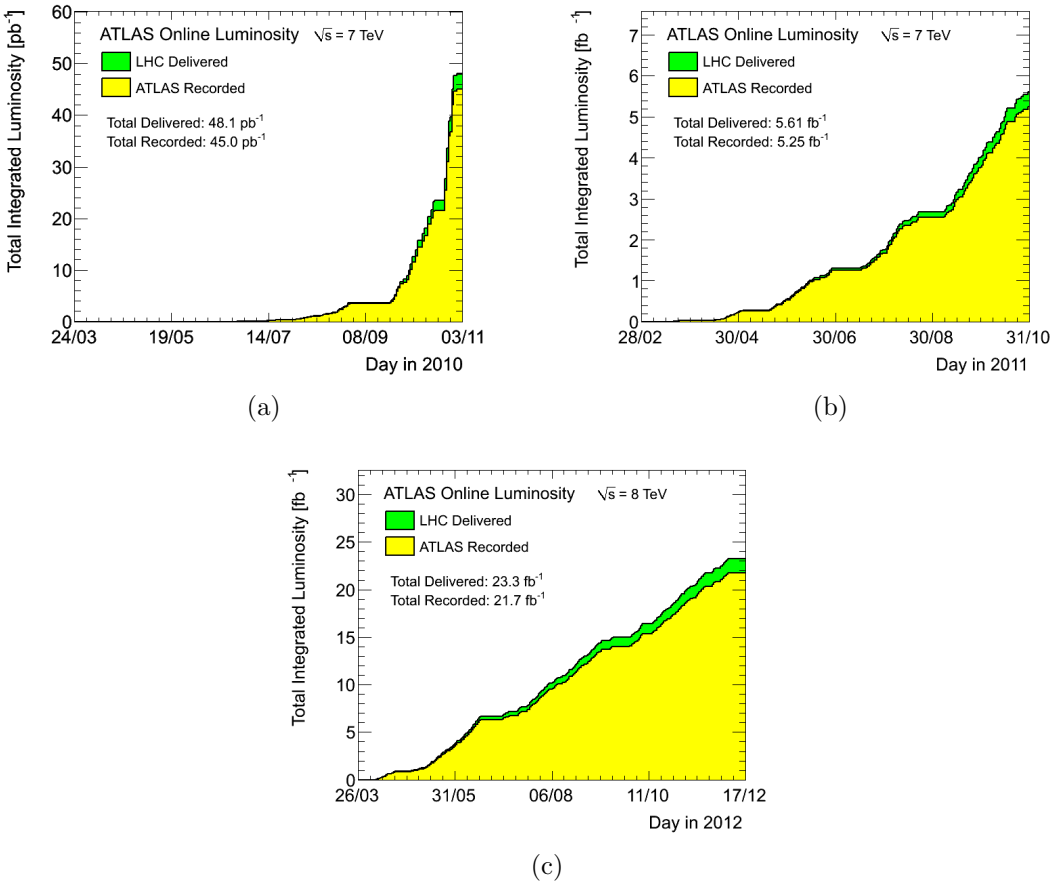

Figure 1.3: Evolution of the delivered and recorded integrated luminosity delivered for the ATLAS experiment in (a) 2010, (b) 2011, and (c) 2012 [49].

1.2.4 Upgrade Roadmap

To make the rare channels discussed above accessible, upgrading the LHC is planned in three steps, each coinciding with a Long Shutdown (LS) of the machine lasting between one and two years. Each shutdown has a slightly different focus.

LS1 – Consolidation

LS1 is dedicated to the consolidation of the LHC needed to reach the nominal performance in energy as well as in luminosity. Starting from early 2013 until the end of 2014 the connections between the magnets will be improved to allow for a higher current flow within the magnets leading to stronger magnetic fields, which are mandatory for LHC operation at $\sqrt{s} = 14\,\text{TeV}$. The higher beam energy additionally allows for a further decreased β^*, such that in combination with the higher energy a fourfold increase with respect to the present luminosity is expected

after the LS1 [2]. Given the present excellent performance of the LHC it is expected that the nominal peak luminosity will be exceeded already after LS1.

LS2 – LINAC 4

In the second LS, planned for the year 2018, a newly build LINAC [51] will be connected to the LHC accelerator complex as a replacement for the now used LINAC 2. This upgrade in combination with collimation upgrades in the accelerator complex allows for an increase of the number of particles per bunch, since the higher energy of 160 MeV of the protons after leaving the LINAC leads to a reduction of space charge induced losses in the transition from the LINAC into the Booster. The same effect is exploited in the next step, by increasing the final energy of the Booster to 2 GeV. Because of the quadratic contribution of N_b to the luminosity (cf. Equation 1.2) this leads to an estimated peak luminosity of $L \approx 2.5 \cdot 10^{34}\,\mathrm{cm}^{-2}\mathrm{s}^{-1}$ after the LS2 [2].

LS3 – HL-LHC

The target for the LS3—planned for 2021/2—is to increase the luminosity to $(5\text{–}8) \cdot 10^{34}\,\mathrm{cm}^{-2}\mathrm{s}^{-1}$ and thus allowing for an integrated luminosity of 200–300 fb^{-1}/a. Several approaches are studied at the moment to achieve this luminosity increase. Besides, the obvious decreasing of the colliding area and filling the bunches with more particles, also the geometric luminosity reduction factor, Equation 1.3, at the IP will be optimised. One idea investigated, is the use of crab cavities [52,53], which effectively reduce the crossing angle θ_c by rotating the bunches shortly before the collision as illustrated in Figure 1.2(c).

One important boundary condition is the number of pile-up events μ, since it is a challenging task to disentangle these events within the experiments. In the planning for the HL-LHC a $\langle\mu\rangle$ below 140 is envisaged. To reduce it and simultaneously increase the life-time of the beam, the bunches will be collided slightly off centred, such that the luminosity is levelled to a constant value over the fill, see Figure 1.2(d). Although, this decreases the instantaneous luminosity at the beginning of a run, the integrated recorded luminosity can be increased by this technique since the fill time of the machine is increased considerably.

The momentarily two most favoured parameter sets for HL-LHC operation are summarised in Table 1.1.

1.3 ATLAS

Aiming for the widest physics reach, ATLAS is built hermetical to cover almost 4π solid angle and to measure as many different physics signatures as possible. As other colliding beam experiments ATLAS has an onion shell layout, where each layer is specialised for a different purpose. Figure 1.4(a) gives an overview of the ATLAS experiment. Its structure and detection principles will be shortly summarised in the following. As the focus of this thesis is on the pixel detector, in Section 1.3.1 a more detailed description of this detector component is given. For the other sub-detectors the reader can find further details in the given references.

The detector parts can mostly be grouped in four functional groups: tracking, calorimetry, magnets, and data acquisition. The tracking system is composed of the inner detector [56, 57], which is embedded into a 2 T solenoid [58, 59] magnet and the muon system [60], which is

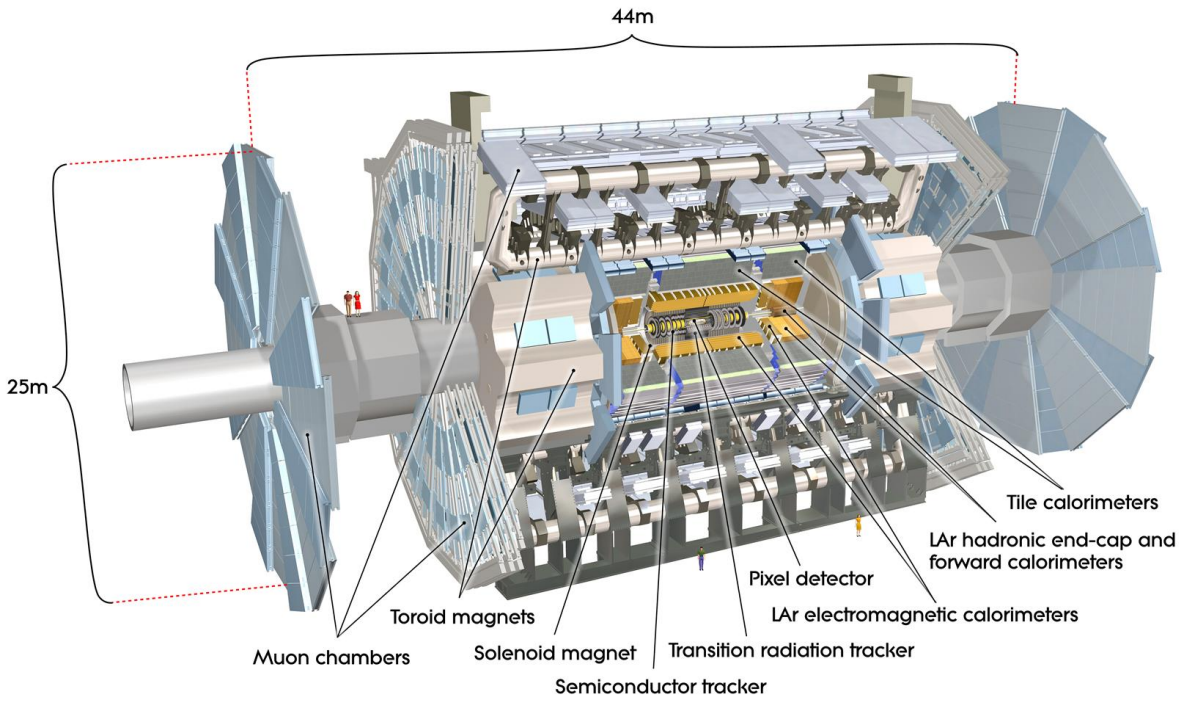

(a)

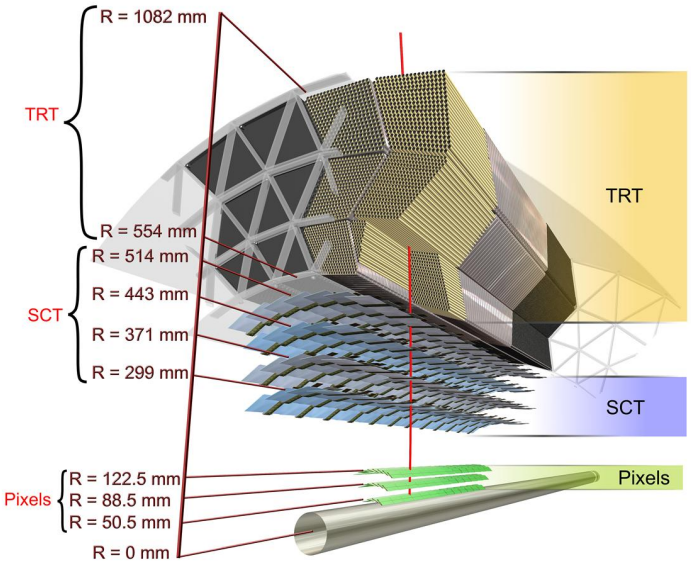

(b)

Figure 1.4: Illustrations of (a) the ATLAS detector [54] and (b) the components of its inner detector [55].

embedded into a 4 T toroid magnet [58, 61, 62]. Exploiting the Lorentz force, the magnets, allow for a momentum determination of the charged particles measured in these detector parts.

The inner detector, see Figure 1.4(b), is composed by three sub-detector systems. The centre-most pixel detector and the surrounding SemiConductor Tracker (SCT) are based on segmented silicon sensors. While in the case of the SCT these segments are called strips, being several centimetres long with a pitch between 57 μm and 94 μm, for the pixel detector they are called pixels and their pitch is $50\,\mu m \times 400\,\mu m$. The Transition Radiation Tracker (TRT) employs straw-tubes filled with ioniziable gas and an anode wire in the centre. These tubes are interluded with fibres (barrel) and foils (end-caps) which evoke transition radiation and thus allow for discrimination of electrons and pions.

The muon system sheaths the detector and exploits four different technologies: the Monitored Drift Tubes (MDTs), the Cathode Strip Chambers (CSCs), the Thin Gap Chambers (TGCs), and the Resistive Plate Chambers (RPCs). While the first three detectors are devoted to tracking purposes, the last two ones are used for triggering. The detection principle of the MDTs which comprise for the majority of the muon system relies on straw-tubes filled with ioniziable gas and an anode wire in the centre. In high rate regions, i. e. in the pseudorapidity[5] range $|\eta| \geq 2$, CSCs, which are Multi-Wire-Proportional Chambers (MWPCs) [63], are used. The TGCs, also MWPCs, but with a larger anode-anode distance than anode-cathode distance, are used for tracking as well as triggering in the forward part. Finally the RPCs are used solely for triggering within the muon system and are built from parallel plates separated by a gaseous volume.

The calorimetry system [64], situated between the inner detector and the muon system, consists of two major parts: the electromagnetic [65] and the hadronic calorimeter [66]. The former one is accordion shaped with lead as absorber and liquid argon as active medium. It stops photons, electrons and low energetic, charged hadrons, while allowing for their energy determination; the hadronic calorimeter is optimised to stop hadrons by using materials with a large hadronic attenuation length. It uses scintillating polystyrene [67] tiles and iron absorbers in the barrel part; liquid argon with copper and tungsten absorbers are used in the endcap region.

A multi-level trigger system [68] ensures that out of the 40 million interactions per second the right ones can be selected and recorded with a manageable rate, of the order of 300 Hz.

1.3.1 The ATLAS Pixel Detector

The ATLAS pixel detector [69, 70] is composed of three concentric barrel layers and two end-caps on both sides with three disks each. This geometry, formed by 1744 assemblies is optimised to ensure three hits in the pixel detector up to $|\eta| = 2.5$. The B-layer, which is located at a radius of 5.05 cm, is closest to the interaction point. In Figure 1.5 the structure of an assembly is illustrated. The active part is an n-in-n pixelated silicon sensor of 250 μm thickness and an area of $16.4 \times 60.8\,\mathrm{mm}^2$ yielding a position resolution of 10 μm in Rφ and 110 μm in z. This sensor is connected via solder bump technology to 16 FE-I3 [71] read-out chips, with 2880 read-out channels each, adding up to more than 80 million read-out channels over the whole

[5] The ATLAS coordinate frame is spanned by x, y, and z. The point (0,0,0) is located in the centre of the detector. The x axis points to the centre of the ring and the y axis upwards; righthandedness defines the z axis, which goes along the beam pipe. Alternatively the notation with the azimuth angle φ and the polar angle ϑ is used. The angle $\varphi = 0$ points to the centre of the ring and $\vartheta = 0$ points towards positive z. The pseudorapidity η is defined by $\eta := -\ln\tan(\vartheta/2)$.

pixel detector. The 16 read-out chips on an assembly are connected via the flex—a flexible printed circuit board—to the Module Control Chip (MCC) [72], which coordinates, configures, triggers and reads-out the individual FE-I3 read-out chips. The data are then passed through the pig-tail onto the central read-out architecture. Evaporative C_3F_8-cooling is used to ensure that the pixel detector can always be cooled down to and be operated at $-13\,°C$.

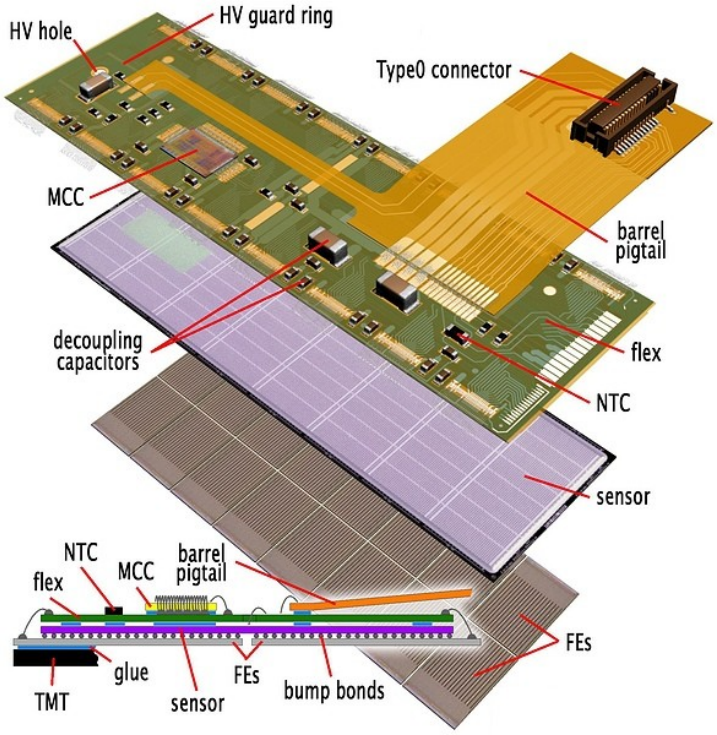

Figure 1.5: Composition of an ATLAS pixel assembly [73].

1.3.2 Upgrade Roadmap

Alongside with the upgrade of the LHC the ATLAS detector will be upgraded in three phases to cope with the increased luminosity rates, which manifest themselves from the detector point of view in high radiation, trigger, and pile-up levels. Additionally, in all upgrade phases the repair and consolidation of detector parts, which where found to be failing during the preceding operational years is foreseen.

Phase 0

During the LS1 a new innermost pixel layer, the Insertable B-Layer (IBL) [74] will be installed at a radius of 3.2 cm between the existing pixel detector and a new beam-pipe. Two sensor technologies are planned to be used for the IBL detectors: silicon 3D [75] and n-in-n silicon planar sensors. Additionally, a new read-out chip FE-I4 [76], which features smaller pitch sizes of $250\,\mu m \times 50\,\mu m$ and an approximately six times larger area than the present ATLAS read-out chip FE-I3 [71] was developed for the IBL. The finer granularity of the pixels, leading to an improved vertex-resolution, is crucial to disentangle the individual vertices in the high pile-up regime after the consolidation phase of the LHC and improves the overall tracking performance.

Because of the small radius and the constrained space it is not possible to arrange the pixel modules with an overlap in z as it is done in the present pixel detector. Thus in the design for the sensors emphasis was put on the maximization of the active fraction.

Phase I

In the second upgrade phase, the aim is to preserve the nominal luminosity trigger acceptance after the LS1 upgrade and to prepare the detector for the LS2 upgrades. The Letter-Of-Intent (LOI) [77] was finished at the end of 2011 and focuses especially on upgrades to the forward regions ($|\eta| \geq 2.5$) of the muon and calorimetry systems, where high occupancies are expected after the LHC upgrade. For the muon system this will be achieved by a small wheel in the forward region equipped with the MICROMEGAS [77, 78] detectors. These micro-pattern gas detectors provide tracking and trigger information. For the calorimetry system the investigations are still ongoing if the forward parts have to be replaced completely already at this point in time or if minor upgrades are able to allow for operation until phase II.

Phase II

In the last currently foreseen upgrade phase, corresponding to the LS3 of the LHC, the focus will be on the inner detector, which by then will be deteriorated by radiation to its design limits and likely require a complete replacement. Additionally, the increased track density will make an improved resolution mandatory at this point in time. A replacement completely based on silicon sensors is planned, and different layouts are under investigation at the moment. The currently planned baseline layout [79] is shown in Figure 1.6. It incorporates four pixel, three short strip (striplet), and two strip layers in the barrel part and six pixel as well as seven strip discs in the forward region. Depending on the physics performance found in future simulations it is planned to readjust the exact numbers of layers for the different technologies, e. g. by adding a fifth pixel layer instead of a striplet layer. In all cases a total of at least 14 hits is envisaged for each particle.

Due to the large total area of at least $7\,\mathrm{m}^2$ foreseen for the future pixel detector, a cost reduction is required for all different components and steps of the assembly procedure, i. e. starting from the sensor over the interconnection to the read-out chip. Additionally, in this harsh radiation environment the innermost layers will have to sustain very high integrated fluences of more than $10^{16}\,\mathrm{n_{eq}/cm^2}$ (1 MeV equiv.) [79]. The performance of differently produced silicon sensors at these extreme levels are explored at the moment by the experiments and within the RD 50 collaboration [80]. Especially, the inner layers have to resolve unprecedented track densities, which are foreseen to be addressed by reducing the pitch for the assemblies in these layers to $25\,\mu\mathrm{m}$ in $R\varphi$. This makes an improvement of the currently used solder bump interconnection technology, or the development of a new one, mandatory, since at the moment only pitches down to $50\,\mu\mathrm{m}$ are possible on a large scale. As for IBL, the innermost layer will be mounted as close as possible to the interaction point impeding overlapping assemblies. This reflects in the requirement of a maximised active fraction of the assembly. Finally, the material budget should be minimised as far as possible, to reduce multiple scattering. Although, the contribution to the material budget by the sensors and read-out chips is small[6] compared to the services, the use of thin sensors and read-out chips is envisaged, since their subsequent lower power consumption also reduces the amount of needed services considerably.

[6] The radiation length of silicon is $X_0 = 21.8234\,\mathrm{g/cm^2} \equiv 9.366\,\mathrm{cm}$ [81, 82].

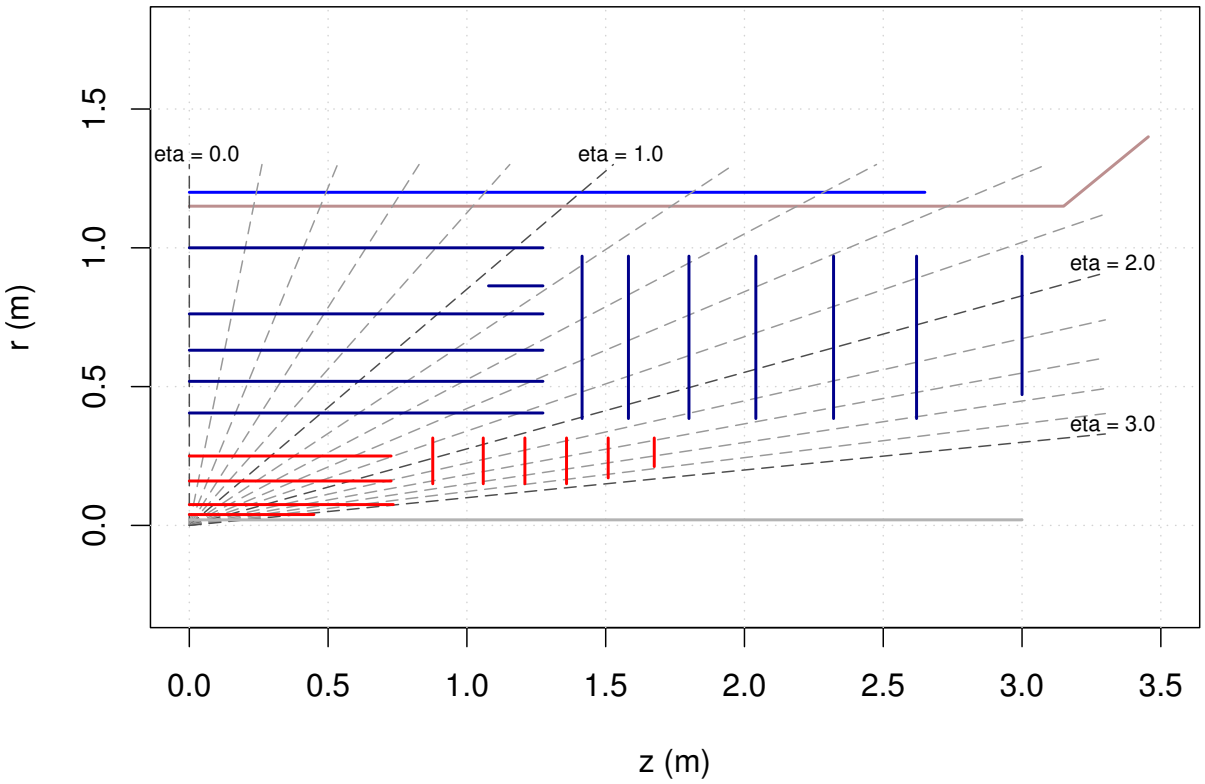

Figure 1.6: Baseline layout of the new inner detector foreseen in the LOI for the Phase II upgrade [79]. Pixel layers are indicates in red, strip and striplet layers are indicated in blue.

In addition to the upgrade of the inner detector, the calorimeter and the muon system will be upgraded mostly in terms of read-out electronics, which are believed to be not radiation hard enough, but also in some of the parts encountering high radiation levels after the upgrade.

1.4 The MPP/MPI-HLL Pixel Assembly Concept

In this thesis an assembly concept designed to answer the challenges of the ATLAS phase II upgrade is investigated. For comparison the current and the investigated pixel assembly concept is illustrated in Figure 1.7. The assembly concept builds upon five novel technologies in the field of pixel detectors and an optimised sensor design. n-in-p pixel sensors are thinned using a process developed at the Max-Planck-Institut HalbLeiterLabor (MPI-HLL) [83] and are connected to the read-out chip via the Solid Liquid Inter-Diffusion (SLID) technology of the Einrichtung für Modulare Festkörper-Technologien (EMFT). Signals are then routed via Inter-Chip-Vias (ICVs) through the read-out chip to the subsequent data acquisition chain. In addition, a newly designed edge area of the sensors is introduced to increase the active area of the detector or prospectively decrease the size of the inactive edge d_{inactive}.

The main arguments in favour of this design and the challenges of these technologies will be given shortly in the following subsections. In the subsequent chapters they will be investigated in depth. This discussion is preceded by an introduction into semiconductor physics, up to the level needed for an understanding of the following investigations in Chapter 2.

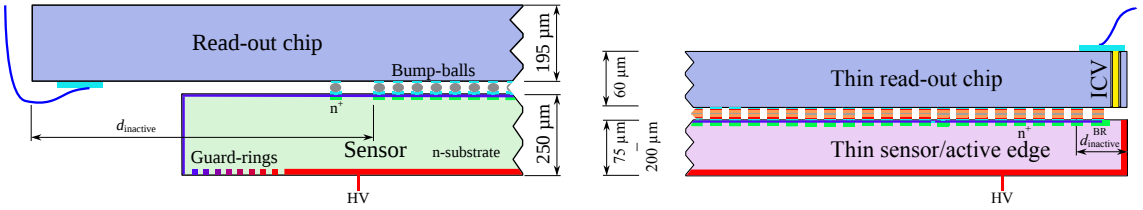

Figure 1.7: (a) Schematics of the current pixel detector assembly structure within the ATLAS experiment and (b) the proposed design. The read-out chip is shown in blue, the sensor in light green (violet) for the current (new) concept. The pixel implants as well as the bias ring n^+-implants are indicated in green, where the implant closest to the edge is the bias ring implant. The back-side and in the new concept case also the edge implantation is indicated in red. Wire bond pads are drawn in light blue, ICVs in yellow. (a) is adapted from and (b) inspired by [84].

1.4.1 n-in-p Sensors

In this assembly concept the n-type silicon substrate used in the current detectors is replaced by a p-type silicon substrate. This approach allows to place the electric field shaping implants, the so-called guard rings, on the same side as the pixel implantations. Consequently, only one side needs expensive patterned processing, resulting in a cost reduction by the sensor fabrication. Up to now n-in-p pixel detectors were not employed in high energy physics experiments due to the prior unavailability of detector grade, high resistivity material and concerns on destructive discharges, due to the close distance between the sensor at high voltage and the read-out chip operated at ground potential. These novel devices were built for the first time in course of this thesis and their overall performance and in special their radiation hardness will be discussed and compared to the currently used n-in-n technology in Chapter 4. Following these investigations the ATLAS collaboration is currently planing to use n-in-p pixel sensors also for the outer layers of the phase II upgrade [79].

1.4.2 Thin Sensors

Exploiting thinner sensors reduces on the one hand the material budget and therefore multiple scattering. On the other hand they have higher electric fields than thicker devices, when the same bias voltage is applied. Thus they exhibit a higher signal collection efficiency after the high radiation doses expected in the environment of the HL-LHC, when employing a read-out electronics capable of working with reduced signal sizes. Since the smaller signal sizes need less read-out time in the ATLAS read-out chips, a lower signal also leads to a lower occupancy of the pixel detector. In addition, the lower needed operation voltages lead to a drastically reduced energy dissipation and lowers the noise levels especially after irradiation. Finally, preliminary simulations are suggesting that the vertex resolution is improved for tracking algorithms, when employing thin sensors, since the reduced diffusion confines the signal to a smaller region in space. Thin pixel sensors with $d_{\text{active}} = 75\,\mu\text{m}$ and $d_{\text{active}} = 150\,\mu\text{m}$ were built and investigated together with thin strip sensors of the same thickness. The results are presented in Chapter 5. After encouraging results obtained in the prototyping runs, 200 μm thick sensors will be used for the IBL-upgrade [74, 85]; for the phase II upgrade 150 μm or thinner sensors are envisaged [79].

1.4.3 3D-Integration

A rather new concept in the field of semiconductor based electronics is 3D-integration [86, 87]. Here several layers of electronics are stacked vertically and are interconnected through the volume of the chip, i. e. its 3^{rd} dimension. As a consequence the lines connecting different logic blocks of the chip become shorter resulting in possibly lower latencies, and lower line capacitances. This leads to a decrease of the noise and lowers the power consumption. When the functional blocks of the chips are distributed over different layers, also the area required to host them is reduced, allowing either for more sophisticated logic blocks in the same area or a decrease of the pixel cell size in the case of pixel detectors.

Furthermore, the different chip layers can either be done within the same processing technologies or with different processes, for example optimised separately for the analogue and digital section of the chip, and then vertically interconnected. In the latter case an interconnection technology is needed that allows for consecutive interconnection of layers without breaking the connections of already connected layers. In this thesis the SLID interconnections, developed by the EMFT [88] is employed, which fulfils this criterion. For the vertical signal transport ICVs are envisaged.

SLID Interconnection

The SLID interconnection, developed by the EMFT [88], is a possible alternative to the currently used solder bump-bonding. After formation of the interconnection at around 300 °C, it has a melting point around 600 °C, and thus fulfils the requirement discussed above. The interconnection pitch can eventually be reduced down to approximately 20 μm [89], which is sufficient for the planned ATLAS phase II upgrades. Additionally, these interconnections can have arbitrary and different geometries. Furthermore, when compared to the currently used solder bump-bonding less process steps are needed, and thus an eventually lower cost is expected.

Inter-Chip Vias

In the assembly concept investigated here ICVs are used to transfer the signal to the back-side of the chip for read-out. By this the active area of the assembly can be increased considerably since the overhanging part of the read-out chip over the sensor, where traditionally the wire bonding pads are placed, can be shortened significantly. Together with the optimised edge region design d_{inactive} is almost completely removed. During the ICV process the read-out chip is thinned to about 60 μm, which leads to a further reduction of the assembly thickness and thus of multiple scattering. After establishing the process and using a adequate read-out chip, the high aspect ratio vias[7] as they are investigated in this thesis could be transferred to a per pixel level. In this scenario two specialised chips—one for analogue and one for digital processing—could be stacked and the remaining overhang could be abolished completely.

1.4.4 Slim and Active Edges

In the present ATLAS pixel design the distance between the last pixel implant and the sensor edge is about 1.1 mm [70]. Additionally, the overhang of the read-out chip contributes about 2 mm to d_{inactive} on one side. This area is insensitive to traversing particles. In the proposed

[7] The aspect ratio is defined by the width of the via divided by its length.

assembly design d_{inactive} is reduced considerably in two ways. First, the ICVs discussed in the preceding paragraph eventually allow to completely remove the balcony. Second, an improved guard ring design and an edge implantation reduces the distance between the last pixel implant and the sensor edge by a factor of 20.

1.4.5 Intermediate Designs for the R&D Process

To disentangle different effects and to study the implications of the individual new technologies presented in the previous sections, these were studied first in an independent way and then integrated into the same module. First the novel p-type bulk material was investigated using the presently used structure of the ATLAS pixel assembly. Additionally, here different variations of the edge designs were studied to increase the active fraction of the assembly. These results will be discussed in Chapter 4. Thin sensors were studied in a two-fold approach: first, as strip sensors, which due to their easier read-out result in shorter R&D cycles, second, as pixel detectors connected via conventional solder bump bonding and SLID inter-connection. The results of thin sensors are presented in Chapter 5. Additionally, a production of thin sensors incorporating active edges was conducted, and first results are reported in Chapter 5 as well.

Aiming for a demonstrator assembly incorporating four of the five new technologies—i. e. n-in-p bulk material, thin sensors, SLID, and ICV—a two step approach was chosen. In the first step the first three technologies are included, while in the second step also ICVs are employed. Both concepts are illustrated in Figure 1.8.

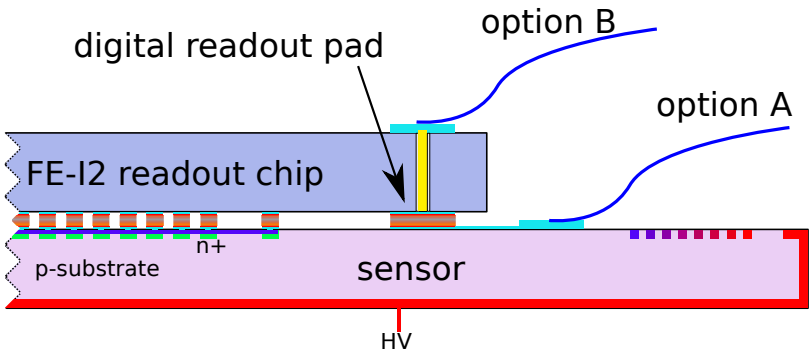

Figure 1.8: Design of the assembly used for the R&D phase of the SLID and ICV technology [84].

In contrast to the currently used ATLAS assemblies both concepts rely on SLID pads instead of solder bump-bonds to connect the sensors pixel cells to the read-out pixel cells. Since the currently used ATLAS read-out chips are employed in this demonstrator assembly, additional SLID pads are placed below the balcony to guarantee mechanical stability. The read-out of the chip is handled differently in both variants. In the first variant, which will be treated in Chapter 6, the wire bonding pads are connected via SLID pads to a fan-out structure incorporated into the sensor design. In the second variant, the signals are routed to the back-side of the chip employing ICVs. This variant will be discussed in Section 6.2.

2 Theory of Radiation Hard Pixel Detectors

In high energy physics experiments, semiconductor based detectors have been replacing gas based detectors in the tracking systems, since they offer a much better position information and an improved energy resolution. Today all experiments, which require high spatial resolution for tracking, employ semiconductor based detectors.

Pixel detectors are segmented semiconductor devices with an area smaller than $1\,\mathrm{mm}^2$ per segment and more than 10^3 segments [90]. The individual segments are called pixels. Given the high cell multiplicity, signals cannot be routed easily from the centre to the edges of the devices and so every pixel cell is individually connected to the corresponding read-out channel of the read-out chip. This approach is commonly called hybrid pixel detector, while special realisations are generally referred to as module or assembly.

Within the read-out chip of a hybrid pixel detector some logic blocks, like the communication interface to the subsequent read-out chain, cannot be distributed to the individual pixel cells because of space constraints. Thus, a region without active counterpart on the sensor side at one side of the chip is needed for connection to the subsequent read-out, leading to a blind spot of the assembly. An alternative approach would be to route the signals to the other side of the read-out chip by etching ICVs through the chip and placing the read-out logics on the back-side.

In the following chapter an introduction to pixel sensors is given with a focus on effects relevant for the investigations presented in this thesis. The chapter is not aiming for a complete introduction to semiconductor physics, which can be found for example in [90–92], and thus many details are omitted.

2.1 Physical Foundations

While electrons in free atoms are confined to discrete energy levels, these levels merge and become bands if atoms are brought to distances typical of the crystal reticule. Depending on the specific element forming the crystal at a temperature T of $0\,\mathrm{K}$, the highest energetic populated band, the valence band, is either fully or partially filled. In the latter case the material is a conductor since the electrons move freely through the crystal within the not filled phase space region. If the valence band is fully filled the material becomes an insulator or semiconductor. The transition between the two states is smooth and is mainly defined by the energy difference between the highest possible energy in the valence band E_V to the lowest energy of the next free band E_C, called conduction band. This energy difference is also called band gap E_g.

If the band gap is small enough, electrons from the valence band can be thermally excited to the conduction band. The probability that a specific phase space state in the band structure is occupied by a charge carrier is described by the Fermi-Dirac-function

$$f_e(E) = \frac{1}{1 + \mathrm{e}^{(E-E_\mathrm{f})/\mathrm{k}T}} \tag{2.1}$$

with k the Boltzmann constant and E_f the Fermi energy. E_f is defined via the macroscopic neutrality of the crystal and thus:

$$E_\mathrm{f} = \frac{E_\mathrm{C} - E_\mathrm{V}}{2} + O(0.01\,\mathrm{eV}) \approx \frac{E_\mathrm{g}}{2} \tag{2.2}$$

which corresponds to the middle of the band gap.

Silicon is the most commonly used semiconductor material thanks to its wide availability, its low price and the high technological level reached in its processing. It is an element semiconductor which crystallizes in the diamond structure and has a minimal band gap of $E_\mathrm{g}(300\,\mathrm{K}) = 1.12\,\mathrm{eV}$.

2.1.1 Intrinsic and Extrinsic Semiconductors

If the crystal is *intrinsic*, i. e. without or with a negligible amount of impurities, the charge carrier concentrations, measuring the occupied phase space states which can move freely through the crystal, for electrons $\mathrm{n_e}$ and positive states—also called holes—$\mathrm{n_p}$ are in an equilibrium state and equal the so-called intrinsic charge carrier concentration $\mathrm{n_i}$. For silicon this is $\mathrm{n_i}(300\,\mathrm{K}) = (1.09 \pm 0.09) \cdot 10^{10}\,\mathrm{cm}^{-3}$ [93]. This is typically below minimum concentration of impurities that can be achieved in the semiconductor industry, lying at $10^{12}\,\mathrm{cm}^{-3}$.

To define and control the properties of the silicon, additional dopants are used, which means certain impurities are introduced artificially to enhance either $\mathrm{n_e}$ or $\mathrm{n_p}$. The most commonly used dopants are atoms from the III (e. g. boron) or the V (e. g. phosphorus) main group of the periodic system of the elements. The former type of dopants leads to additional holes in the crystal since these atoms are not able to form bonds with all their neighbours. In the band scheme this corresponds to the introduction of an additional acceptor level E_A at (20–60) meV above the valence band (Figure 2.1(a) left) depending on the element used [91]. Silicon doped in this way is called p-type silicon. If instead atoms of the V main group are used for the doping, additional electrons are introduced since they are superfluous to form the bonds in the crystal. In the band scheme this is represented as a new donor level E_D at (40–50) meV below the conduction band (Figure 2.1(a) right) depending on the element used [91]. This type of silicon is called n-type silicon. In both cases the newly introduced levels are so close to either the valence or the conduction band that thermal excitation leads to an almost complete excitation of the newly introduced states resulting in a shift of the Fermi energy towards the respective newly introduced level. Hence, electrons are the majority charge carriers in the n-type material ($\mathrm{n_e} \gg n_\mathrm{p}$) and holes respectively in p-type material ($\mathrm{n_p} \gg n_\mathrm{e}$).

2.1.2 The pn-Junction

The basic principle of a pixel sensor is a pn-junction which is reversely biased and thus leads to an electric field able to collect the charge. A pn-junction is created by bringing together p-type silicon with n-type silicon as shown in Figure 2.1(b).

In the transition zone from n- to p-type the free electrons from the n-type will diffuse to the p-type part and neutralize free holes, which themselves will diffuse into the n-type part and neutralize free electrons. Since the movable charge carriers are neutralised only the fixed charges stay, namely the ionised donors in the n-type part and the ionised acceptors in the p-type part. In sum this leads to a region with a non vanishing charge ρ, the space charge region. The

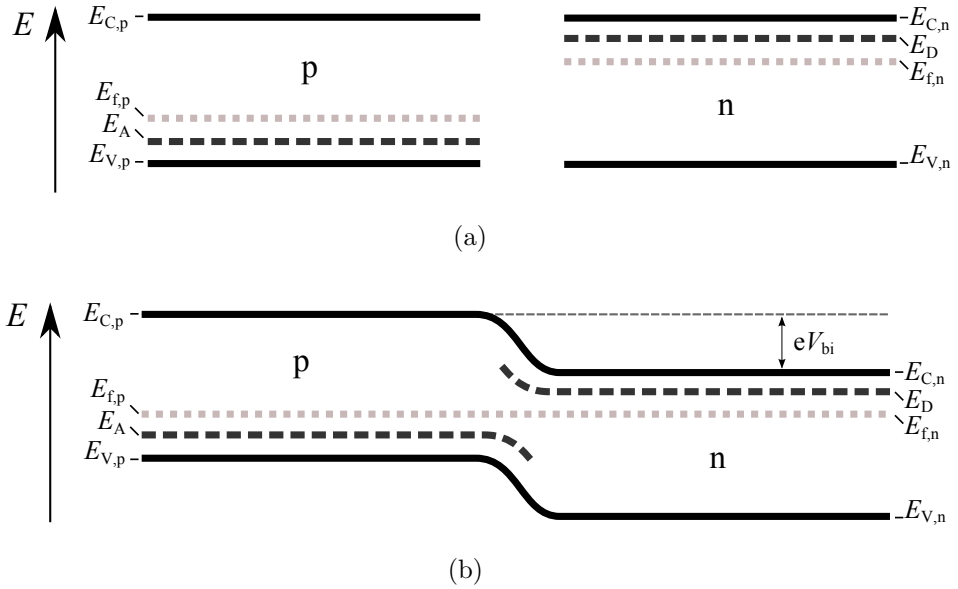

Figure 2.1: Schematics of a pn-junction. (a) Illustrates on the left (right) the different energy levels in p-type (n-type) silicon. In (b) the configuration after bringing the differently doped regions together is drawn. Four different energy levels E are indicated for each type by an index, where C (V) denotes the lowest (highest) level in the conduction (valence) band, A (D) the acceptor (donator) levels and f the Fermi energy. Additionally, states in p-type and n-type silicon are differentiated by the index p and n.

resulting potential ϕ prevents further diffusion of charge carriers and can be calculated via the Poisson equation:

$$-\nabla^2\phi = \frac{\rho(x)}{\epsilon\epsilon_0} \tag{2.3}$$

Outside of the space charge region, $\rho(x)$ vanishes, since the mobile charge carriers neutralise the acceptors and donors. The maximal potential difference ϕ is called built-in voltage V_{bi}, which is of O(1 V), see Figure 2.1(b). If an external voltage is applied to the pn-junction it can be either of opposite or same polarity as V_{bi}. The former scenario is referred to as forward bias, the second as reverse bias. Since the latter is the standard operation setting for pixel detectors, in the following reverse bias will be defined as positive.

In forward bias, charge carriers are forced back into the depleted zone, which eventually becomes a conducting zone. This leads to an exponentially rising current. On the contrary reverse bias further removes free charge carriers from the not yet depleted regions and thus enlarges this region. The width of the depleted zone W is proportional to

$$\sqrt{V + V_{\mathrm{bi}}} \approx \sqrt{V} \tag{2.4}$$

where V is the applied bias voltage. Since charge creation takes place predominantly in the depleted region, its width before irradiation is proportional to the obtainable signal height. The voltage for which the width of the depleted zone equals the thickness of the detector d is called full depletion voltage V_{fd}. A pn-junction operated at even higher voltages is said to be over-depleted and the electric field is incremented by a constant field of $(V - V_{\mathrm{fd}})/d$.

2.1.3 Charge Generation

The two most important effects of charge carrier generation in pixel detectors in stable operation are the mentioned thermal excitation and the generation by charged particles.

The signal generation by heavy charged particles originates from many scattering interactions of the particles with the electron clouds of the crystal lattice leading to an energy transfer. The average energy transfer per traversed length of material is described by the Bethe-Bloch-function [94, 95]. Dividing the resulting energy by the average energy needed to create an electron hole pair in silicon, of 3.6 eV/e [96] leads to the average signal height which can be expected from a device. This average value is higher than the Most Probable Value (MPV) Δ_p since the former also accounts for large energy deposits resulting from knock-on- and δ-electrons[1]. The whole spectrum is described by a Landau-distribution shown exemplary in Figure 2.2(a) for different sensor thicknesses. As shown, the effect of knock-on and δ-electrons gets smaller for thinner detectors since they are not fully stopped within the sensor volume. In Figure 2.2(b) the MPV of the charge corresponding to the generated electron-hole pairs is drawn as a function of the sensor thickness for different impinging particle types and energies and momenta respectively. The curves are calculated using the equations given in [97, 98] and the values of the occurring physical constants and material parameters from [82, 96, 97]. Particle types used in this thesis

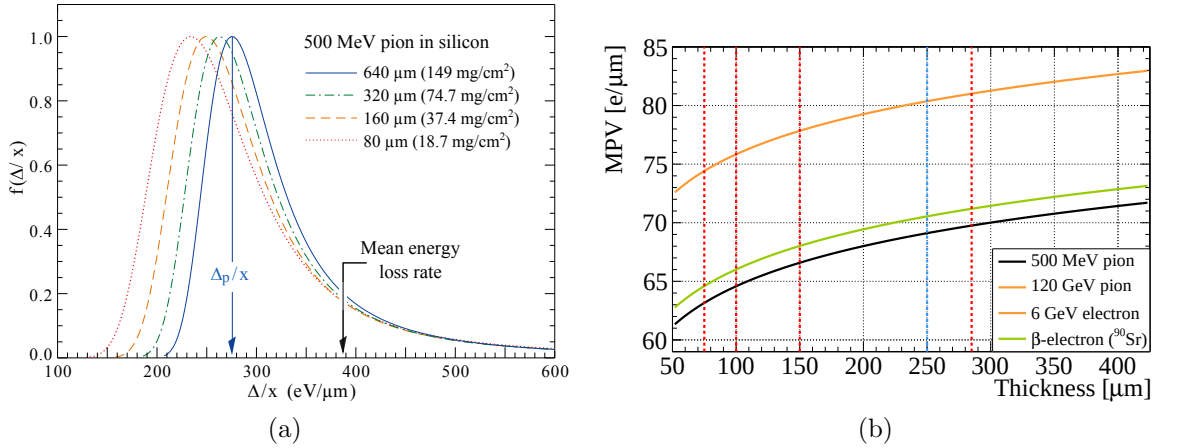

(a) (b)

Figure 2.2: (a) Probability distribution for charge deposition in silicon for $E = 500\,\text{MeV}$ pions, normalised to unity at the MPV Δ_p/x. Adapted from [97]. (b) Dependence of the MPV of generated electron-hole pairs per μm on the thickness of the sensor for pions with the same energy as in (a) (black line), for $p = 120\,\text{GeV}$ pions delivered by the CERN SPS (orange line), and for $E_\text{max} = 2.280\,\text{MeV}$ β-electrons from the ^{90}Sr decay chain (green line). Electrons with 6 GeV as delivered by the DESY II facility are indistinguishable from pions with 120 GeV and thus not indicated by the same colour. The dotted lines indicate the thicknesses of the sensors investigated in this thesis (red) and of the currently used ATLAS sensors (blue). The curves are calculated using the equations given in [97, 98] and the values of the occurring physical constants and material parameters from [82, 96, 97].

[1] Knock-on-electrons are electrons which acquired energy by inelastic scattering with the impinging particle. δ-electrons are secondary electrons arising from the ionisation process.

are highlighted in colour. The β-electrons indicated by the green line originate from the ^{90}Sr decay chain [99]

$$^{90}Sr \rightarrow e^- + \overline{\nu}_e + ^{90}\mathrm{Y} \quad (T_{1/2} = 28.8\,\mathrm{a}, E_{\max} = 0.546\,\mathrm{MeV}) \tag{2.5}$$

$$^{90}\mathrm{Y} \rightarrow e^- + \overline{\nu}_e + ^{90}\mathrm{Zr} \quad (T_{1/2} = 2.67\,\mathrm{d}, E_{\max} = 2.280\,\mathrm{MeV}). \tag{2.6}$$

Electrons with an energy of four to six GeV delivered by the DESY II facility are indistinguishable from pions with 120 GeV and thus indicated with the same colour. For the currently employed 250 μm thick sensors of the ATLAS pixel detector, a MPV of 80 electron-hole pairs per μm is found and often used as estimator.

The leakage current, i. e. the remaining current in the static reverse bias mode is mostly driven by charge carriers generated by crystal impurities within the depleted region. Thus, this current is

$$I_{\mathrm{vol}} \propto W n_{\mathrm{i}} \propto W T^2 \mathrm{e}^{-E_{\mathrm{g}}/2\mathrm{k}T} \tag{2.7}$$

scaling strongly with the temperature T and the size of the band gap E_{g}. Approximately for every 8 K temperature increase the leakage currents doubles. The leakage current, that is detrimental for the noise performance of the tracking detectors, can thus be considerably reduced by cooling. In extreme environments, where no sufficient cooling can be supplied, diamond based detectors are a possible choice, given their large band gap of 5.5 eV [100] that induces lower leakage currents, at the price of a reduced signal size.

2.1.4 Charge Carrier Transport

To induce a measurable signal on the electrodes the charge carriers have to move along the electric field direction, in addition to the thermal diffusion that happens homogeneously in space. On top of the thermal diffusion the applied electric field imposes a preferred drift direction on the free charge carriers. Due to the structure of the crystal the mean free path between two collisions with the lattice is O(1 μm). At an electric field of the order of 100 kV/cm [91] this eventually leads to a saturation of the drift velocity v_{drift}, which up to the saturation is proportional to the electric field with the proportionality factor mobility denoted with μ. At 300 K the mobilities for intrinsic silicon are [93]:

$$\mu_{\mathrm{n}} = (1430 \pm 46)\,\mathrm{cm}^2/(\mathrm{Vs}) \tag{2.8}$$

$$\mu_{\mathrm{p}} = (480 \pm 17)\,\mathrm{cm}^2/(\mathrm{Vs}) \tag{2.9}$$

with μ_{n} (μ_{p}) being the mobility of electrons (holes); so electrons are moving a factor three faster than holes and are thus less prone to be trapped in crystal defects.

2.2 Radiation Damage

The vicinity of semiconductor tracking detectors to the interaction point leads to high particle fluxes on the detectors inducing two main classes of defects: surface and bulk defects.

The former class refers to all defects in the interface region and in the dielectric layers deposited on the surface of the sensors for protection purposes. In case of the very high fluences of charged hadrons in the tracking detectors at HL-LHC, the bulk damage is the limiting factor in the operation of silicon detectors and it will be the focus of the following discussion.

2.2.1 Bulk Defects

Bulk defects are displacements of atoms within the volume of the crystal lattice caused by energy transfers by the impinging particles. In high energy physics experiments they are predominantly caused by charged hadrons and neutrons interacting with crystal atoms rather than by interacting with the electron cloud. Depending on the energy of the impacting particle, either point defects, like interstitials and vacancies (cf Figure 2.3), or clusters of defects can be

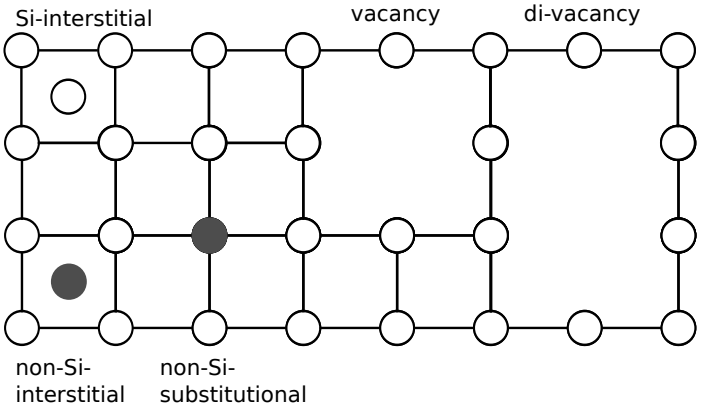

Figure 2.3: Illustration of the different elementary defect classes after [101].

formed. Charged hadrons (i. e. pions and protons) interact with silicon primarily due to Coulomb interaction and ionization of lattice atoms whereas neutrons (with no charge) interact only with the silicon nuclei. To study the irradiation induced effects on sensors, these are irradiated with different particle types and fluences to reproduce the radiation environment in the inner detector at HL-LHC. A basic hypothesis called Non-Ionizing Energy Loss (NIEL) states that any damage induced change in the material scales linearly with the energy transferred in the collision. As one is usually dealing with different irradiation sources with continuous energy spectra, it is convenient to define a so-called hardness factor k that integrates the damage function $D(E)$ [102] over the energy spectrum and scales it to the equivalent displacement damage cross section of mono-energetic 1 MeV neutrons (n_{eq}). The hardness factor can be derived from leakage current measurements of diodes. For all commonly used irradiation facilities it is known and published. An overview of the key parameters for the irradiation sites used for the investigations presented in the following is given in Section 3.3.

Effects of Radiation in Silicon Detectors

While primary point defects like vacancies and interstitials can move freely through the crystal, more complex combinations of these and clusters are stationary in the crystal. Because of their charge they can be understood as additional energy levels in the band gap like the ones introduced by the doping process. They change the concentration and distribution of the space charge depending on their nature towards a more negative or more positive regime. To account for this effect the doping concentrations are substituted by the effective doping ΔN_{eff} or $|N_{\mathrm{eff}}|$ defined as the absolute difference of all acceptor like states and all donor like states. It can be shown that

$$V_{\mathrm{fd}} \propto |N_{\mathrm{eff}}| \tag{2.10}$$

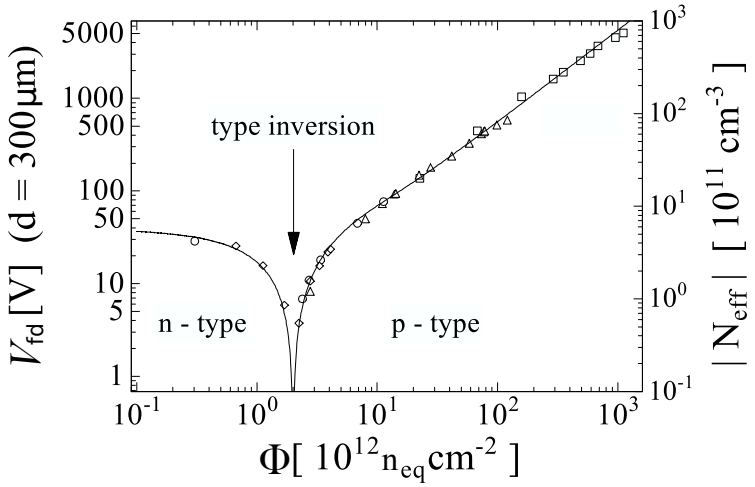

Figure 2.4: Evolution of V_{fd} and $|N_{\mathrm{eff}}|$ for an n-type sensor with the received NIEL-fluence [101].

The typical evolution of V_{fd} and $|N_{\mathrm{eff}}|$ with the received fluence for an n-type sensor is shown in Figure 2.4. After a received fluence of $\sim 10^{12}\,\mathrm{n_{eq}/cm^2}$ initially n-type doped material changes to be effective p-type material. This point was reached in ATLAS for the innermost pixel detector layer in the summer of 2012, i. e. after collecting about $20\,\mathrm{fb}^{-1}$ of collision [103]. The increase of V_{fd} makes it technically difficult to fully deplete the sensor after irradiation at high fluences. If this happens, due to the reduced active volume also the signal height is reduced, demanding read-out electronics capable of handling the high dynamic range reaching from high signals, that can be obtained before irradiation, to small signals typical of irradiated devices.

Besides, the increased full depletion voltage also the leakage current I_{leak} per volume V increases as

$$\frac{I_{\mathrm{leak}}}{V} = \frac{I_{\mathrm{vol},\Phi=0}}{V} + \alpha\phi \tag{2.11}$$

where ϕ is the equivalent fluence and $\alpha = I_{\mathrm{vol},\Phi}/V$ is the current related damage rate. All currents have to be taken for a fully depleted sensor at 20 °C. On the one hand an increased leakage current leads to a higher noise and on the other hand it significantly increases the dissipated power, especially in combination with the given higher voltages needed to deplete the sensor. Since the subsequent rise of temperature enhances further the current (cf. Equation 2.7) this develops into a positive feedback loop and thus sufficient cooling is needed.

A third issue arising from radiation damage is charge trapping. Predominantly, in the depleted regions, crystal defects acting as traps are empty and can trap charge carriers. As typical trapping times are higher than read-out times used at high energy physics experiments [104], trapped charges are lost for signal generation leading to a further reduced signal. Due to their lower mobility holes are much more prone to be trapped in different crystal defects.

Annealing

As some defects can move freely through the crystal, they can anneal, e. g. a silicon interstitial could fill a vacancy in the lattice. The velocity of the annealing process depends on the average velocity of the movable defects, which in turn depends heavily on the temperature. A summary

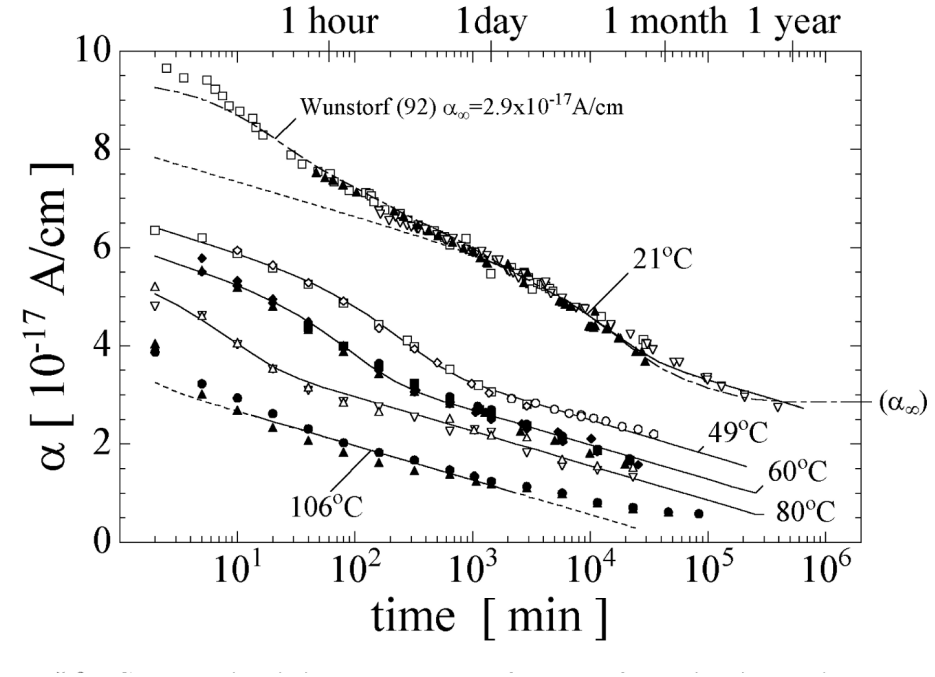

(a)

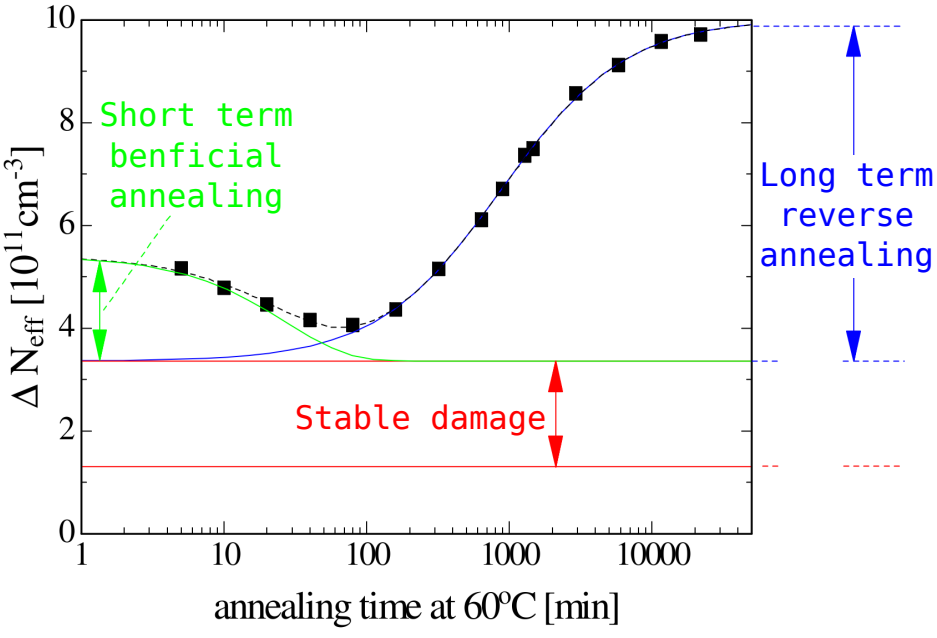

(b)

Figure 2.5: (a) The damage factor α as a function of the annealing time at different temperatures. (b) Annealing behaviour of $|N_{\text{eff}}|$ at 60 °C. Both figures are taken from [105].

of the damage factor evolution for different annealing times at different temperatures is given in Figure 2.5(a). The beneficial impact on the leakage current is reflected in the decrease of the damage factor.

For the effective doping or the bias voltage respectively the annealing process is subdivided into two periods, cf. Figure 2.5(b). In the beneficial annealing period which extends roughly for the first 100 minutes at 60 °C, V_{fd} is reduced to a minimum. Afterwards, the reverse annealing process sets in and leads to an increase of the V_{fd}, exceeding the initial V_{fd} directly after irradiation. To prevent entering the reverse annealing phase, the cooling systems of the LHC experiments are kept running whenever possible.

2.2.2 Charge Multiplication

Recent results [106–108] indicate that for high received fluences of $\mathrm{O}(10^{15}\,\mathrm{n_{eq}/cm^2})$ and high bias voltages more charge carriers are collected within the sensor than predicted by the generally accepted trapping model [104, 109]. This effect is referred to as charge multiplication and up to now was reported only for strip sensors, but not for pixel sensors. It was found that in segmented devices for tracking in high energy physics experiments it originates in the high electric field regions under the electrode implants [110, 111]. Nonetheless, a full theoretical understanding was not yet obtained. If multiplication is exploited in a controlled way, it is an excellent mechanism for highly irradiated detectors in hadron colliders, since the signal to threshold ratio is improved.

2.3 Basic Design Considerations

In the following section an introduction to the basic design considerations for segmented silicon sensors, and pixel sensors in special, are given. First some commonly used special structure types in the design are described. This is followed by a review of possible bulk and pixel implant choices.

2.3.1 Special Structures

In addition to the pixel implants and metallizations, some additional structures are included in most pixel detectors. The most important are described in this section.

Guard Rings and Active Edges

Due to the cutting process of the wafer and the thereby induced damage, the sensor sides have to be considered conductive and highly inhomogeneous. Thus any potential applied to the back-side will eventually be present along the sides and at the upper edge of the sensor. In contrast, the nearby pixels are kept at ground potential and the transition to the edge would be uncontrolled without the presence of dedicated field-smoothing structures. Depending on the actual field shape this could lead to high leakage currents and/or low breakdown voltages. Additionally, when the depletion zone reaches the sensor side, characterised by a damaged crystal structure, it would induce the electrical breakdown of the device.

As a counter-measure, additional implants and metal layers are inserted into the sensor design to shape the field in a defined way. These so-called guard rings are self-biasing via the punch-through mechanism [92]. They are typically placed on the same side as the pn-junction, i. e. on the back-side in the n-in-n case, Figure 2.6(a), or on the pixel side in the n-in-p case,

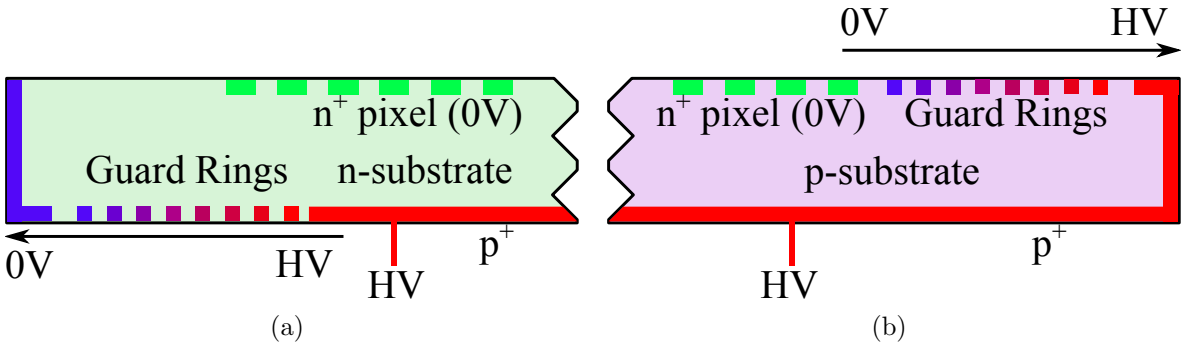

Figure 2.6: Schematic of electric potential distribution for (a) n-in-n sensors and for (b) n-in-p sensors. The $^+$ indicates a higher doping concentration.

Figure 2.6(b), since depletion starts from this side. Another option, which can be used also in combination with guard-rings, is to extend the back-side implant to the vertical sides, and thus define the electric field also in this region. This latter concept is commonly called active edge. It is not yet widely used in experiments, since the concept was introduced only recently and has special processing requirements. Since the number of guard rings and the safety margin to the side can be reduced, it allows to drastically increase the active fraction of the sensor.

Punch Through

To increase the module yield, testing of the most expensive detector components—i. e. the sensor and the read-out chip—before interconnection is desirable. While this is easily implemented for the read-out chips via probe cards attached to the read-out connections, for the sensor a grounding of all individual pixels is needed to accomplish a realistic field distribution.

This is achieved by implementing a biasing structure directly into the sensor using an additional implant in proximity to the implant to be biased. The additional implants are then all connected to a common metal line which can be contacted with a needle. A further advantage of this approach is that even not connected pixels are kept at ground potential after connecting the sensor to the read-out chip and thus the risk of electrical discharges is reduced. On the other hand, the additional implants are not connected to the read-out and thus charges drifting to the punch-through structures are lost. So a lower charge collection efficiency is expected here.

Interpixel Isolation

Close to the surface of the sensor an electron accumulation layer is formed due to the positive space charge of the oxide or nitride layer used as passivation. This layer would lead to a shortening of neighbouring pixels, and thus destroy the position resolution if the used read-out electrodes are n-type. Therefore these pixel cells are typically isolated from each other using either a so-called p-stop or a p-spray interpixel isolation. Both approaches employ an additional p-type implantation. In the case of p-stop, a high dose implantation is placed in between two n-type implants as drawn in Figure 2.7(a). Since this process demands a very good alignment it limits the minimal pitch. Also an additional mask for patterned implantation is needed, thus rendering this process more expensive. For the p-spray isolation, Figure 2.7(b), a homogeneous

low dose p-implantation is used. Its implantation dose has to be chosen very carefully, since a too high dose creates a region with high electric field at the border with the n^+-implantation[2] of the electrode, leading to a breakdown of the junction [112], and a too low dose does not isolate the pixels from each other. The advantage is that lower pitches are possible and that, provided the correct dose is found, the production yield is higher since no alignment is needed. Sometimes an intermediate form the so-called moderated p-spray, Figure 2.7(c), is used. Here the implantation doses can be chosen lower, leading to less pronounced electric fields in these critical regions and thus lower risk of breakdowns occurring here. Still it has the same alignment requirements as the p-stop isolation approach.

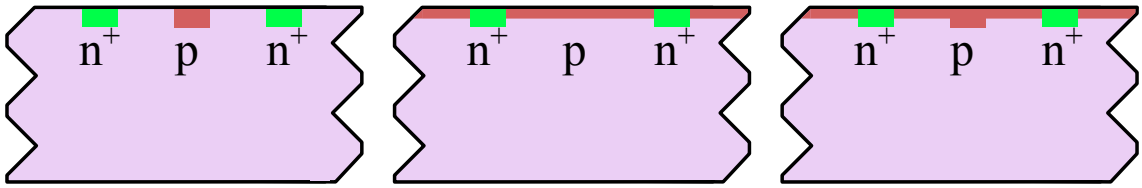

(a) (b) (c)

Figure 2.7: Schematic of different inter-pixel isolations: (a) p-stop, (b) p-spray, and (c) moderated p-spray.

2.3.2 Bulk Materials

When designing a pixel detector four combinations are possible. Either n- or p-substrate can be used, which then may be combined with either n- or p-type collection electrodes. If the collection electrodes have an opposite doping (i. e. p-in-n and n-in-p) the pn-junction is formed at the read-out electrode side and the sensor depletes from there. If the same doping is chosen (i. e. p-in-p and n-in-n) the junction will develop from the unstructured back-side implantation, and position resolved information can only be obtained after fully depleting the sensor.

Currently implantations penetrating only the surface as shown in Figure 2.6 are used. These detectors are called planar. For the IBL upgrade for the first time in large high energy physics experiments so-called 3D sensors [75] may be used in addition. In these devices the read-out electrodes extend into the substrate. This has the advantage that the effective charge collection distance is reduced dramatically, if the columns are placed close enough. But since the production of these sensors is extremely complicated and relies on many not yet industrially used processes, their price is much higher, rendering their use for large scale applications unattractive. The four types of planar pixel detectors will be shortly introduced with their respective advantages and disadvantages.

p-in-n

Historically only n-type material was available with the purity and high resistivity needed for detectors in high energy physics experiments, that rely on the full depletion of the sensor volume. The simpler technology to be used with n-type detectors is a pixelated junction on the front-side. The depletion starts from the electrodes, allowing for the use of the sensor already before it is fully depleted. Also the pixels are naturally insulated from each other, making

[2]The $^+$ stands for a higher doping concentration.

special inter-pixel-isolation techniques superfluous and thus the sensor less prone to processing irregularities leading to early breakdown voltages.

Since the p-type electrodes correspond to a signal collection via the slower holes, these detectors are affected more by trapping effects than sensors collecting electrons, which is especially a challenge after irradiation. After the type inversion the detector is depleting from the back-side which poses the additional challenge that the field is lowest at the electrodes and it may not be possible to fully deplete the sensor at all.

Still, if radiation fluxes are not too high, e. g. further away from the interaction point, they are the method of choice for their cost effectiveness and simplicity in design. They are used for example in the SCT detector of ATLAS.

n-in-n

Instead of using p-type electrodes, n-in-n detectors use n^+-type implants for the electrodes. To achieve the pn-junction an additional unstructured p-type electrode is implanted on the back-side, from which the depletion zone develops. Thus, n-in-n detectors before type-inversion can only be used fully depleted and should be operated over-depleted since the electric field is weakest at the pixel implant side. Since the edges of the sensors are conductive due to the cutting-process the p-type implantation has to be insulated from these edges to prevent a short in the junction. This can be achieved by placing the anyhow needed guard rings to the back-side as well. This has two further advantages. Since the edge of the backside is already at ground potential, the high voltage is neither present at the front-side edge close to the read-out chip at ground potential nor near the individual pixel implants at ground potential. In addition the pixelated area on the front-side could be extended further towards the edges, i. e. above the guard rings on the back-side thus increasing the active area of the sensor [113, 114]. This approach was adopted for example for the IBL planar n-in-n sensor [85].

n-in-p

Nowadays, also p-substrate is available at the needed quality for high energy physics applications in terms of purity and resistivity and n-in-p detectors have become attractive in this field. The n^+ electrodes that form the pn-junction are placed on the front-side and hence these detectors do not need a structured processing of the back-side if the guard rings are placed on the front-side as well. This makes them cost effective—an important factor to build large area pixel detectors. Also, due to the depletion from the front-side they can be operated before full depletion and the electric field is always strongest at the front-side. As n-in-n detectors they collect electrons and are thus more robust against trapping effects.

A potential challenge is the high voltage which is also present at the edge of the front-side via the cutting edge and needs to be shielded from the read-out chip, that has its surface at ground potential and faces the sensor at distances of the order of 10 μm. Here destructive electrical discharges are a concern and were observed [115].

Nonetheless, this is a solvable issue as will be shown in Chapter 4 and thus n-in-p pixel sensors are a cost-effective competitor on par with n-in-n detectors.

p-in-p

The last option is not used since it is expensive due to the double sided processing and suffers from trapping due to read-out based on hole collection.

3 Methodology

Several experimental set-ups and methods were used to obtain the results discussed in the following chapters. They are introduced together with a discussion of their respective advantages, disadvantages and uncertainties. First, two basic methods are described; in Section 3.1 the measurements of IV characteristics and in Section 3.2 an infra-red light method with a general scope. This is followed by an overview on the employed irradiation sites. Sections 3.4 and 3.5 cover two methods for charge collection measurements of strip sensors. Finally, the laboratory (Section 3.6) and beam test (Section 3.7) set-ups for pixel detectors are discussed.

3.1 Measurement of IV Characteristics

IV characteristics, i. e. the leakage current as a function of the applied bias voltage, are a powerful tool in sensor evaluation. Besides, the determination of the operational boundaries, like leakage currents and breakdown voltages, it allows to spot defects, like scratches, of the devices and processing inhomogeneities easily, since most production issues result in an increase of the leakage current.

IV characteristics are taken using the Keithley 6517A or 6517B picoampermeters in an automated way. Each measurement is repeated ten times to allow for a determination of statistical uncertainties. Irradiated structures were cooled either by a coolable chuck or within a climate chamber. In the first case $-10\,^{\circ}\mathrm{C}$ can be reached, while in the second case environmental temperatures down to $-70\,^{\circ}\mathrm{C}$ are possible.

3.2 PHEMOS

To identify critical points within the sensor design the infra-red emission of sensors, operated close to their operational limit, is analysed. Infra-red light arises from recombination or emission of photon bremsstrahlung in high charge carrier regimes as they occur when a junction breaks down.

For these measurements the Hamamatsu PHEMOS-1000 [116] is used, which is composed by a low noise infra-red-sensitive CCD camera cooled to $-50\,^{\circ}\mathrm{C}$ coupled to microscope optics allowing for magnification factors up to 100. High voltage and ground potential are applied via probe needles to the biasing and grounding structures. The whole set-up is situated within a box which shields ambient light.

To obtain an infra-red picture, the sensor is operated as close as possible to the operational limit, e. g. in a breakdown or in a high current regime. The obtained infra-red image is then overlayed with an image taken in visible light. In Figure 3.1 a picture obtained with the PHEMOS system is shown for a strip sensor with a visible breakdown (red point) occurring in a punch-through structure. In grey the metallization and the silicon is visible, while the infra-red light emitted during the measurement is indicated in false colours.

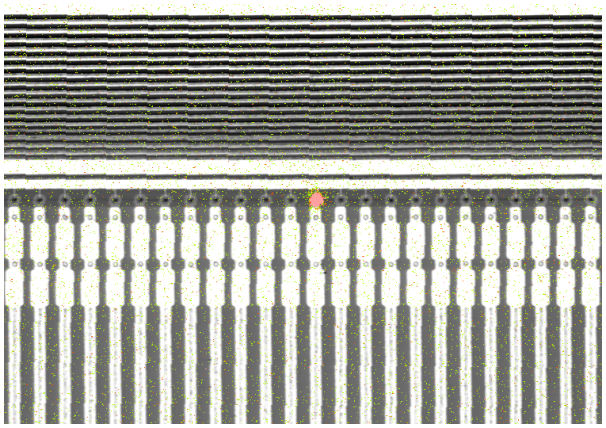

Figure 3.1: Exemplary PHEMOS picture for a strip sensor with a visible breakdown (red point) in a punch-through structure.

3.3 Irradiation Sites

During the course of the investigations several different irradiation facilities were used. They are briefly described in the following and their parameters like energy and hardness factor for scaling the received fluences to n_{eq}/cm^2 are given.

TRIGA Mark II research reactor (Ljubljana)

The reactor centre of the Jožef Stefan Institute (JSI) in Ljubljana [117] offers the possibility for irradiations with reactor neutrons having a continuous energy spectrum. Neutrons having an energy above 100 keV are available with a steerable flux up to $5 \cdot 10^{12}\,n/cm^2s^{-1}$ and a damage factor of 0.9. Since the size of the irradiable objects is limited and shielding is difficult in the reactor environment only bare sensors or assemblies can be irradiated. The subsequent handling to remount the assemblies demands for some unavoidable annealing of around 1.5 d at room temperature. The irradiation of FE-I4 assemblies is problematic since tantalum contained in the read-out chip is activated during irradiation and thus the assemblies cannot be handled without severe radiation protection for several months. The dosimetry is obtained indirectly from the known flux of the reactor, which is periodically calibrated by measuring the leakage current of silicon diodes.

PS (CERN)

For high energy protons the CERN PS irradiation facilities in the east hall can be used. The momentum of the protons is 24 GeV and the flux reaches $(2\text{–}9)\cdot 10^9\,p/cm^2s^{-1}$. This in combination with the hardness factor of 0.62 [118] leads to rather long irradiation times. The diameter of the beam is 2 cm which allows to irradiate samples up to this size without scanning over the sample. The dosimetry is either measured through the activation of an Al foil or with an NaI, or Ge spectrometer.

LANSCE (Los Alamos)

Protons with 800 MeV are available through the Los Alamos National Laboratory spallation neutron sources (LANSCE) [119]. The achievable flux lies at approximately $1.5 \cdot 10^{12}\,\mathrm{p/cm^2 s^{-1}}$ and the hardness factor is 0.71. Given the beam spot size of roughly 2 cm even for FE-I4 assemblies almost no scanning of the beam over the sample is needed. There is no cooling available during the irradiation and due to the activation of the boards only bare sensors or assemblies can be irradiated, leading to an unavoidable annealing time of 1.5 d at room temperature due to the remounting time.

Compact Cyclotron (Karlsruhe)

Low energy protons are delivered for irradiation by the Zyklotron AG which operates a cyclotron at the Karlsruher Institut für Technologie (KIT) [120, 121]. The protons have an energy of 23 MeV and are delivered with a typical beam current of approximately $9 \cdot 10^{12}\,\mathrm{n/cm^2 s^{-1}}$. A scanning table allows to homogeneously irradiate samples which are bigger than the beam spot size of 7 mm. The hardness factor is 2.0. To prevent annealing, samples are cooled during irradiation. The dosimetry is achieved via a measurement of the ^{57}Ni-activity in a Ni-foil. Due to the availability of shielding and space, samples can be irradiated with attached read-out boards, which saves re-bonding and thus handling time at room temperature. A big drawback is that the ATLAS read-out chip FE-I3 cannot withstand fluences of these low energy protons higher than $10^{15}\,\mathrm{n_{eq}/cm^2}$ and thus higher fluences are not accessible for these.

3.4 ALiBaVa Readout System

Within the RD 50 collaboration the Analogue Liverpool Barcelona Valencia (ALiBaVa) read-out system [122, 123] was developed to allow charge collection measurements using LHC read-out electronics. It is based on the Beetle ASIC[1] [124], which was developed for the LHCb experiment [11]. Fast and cost effective R&D cycles are achieved with strip sensors, since wire-bonding allows for reuse of the read-out chips, and it is performed at the Max-Planck-Institut für Physik (MPP).

In Section 3.4.1 the instrumentation of the system as used at MPP will be introduced followed by a discussion of the data acquisition and analysis chain in Section 3.4.2. Finally, the measurement uncertainties are introduced in Section 3.4.3.

3.4.1 Instrumentation

The system consists of two main components—the mother and the daughter board, see Figure 3.2(a). Test structures are wire-bonded via an 80 μm pitch adapter to a Beetle chip, of which two are located on the daughter board for parallel operation. While the daughter board together with the sensor under test can be placed in a cooled environment, as it is necessary for the measurement of heavily irradiated sensors, the mother board is operated at room-temperature. It receives the signals of the daughter board, as well as of the trigger system. An USB[2] interface on the mother board allows for steering of the system with a computer.

A Beetle chip has 128 input channels (see Figure 3.3) with independent amplifiers and pulse shapers. The output signal of the shaper rises in around 25 ns from 10 % to 90 % of the peak

[1] Application Specific Integrated Circuit
[2] Universal Serial Bus

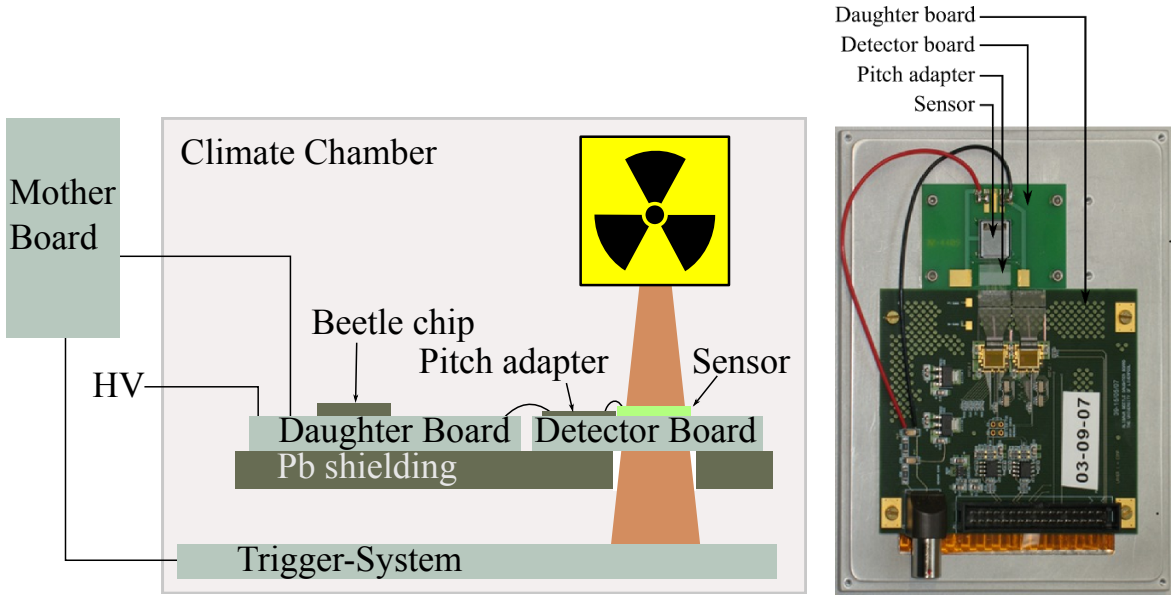

Figure 3.2: (a) Schematic drawing of the ALiBaVa set-up. (b) Photograph of the daughter and detector board with a sensor and the decoupling pitch adapter.

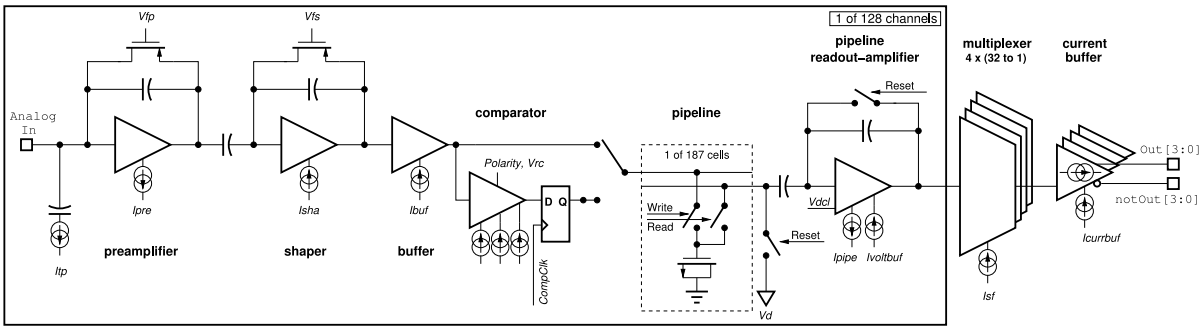

Figure 3.3: Schematic block diagram of a Beetle input channel. Adapted from [124].

signal and falls below 30 % of the peak signal within another 30 ns. The shaper is followed by a buffer and a comparator, of which the latter is not used in the ALiBaVa set-up, but the signal is sampled with 40 MHz and directly transferred into an analogue pipeline.

Following a trigger pulse, a starting time stamp is set with a precision of 600 ps. A second time stamp is created by a 10 MHz clock. The time elapsed between the first, trigger induced, and the second, clock induced, time stamp thus is uniformly distributed between 0 and 100 ns. After 128 clock cycles of 25 ns length, i. e. 3.2 μs after the second time stamp the trigger signal is passed from the mother board through the daughter board to the two Beetle chips, which returns the serialised output of all 256 channels for that time slice. The analogue data, are then digitised with a 10-bit Analogue to Digital Converter (ADC) and passed onto the computer together with the timing information. For each event, one sampling point of the signal pulse is

obtained, which after averaging over a sufficiently large sample, yields an average signal pulse as it is shown in Figure 3.4(a).

The equivalent noise charge (ENC) in elementary charges e of the Beetle chip is given [124] as

$$ENC = 539.1\,\mathrm{e} + 51.89\,\mathrm{e/pF} \cdot C_{\mathrm{in}} \approx 670\,\mathrm{e} \tag{3.1}$$

where C_{in} is the input capacitance of the sensor under test, which amounts for the sensors used in the measurements described below to about 2.5 pF. Additional corrections to Equation 3.1 in combination with other ENC contributions, like shot noise caused by the leakage current lead to typical noise levels of ENC_{total} =(800–900) e for the measurements reported below.

In the MPP set-up the daughter board, together with a small detector board, see Figure 3.2(b), is placed in a climate chamber for cooling, especially necessary for highly irradiated sensors. The trigger system consists of a Nuplex 3 plastic scintillator attached to a Hamamatsu H6780 photomultiplier tube [125]. Since the high leakage currents occurring after irradiation of directly coupled sensors harm the Beetle chip, a special decoupling pitch adapter [126], consisting of a resistance and a capacitance, is used to decouple the signal induced by the traversing Minimal Ionizing Particles (MIPs) from the DC signal induced by the leakage current. As MIPs β-electrons from the ^{90}Sr decay chain, see Equations 2.5 and 2.6, are employed.

3.4.2 Data Acquisition and Analysis Chain

Before taking data, the pedestals, i. e. the 0- and noise-levels of each individual channel are determined in a special operation mode of the ALiBaVa system by sending random triggers generated on the mother board to the Beetle chip. Based on the resulting map, noisy channels are masked from data taking and the following measurements are corrected for the measured pedestal in the active channels.

The chip is calibrated by injecting signals between 0 ke and 100 ke via special pulse generator circuits within each Beetle chip cell at a rate of 50 Hz. An artificial trigger ensures that the signal is read out near the peak of the shaped signal. Based on these test pulses a linear fit gives the relation between chip units and charges expressed as multiples of the elementary charge e on a per channel level. Since this calibration is highly temperature dependent, usually only the Charge Collection Efficiency (CCE) is determined, using the a pre-irradiation measurement at the same temperature as reference.

Data with the ^{90}Sr source are taken by triggering with the scintillator system as described above. After correcting for the pedestals and applying the calibration, clusters corresponding to the same impinging MIP are searched for on neighbouring strips. Among all strips, the one with the highest signal not yet assigned to any cluster is chosen as seed strip if it exhibits a signal-to-noise ratio higher than the adjustable parameter sn, where the noise is determined from the pedestal scan. The signal of hits measured in the neighbouring strips is added as long as the signal-to-noise ratio is higher than the adjustable parameter snn, which is always chosen smaller than sn. If no more neighbours can be added the algorithm starts over with the highest remaining signal strip until no strip fulfilling the signal-to-noise criterion is left in the event.

The cluster charges are averaged for every 2 ns time bin within the 100 ns trigger window. The resulting average pulse shape resembles the shaper pulse, i. e. the maximum is found around 20 ns and for timestamps greater than 60 ns only noise is found. The distribution is well described by

$$\mathrm{Gaussian}(N, \mu, \sigma) + \mathrm{const.} \tag{3.2}$$

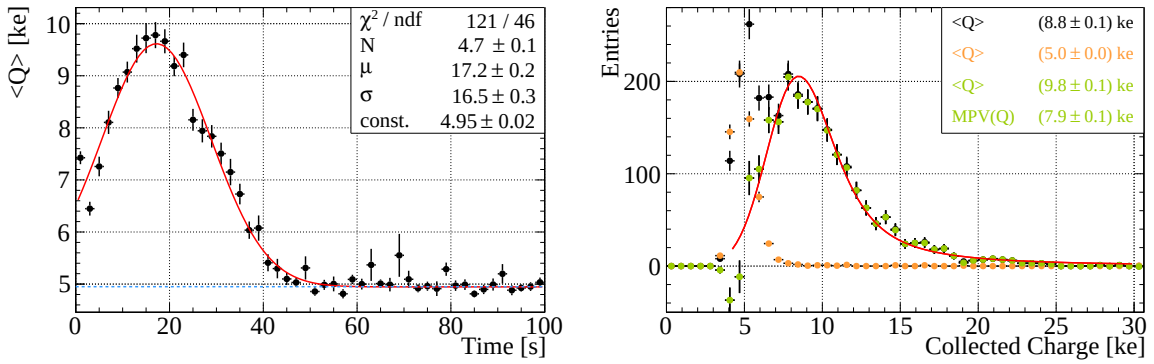

(a) (b)

Figure 3.4: Exemplary plots of the collected charge for a sensor with $d_{\text{active}} = 75\,\mu\text{m}$ irradiated to a fluence of $10^{16}\,\text{n}_{\text{eq}}/\text{cm}^2$. (a) Average collected charge $\langle Q \rangle$ as a function of the time after the trigger signal together with the fit function. The dotted blue line indicates the constant part of the fit function. (b) Corresponding collected charge distribution (black). The orange circles show the normalised noise distribution (see text) while the green circles indicate the signal distribution after subtraction. The signal distribution is fitted with a Landau distribution convoluted with a Gaussian (red). All shown uncertainties are statistical. For systematic uncertainties please refer to the text.

as depicted in Figure 3.4(a). All events corresponding to a timestamp within $\mu \pm \sigma/4$, with μ being the mean of the Gaussian and σ^2 its variance, are selected for further analysis. A resulting distribution is shown in Figure 3.4(b) (black circles) for a sensor with $d_{\text{active}} = 75\,\mu\text{m}$ irradiated to a fluence of $10^{16}\,\text{n}_{\text{eq}}/\text{cm}^2$.

For these highly irradiated samples a further noise reduction is mandatory and the algorithm described in [84] is used. Based on events in the time range between 60 ns and 90 ns a noise distribution is obtained and normalised for subtraction by the following prescription: the signal as well as the noise distribution are integrated up to a charge $q_{\text{max}} = sn \cdot n_{\text{max}}$, with n_{max} being the maximum noise charge of all active channels. By this, low charge signals that only pass the sn criterion in low noise channels are included in the calculation of the noise normalisation but the ones that exhibit a signal-to-noise ratio high enough to surpass the requirements of all channels are excluded. Thus, especially largely fluctuating noise is reduced. The ratio of the two integrals is used for the normalised subtraction of the noise from the signal distribution. In Figure 3.4(b) the subtracted normalised noise distribution is indicated in orange and the resulting signal distribution in green. Close to the noise level, the corrected distribution may be below zero. Anyhow, the significance is typically low and thus does not bias the fit.

3.4.3 Uncertainties

On the one hand uncertainties on the collected charge arise from the charge calibration and on the other hand from the specific choice of the sn and snn parameters as well as from an offset and width variations of the signal time window.

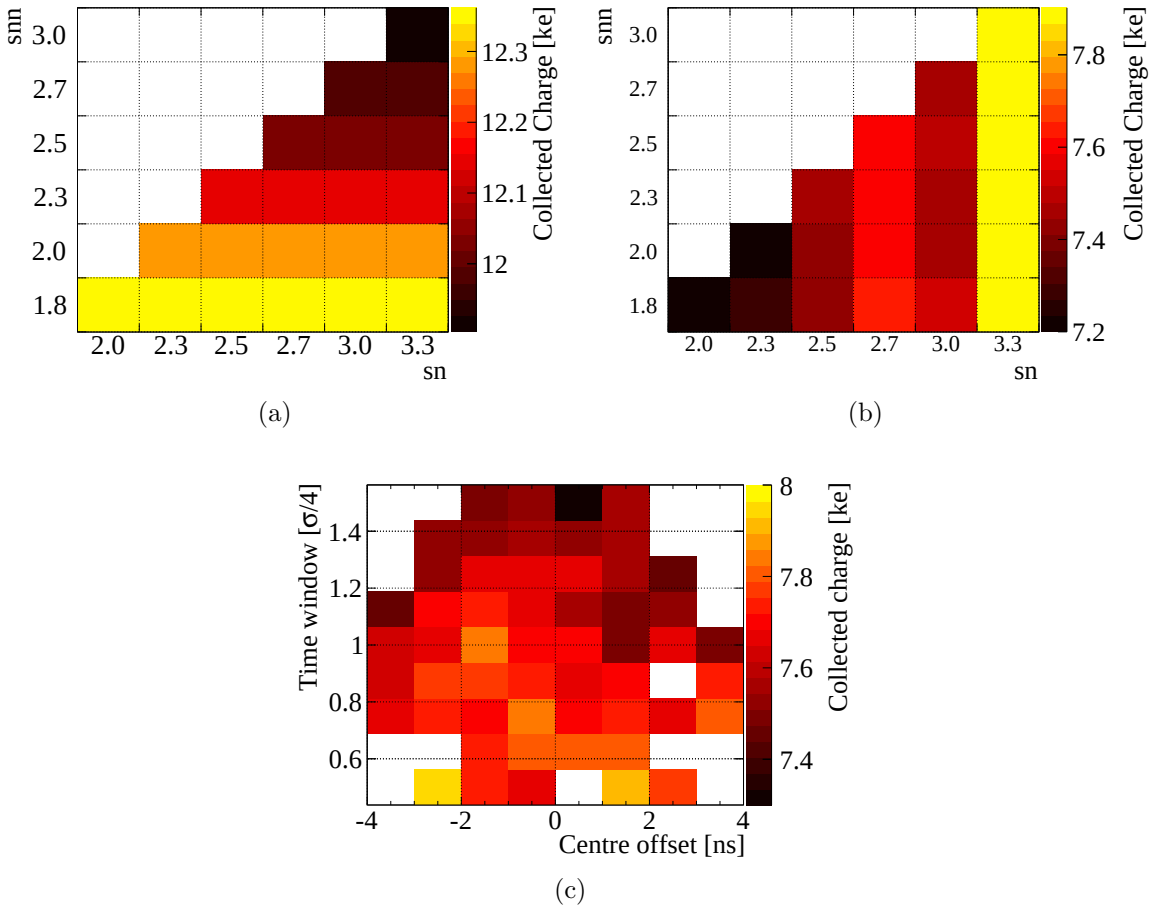

Figure 3.5: Dependence of the collected charge on the *sn* and *snn* parameter with standard time window settings (a) for a sensor with $d_{\text{active}} = 150\,\mu\text{m}$ irradiated to a fluence of $10^{15}\,\text{n}_{\text{eq}}/\text{cm}^2$ and biased at 400 V, and (b) for a sensor with $d_{\text{active}} = 75\,\mu\text{m}$ irradiated to a fluence of $10^{16}\,\text{n}_{\text{eq}}/\text{cm}^2$ and biased at 750 V. (c) Dependence of the collected charge on the width of the signal time window in units of the standard width $\sigma/4$ and on the offset of the time window centre.

In Figure 3.5(a) the dependence of the collected charge on the *sn* and *snn* parameter for a sensor with $d_{\text{active}} = 150\,\mu\text{m}$ irradiated to a fluence of $10^{15}\,\text{n}_{\text{eq}}/\text{cm}^2$ and biased at 400 V is shown as an example. As expected from the comparably large absolute signal, the influence of the *sn* parameter is negligible, but lowering the *snn* parameter increases the cluster charge, since more neighbour strips are eligible for the cluster.

For thinner sensors, where the overall signal size is smaller, the importance of higher multiplicity clusters decreases, but the signal size of the seed strip becomes more important. In Figure 3.5(b) the same quantities are shown as in Figure 3.5(a), but for a sensor with $d_{\text{active}} = 75\,\mu\text{m}$ irradiated to $10^{16}\,\text{n}_{\text{eq}}/\text{cm}^2$. The switched influence of the *sn* and the *snn* parameter are apparent. The systematic uncertainty associated to the *sn* and *snn* parameter is estimated to be half of the largest fluctuation found in the determined collected charge, i. e. 0.4 ke.

In Figure 3.5(c) the influence of the signal time window size and of its centre position on the determined collected charge is illustrated. Choosing too small or too large signal time windows in combination with a large mis-estimation of the signal peak position leads to a non-convergence of the fit function (white bins). Just decreasing the width of the signal time window enhances the signal size, since only maximal events are processed further. Simultaneously, this considerably decreases the statistics and thus results in higher statistical uncertainties. Given the observed fluctuations the corresponding systematic uncertainty is estimated to be half of the fluctuation found excluding extremes, i. e. 0.2 ke.

The uncertainty contribution by the charge calibration is estimated to be 0.1 ke, since most of it is removed by normalizing the charge to the pre-irradiation values, as in the approach followed in this thesis.

Thus, by linearly adding the three sources, the overall systematic uncertainty on the charge collection measurements using the ALiBaVa set-up is estimated to be 0.7 ke.

3.5 Edge-TCT

While the ALiBaVa set-up allows for the measurement of the induced charge normalised to pre-irradiation value the edge-TCT[3] method [110], described in this section, offers the possibility to obtain a relative measurement of the charge collection as a function of the depth within the sensor.

The instrumentation and data acquisition are introduced in Section 3.5.1, followed by the description of the analysis chain, Section 3.5.2, and a discussion of the uncertainties in Section 3.5.3.

3.5.1 Instrumentation and Data Acquisition

For the edge-TCT measurements (see Figure 3.6) reported below a pulsed infra-red laser, with $\lambda = 1064\,\text{nm}$, is focused on the polished side perpendicular to the one containing the implanted strips and scanned from the top to the bottom. At this wavelength the attenuation length in silicon is around 1 mm [127] and electron hole pairs are created homogeneously along the laser beam within the sensor. The focus is adjusted to reach a minimal Full Width Half Maximum (FWHM) of the beam beneath the read-out strip. In the set-up used at the JSI a FWHM of (8–12) μm can be achieved. The ground potential is applied close to the conductive sensor edge and to the back-side. To obtain a homogeneous electric field close to the analysed strip, the first 15 strips starting from the polished side are connected via wire-bonds to the high voltage potential. For the read-out strip, which signal is to be investigated, the high voltage is decoupled via a so-called Bias-T [128], consisting of a capacitor and a resistor to decouple the AC charge signal pulse from the DC high voltage. The remaining strips are biased directly. The AC charge signal is then routed via a 50 dB wide band charge amplifier Miteq 1309 [129] to an oscilloscope, which averages over 400 laser pulses. The laser pulse frequency is typically set to 200 Hz. Each laser pulse has a FWHM of 100 ps in time, while a typical induced signal pulse in the silicon bulk has a duration of about (5–15) ns depending on the thickness and the received fluence.

For cooling during the measurement as well as for heating while annealing, the sensor is mounted on a grounded copper block, which is screwed to an aluminium support, connected to

[3] Transient Current Technique

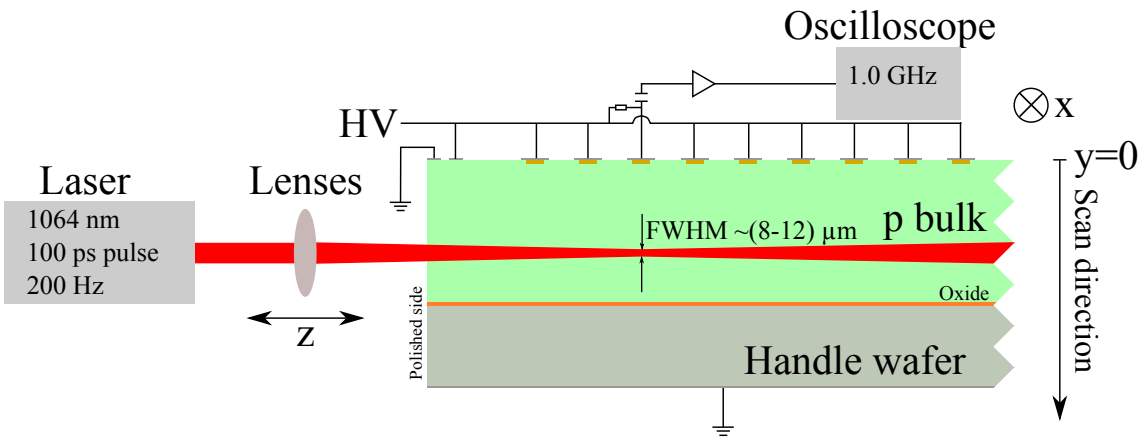

Figure 3.6: Sketch of the edge-TCT set-up with the definition of the coordinate system.

two 40 W Peltier elements [130]. The accessible temperature ranges from −20 °C to 60 °C with a stability of 0.1 °C.

3.5.2 Analysis Chain

Along the analysis chain three main steps are taken, where each step allows to draw distinctive conclusions. The starting point is the averaged induced current pulse recorded with the oscilloscope. An exemplary pulse for a not irradiated sensor is depicted in Figure 3.7. The first peak starting at a time of 0 ns, as defined by the trigger given by the laser system, corresponds to the charges induced by the laser light. After 20 ns a second pulse occurs, caused by reflections within the cables and the electronic components as the amplifier and the oscilloscope. Since the laser induced signal ends well before this reflection, it can be disregarded.

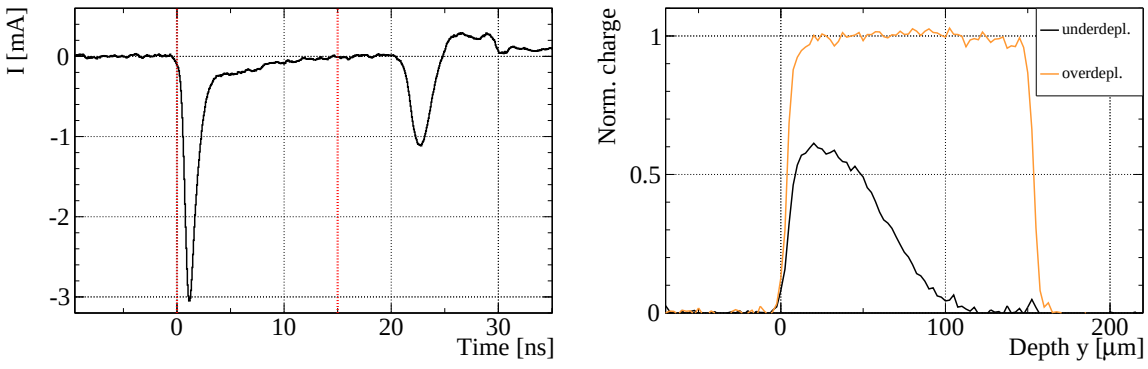

(a) (b)

Figure 3.7: Exemplary (a) induced current pulse shape for a sensor with $d_{\text{active}} = 150\,\mu\text{m}$ before irradiation. (b) The depth profile of charge is shown for a sensor biased below full depletion (black line) and for the over-depletion case (orange line). The charge is normalised to the plateau of the over-depleted case.

To obtain a measure for the charge, the signal pulse is integrated over the time for each injection depth. The integration time window is chosen such that the full signal pulse is contained, while the reflection is excluded. In this thesis an integration time of 15 ns as indicated by the red lines in Figure 3.7(a) is chosen. Injections at negative y-positions outside the sensitive volume of the sensor, are used as reference to correct global offsets in the measurement. Two profiles are shown in Figure 3.7(b) for a sensor with an active thickness of 150 μm. While the orange curve corresponds to a bias voltage above full depletion and thus is homogeneous over the entire volume, the black curve corresponds to a voltage below full depletion and thus only exhibits signal contributions in the already depleted parts of the sensor bulk.

For a comparison of edge-TCT with ALiBaVa and pixel assembly measurements a final integration over the profile is needed since the y-dependence is not resolved there.

3.5.3 Uncertainties

Uncertainties arising within the edge-TCT measurements are discussed in this subsection. As main influence the polishing is discussed first, followed by a discussion of the influence of the laser focus. Uncertainties introducing a global offset, as for example a larger integration time window are not evaluated since an absolute measurement of the charge is impeded by the polishing uncertainty.

As discussed above, the sensors are polished on one side. Since this is a manual process, each sensor is polished differently; especially the amount of material removed varies. Thus, the absorption occurring before the measured strip is different for each sensor. This impedes direct comparisons of the absolute scale between different sensors. Within each sensor an important question is the homogeneity of the surface, since points at different depths are to be compared. To asses this uncertainty two independent scans, displaced by 50 μm in x were conducted. Over the full voltage range the deviation in integrated collected charge was found to be smaller than 2 %. This is used as a conservative upper limit.

This uncertainty is also reflected in the scanning granularity in y, which is typically between 1 and 5 μm. Although measurements at neighbouring points are highly correlated due to the larger FWHM of the beam, slightly different surface regions are probed. To asses this a scan with a 5 μm spacing was compared to scan with a 2.5 μm spacing. Again, the deviations were consistently found to be smaller than 2 %.

To determine the FWHM of the laser beam under the read-out strip, the depleted part of a sensor is scanned for different focal settings of the laser system determined by the z position of the laser collimator. For each scan a profile as shown in Figure 3.8(a) is obtained by integrating over the oscilloscope pulses as discussed above. The FWHM below the read-out strip corresponds to 2.35 times the standard deviation σ of the error function describing the turn on characteristics. The optimal focus is reached at the minimum of the parabola

$$\mathrm{FWHM} = \mathrm{FWHM}_0 + \mathrm{a}z + \mathrm{b}z^2 \tag{3.3}$$

describing the FWHM dependence on the focus, cf. Figure 3.8(b).

The dependence of the measured charge on the focus quality is shown in Figure 3.8(c), where the collected charge normalised to the value at the minimal FWHM focus is depicted for a sensor with $d_{\mathrm{active}} = 150\,\mu$m and a received fluence of $10^{16}\,\mathrm{n_{eq}/cm^2}$. This effect influences the charge measurement in two ways. First globally, but as discussed above, global shifts will be disregarded in this discussion, since absolute measurements are impeded by the polishing. Secondly, small tilts of the sensor can lead to a change of focus while scanning in y. Assuming

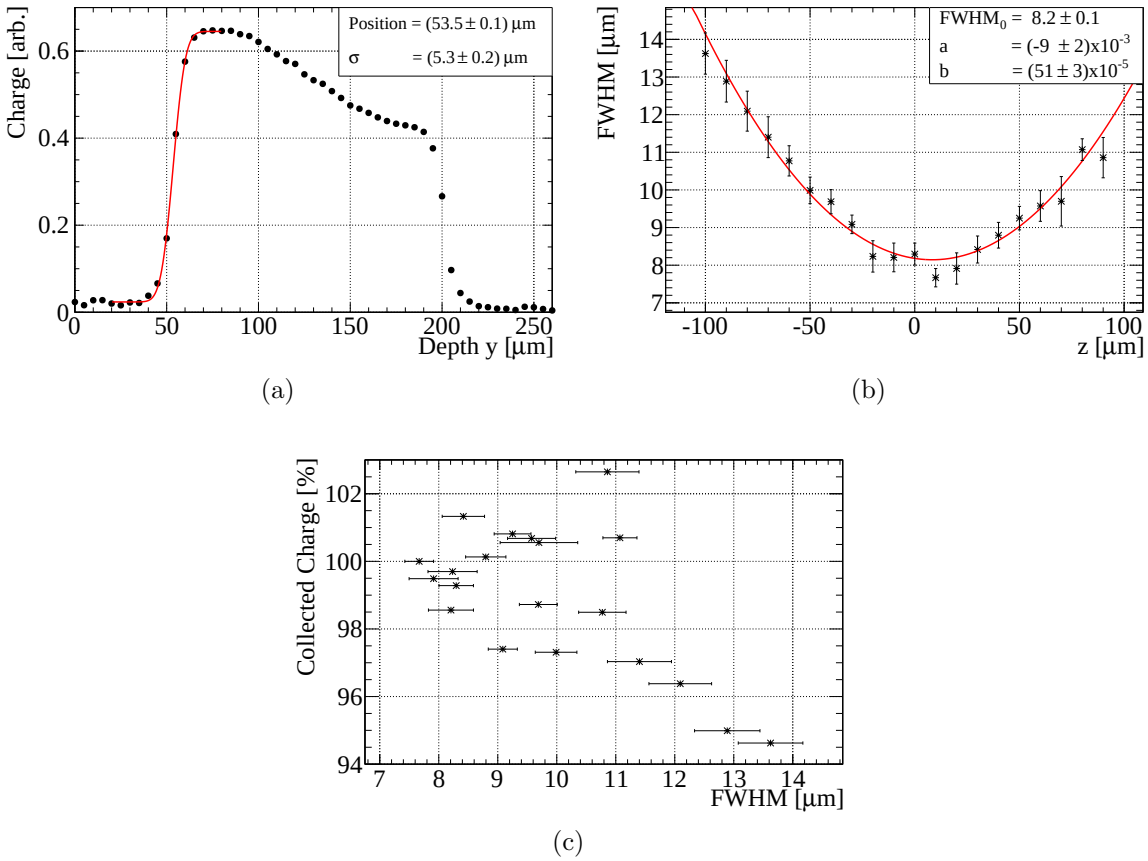

Figure 3.8: (a) An exemplary fit to the turn-on characteristics. (b) The resulting parabola indicating the optimal value for the focus. (c) Dependence of the integrated charge on the FWHM normalised to the charge at the minimal FWHM.

that the focus can always be chosen close to the optimum in the beginning, the uncertainty introduced here is taken as the symmetrised spread observed in Figure 3.8(c) and amounts to less than 3 %.

In total a 5 % uncertainty is estimated on the obtained total collected charges within the edge-TCT measurements.

3.6 Operation of ATLAS Read-Out Chips

In this thesis, several different hybrid pixel detectors will be discussed. Although they are composed by different sensors connected to three different read-out chips—namely the FE-I2, FE-I3, and FE-I4—they can be all read-out with a common read-out system, the USBPix system [131]. In this section first an introduction to the read-out chips is given (Section 3.6.1), followed by an explanation of the USBPix system functionalities needed for an understanding of the measurements discussed later (Section 3.6.2). Finally, the tuning and the respective measurement uncertainties are introduced (Section 3.6.3).

3.6.1 ATLAS Read-Out Chips

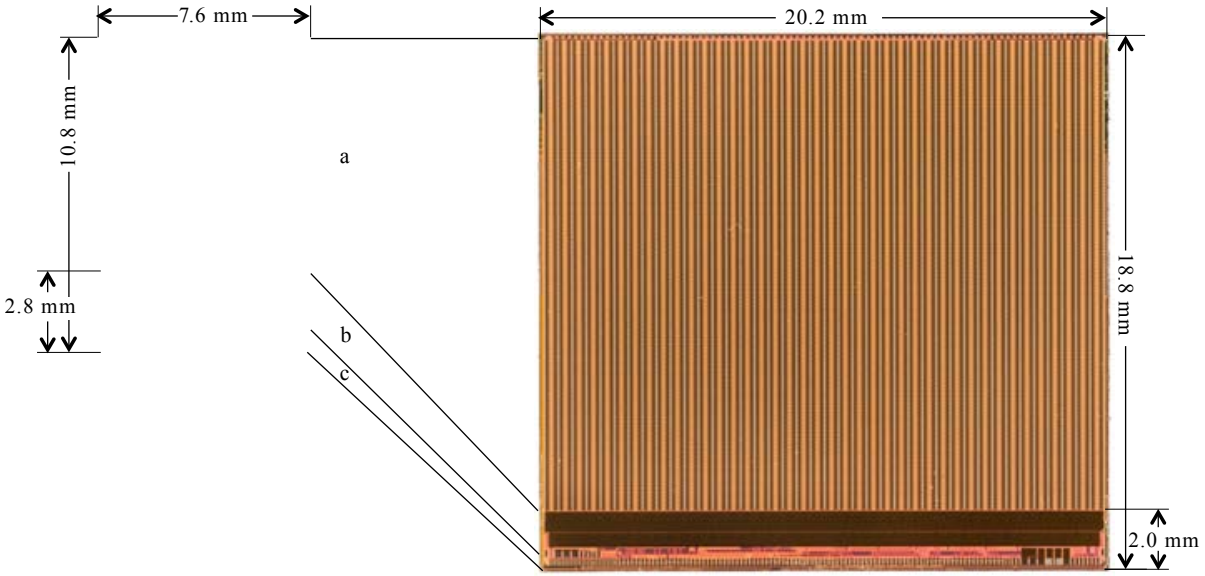

Figure 3.9: Photographs, to scale, of the FE-I2/3 (left) and the FE-I4 (right) [85] read-out chips. The dimensions indicate the total size and the size of the inactive areas. For the description of the three functional areas of the chip a) the active area, b) the end-of-column area, and c) the wire-bonding area please refer to the text.

The FE-I2 and FE-I3 Read-Out Chips

The FE-I3 read-out chip [71] is employed as the present ATLAS Pixel Detector read-out chip and only differs in minor details, e. g. slightly different chip analogue and digital voltages, from the FE-I2 read-out chip [132]. Since these differences are not relevant for the work presented in this thesis they will be omitted here, but can be found in [133].

The chips are produced in the 250 nm CMOS[4] [134, 135] technology and house 3.5 million transistors on an area of $7.6 \times 10.8\,\mathrm{mm}^2$. A photograph is shown in Figure 3.9 on the left. As they were designed for the ATLAS experiment their clock speed matches the LHC bunch crossing rate of 40 MHz and the target radiation hardness in the design process was a total dose of 500 kGy which corresponds to $10^{15}\,\mathrm{n_{eq}/cm^2}$ [70].

The chip area is divided into three functional regions, the active, the End-Of-Column (EOC) and the wire-bonding area, see Figure 3.9. In the active area 2880 pixel cells are arranged in 18 columns and 160 rows. Each pixel cell has a size of $50 \times 400\,\mu\mathrm{m}^2$ and features an analogue as well as a digital part, which allows to compare a charge signal to an adjustable threshold and measure the Time-over-Threshold (ToT) with an 8-bit resolution, see Figure 3.10 (left). Due to the linear discharge of the feedback current, the ToT is proportional to the deposited charge in the sensor. The feedback is adjusted such that it is a good compromise between a maximal ToT resolution for the expected signal and a minimal pixel dead time. The result is transferred together with the corresponding pixel address and the time stamp to an EOC logic block, which exists for every two columns and features circuits for further signal processing. Hits which are

[4] Complementary Metal Oxide Semiconductor

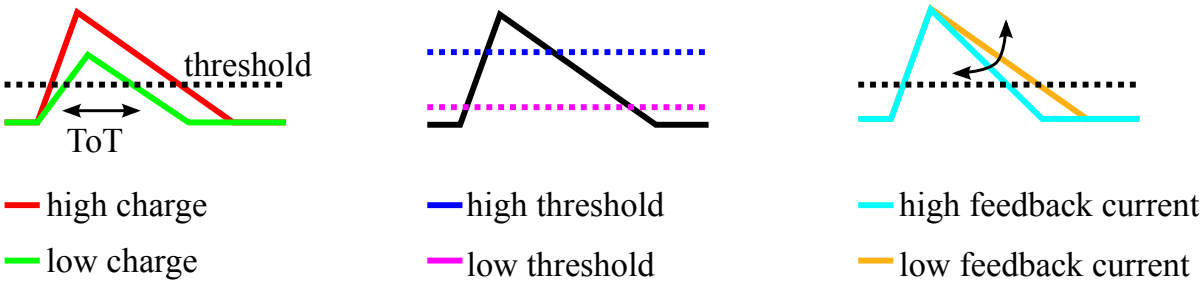

Figure 3.10: Preamplifier output signals in dependence on the chip DAC values and input charge, figure adapted from [136].

marked by trigger signals are selected for read-out. Triggered hit data are transmitted serially out of the chip in the order of trigger arrival. In the wire-bonding area 30 wire-bonding pads are used to supply power to and to communicate with the chip. Additional 17 wire-bonding pads allow for testing different features of the chip or are back-up pads used in laboratory testing. In addition to the signal processing circuits several calibration and testing circuits are integrated into the chip. Of special importance for sensor characterisation are the capacitors used to inject test charges into the chip circuits within the pixel cell, because the algorithms for charge calibration and threshold adjustment are based on them. By design, the capacitors have a value of $C_{\text{low}} = 8\,\text{fF}$ for the lower charge range up to 100 ke [137]. For higher charges a second capacitance can be added yielding $C_{\text{low+high}} = 40\,\text{fF}$. Since all charges discussed in this thesis are well below 100 ke, this option will not be used here. The lower limit for charge measurements is set by the threshold, which was designed to be around 4 ke and can be adjusted down to about 2.5 ke, or for some chips even to 1.8 ke. Another feature of special importance when measuring γ-sources is the internal trigger functionality.

The FE-I4 Read-out Chip

Exploiting the advances in industrial semiconductor integrated circuit fabrication and given the demand for a more radiation hard read-out-chip for the IBL upgrade project, the FE-I4 [76] read-out chip was designed. It is produced in the 130 nm CMOS technology and contains 87 million transistors on an area of $18.8 \times 20.2\,\text{mm}^2$. The larger size allows to reduce flip-chipping costs, which is crucial for later large area upgrades of the pixel detector, and also significantly increases the fraction of the active area, which is mandatory for the IBL since the use of a layout with partly overlapping assemblies along the beam direction is not possible due to the tight radial space restrictions. The functional division of the area is the same as in the FE-I3 (see Figure 3.9). The main area is populated with 26880 pixel cells arranged in 80 columns and 336 rows and the pixel cell dimensions are $50\,\mu\text{m} \times 250\,\mu\text{m}$. While each pixel cell contains analogue circuits, the digital circuit is shared amongst four adjacent pixel cells. In this digital part, the signal is stored and only passed on to the EOC-logic block if a trigger signal is received. In combination with additional logic within the EOC-logic-block this enables for the operation of multi-chip assemblies without the need of a MCC as it is used in the ATLAS Pixel Detector to control the 16 FE-I3 read-out chips composing an assembly. The communication with the chip and its powering is achieved via 144 wire-bonding pads. Additional 86 wire-bonding pads offer access to special test circuits.

To reduce the dead time and the risks of high occupancy at high luminosities, the resolution on the ToT was reduced to four bits. A lower threshold range was achieved for the FE-I4 chip, which starts in some cases below 1 ke with beneficial increase of the hit efficiency for the detection of the smaller charges in thinner sensors. Furthermore, this keeps the signal-to-threshold ratio high after high received fluences, e. g. the design maximum fluence of the FE-I4 of 250 MRad or $5 \cdot 10^{15}\,\mathrm{n_{eq}/cm^2}$ [74], where the charge collection efficiency of the sensors is degraded.

In this thesis exclusively assemblies employing the first version of the FE-I4 read-out chip, the so-called FE-I4A are used. Some additions [138] to the design described, were implemented in several pixel cells to test the performance of different circuit designs. Examples are the different injection mechanisms used for the first and the last three columns. Since their performance is not representative they won't be employed in this thesis. Furthermore, two different injection capacitance implementations were used in different columns[5]. These are expected to only slightly alter the response of the individual columns and thus can be used in parallel. The second version of the read-out chip, called FE-I4B is reserved for the IBL assembly construction and features besides some minor bug fixes additional circuits to calibrate the ToT to charge.

3.6.2 USBPix Read-Out-System

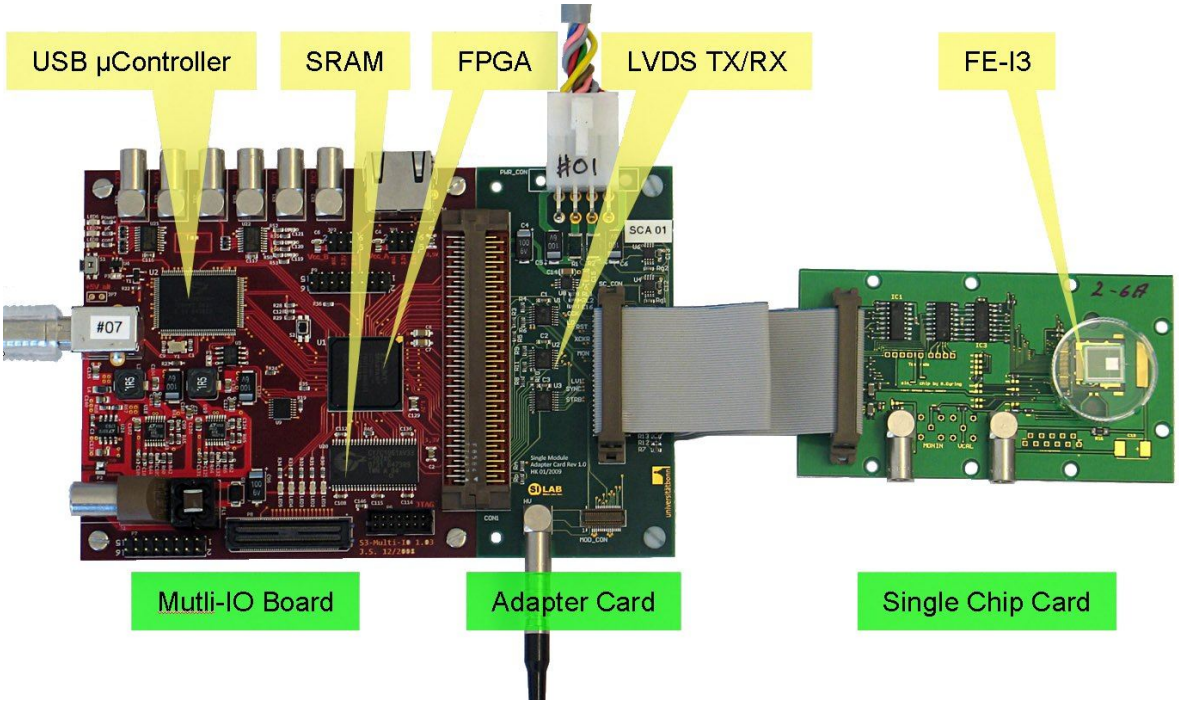

Figure 3.11: Photograph of the USBPix system components [139] with a Single Chip Card for FE-I3 assemblies.

The USBPix read-out-system [131] is used to characterize assemblies built from sensors connected to one of the three described read-out chips. The system consists of three main parts depicted in Figure 3.11. On the Multi-IO Board the communication between the computer used for steering, the trigger systems, and the Adapter Card is coordinated. The Adapter Card

[5]The columns with non standard capacitors are: 3–4, 13–14, 23–24, 27–28, 31–32, 35–36, 45–52, 61–76, 79–80.

is specific to the read-out chip generation—i. e. there is one for the FE-I2/3 as well as one for the FE-I4—and houses most of the electronics needed to communicate with the specific read-out chip. The last component is a board to which the assembly is mounted and wire bonded. Depending on the assembly type several different designs are available. In this thesis the so-called Single Chip Cards (SCCs) designed for assemblies composed of one chip and one sensor, as often employed in R&D campaigns, were used. In Figure 3.6.2 the SCC used for the FE-I3 (FE-I4) based assemblies is shown on the left (right). For the FE-I2 assemblies, the design of the FE-I3 SCC was slightly modified, because these assemblies were read-out through an additional fan-out structure on the sensors and the order of the wire-bonding pads is mirrored, cf. Figure 1.8.

Since the initial design of the FE-I3 SCC was not capable for voltages $\gtrsim 600\,\mathrm{V}$ a small extension board was added to increase the distances between the high and ground lines on the SCC. It is visible on the left side in Figure 3.12(a).

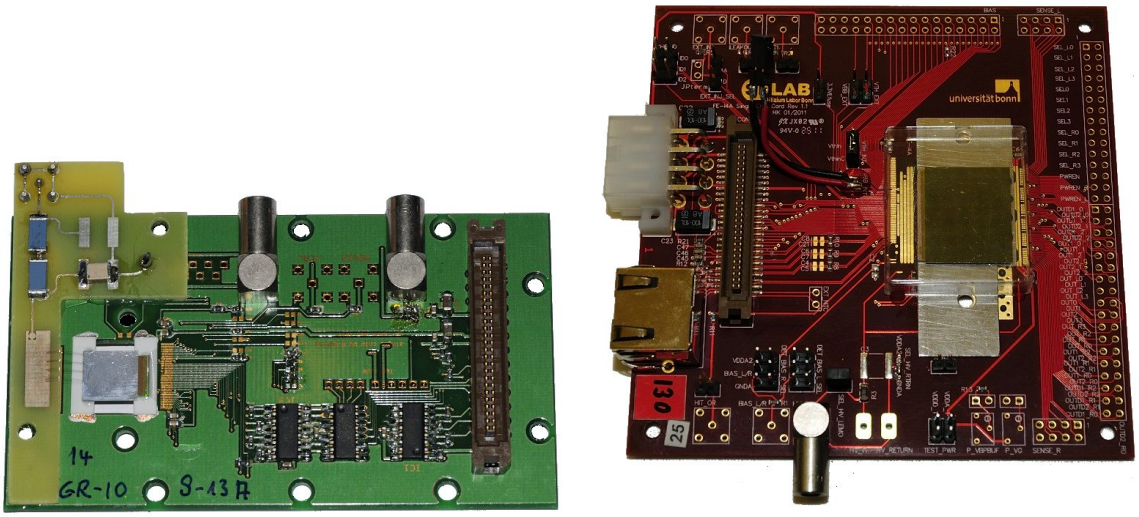

(a) (b)

Figure 3.12: Photograph of assemblies mounted on an SCC. The FE-I3 version is shown in (a), while the FE-I4 version is shown in (b). The assembly can be seen on the left hand side of the FE-I3 SCC and in the right centre of the FE-I4 SCC.

3.6.3 Tuning

Due to process variations each pixel cell exhibits a slightly different signal response. To account for this, the ATLAS read-out chips can be tuned via several chip registers to achieve an uniform behaviour. The two most important parameters—threshold and ToT to charge calibration—as well as their uncertainties will be described in this section. Further details can be found in [140].

Threshold Tuning

The threshold is a digital discriminator to which the output signal of the pre-amplifier (left sketch in Figure 3.10) is compared. Only signals above this threshold are processed further. The threshold can be adjusted globally and per pixel cell. The value of the pixel cell threshold

is defined as the charge for which the pixel cell exhibits an efficiency of 50 % as indicated in Figure 3.13. Due to electronic noise the theoretical step function is convoluted with a Gaussian distribution and transformed into an error-function. Its standard deviation σ_{noise} corresponds to the electronic noise of the pixel cell

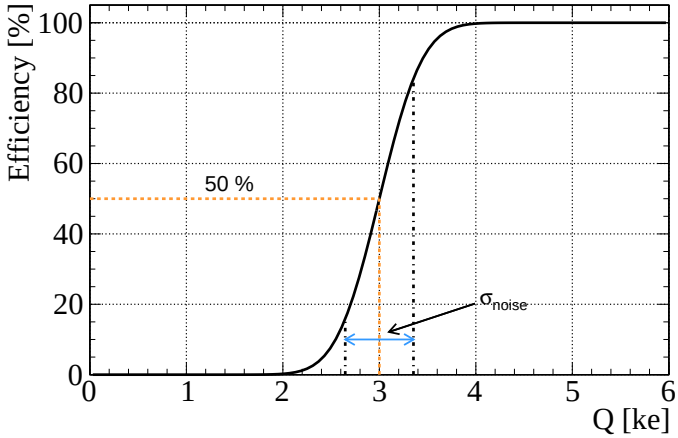

Figure 3.13: Schematic drawing of the threshold characteristics. Indicated are the found threshold in orange as well as the electronic noise in blue. Schematics adopted from [137]

To tune the threshold to a given value, reference charges around the desired threshold value are injected via the calibration capacitors C_{low} and the response of the assembly is measured as a function of the global and local threshold DAC settings. The result of the tuning is a threshold distribution which, for not irradiated modules, is uniform over the whole pixel cell matrix to about some tens of elementary charges e. Since the threshold changes by approximately 10 e/K it is important to operate the assembly at a stable temperature and perform the tuning at a temperature as close as possible to the operational temperature.

ToT to Charge Calibration

To compare results between different communities and experiments converting ToT values to measured charges is needed. While for the FE-I2/3 the relation is known to an extent satisfactory for any practical application, this conversion has not yet been fully achieved for the FE-I4 read-out chip. The algorithmic details in the following description apply only to the FE-I2/3, but a similar procedure is under investigation for the FE-I4B as well. For the FE-I4A basic studies indicate a linear behaviour near the tuning point and a deviation from linearity elsewhere [141].

To calibrate the ToT to the charge, known reference charges Q_{inj} are injected via the calibration capacitors using a voltage steerable by the DAC V_{cal}:

$$Q_{\text{inj}} = C_{\text{low}} \cdot V(V_{\text{cal}}). \tag{3.4}$$

The corresponding ToT is measured as a function of the feedback current (see Figure 3.10 right), which can be set both globally and for each pixel cell. The result is described with an empirical function [142]:

$$Q = \frac{\text{ToT} \cdot C - A \cdot B}{A - \text{ToT}} \quad \text{or} \quad \text{ToT} = A\frac{B+Q}{C+Q} \tag{3.5}$$

with three fitting parameters A, B, and C. A typical function is drawn together with an exemplaric scan result in Figure 3.14. The functional behaviour is nearly linear, except for charges close to the threshold.

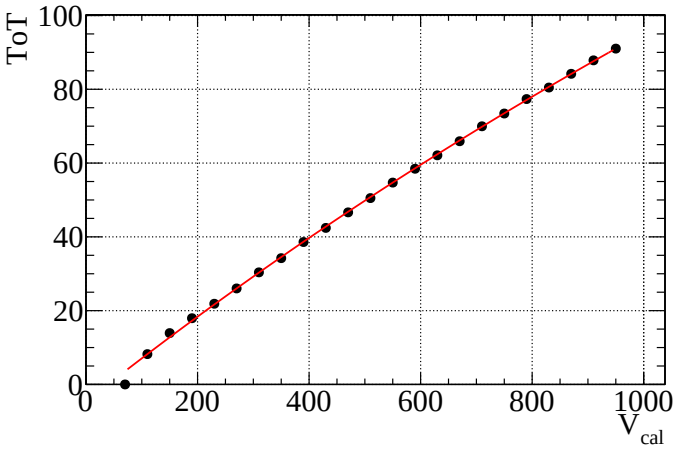

Figure 3.14: Exemplary ToT to charge calibration scan. V_{cal} is the internal chip representation for the injected charge.

Several uncertainties are inherent to this calibration. First, the injection capacitors exhibit process variations over the read-out chip and the wafer. During the production of the ATLAS pixel detector all capacitors were measured at wafer level, and a variation within 5 % was found. Additionally, the difference of neighbouring chips was investigated, and found to be around 2 % [143]. The latter value is important, since for the calibration only a single capacitance value for the entire chip is used. The first value is however relevant for the FE-I2 and some FE-I3 read-out chips because here the actual capacitance values are unknown, since no survey was undertaken at wafer level. Furthermore, the V_{cal} fluctuates within 5 % of the nominal DAC value by which it is steered. Again for the FE-I3 chips used in this thesis, the exact values are known from the ATLAS production survey, while for the FE-I2 chips they are unknown. Also it was found that the used calibration curve (Equation 3.5) has a systematic bias towards lower values of 10 to 15 % for charges around 16 keV [143]. To correct for this, measurements with sources with well defined γ-lines can and will be used.

Assuming the above mentioned uncertainty contributions to be fully uncorrelated, in the following, for the FE-I2 assemblies and the FE-I3 assemblies without prior survey an uncertainty of 7.3 % will be assumed for charge values expressed in elementary charges, and of 5.4 % for the FE-I3 assemblies where survey results are available. The systematic bias will be corrected based on measured γ lines, and half the correction will be used as uncertainty. For the FE-I4 the tuning point was chosen such that the most probable value of the charge falls into the linear region. The uncertainty on the MPV is conservatively estimated to be ± 20 %.

3.7 Beam Test

Measurements using a minimal ionizing particle beam and a beam telescope are the ultimate test for high energy physics detectors since this allows to determine their performance, while most closely mimicking the situation in the real experiment.

In this section first the beam-lines used to characterize the pixel assemblies are introduced, followed by a discussion of the EUDET telescope and the analysis chain. Further details on the beam test instrumentation can be found in [144].

3.7.1 Beam-Lines

Beam test studies were conducted at the CERN SPS H6 and H8 beam-lines as well as at the DESY[6] II beam-line. The CERN SPS H6/8 beam-lines deliver high momentum π^+, which minimize multiple scattering and allow for the simultaneous measurement of many devices in series. In the different beam test periods the momentum was adjusted to be 120 GeV or 180 GeV. In contrast, at the DESY II facility the delivered particles are positrons with an energy between four and six GeV, and thus only two devices can be simultaneous investigated in the beam, due to multiple scattering.

3.7.2 Instrumentation

The following subsection covers the important details of the EUDET telescope as well as the most important mechanical and cooling details of the beam test set-up. Finally, the beam test read-out systems will be described.

The EUDET Telescope

The trajectories of the beam particles were reconstructed using the high resolution EUDET telescope [145]. The telescope has six planes, of which three are mounted upstream with respect to the devices under test (DUT) and three downstream of the DUTs. In the telescope planes Mimosa26 [146] active sensors with an active area of $21.2 \times 10.6\,\mathrm{mm}^2$ and square pixel cells of $18.4\,\mu$m are used as sensitive elements. The tracking resolution of the telescope at the location of the DUTs is estimated to be $2\,\mu$m at CERN-SPS, while for the samples mounted downstream of the telescope it is around $10\,\mu$m [147].

Since $112\,\mu$s are needed to read out the MIMOSA26 sensors with its rolling shutter read-out technique, while the DUTs only record and keep events stored in their memory for 400 ns, some particles can only be recorded by the telescope but not by the DUTs. To ensure that reconstructed tracks could be measured in principle by the DUTs only tracks which also exhibit a hit on a reference DUT are considered. In the following such tracks will be called in-time, while objects not seen by the reference plane will be called out-of-time. Although this pre-selection reduces the statistics it does not introduce a systematic bias and allows for an absolute determination of module efficiencies. To account for false positives induced by noisy pixel cells in the reference DUT anyhow an uncertainty of 0.3 % is assumed.

A pair of scintillators covering an area of $2 \times 1\,\mathrm{cm}^2$ before and after the telescope are used for triggering.

[6] Deutsches Elektronen-Synchrotron

Cooling and Mechanics

To shield the DUTs from light and to ensure cooling, a PPE[7]-box with two different compartments shown in Figure 3.15 was used during the beam tests. In the first compartment the DUTs are mounted. The second compartment is filled with dry ice for cooling and can be opened independently for refilling. Metal base- and compartment-separation-plates guarantee for a good heat transfer. Several Pt1000 thermistors [148] are distributed within the DUT-compartment to survey the temperature, which typically varies between $-40\,^{\circ}\mathrm{C}$ and $-50\,^{\circ}\mathrm{C}$.

DUTs analysed in this thesis are either oriented perpendicular to the beam or with an inclination of $\varphi = 15^{\circ}$ as drawn in Figure 3.16, where all used coordinate systems are defined.

The high momentum of the pions of the SPS H6/8 beam-lines allowed for mounting an additional batch of DUTs behind the last telescope plane. To minimize the track extrapolation uncertainty downstream of the telescope the DUTs were mounted as close as possible to the last telescope plane.

Read-Out Systems

Two different read-out systems were used in the different beam test periods. In 2010 the TurboDAQ [150] system in combination with the MCC of the ATLAS Pixel detector was used. In the following beam tests independent USBPix systems (cf. Section 3.6.2) for the individual DUTs were employed.

The TurboDAQ is a VME[8] based read-out and steering system for the FE-I3 read-out chip, which offers a similar functionality as the USBPix system. The parallel operation of several assemblies was achieved via the MCC, which within the ATLAS pixel detector steers the 16

[7] Poly Phenylene Ether
[8] Versa Module Eurocard

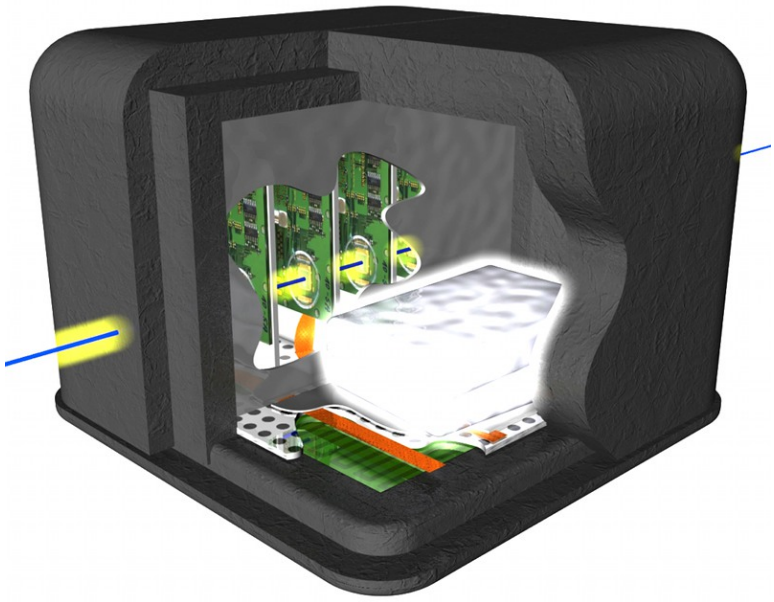

Figure 3.15: CAD model of the box used within the beam test for housing the DUTs shielded from light and to ensure cooling [149].

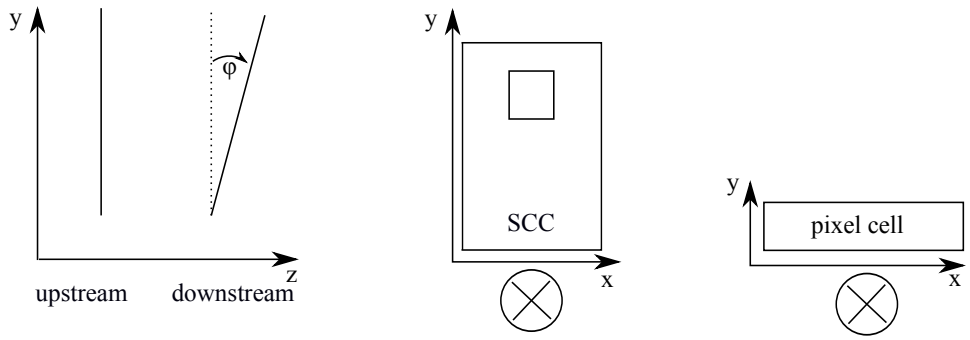

Figure 3.16: Coordinate systems used in the beam test analyses. In the left sketch the coordinates as seen from the side with the beam going in positive z-direction are shown. The middle sketch illustrates the coordinates in the DUT plane looking along the beam. In the right sketch the local coordinates within a pixel cell are drawn.

FE-I3 read-out chips composing a module. Unfortunately a noisy assembly can lead to a desynchronization of the DUTs connected to the same MCC with respect to the telescope, inhibiting measurements relying on a reference plane.

3.7.3 Analysis Chain

Within the EUDET telescope framework a preliminary clustering and alignment procedure is conducted. Afterwards, tracks are reconstructed and stored together with the hit information of the DUTs.

The reconstructed data is analysed in five steps. First, pixel cells that are either unresponsive, i. e. with zero hits, or noisy, i. e. with more than $5 \cdot 10^{-4}$ of the hits out of time, are identified and excluded. Furthermore for each DUT a fiducial region is defined based on geometrical and operability parameters. In addition, all pixel cells that were masked in previous lab-measurements are disregarded. This leaves the central region of each DUT, excluding defect pixel cells. Additionally, tracks exhibiting a $\chi^2 > 50$ or $\frac{\chi^2}{n_{\mathrm{dof}}} > 8$ in the initial telescope track reconstruction are discarded.

Using the data of the remaining pixel cells and the tracks fulfilling the quality criteria the alignment is checked on a per run basis, to compensate for movements due to temperature changes. This is achieved by using the mean of the residual distributions. In the next step the non-linear contributions of the charge cloud diffusion for the charge weighting algorithm, the η correction factors [151, 152], are determined and the alignment is checked a second time using this improved determination of the hit positions.

Tracks extrapolated from the telescope were considered belonging to a specific hit if closer than one pixel cell pitch in the long pixel cell direction and three pixel cell pitches in the short pixel cell direction. These tracks and hits are defined as matched from now on.

After these preparatory steps several analyses were conducted, which are shortly introduced in the following.

Cluster Size

A collection of hits, close in space and time and thus assumed to be originating from the same passing MIP is called cluster. Clusters are searched for among all hits within one event. Out of

all possible hits the first hit not yet assigned to any cluster is chosen as seed. Starting from this, neighbouring pixel cells above threshold are added to the cluster. While along the long pixel cell pitch a neighbour may only be the adjacent pixel, for the short pixel cell pitch the two pixel cells above and below the seed pixel cell are used for clustering. The algorithm ends if, for none of the pixel cells within a cluster, a neighbouring pixel cell is active. If further hits exist, the next seed pixel cell is then chosen to form the next cluster. The cluster size is defined to be the number of pixel cells forming the cluster.

The cluster centre is the centre of the pixel cell for single-hit clusters. For higher multiplicity clusters the individual centre positions are averaged using the respective charge as weight. Additionally, for two-hit clusters the η corrections are applied within the charge weighting.

Residuals

To estimate the intrinsic spatial resolution of the DUTs the residual distribution is used. The residual is defined as the difference between the reconstructed cluster position on the DUT and the extrapolation of the telescope track to the DUT plane.

For single-hit clusters the standard deviation of the residual distribution in x and y is a measure for the resolution; for higher multiplicity clusters a sum of two Gaussians correctly describes the residual distributions. The core Gaussian accounts for clusters, which profited significantly from the charge weighting algorithm. The second Gaussian represents clusters, which did either not profit from charge weighting or are mis-reconstructed. The intrinsic resolution of higher multiplicity clusters is identified with the width of the core Gaussian.

Charge Collection

Combining the collected charge and tracking information a position resolved charge collection profile of the sensor is obtained. This kind of analysis allows to identify problematic areas within the pixel cell design in terms of charge collection. Since it is typically not possible to record sufficient statistic, to obtain a significant fit for each bin, the mean charge is used in this analysis. As discussed in Section 2.1.3, this value is systematically higher than the MPV of the collected charge.

Charge Sharing Probability

The charge sharing probability P(share) is defined as the fraction of hits sharing charge with their respective neighbours at a defined position.

To determine P(share) for each track, the fraction of events where a pixel cell adjacent to the pixel cell penetrated by the track exhibits a hit, is determined. The probability rises towards the edge of the pixel cell since in this region the charge carriers will diffuse or drift more likely to the neighbouring pixel.

Hit Efficiency

The hit efficiency is determined as the fraction of matched tracks to a hit in the DUT. It can be determined as an overall figure for the module, or as a function of the position in the pixel cell area. The hit efficiency map may indicate problematic design features of the pixel cell, and can be understood better in combination with the charge collection profile and the design of the pixel cell.

4 n-in-p Pixel Detectors

In this chapter the properties of n-in-p pixel detectors are presented and compared to the currently used n-in-n pixel detectors. First, the relevant details of the sensor production are given in Section 4.1, then the performance before and after irradiation will be discussed in Section 4.2 and Section 4.3.

Emphasis will be put on the quantities decisive for high energy physics experiments. These are first the basic operational quantities, namely the leakage current as a function of the bias voltage and the breakdown voltage as compared to the full depletion voltage. While before irradiation these are indicators for the quality of the production and detector material, after irradiation the leakage current drives the power consumption and hence the needed cooling capacity. The breakdown voltage relates to the part of the detector volume usable for signal generation, see Equation 2.4. Second, the uniformity of the assembly response will be discussed alongside with the electronic noise. Both quantities are important for stable operation of the detector. Thereafter, the collected charge is discussed. A high absolute value when compared to the read-out chip threshold and a high charge collection efficiency after irradiation are essential for a good hit efficiency within the experiment and relax the constraints on the read-out chip specifications. The achievable spatial resolution is investigated through the hit residuals in combination with the fractions of the different cluster sizes. Additionally, these distributions bear information on the occupancy of the assembly. Last, the hit efficiency is discussed.

Parts of the results presented in this chapter, were already published in [144, 153–155].

4.1 CiS Production

Within the framework of the CERN RD50 collaboration and the ATLAS Planar Pixel Sensor Group 18 high resistivity ($\rho > 10\,\mathrm{k\Omega cm}$) Float-Zone (FZ) 4-inch-wafers of 285 μm thickness were processed on the CiS[1] production line using a design developed by MPP/MPI-HLL.

The layout of the wafer is shown in Figure 4.1. The left part of the wafer houses ATLAS structures, while the right one contains CMS structures. In the following the discussion is restricted to the ATLAS structures relevant for this thesis—namely the pixel structures.

4.1.1 Sensor Design

Each wafer hosts ten FE-I3 [71] and two FE-I4 [76] compatible pixel sensors, see Figure 4.1(b). The active area design follows the one of the currently used ATLAS pixel sensors and thus allows for good comparability of the results with standard sensors. An overview of the sensors discussed in the following two subsections is given in Table 4.1.

[1] CiS Forschungsinstitut für Mikrosensorik und Photovoltaik GmbH

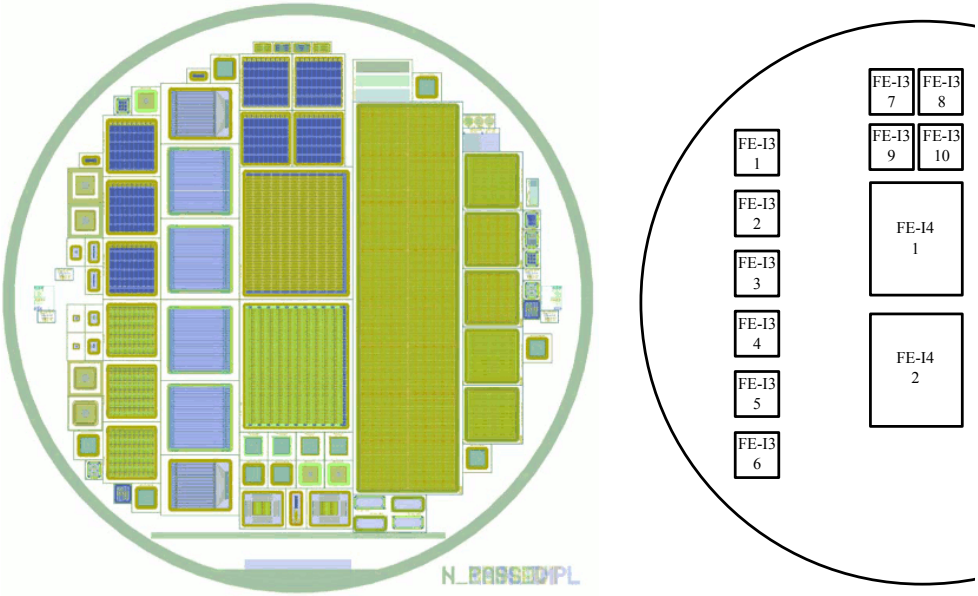

(a) (b)

Figure 4.1: (a) Wafer layout of the CiS production. (b) Sketch of the position and names of the ATLAS pixel structures.

FE-I3 Compatible Structures

The active area of the sensors, i. e. the area within the guard rings, is designed identically in all FE-I3 compatible structures. Four different kinds of pixels are arranged in 18 columns and 160 rows. The "normal" pixels cover the central region between the second and the 17th column and extend from row zero to 152. They have an extension of $400\,\mu\text{m} \times 50\,\mu\text{m}$. The first and the last column in the first 152 rows consist of "long" pixels measuring $600\,\mu\text{m} \times 50\,\mu\text{m}$. A sketch of the design in a corner incorporating normal and long pixel is shown in Figure 4.2(a). Since the last four rows are not bump-bonded to the read-out chip, they are connected pairwise with the rows 153, 155, 157, and 159 and the corresponding pixel cells are called "ganged" pixels. The pixel cells, which are crossed by the connecting metal are called "inter-ganged" pixels. For better comparability the design for this special pixels is mirrored up in Figure 4.2(b).

Each pixel can be biased via a punch-through structure of $20\,\mu\text{m}$ diameter (cf. Fig. 4.3 on the right) allowing for a characterization before interconnection to a read-out chip. Since the central dot of its n^+ implantation is not directly connected to the pixel structure, a reduced charge collection efficiency in this region is expected.

To increase the active fraction different guard ring schemes and safety margins to the dicing line were implemented in the design. As a reference, structures 1–6 follow the present ATLAS pixel sensor design with 19 guard rings, see Figure 4.2(a), and have an edge distance d_{edge} of $1055\,\mu\text{m}$ between the last pixel implantation and the dicing line. This also includes a safety margin between the guard ring and the dicing line. In the other four structures the number of guard rings was reduced to 15, see Figure 4.2(c), and 8, see Figure 4.2(d). In combination with a reduced safety margin a $d_{\text{edge}} = 625\,\mu\text{m}$ is achieved.

Furthermore, for the six structures incorporating the standard guard ring layout two different inter pixel isolation schemes (cf. Section 2.3.1) were used. While for structures 1–3 homogeneous

Table 4.1: Overview of ATLAS pixel structures within the design of the CiS production. Given are the design compatible read-out chip, the p-spray type for the inter-pixel isolation, the number of guard rings, the size of edge distance, the radial distance of the structure from the wafer centre, and the yield. The yield and its uncertainty is discussed in Section 4.2.1

Type	No.	p-spray type	Guard rings	Edge distance [μm]	Radius [mm]	Yield [%]
FE-I3	1	homogeneous	19	1055	43.7	44 ± 12
	2				36.8	72 ± 11
	3				32.8	83 ± 9
	4	moderated			32.8	78 ± 10
	5				36.8	56 ± 12
	6				43.7	33 ± 11
	7	homogeneous	8	625	41.7	31 ± 8
	8				41.4	
	9		15	625	31.0	69 ± 11
	10				30.7	
FE-I4	1	homogeneous	19	1055	11.1	61 ± 11
	2	moderated			11.1	17 ± 9

p-spray was used, 4–6 are implemented with moderated p-spray. The isolation for the four structures with a reduced inactive area is realised via homogeneous p-spray.

FE-I4 Compatible Structures

Except for the dimensions the design of the 26880 single pixels in the FE-I4 structures mimics the FE-I3-design shown in Figure 4.3. The normal and long pixels are arranged in 80 columns and 336 rows. The central 78 columns are equipped with $250\,\mu\text{m} \times 50\,\mu\text{m}$ wide normal pixels. The last and the first column house the long pixels measuring here $450\,\mu\text{m} \times 50\,\mu\text{m}$. Again two different inter pixel isolation schemes were used—homogeneous p-pray in the first FE-I4 and moderated p-spray in the second one. Only the standard guard-ring scheme, consisting of 19 guard rings, was chosen.

4.1.2 Post-Processing at IZM

All post-processing steps described in this subsection were performed at the Fraunhofer Institut für Zuverlässigkeit und Mikrointegration (IZM). In the n-in-p devices the high voltage, which is applied to the back-side of the sensor, is—via the highly conductive cutting edge—also present on the front-side edges of the sensor facing the read-out chip, which is held at ground potential with a small distance of only approximately $20\,\mu\text{m}$. A passivation layer of $3\,\mu\text{m}$ BenzoCycloButene (BCB) [156, 157] has been applied on 10 wafers selected for interconnection to prevent destructive electric discharges between the sensor and the read-out chip. BCB is a material with a much higher dielectric constant of $\epsilon = 2.65$ and a breakdown voltage of 5.3 MV/cm compared to air, which has values of $\epsilon \sim 1$ and a breakdown voltage of only

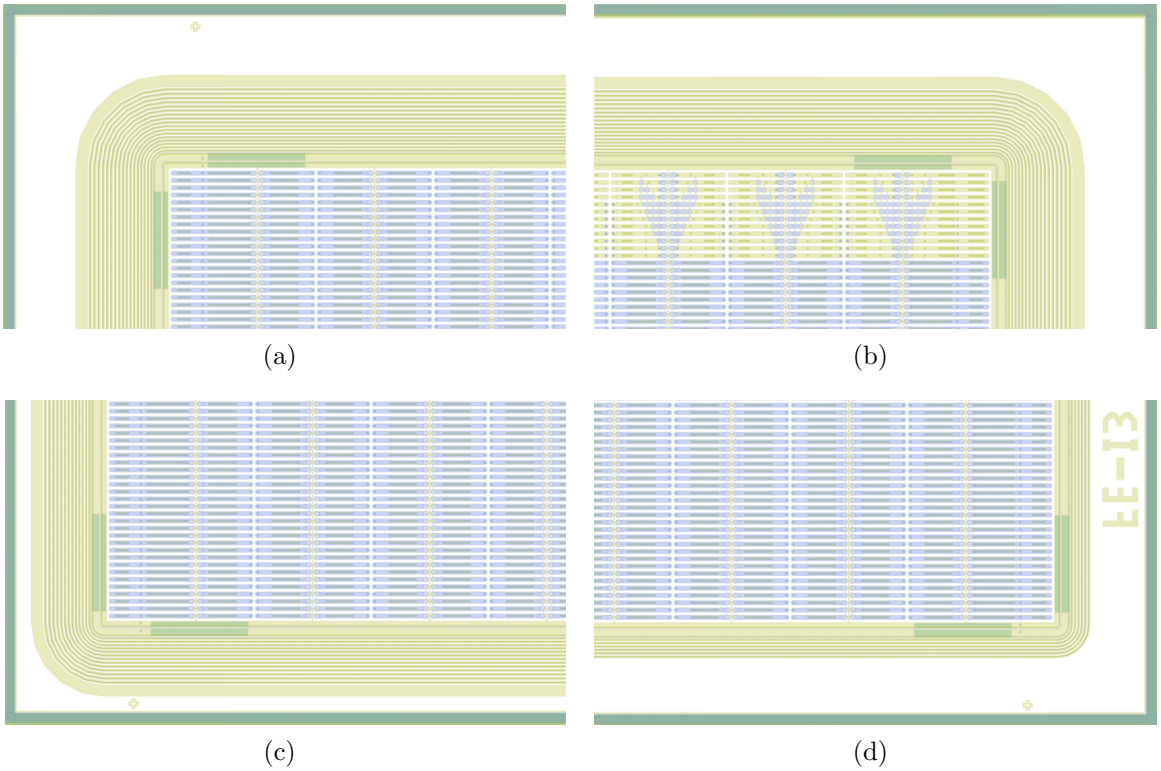

Figure 4.2: Design of (a) normal and (b) (inter)-ganged pixel rows. Comparison of the different guard-ring designs shown to scale. (a) & (b) show the standard 19 guard ring design. In (c) the design with 15 is outlined and in (d) the one with 8 guard rings. The dicing line is drawn in dark green.

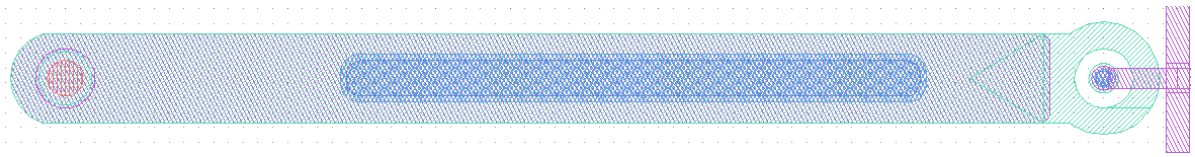

Figure 4.3: Design of a single pixel cell. The metal layer is shown in pink, the implantation in green, the location of the opening in the nitride and oxide in blue, and the one in the passivation layer in red.

25 kV/cm [158]. Furthermore, the values for air are depending for other parameters as the humidity, while they are much more stable for the solid BCB layer.

Since the process has been performed at wafer level the dicing lines and the vertical sides of the sensors are not protected in this approach. The chip lies inside the sensor guard-ring structure except for the side where the chip balcony with the end of columns logic is located.

The BCB layer was opened in correspondence to the bump bonding pads, on which the Under-Bump-Metallization (UBM) was subsequently deposited. Composed by these sensors and FE-I3 chips, 21 assemblies were flip-chipped using SnAg bump-bonds [159] in three batches.

4.2 Properties Before Irradiation

In the following section the properties of n-in-p pixel sensors and assemblies before irradiation will be discussed and compared to standard n-in-n assemblies.

4.2.1 IV Characteristics

The pixel structures were electrically characterised after major production steps to verify their basic functionality and to select the best wafers or structures for further processing. All measurements discussed in this section were taken at room temperature.

Yield and Wafer Selection

All pixel structures on all 18 wafers were electrically characterised to allow for a production yield determination and a selection of the best 10 wafers for further processing. The IV characteristics for all structures are shown in Figure 4.4. On the left, all structures on selected wafers are shown. On the right, the not selected wafers and their structures are presented. The full depletion voltage, as measured by CiS, is indicated by a red line.

The IV characteristics exhibit dedicated differences for the different structures. This is visible for example in Figure 4.4(a), where the IV characteristic of structure 1 (black) exhibit a worse behaviour—i. e. higher leakage currents and lower breakdown voltages—than the ones of structure 2 (green) and 3 (orange). The same is true for structure 2 when compared to structure 3. For a quantitative evaluation of this qualitative features, the yield was defined based on the measured current at an operation voltage of 150 V. For FE-I3 structures the leakage current limit was set to 700 nA, while for FE-I4 structures 2 μA were chosen. The resulting yields vary from 31 % to 83 % with a strong dependence on the radial position on the wafer pointing to process inhomogeneities. All yields are given in Table 4.1. The yield of the structures with 15 guard rings is comparable to the yield of the structures with 19 guard rings at similar radius and the same p-spray implementation, i. e. structures number 2 and 3. The position at larger radii of the 8 guard ring structures makes it impossible to disentangle the effect on the production yield caused by the guard ring scheme from the process inhomogeneity. Anyhow, PHEMOS measurements did not indicate the guard ring structure to be a critical point for the break-down.

For structures at the same radial position on the wafer but with a different isolation scheme, higher leakage currents are found for the moderated p-spray, when compared to the homogeneous p-spray. Also the breakdown voltages are on average lower for the structures with moderated p-spray. Most drastically the yield difference is seen in the two large FE-I4 structures having 61 % yield in the homogeneous p-spray case, but only 17 % yield for the moderated p-spray.

The FE-I4 structures were dedicated to the development of slim edges by University of California Santa Cruz (UCSC) since no FE-I4 read-out chips were available at this point in time. In the following the discussion will be restricted to the FE-I3 structures. Further results for the FE-I4 structures can be found in [160].

Properties After Post-Processing

On the ten wafers with the highest yield BCB and UBM were deposited by IZM. Subsequently the structures were characterised again. For the FE-I3 structures, fulfilling the quality criteria before the post-processing, Figure 4.5(a) shows the correlations for leakage currents at 150 V before and after this step. Structures which exhibit a breakdown before reaching 150 V are

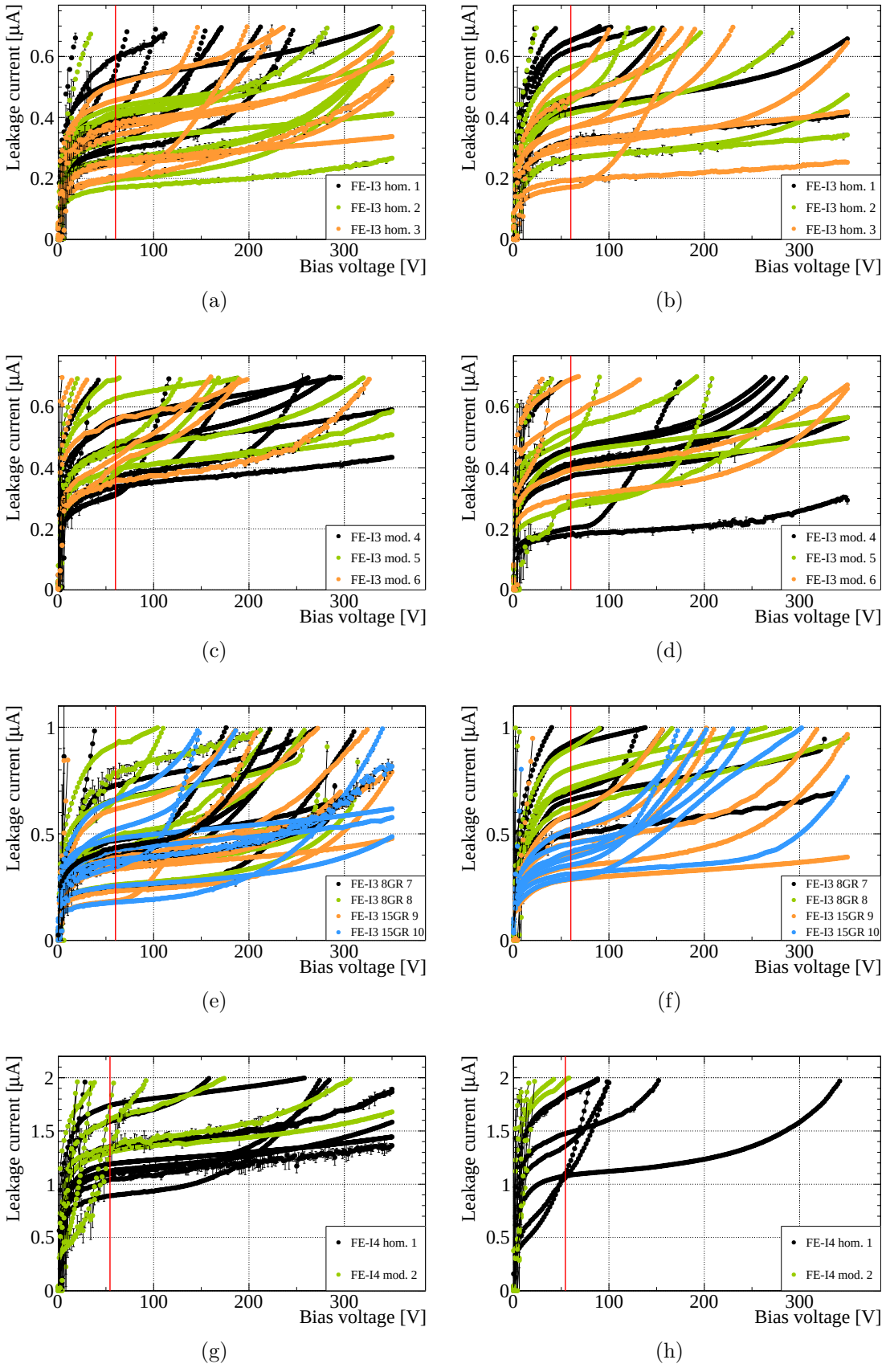

Figure 4.4: IV characteristics for the selected (left) and not selected (right) wafers. The sensor types are given in Table 4.1. The first (second) row shows the standard guard ring layout FE-I3 structures with homogeneous (moderated) p-spray. The FE-I3 structures with 8 and 15 guard rings using homogeneous p-spray are shown in the third row. FE-I4 structures can be found in the last row. The red line indicates the full depletion voltage. Statistical uncertainties are mostly smaller than the markers.

indicated with a leakage current of 0 μA afterwards. For most of the structures the leakage current did not change considerably, but for some of them the leakage current lowered during the post-processing, most likely due to thermal annealing of defects left from the earlier process steps in the silicon bulk.

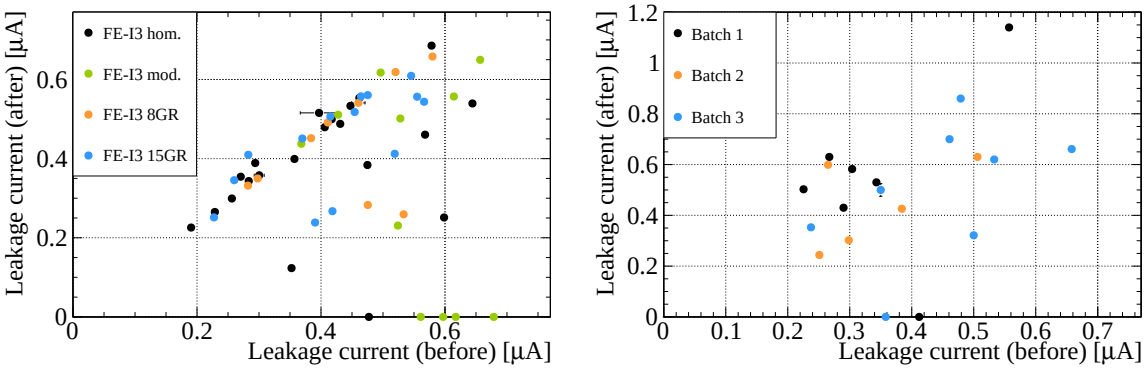

(a) (b)

Figure 4.5: Correlation of leakage currents for the structures which fulfilled the quality criteria before the post processing steps, at $V_{\text{bias}} = 150\,\text{V}$ before and after (a) BCB and UBM deposition in the first place and (b) flip-chipping for the selected assemblies. Structures which failed after the respective process are indicated with zero leakage current. Statistical uncertainties are mostly smaller than the markers.

Based on the IV characteristics 21 FE-I3 structures with homogeneous p-spray were selected for flip-chipping. Breakdown voltages of these assemblies are typically in excess of 350 V, while the full depletion voltage is reached at around 55 V. Only two assemblies failed after the flip-chipping. For all other assemblies the correlation of the currents before and after flip-chipping is summarised in Figure 4.5(b). All leakage currents before as well as after flip-chipping are well below the operational limit of 300 μA [70]. The comparably higher leakage current for the assembly having 1.2 μA after flip-chipping was caused by a handling issue in the flip-chipping process, which was optimised in the latter batches. Still this assembly is working properly.

4.2.2 Assembly Tuning

To be properly operated, the assemblies have to be tuned, i. e. the chip registers have to be set such that each pixel cell performs equally. For the FE-I3 read-out chip the key quantities are the threshold and the ToT-to-charge calibration (cf. Section 3.6.3). A threshold of 3200 e was chosen since this value was found to be an optimal compromise between low threshold and low noise occupancy [161]. The ToT calibration was chosen to be 60 ToT for a reference signal of 20 ke.

An exemplary tuning is shown in Figure 4.6. On the left the threshold and on the right the noise distribution is shown. The three representations are the same for threshold and noise. In the top two-dimensional histograms the threshold of each individual pixel is shown as a function of its geometric position on the assembly. In this plot spatially confined problems can be easily recognised. Such problems were not found for any of the FE-I3 assemblies studied.

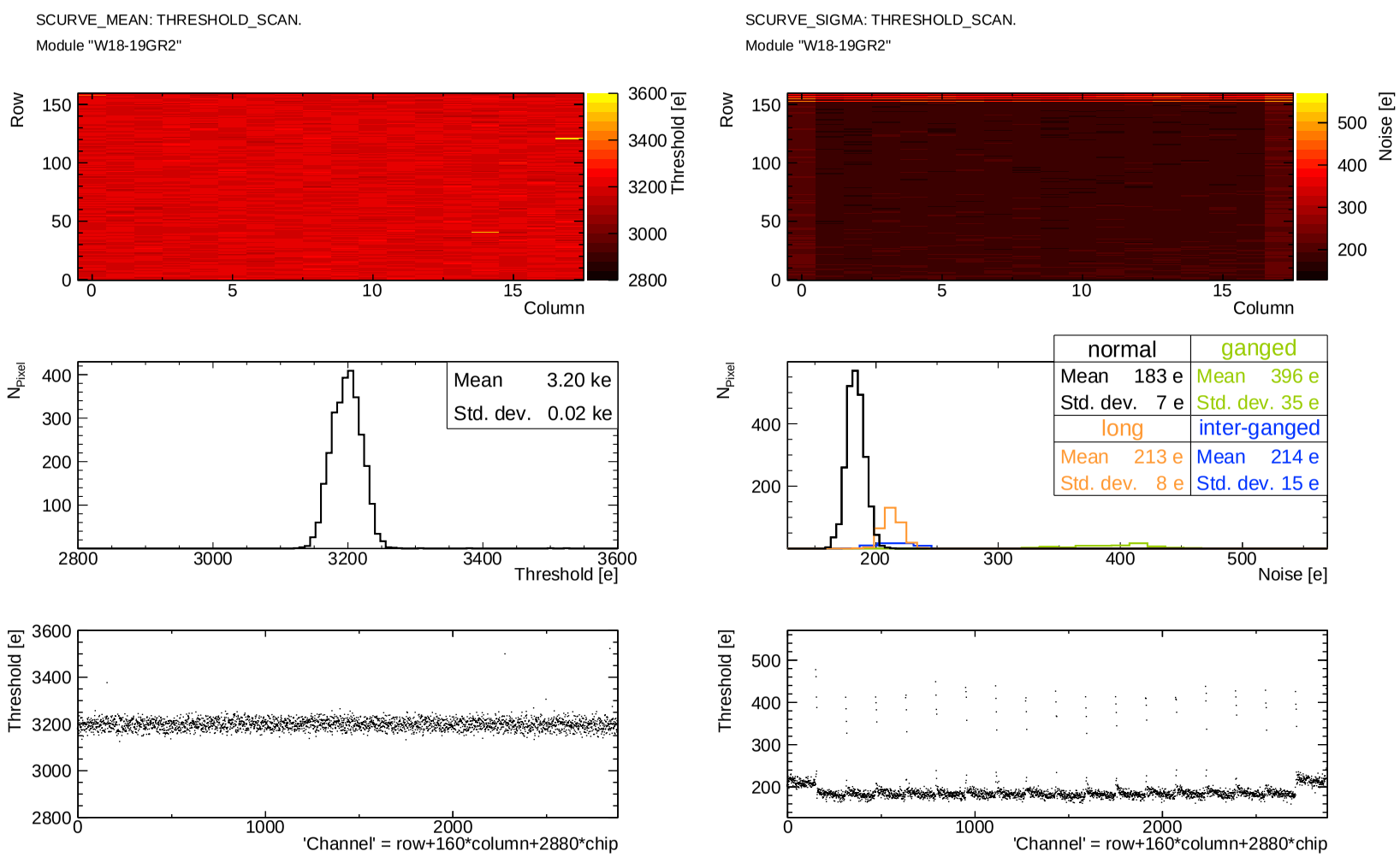

(a) (b)

Figure 4.6: Exemplary threshold tuning for an FE-I3 n-in-p assembly. In (a) the threshold and in (b) the corresponding noise is shown. In the top two-dimensional histogram each pixel is shown. The middle histograms show a cumulative view, which for the noise is split up by pixel type. In the lower graph the value is again displayed versus raising pixel number.

The standard deviation is obtained from the middle representation. Trends over the assembly show up clearest in the lower graph, where the channels are drawn consecutively.

These results are similar for all tuned assemblies and the average standard deviation of the tuned threshold evaluates to (24±3) e. This is in good agreement with the corresponding values for the current standard n-in-n technology used in the ATLAS detector [70].

At a bias voltage of 150 V the noise for normal pixels, e. g. black histogram in middle Figure 4.6(b), is (171±17) e when averaged over all studied assemblies and thus also compatible with the current ATLAS sensors [70]. The noise of the bare chip is of the order of 120 e [162]. For higher bias voltages the noise tends to decrease (Figure 4.7) since the capacitance of the sensor decreases—first in the bulk and eventually between the pixels. In contrast, if the bias voltage is lowered the capacitance of the sensor rises sharply, which is reflected in the noise.

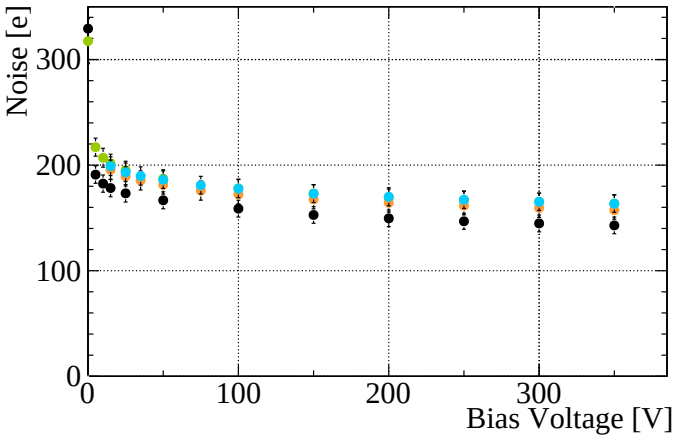

Figure 4.7: Noise as a function of the applied bias voltage for the normal pixels of four assemblies. The uncertainties indicate one standard deviation of the distribution.

The noise for the other pixel flavours is higher than for normal pixels. The long pixels (orange histogram in Figure 4.6(b)) exhibit a higher noise according to the 50 % larger pixel area. Also the ganged (green histogram) and inter-ganged (blue histogram) pixels are more noisy due to their higher capacitance, stemming from their complex shape. In the following the focus will be put on the normal pixels, since these reflect the sensor properties of future designs in the most direct manner.

4.2.3 Charge Collection and Sharing

As foundation of the detection principle, the collected part of the charge induced by traversing particles and its evolution with the applied bias voltage is crucial for semiconductor tracking detectors. In the course of this thesis it has been measured in the laboratory with radioactive sources and at beam tests with pions.

In the following subsection first the response to an ^{241}Am and a ^{109}Cd γ-source with known spectra will be discussed, which will be used for calibration in the following. Second, results for minimum ionizing particles from a ^{90}Sr β-source and in a pion beam test will be presented. Finally, the performance within one pixel cell and the diffusion between several pixel cells are investigated.

Americium Source

Measurements with an ^{241}Am γ-source have been performed to verify the integrity of the bump-bond connections between the sensor and the read-out chip as well as to study the charge collection behaviour for further calibration. For reference a high resolution energy spectrum taken with a high purity Germanium detector adapted from [163, 164] is shown in Figure 4.8(b). For the measurements presented here especially the 59 keV γ-line is interesting, since it corresponds to a signal of 16.4 ke in Si, which is close to the charge deposited by a minimal ionizing particle in a sensor with a thickness of 250 μm (cf. Figure 2.2). Since for measurements with fully absorbed photons, the use of an external trigger is not possible, the internal trigger logic of the read-out chip was employed instead.

Figure 4.8(a) shows the ^{241}Am γ-source energy spectra obtained with an assembly biased at different bias voltages between 5 V and 200 V. The number of entries is normalised to the bin with maximum content.

At the nominal operation voltage of 150 V the prominent 59 keV γ-line is measured at $(14.5 \pm 0.5(\text{fit}) \pm 0.8(\text{syst.}))$ ke (Gaussian fit not shown). The former uncertainty denotes the fit uncertainty and the latter uncertainty the systematic uncertainties from the ToT to charge calibration as discussed in Section 3.6.3. Since in this measurement a known spectrum is induced, this can be used as a cross check for the systematic uncertainties. As discussed in Section 3.6.3 a bias of about 10 % to 15 % towards lower charge signals is expected for charges around 16 ke, which is in good agreement with the about 11 % measured. The width of the peak is fully dominated by the resolution of the charge to ToT calibration, which is about 300 e/ToT. The second prominent line in the spectrum at 26 keV is expected at 7.2 ke. Due to the charge resolution it merges with the lines below, such that only the upper edge is appreciable between 6 ke and 7.5 ke.

At lower bias voltages a seizable fraction of the sensor volume does not contribute to charge collection and thus the internal trigger of the chip is caused mainly by the electronics noise slightly below the threshold—the 50 % efficiency point. The full charge is only collected for

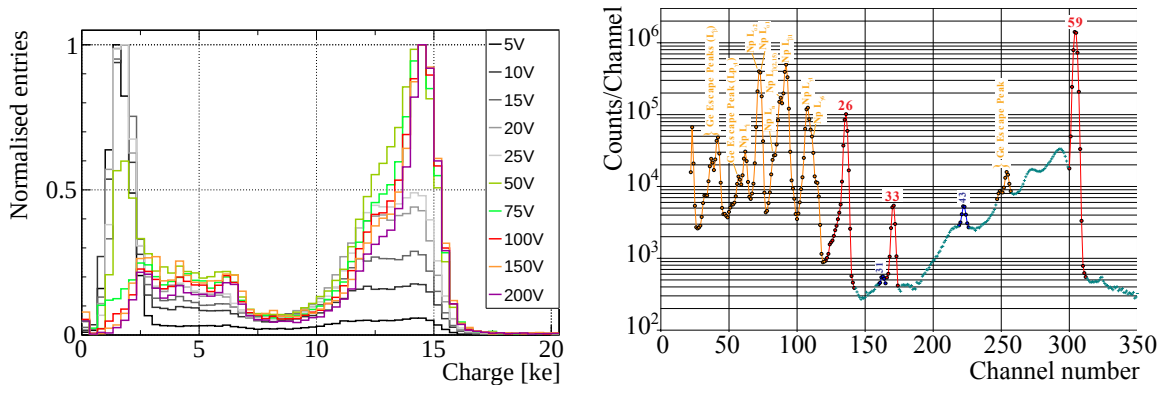

(a) (b)

Figure 4.8: (a) Evolution of the ^{241}Am source energy spectrum with the applied bias voltage. All spectra are normalised to their respective bin with maximum content. (b) ^{241}Am spectrum measured with a high-purity Germanium detector. The numbers given for the different peaks are in keV. High resolution spectrum adapted from [163, 164].

events, where the photo-electric process occurs in an already depleted region. In the not yet depleted part, only the fraction of the charges diffusing into the depleted volume can be measured. This leads to a broadening of the peaks and a less well defined spectrum. The extreme of this scenario can be seen for the spectra well below full depletion (grey to black spectra), the transition at full depletion is visible in the green spectra. Finally, the improvements due to the depletion of the region in between the pixels can be seen in the red to violet spectra. Nonetheless, already in the under-depleted state an operation of the assembly as a tracking detector would be possible, while an n-in-n assembly would not work at all in this regime before the type inversion point occurring with irradiation.

Cadmium Source

For lower induced charges the bias induced by the ToT-to-charge calibration is expected to be smaller. To verify this a ^{109}Cd γ-source with two prominent, non-resolvable lines around 22 keV from the subsequent decay of silver was employed. These lines correspond to a induced charge of 6.1 ke. In Figure 4.9 the measured energy spectrum at an applied bias voltage of 150 V and a reference high resolution energy spectrum, taken with a high purity Germanium detector adapted from [163–165] are depicted. Indeed the line is observed at a collected charge of $(6.1 \pm 0.8(\text{fit}) \pm 0.3(\text{syst.}))$ ke as derived from a description with a Gaussian.

To accommodate for the bias of the ToT-to-charge calibration, in the following measured collected charges above 6.1 ke will be corrected, based on these γ source measurements. The correction factor is 0 % at a measured charge of 6.1 ke and 13.1 % at measured charge of 16.4 ke. Scaling factors between and above are calculated by linear inter- or extrapolation. Half of the correction is then added to the uncertainty.

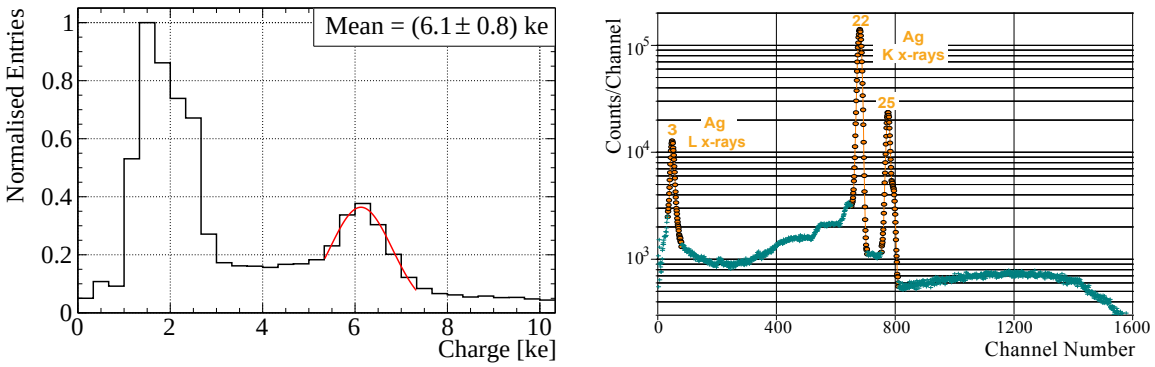

(a) (b)

Figure 4.9: (a) ^{109}Cd source energy spectrum at an applied bias voltage of 150 V. The spectrum is normalised to the bin with maximum content. In red a Gaussian fit is shown. (b) ^{109}Cd spectrum measured with a high-purity Germanium detector. The numbers given for the different peaks are in keV. High resolution spectrum adapted from [163–165].

Minimal Ionizing Particles

The charge distribution caused by minimal ionizing electrons of a ^{90}Sr source was studied at different bias voltages. The distributions are well described by a Landau distribution convoluted with a Gaussian. As an example a distribution at 150 V is shown together with the fitting function in Figure 4.10(a). The tail below approximately 15 ke on the left of the Landau distribution is resulting from the not directly connected n^+ implant in the bias dot region, visible on the right in Figure 4.11.

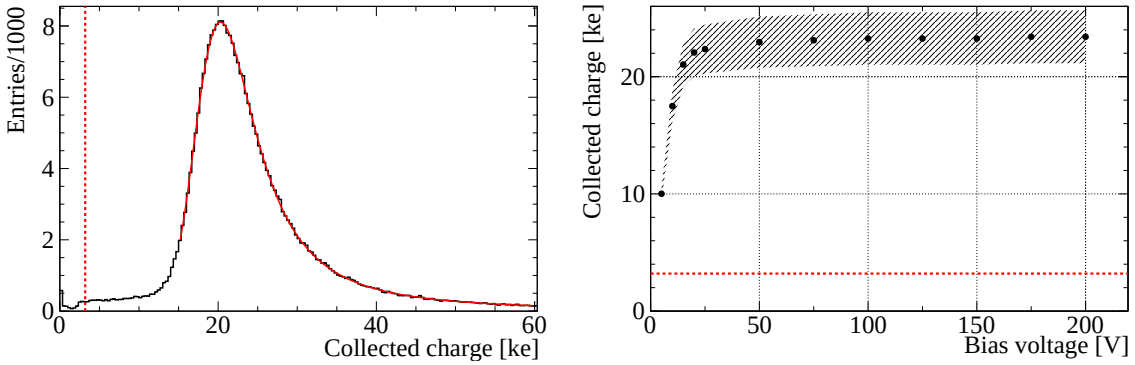

(a) (b)

Figure 4.10: (a) Distribution of collected charges together with a fit indicated in red. (b) MPV of the collected charge as a function of the bias voltage. The uncertainties account only for the systematic uncertainties discussed in Section 3.6.3. The dotted line in both figures indicates the threshold at 3.2 ke.

The evolution of the determined MPV as a function of the bias voltage is shown in Figure 4.10(b). Only the systematic uncertainties discussed in Section 3.6.3 are shown. Statistical uncertainties are below 0.01 ke. As expected the collected charge saturates around the full depletion voltage of 60 V, but also well below most of the charge is already collected within the trigger time window of 25 ns. Within uncertainties, the saturation value of (22.9 ± 2.3) ke agrees well with the expected value of 22.8 ke for a sensor of 285 μm thickness. Compared to the threshold of 3.2 ke a signal-to-threshold ratio of seven is found which indicates a very good expected hit performance, as later confirmed by the beam tests data.

In the beam test performed at the CERN SPS with 120 GeV π^+, the homogeneity of the charge collection was investigated. A map of the mean collected cluster charge as function of

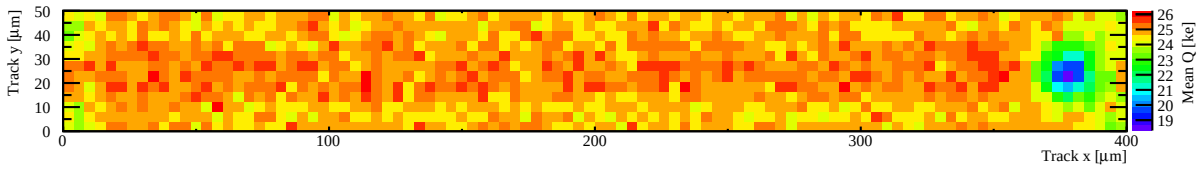

Figure 4.11: Mean collected charge as function of the impact point predicted by the beam telescope. The mean charge is systematically higher than the MPV of the collected charge, cf. Section 2.1.3.

the impact point predicted by the beam telescope is shown in Figure 4.11 for an assembly biased at 150 V. As discussed in Section 2.1.3 the mean charge is systematically higher than the MPV.

The design of the pixel (see Figure 4.3) is reflected in the figure. On the right hand side the bias dot leads to a lower mean collected cluster charge. Also in the four corners the collected charge is slightly lower, because the deposited charges can diffuse into several neighbouring pixel cells, of which some can be below threshold, when obtaining only a fraction of the entire signal. Since before irradiation all charges are well above threshold this imposes no constraints for operation. However, since this poses a challenge after high levels of irradiation for perpendicular impinging particles, within the ATLAS Planar Pixel Sensor R&D Project [166] several ideas are investigated on how to alter the punch through biasing to minimize this effect [113, 167].

The diffusion into neighbouring cells also leads to charge sharing among several pixels and the composition of n-hit clusters, where n is the number of pixels involved. Taking charge sharing between different pixels into account, the position resolution of the detector is improved. On the other hand, if the charge measured in one pixel is below threshold, the hit efficiency will be diminished. The latter effect is only important if the collected charge is close to the threshold, e. g. after irradiation. The charge sharing probability P(Share) (cf. Section 3.7.3) was studied in the beam test and is shown in for Figure 4.12 perpendicular incidence of the pions and a (a) slightly tilted incidence angle of $\varphi = 15°$ (b) with respect to the short pixel direction y as it is also foreseen in the IBL. See Figure 3.16 for the coordinate definition.

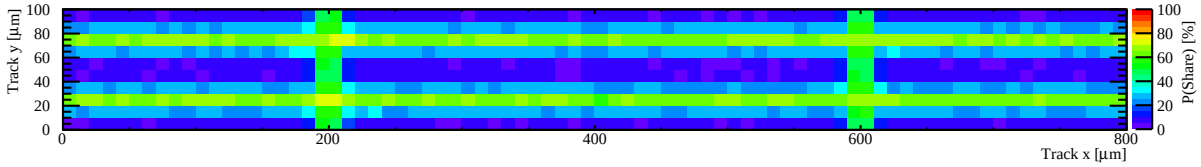

(a)

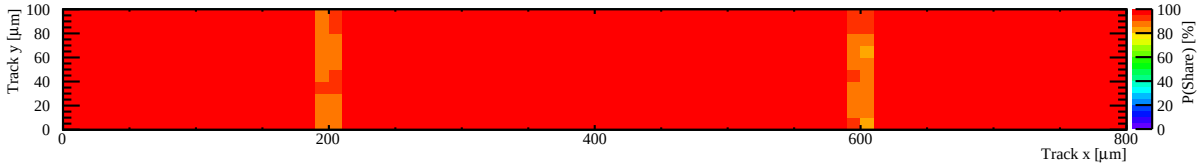

(b)

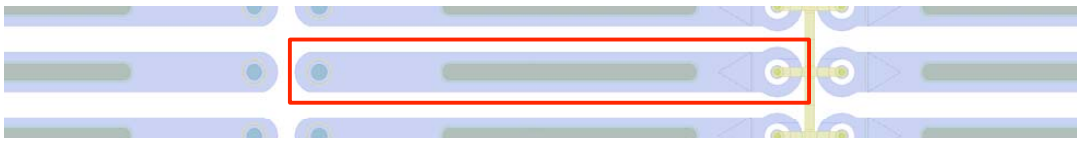

(c)

Figure 4.12: Probability for a deposited charge to be shared among neighbouring pixels P(Share) as a function of the impact point predicted by the beam telescope. (a) and (b) show the same assembly operated at a bias voltage of 150 V. In (a) $\varphi = 0°$, in (b) $\varphi = 15°$. For reference (c) shows the geometry of (a) and (b) in the design. The central pixel cell is indicated by the red frame.

In the perpendicular case, the P(Share) is highest at the side opposite to the bias dot, and in between four pixels, i. e. at $(x, y) \in \{(200\,\mu\text{m}, 25\,\mu\text{m}), (200\,\mu\text{m}, 75\,\mu\text{m})\}$. The other zones of high sharing probability align naturally with the borders of the pixel cell. When tilting the assembly the situation changes dramatically. Now, the charge is deposited over approximately $70\,\mu$m along the short pixel direction y, i. e. over almost 1.5 pixels. Thus, the charge sharing probability is 100 % almost everywhere, but in the region of the short pixel borders, where it drops to 90 %. This is because of charges that are shared among at least four pixels and thus some of the neighbouring pixels may be below threshold.

Averaged over the sensor (27.3 ± 0.06) % of the tracks are shared between pixels in the perpendicular setting and (98.5 ± 0.02) % in the titled setting. All uncertainties are calculated according to [168]. The level of charge sharing as well as the geometrical features are in good agreement with the values found for n-in-n standard assemblies [113, 169].

4.2.4 Spatial Resolution

Spatial resolution—a quantity of key importance for tracking detectors—is studied with beam test data via residuals in combination with the relative abundance of different cluster sizes. In the following first the abundance of different cluster sizes is discussed followed by a discussion of the position resolution as a function of the cluster size.

All measurements in this section are taken at a bias voltage of 150 V.

Cluster size

The cluster size distributions reflect the charge sharing probability. For perpendicular incidence on average around 71 % of the clusters consist of a single hit. Another 25 % are two-hit clusters[2], while the rest accounts for three and more hit clusters. As larger clusters allow to additionally use charge information to determine the incident point and thus yield a higher resolution they are of special interest for tracking. In Figure 4.13 the cluster size distribution is divided further by the long (x) and the short (y) pixel coordinate. Naturally, higher multiplicity clusters occur much more frequently in the short pixel direction. Tilting the sensor in φ enhances higher multiplicity clusters in y while it has no effect in x. For tilted φ the average for two-hit clusters is 76 % and 20 % for three hit clusters, while single hit clusters are barely contributing. In all cases the uncertainties calculated according to [168] are smaller than 0.1 %.

Residuals

The residual distributions for single- and two-hit clusters are shown in Figure 4.14. On the left the residuals with respect to the long pixel coordinate x are shown, the corresponding histograms for the short pixel coordinate y are shown on the right.

Given the uniform illumination with pions the standard deviation of the single-hit distributions is expected to be pitch$/\sqrt{12}$, i. e. 115.5 μm and 14.4 μm respectively. The experimental values are found to be $(116.1 \pm 1.6)\,\mu$m and $(16.1 \pm 1.8)\,\mu$m, where the uncertainty accounts for the space point resolution and alignment of the telescope (cf. Section 3.7.2). The statistical uncertainty is less than $0.01\,\mu$m. Residuals of the order of half the pitch are suppressed since charges induced in this region are shared between two or more pixels and thus lead to higher multiplicity clusters and a partial suppression of one-hit clusters. Oppositely, when the charge

[2] Two hit clusters can be restricted to one row or column or occur diagonally

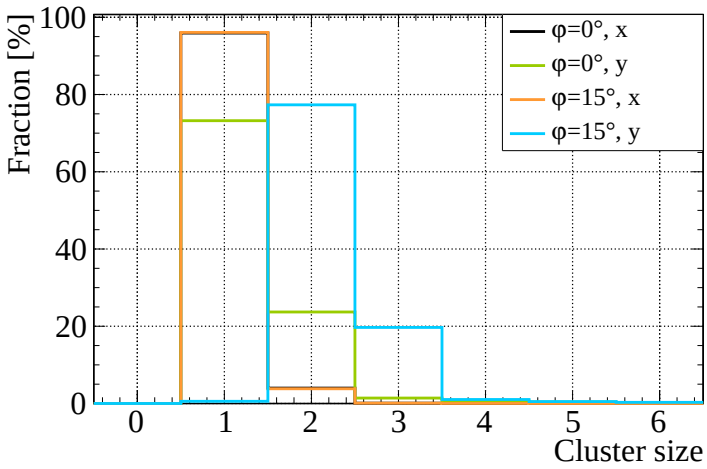

Figure 4.13: Fraction of the different cluster sizes restricted to a column (x) or row (y) in the beam test for perpendicular and tilted incidence of the pions. In the latter case the assembly is tilted by $\varphi = 15°$. The black line is mostly covered by the orange line. In all cases the uncertainties calculated according to [168] are smaller than 0.1 %.

deposited in the pixel cell penetrated by the particle is below threshold, because most of the charge diffused to a neighbouring cell, this results in residuals for the one-hit clusters exceeding half a pitch. This leads to smoothed edges of the distributions and thus increases the standard deviation slightly.

For two-hit clusters the resolution obtained is similar in x and y since they occur mainly in the border regions. It is defined as the width of the core peak in the charge-weighted [151] two-hit cluster distributions shown in Figures 4.14(c) and 4.14(d). The distributions are well described by two Gaussians. The first, broader Gaussian accounts for misrecontructed tracks and events for which the used ATLAS charge weighting algorithm did not yield an improved result; the core Gaussian gives the resolution. For the perpendicular case the resolution is calculated to be $\sigma_x = (8.9 \pm 2.0)\,\mu$m and $\sigma_y = (7.3 \pm 0.7)\,\mu$m, with in both cases 80 % of the events contained in the core Gaussian.

While in the x-coordinate the resolution stays unchanged with tilting the module in the φ, the standard deviation of the single-hit distribution is degraded to $(19.2 \pm 1.7)\,\mu$m, hence larger than the theoretically predicated value. This is due to tracks impinging close to the edge of one pixel, but only creating a cluster centred in the neighbouring pixel. Anyhow, the impact of single hit clusters is negligible in the tilted regime. For the two-hit clusters $\sigma_y = (11.3 \pm 1.9)\,\mu$m is found and for the three-hit clusters $\sigma_y = (13.2 \pm 1.9)\,\mu$m, where in the three-hit case the same fitting function has been used as in the two-hit case.

All values agree with theoretical expectations and exhibit the same performance as standard n-in-n sensors [70].

4.2.5 Hit Efficiency

The hit efficiency, defined as the fraction of hits matched to reconstructed tracks, is shown in Figure 4.15 as a function of the impact point predicted by the beam telescope, within the pixel geometry. For not irradiated assemblies a hit efficiency of (99.3 ± 0.3) % is measured, with a

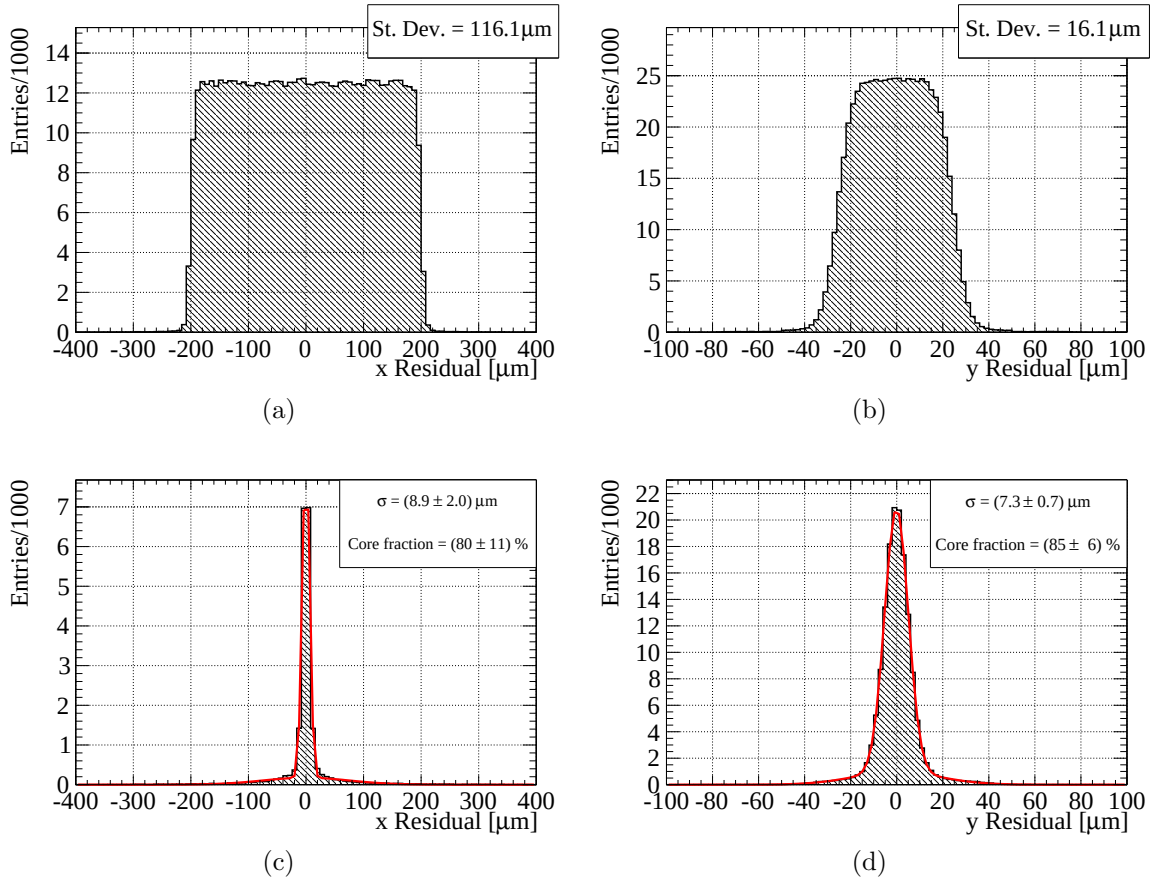

Figure 4.14: Residual distributions for single- (top) and two-hit (bottom) clusters for the long pixel coordinate x (left) and for the short pixel coordinate y (right).

homogeneous behaviour over the pixel. The uncertainty is systematic and accounts for tracks, which are equivocally considered in-time, cf. Section 3.7.2. Uncertainties calculated according to [168] are smaller than 0.05 %. Since these measurements are taken for a perpendicular incidence angle, they can be considered conservative when compared to the real conditions in the tracker of an LHC experiment.

Unfortunately, desynchronization of the beam telescope read-out chain and the assemblies prevented the determination of the hit efficiency for the tilted case, since no reliable reference plane is available in these data. See Section 3.7.2 for further details.

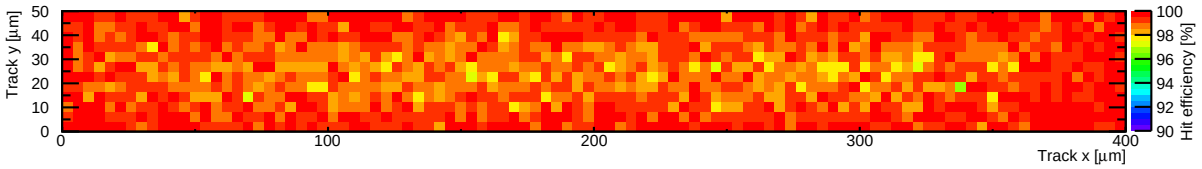

Figure 4.15: Mean hit efficiency as functions of the impact point predicted by the beam telescope.

4.3 Properties After Irradiation

In view of the upgrade of the tracker systems for HL-LHC the study of the performance of the pixel modules after high received fluences is extremely relevant. In this section the results on the radiation hardness of n-in-p assemblies will be reported up to a fluence of $10^{16}\,\mathrm{n_{eq}/cm^2}$ and compared to the standard n-in-n assemblies wherever data are available.

After a short overview on the received fluences and irradiation types the discussion of these results follows the structure of Section 4.2.

4.3.1 Overview of Irradiated Assemblies

The n-in-p pixel assemblies were irradiated with reactor neutrons at JSI, low energy protons at KIT, and high energy protons at CERN PS, all described in Section 3.3. Since the FE-I3 read-out chip was designed for a maximum fluence of $10^{15}\,\mathrm{n_{eq}/cm^2}$ or a total dose of 500 kGy [70] some of the measurements were done well outside of its specifications. Unfortunately, this limited the maximum explorable fluence at KIT to $10^{15}\,\mathrm{n_{eq}/cm^2}$ and for all assemblies irradiated at CERN PS the read-out chips failed after irradiation. All assemblies discussed further in this section are summarised in Table 4.2.

Table 4.2: Overview of irradiated CiS n-in-p assemblies. The irradiation site is given together with the information whether the assembly was studied in a beam test.

Fluence [$10^{15}\,\mathrm{n_{eq}/cm^2}$]	Irradiation site	Beam test
1	JSI	yes
1	KIT	yes
1+1	JSI+KIT	no
2	JSI	no
3	JSI	no
5	JSI	yes
10	JSI	yes

4.3.2 Electrostatic Properties

In the following section first the IV characteristics are discussed as a basic functionality test and to determine the actual sensor temperature. Subsequently, results on the effectiveness of the electric discharge protection will be given.

IV Characteristics

Figure 4.16(a) shows the IV characteristics of the assemblies irradiated with neutrons up to fluences between $10^{15}\,\mathrm{n_{eq}/cm^2}$ and $10^{16}\,\mathrm{n_{eq}/cm^2}$ scaled [105] to a temperature of $-20\,^{\circ}\mathrm{C}$—the design operation temperature of the IBL. As expected, the breakdown voltage of the irradiated sensors shifts to higher values, and starting from a fluence of $5 \cdot 10^{15}\,\mathrm{n_{eq}/cm^2}$ exceeds 800 V. The leakage currents are in agreement with expectations, showing increasing leakage currents with increasing fluences.

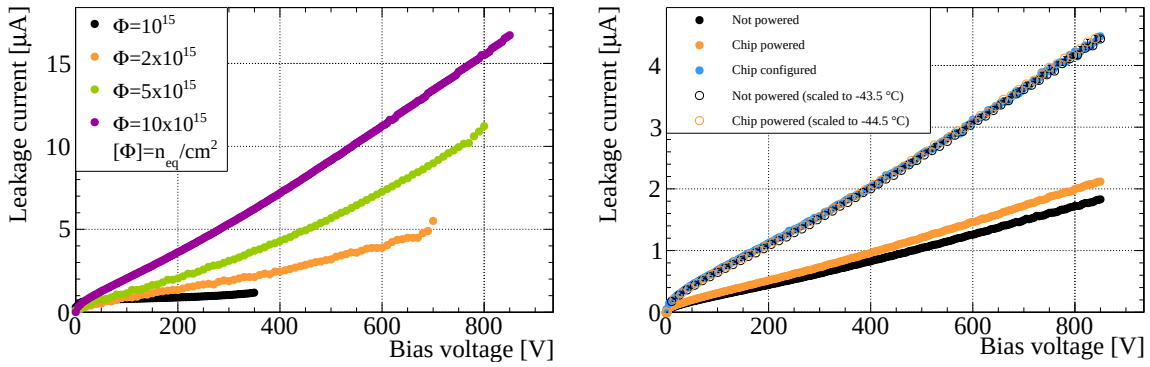

(a) (b)

Figure 4.16: (a) IV characteristics of the irradiated assemblies scaled to −20 °C. (b) IV characteristics taken at an environmental temperature of −50 °C for an assembly irradiated to $5 \cdot 10^{15}$ n_{eq}/cm^2 in three different states: not powered, powered, and configured. Additionally, the not powered and powered states are shown scaled to the expected sensor temperature. To improve the visibility only each third point is drawn for the scaled measurements. All uncertainties are smaller than the symbols.

Measurement Temperature

Because of the higher leakage currents and the danger of thermal runaway, irradiated assemblies have to be operated in a cooled environment. To achieve the best homogeneity over all measurements in the laboratory within a climate chamber and at the beam test with dry-ice cooling a temperature of −50 °C was chosen as reference.

For the laboratory measurements the reported temperatures are the measured air temperatures in the climate chamber. To determine the actual sensor temperature, which is higher due to the dissipated power of the read-out chip, IV characteristics were measured at different operational states of the read-out chip, i. e. not powered, powered and configured. All curves are shown in Figure 4.16(b) for the assembly irradiated to $5 \cdot 10^{15}$ n_{eq}/cm^2. For the not connected state (black circles), the sensor temperature is assumed to be in equilibrium with the environment. After powering the chip the temperature is slightly increased resulting in a slightly higher leakage current of the assembly (orange circles). The power consumption of about 200 mW for the configured chip results in a further increase of the leakage current (blue circles). When scaling [105] the leakage current to higher temperatures a good agreement can be reached (open circles). Based on these measurements the temperature on the sensor is estimated to be 5 °C to 10 °C higher than the environment temperature.

Electric Discharge Protection

The high bias voltage that needs to be applied after irradiation to maintain a good charge collection efficiency demands for an effective protection against destructive electric discharges between the sensor and the read-out chip. For the assemblies investigated, this is realised with a BCB passivation layer. Bias voltages up to 1000 V were applied to the assemblies and no destructive electric discharges were observed during operation for several hours in the laboratory. At beam tests voltages up to 900 V were applied for several days.

Since applying bias voltages considerably higher than 1 kV is not feasible in the inner tracking detectors of high energy physics experiments because of cooling and cabling restrictions in the foreseeable future, BCB is a good choice for electric discharge protection at future high energy physics experiment pixel detectors.

4.3.3 Assembly Tuning

The irradiated assemblies were tuned to the same chip response settings as the not irradiated assemblies, i. e. a threshold of 3200 e and 60 ToT for a reference charge of 20 ke. The assemblies irradiated to the highest fluences of $5 \cdot 10^{15}\,\mathrm{n_{eq}/cm^2}$ and $10^{16}\,\mathrm{n_{eq}/cm^2}$ were additionally tuned to a lower threshold of 2000 e.

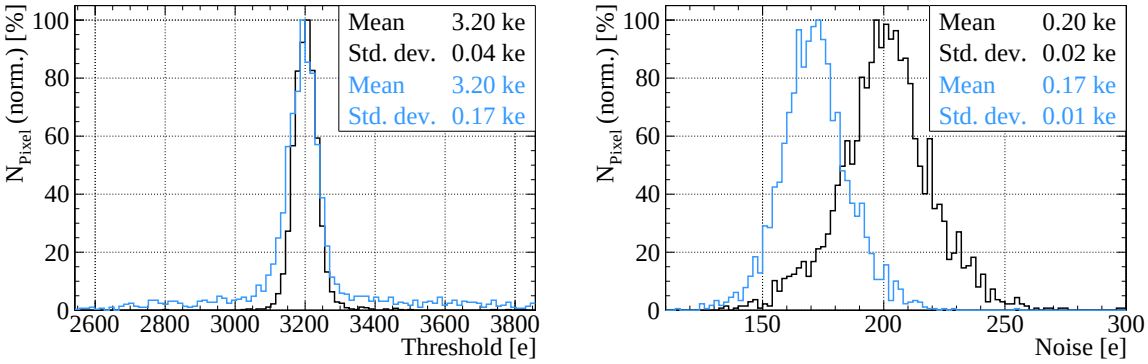

Figure 4.17: (a) Threshold and (b) noise distribution for the assembly irradiated to a fluence of $5 \cdot 10^{15}\,\mathrm{n_{eq}/cm^2}$ in different operation conditions. In the black histogram it is operated at 600 V and −50 °C, in the blue histogram it is operated at 1000 V and −60 °C. All distributions are normalised to the bin with maximum content.

The tuning was possible without changes in the set-up, for the sample irradiated at $10^{16}\,\mathrm{n_{eq}/cm^2}$ operated up to a bias voltage of 950 V. For the assembly irradiated to $5 \cdot 10^{15}\,\mathrm{n_{eq}/cm^2}$ this was only possible up to 700 V at an environment temperature of −50 °C. For higher voltages the environment temperature had to be lowered to −60 °C, since the read-out chip lost its configuration at higher temperatures.

Nonetheless, several pixel cells were not tuneable anymore for the $5 \cdot 10^{15}\,\mathrm{n_{eq}/cm^2}$ assembly when operated above 700 V. For comparison, in Figure 4.17 the distributions of noise and threshold at a bias voltage of 600 V and a environmental temperature of −50 °C (black histograms) are shown, which are also exemplary for the other irradiated assemblies at all voltages. In contrast the tuning achieved at −60 °C at 1000 V (blue histograms) exhibits pronounced tails. Still three quarters of the pixel cells could be tuned. In the noise distributions the effect of the lower temperature is reflected in a shift towards a lower mean noise.

As for not irradiated assemblies the mean threshold is independent of the bias voltage. For high voltages the standard deviation of the threshold increases with bias voltage. This is especially true for the assembly irradiated to $5 \cdot 10^{15}\,\mathrm{n_{eq}/cm^2}$ due to the issues discussed above.

The noise and its standard deviation is shown in Figure 4.18 as a function of the bias voltage for the neutron irradiated samples. It is independent of the bias voltage as well, but a general

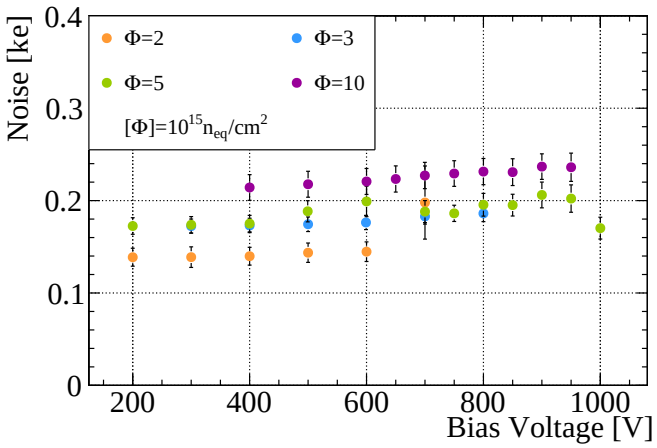

Figure 4.18: Evolution of the noise with applied bias voltage for different received fluences. All points are taken at an environmental temperature of −50 °C, but for the green point at 1000 V, which was taken at an environmental temperature of −60 °C.

trend of increasing noise is found with increasing fluence. Given that the depleted volume is reduced with increasing fluence, resulting in an increased input capacitance, an increase in the noise is to be expected. The impact of the environment temperature is appreciable in the assembly irradiated to $5 \cdot 10^{15}\,\mathrm{n_{eq}/cm^2}$. While the noise and its standard deviation rises towards 600 V both are lowered when switching to −60 °C at 700 V.

4.3.4 Charge Collection and Sharing

Due to radiation defects the charge collection efficiency is reduced while the full depletion voltage increases. The dependence of the charge collection efficiency on the fluence and bias voltage will be discussed and for the assembly irradiated to $5 \cdot 10^{15}\,\mathrm{n_{eq}/cm^2}$ compared to the respective charge collection efficiency of an n-in-n assembly irradiated to the same fluence.

Annealing Uncertainties

After irradiation all assemblies are stored in cooled environments whenever possible to prevent annealing. Since at the JSI only bare assemblies can be irradiated, a remounting of the assemblies onto the detector boards is required. This leads to a total annealing of about 1.5 d. A systematic study of the annealing effects on the collected charge could instead be performed with the assembly irradiated while mounted on its detector board at KIT, where an incessant cooling is guaranteed and the handling annealing time is about 2 h.

Over a time period of nine days, measurements with a ^{90}Sr source at a bias voltage of 550 V where taken. Between each pair of measurements the assembly was kept at a controlled environment temperature of 20 °C. The evolution of the MPV with time is shown in Figure 4.19. As expected, a logarithmic behaviour is found. Over the full time period the collected charge increases by about 63 %, whereof the charge increases by 34 % during the time corresponding to the annealing received by the neutron irradiated assemblies, due to the remounting.

The MPV of the collected charge in the mixed irradiation assembly as a function of the bias voltage is depicted after both irradiation steps in Figure 4.20 up to the operational limit of the

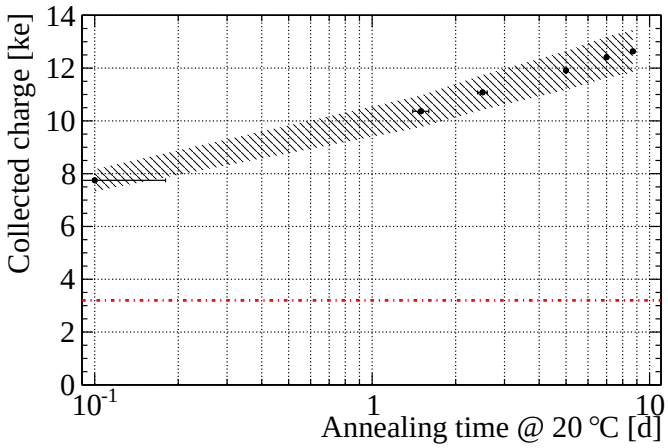

Figure 4.19: Evolution of the MPV of the collected charge over a beneficial annealing time period of about 9 d at 20 °C for the proton irradiated assembly. The uncertainties in the collected charge account only for the systematic uncertainties discussed in Section 3.6.3. Statistical uncertainties are below 0.01 ke. The uncertainties in the annealing time stem from uncertainties in the shipping, and temperature transition times. The dotted line indicates the threshold at 3.2 ke.

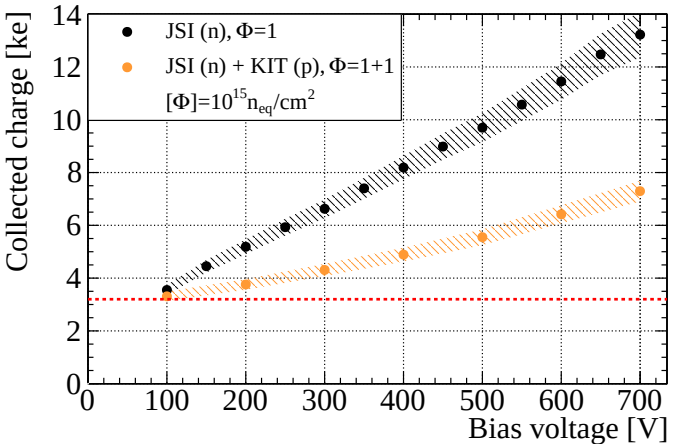

Figure 4.20: MPV of the collected charge as a function of the applied bias voltage for the mixed irradiated assembly after the first irradiation step at JSI (black) and after both irradiations (orange). The uncertainties account only for the systematic uncertainties discussed in Section 3.6.3. Statistical uncertainties are below 0.01 ke. The dotted line indicates the threshold at 3.2 ke.

SCC (cf. Section 3.6.2) of 700 V. In the case of the second irradiation no additional annealing was applied. No saturation is seen due to the higher full depletion voltage.

Minimizing Ionizing Particles

As before irradiation, the charge collection was measured as a function of the bias voltage using a ^{90}Sr source. This was done for the mixed irradiated as well as for the neutron irradiated assemblies.

The MPV of the collected charge after the irradiation with neutrons of (10.6 ± 0.6) ke at a bias voltage of 550 V is in good agreement with the MPV of the collected charge in the assembly irradiated only with protons at same equivalent fluence and voltage after a comparable annealing time of 1.5 d.

Figure 4.21 gives an overview of the MPVs of the collected charges for the different neutron irradiated assemblies as a function of the bias voltage.

The MPV of the collected charge decreases for a given voltage with received fluence as expected; with rising bias voltage the CCE can be partly recovered, since a greater volume of the sensor is depleted.

Although for none of the assemblies a saturation is found, since the expected full depletion voltages exceeded the applied bias voltages, for all the assemblies bias voltages below 1 kV were sufficient to reach an MPV of twice the threshold, which can be considered as safe for tracking

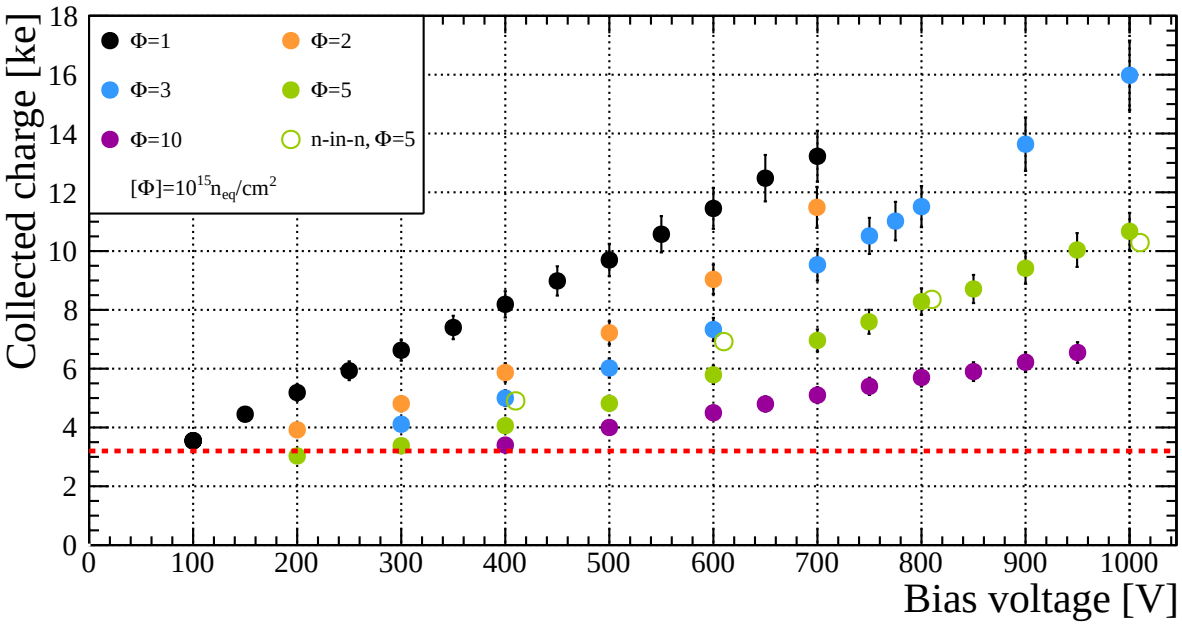

Figure 4.21: MPV of the charge collected by neutron irradiated assemblies, obtained from ^{90}Sr measurements, and as a function of the bias voltage. The uncertainties account only for the systematic uncertainties discussed in Section 3.6.3. To improve visibility the fully correlated uncertainty bands are only indicated by uncertainty bars attached to the data points. The results from the n-in-n assembly are from [170] and displaced by 10 V to improve visibility. The dotted line indicates the threshold at 3.2 ke.

applications. If the threshold is lowered further, as it is possible e. g. for the new ATLAS read-out chip FE-I4 [141], the signal-to-threshold level increases even to higher values, gaining some redundancy for a reliable detector operation.

The n-in-n data given for comparison are taken from [170]. A very similar performance in terms of charge collection is observed between the two technologies.

Charge Collection Profile

For several assemblies the charge collection behaviour was also studied within a beam test (cf. Table 4.2). For low fluences in the context of HL-LHC of $10^{15}\,\mathrm{n_{eq}/cm^2}$ as shown for example in Figure 4.22(a) the characteristics of the mean collected charge as a function of the impact point predicted by the beam telescope resemble the ones before irradiation (cf. Figure 4.11). Also in this case the bias dot is visible. Additionally, since the overall lower charges are more likely to be below threshold in one of the neighbouring pixel cells when shared between two or more pixels, the edges and corners of the sensor now become more pronounced. Nonetheless, over the entire pixel cell, charges highly in excess of the threshold value are measured.

With increasing received fluence, the difference between the collected charge and the threshold becomes smaller, if the voltage is not raised considerably. As an example the assembly irradiated at $5 \cdot 10^{15}\,\mathrm{n_{eq}/cm^2}$ is shown in Figure 4.22(b) biased at 600 V. No structure is visible, since all charges which cannot be fully collected, are below threshold and the event thus lost. If the bias voltage is raised to 900 V, see. Figure 4.22(c), the pixel design becomes visible again.

Consequently, the charge sharing probability P(share) is reduced with increasing fluence. This is depicted in Figure 4.23 for an assembly irradiated up to $10^{15}\,\mathrm{n_{eq}/cm^2}$ operated at a bias voltage of 700 V (a) and for the assembly irradiated up to $5 \cdot 10^{15}\,\mathrm{n_{eq}/cm^2}$ operated at a bias voltage of 900 V (b). The lower P(share) becomes particularly visible at the side of the bias dot. Since charge collection is less efficient here shared charges are likely below threshold in one of the pixels and thus only result in single-hit clusters.

The dependence of the overall charge sharing probability on the applied bias voltage, received fluence, and threshold (T) is shown in Figure 4.24 for neutron irradiated assemblies with received fluences between $10^{15}\,\mathrm{n_{eq}/cm^2}$ and $10^{16}\,\mathrm{n_{eq}/cm^2}$. Due to the higher charge collection efficiencies at higher voltages, and thus increased likelihood of the collected charge exceeding the threshold also in the neighbouring pixel, the probability rises with applied bias voltage. The collected charge decreases with the received fluence, and thus the probability that a hit is below threshold, and not detected, increases accordingly, leading to a lower charge sharing probability. If the threshold is lowered from 3.2 ke to 2 ke P(Share) rises, since the possibility to be above threshold in a second pixel is increased.

4.3.5 Spatial Resolution

In the following section first the abundance of different cluster sizes in dependence of the received fluence and the applied bias voltage will be discussed. Second, the space point resolution is assessed via the residuals.

Cluster Sizes

Lower charge sharing results in a lower abundance of higher multiplicity clusters. An overview on the cluster sizes observed at different bias voltages and received fluences (colour) is given in

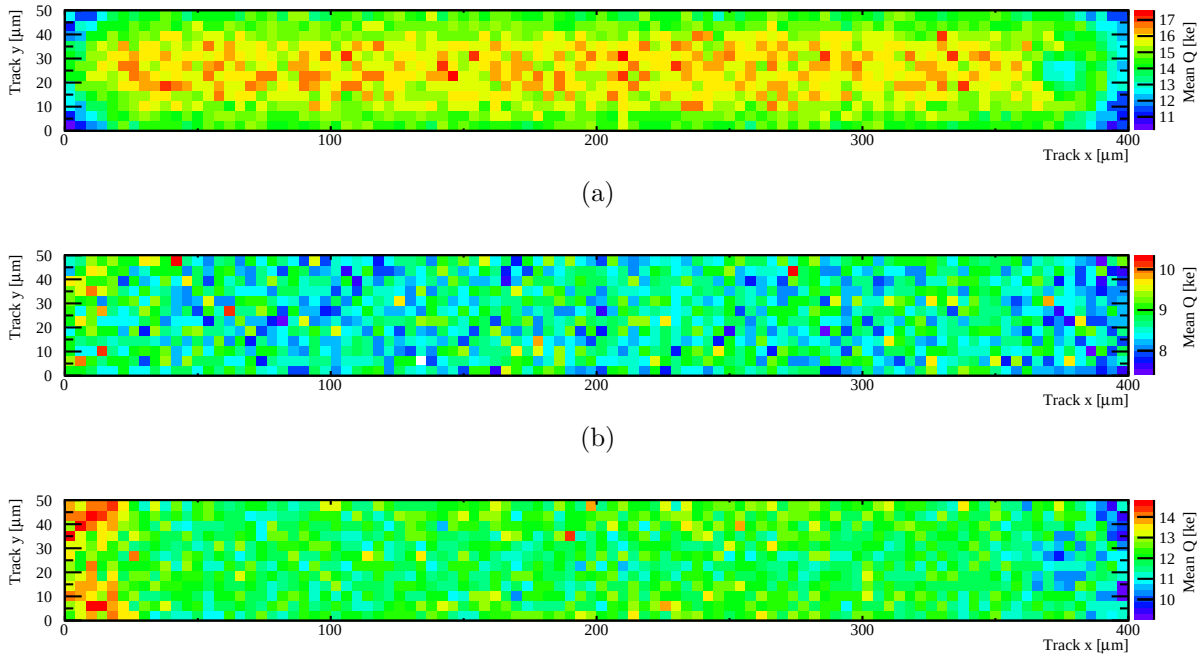

Figure 4.22: Mean collected charge as a function of the impact point predicted by the beam telescope. In (a) for the proton irradiated assembly (at $10^{15}\,\mathrm{n_{eq}/cm^2}$) operated at $V_{\mathrm{bias}} = 500\,\mathrm{V}$ and in (b, c) for the assembly irradiated with neutrons to a fluence of $5 \cdot 10^{15}\,\mathrm{n_{eq}/cm^2}$ operated at $V_{\mathrm{bias}} = 600\,\mathrm{V}$ and $V_{\mathrm{bias}} = 900\,\mathrm{V}$. The colour code is different in the three figures. The mean charge is systematically higher than the MPV of the collected charge, cf. Section 2.1.3.

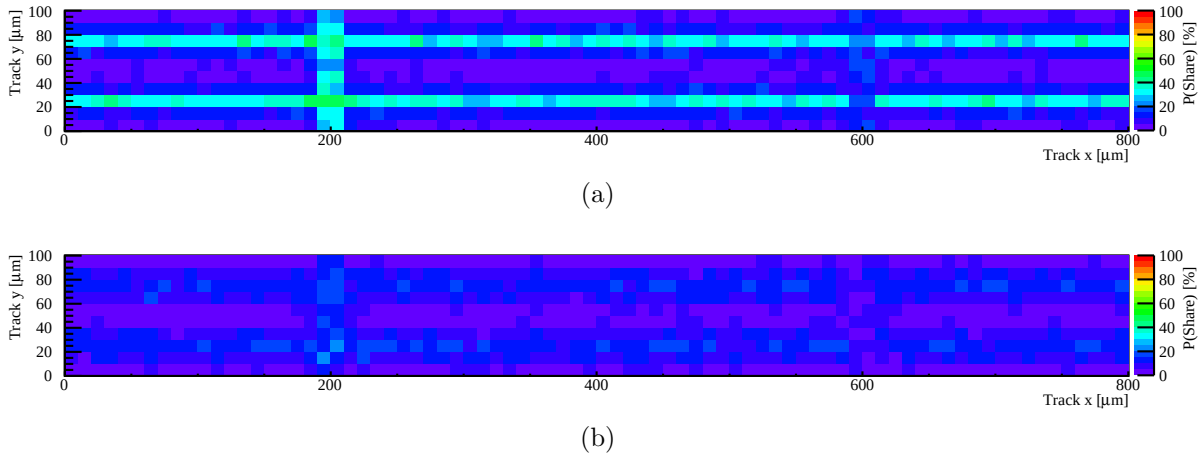

Figure 4.23: Charge sharing probability P(share) as a function of the impact point predicted by the beam telescope for two neutron irradiated assemblies. In (a) the fluence is $10^{15}\,\mathrm{n_{eq}/cm^2}$ and the applied bias voltage 700 V. In (b) the fluence is $5 \cdot 10^{15}\,\mathrm{n_{eq}/cm^2}$ and the bias voltage 900 V.

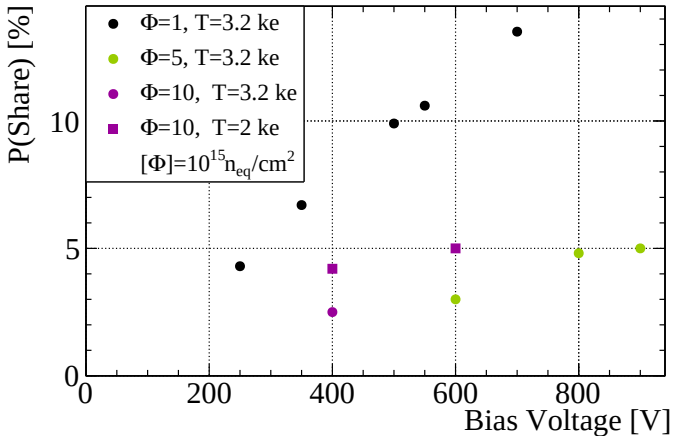

Figure 4.24: Dependence of the charge sharing probability P(Share) on the bias voltage and threshold (T) for the neutron irradiated assemblies with received fluences of $10^{15}\,\mathrm{n_{eq}/cm^2}$ and $5 \cdot 10^{15}\,\mathrm{n_{eq}/cm^2}$, as determined with beam test data. The uncertainties calculated according to [168] are smaller than the symbols.

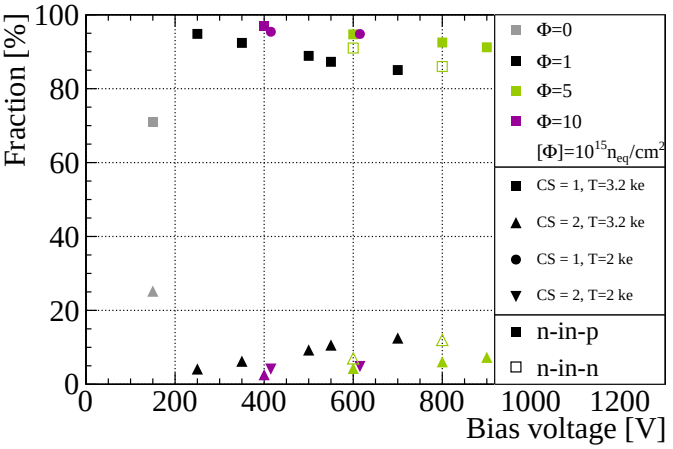

Figure 4.25: Relative cluster size (CS) fraction as a function of bias voltage for several neutron irradiated assemblies. As a reference the values for cluster size one and two of not irradiated assemblies at $V_{\mathrm{bias}} = 150\,\mathrm{V}$ are included (grey markers), and the values for an n-in-n assembly [144] irradiated to a fluence of $5 \cdot 10^{15}\,\mathrm{n_{eq}/cm^2}$ are shown as well. The fluence is given by the marker colour, the CS and the threshold (T) by the marker style, and n-in-p (n-in-n) assemblies are shown with closed (open) markers. The markers at $T = 2$ are drawn displaced for better visibility. The uncertainties calculated according to [168] are smaller than the symbols.

Figure 4.25. For reference the pre-irradiation values discussed in Section 4.2.4 are repeated in the figure (grey markers).

For all irradiated assemblies single-hit clusters by far dominate. The numbers of two-hit cluster rise with increasing bias voltage, since due to the higher charge collection efficiency it becomes more likely, that a neighbouring pixel is above threshold as well. Anyhow, it reaches at most half the pre-irradiation abundance.

For comparison the respective values of an n-in-n assembly irradiated to $5 \cdot 10^{15}\,\mathrm{n_{eq}/cm^2}$ are shown as well [144]. For this assembly higher multiplicity clusters are slightly more abundant than for the respective n-in-p assembly. Still, their contribution is low here as well.

Cluster Residuals

When compared to the pre-irradiation residuals, no significant change in the width of the residual distributions was found, taking the telescope precision into account—i. e. the space point resolution did not deteriorate for correctly reconstructed events. Exemplary the respective distributions for the assembly irradiated to $5 \cdot 10^{15}\,\mathrm{n_{eq}/cm^2}$ biased at 900 V are shown in Figure 4.26. In this example the single-hit residuals exhibit a standard deviation of $(115.1 \pm 2.7)\,\mu m$ in x and $(16.7 \pm 0.8)\,\mu m$ in y where the uncertainties are purely systematic. For the two-hit clusters the core Gaussian σ evaluates to $(12.0 \pm 0.1)\,\mu m$ in x and $(12.2 \pm 0.0)\,\mu m$ in y, where the fit uncertainty is less than $0.05\,\mu$m in the latter case.

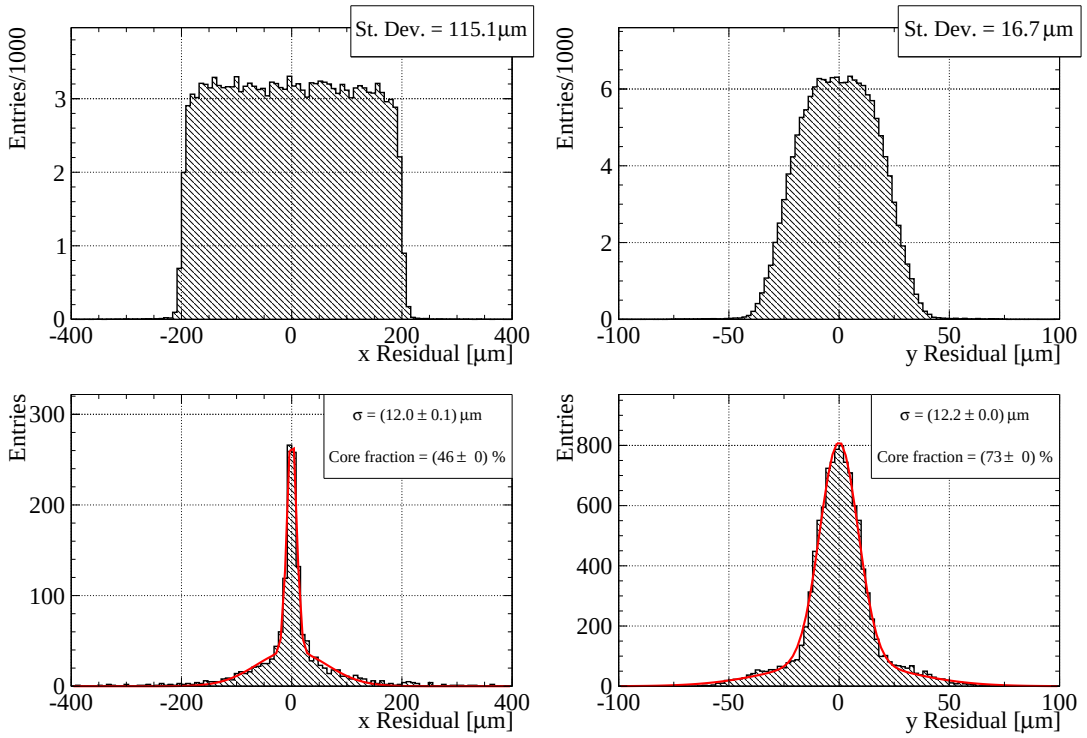

Figure 4.26: Residual distributions for the assembly irradiated to $5 \cdot 10^{15}\,\mathrm{n_{eq}/cm^2}$ biased at 900 V. Single- (top) and two-hit (bottom) clusters are shown for the long pixel coordinate x on the left and for the short pixel coordinate y on the right.

Another issue appreciable from the figure is that the number of events is larger, where the charge weighting algorithm used in ATLAS is not improving the resolution considerably any more. While in y this is the case for 27 % of the hits, in x a bit more than half of the events see no improvement. Similar numbers were found for an n-in-n assembly irradiated to the same fluence [144]. Anyhow, given the low percentage of two-hit clusters the impact of this effect is small.

4.3.6 Hit Efficiency

After several years of operation within a high energy physics experiment the tracking efficiency of the pixel detector is expected to be diminished mainly due to the lower charge collection efficiency causing a decrease of the hit efficiency of the pixel assemblies.

The hit efficiency was studied within the beam test. Unfortunately, due to a desynchronization of read-out system of the telescope and the assemblies, a determination for the assemblies irradiated to $10^{15}\,\mathrm{n_{eq}/cm^2}$ was not possible. Thus in the following the results for the assemblies irradiated to $5 \cdot 10^{15}\,\mathrm{n_{eq}/cm^2}$ and $10^{16}\,\mathrm{n_{eq}/cm^2}$ are presented. It is expected that these results can be considered as an lower bound for the $10^{15}\,\mathrm{n_{eq}/cm^2}$ assembly as well. At a received fluence of $5 \cdot 10^{15}\,\mathrm{n_{eq}/cm^2}$ the hit efficiency is still as high as (98.6 ± 0.3) %, when using a threshold of 3.2 ke and at a bias voltage of 600 V. Operated with the same bias voltage, but a lower threshold of 2 ke the hit efficiency for the assembly irradiated to $10^{16}\,\mathrm{n_{eq}/cm^2}$ was determined to be (97.2 ± 0.3) %. Figure 4.27 shows the mean hit efficiency, as a function of the impact point predicted by the beam telescope, within the pixel geometry for the assembly at the higher fluence. The losses clearly occur in the region of the punch-through biasing and in the corners of the pixel cell. As explained in Section 4.1.1 the first effect arises because of the not connected metal. The latter losses are due to hits shared between several pixel cells, being below threshold in all pixels. Anyhow, these losses can be assumed to be less pronounced for non perpendicular tracks as they are common in high energy physics experiments. This renders the given hit efficiencies lower bounds. When only considering the central region of the pixel cell, as defined by the black box in Figure 4.27, the efficiency is (99.8 ± 0.4) % for the assembly irradiated to $5 \cdot 10^{15}\,\mathrm{n_{eq}/cm^2}$ and (98.1 ± 0.3) % for the assembly irradiated to $10^{16}\,\mathrm{n_{eq}/cm^2}$.

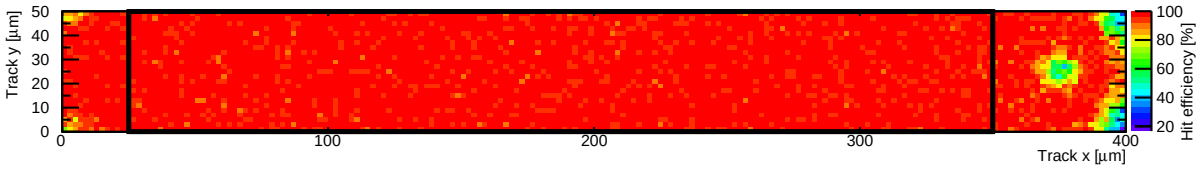

Figure 4.27: Mean hit efficiency for the assembly irradiated to $10^{16}\,\mathrm{n_{eq}/cm^2}$, operated at a bias voltage of 600 V as a function of the impact point predicted by the beam telescope. The black rectangular defines the central area referred to in the text.

For n-in-n assemblies irradiated to $5 \cdot 10^{15}\,\mathrm{n_{eq}/cm^2}$ and $10^{16}\,\mathrm{n_{eq}/cm^2}$ hit efficiencies of about 98.8 % and 95.4 % respectively are reported [169] when operated at 1 kV and a threshold of 3.2 ke. When lowering the bias voltage to 600 V for the $5 \cdot 10^{15}\,\mathrm{n_{eq}/cm^2}$ assembly the efficiency goes back to about 97 % [169]. Comparing these values to the ones found in this works, n-in-p pixel assemblies with the MPP/MPI-HLL design can be considered to be at least as radiation hard as n-in-n assemblies, or slightly better in this respect.

4.4 Conclusion

In this chapter, the properties of novel n-in-p planar pixel detectors were presented before and after irradiation, including a comparison to the respective quantities obtained with the presently used n-in-n assemblies whenever data are available.

An excellent signal over threshold above seven was determined before irradiation. No difference in the operational performance correlated to the different edge designs was observed.

For the irradiated assemblies a signal over threshold larger than two, together with low noise, has been obtained up to a fluence of $10^{16}\,\mathrm{n_{eq}/cm^2}$. At the maximum fluence, a charge of about $(6.6 \pm 0.4)\,\mathrm{ke}$ was collected, at a bias voltage of 950 V, with the discriminator threshold tuned to 3.2 ke. Further lowering the threshold as possible with the new and future read-out chip generations will enable a further enhancement of the charge to threshold ratio. Related measurements on FE-I4 assemblies are discussed in Chapter 5.

For the assembly irradiated to the maximum fluence of $10^{16}\,\mathrm{n_{eq}/cm^2}$, the hit efficiency is $(97.2 \pm 0.3)\,\%$, when setting a threshold of 2000 e, and biasing the assembly at 600 V.

Comparing the operational important quantities—i. e. charge collection, space point resolution, and hit efficiency—for novel n-in-p pixel sensors to the results obtained with presently used n-in-n sensors connected to the same read-out electronics, did not yield any significant difference before and after irradiation.

Thanks to the coating of the sensor surface with a BCB layer, the assemblies can be operated stably, i. e. over days of operating time, at these highest voltages. No destructive electric discharges between the read-out chips and the sensors were observed.

Given the lower production costs thanks to the single sided processing this renders n-in-p pixel sensors a good candidate for the upgrade of the tracking detector at HL-LHC experiments.

5 Thin Sensors

Thin sensors are good candidates for the inner layers of pixel detectors used at the future HL-LHC as discussed in Section 1.4.2. Their properties and operational variables are the focus of the following chapter. The presented results were obtained with strip sensors, Section 5.2, as well as with pixel assemblies, Section 5.3, exhibiting active thicknesses between 75 μm and 150 μm. Predicted benefits of thin sensors, e. g. higher CCE after irradiation and lower occupancies are covered. Additionally, some of the investigated pixel assemblies are designed with extremely small edge distances. Here, especially the performance of the edge region will be discussed. Additionally, for the strip sensors the collection profile within the sensor volume is discussed. The measurements are preceded by an introduction of the production processes used for thin sensors alongside with the discussion of the two thin sensor productions used in this thesis, Section 5.2.

Parts of the results presented in this chapter, were already published in [155, 171, 172].

5.1 Thin Sensor Productions

To investigate the properties of thin sensors and to explore their potential for high energy physics applications, two dedicated sensor productions were conducted at the MPI-HLL facility. They are introduced after a concise description of the MPI-HLL and Valtion Teknillisestä Tutkimuslaitoksesta (VTT) process technologies used to produce thin sensors. The second process was used for the additional thin sensor production incorporating extremely small edge distances and active edges. It will be described in Section 5.1.4

5.1.1 Processing of Thin Sensors

Processing of thin sensors poses a challenging task since the brittleness demands for even more careful handling and is restricting the use of some standard equipment. This scaling with the diameter and inversely with the thickness of the wafer is especially challenging for next generation HL-LHC sensors, which demand reasonable sized wafers for cost-reduction and thin sensors, because of the advantages discussed above.

At the moment there are several process technologies available for thin sensor production, each with its individual advantages as well as disadvantages. As the thin sensors used in this thesis were produced using the MPI-HLL and VTT processes, these will be outlined in the following.

MPI-HLL Thinning Process

In the MPI-HLL thinning process [83] sensors with an active thickness d_{active} down to 50 μm are produced in five steps as shown in Figure 5.1. In the first step a high resistivity oxidised wafer of standard thickness is processed on the back-side with an implantation, that can be either homogeneous or patterned. Subsequently the sensor wafer is oxide-bonded [173] to a handle

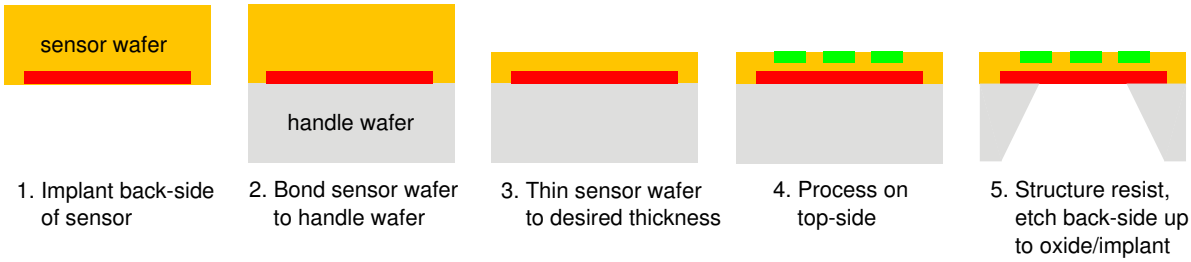

Figure 5.1: Schematics of the MPI-HLL thinning process. Drawing adopted from [83].

wafer (step 2) and thinned from the front-side to the desired thickness. The thinning (step 3) is achieved using Chemical Mechanical Polishing (CMP) [174]. Stabilised by the handle wafer the front-side of the sensor wafer is processed like a wafer of standard thickness (step 4), with the additional advantage that the back-side implantations are protected by the handle-wafer. At this point the sensors which do not need back-side contacting—as n-in-p sensors—are fully operable, since the handle-wafer is electrically isolated by the oxide bonding layer. All results discussed in this thesis were obtained with sensors at this stage. For p-in-n and n-in-n sensors, which need a back-side contact, or in an experiment where a low material budget is desirable, the handle wafer is removed with a patterned geometry. This is achieved by deep anisotropic wet etching using TetraMethyl Ammonium Hydroxide (TMAH), which because of the very different etch rates [175] in the $\langle 100 \rangle$ and the $\langle 111 \rangle$ crystal directions, allows for only etching of the central part of a structure, while leaving a well defined rim which ensures the mechanical stability of the thin active part in the centre. The etch process stops as soon as the etchant reaches the oxide layer connecting the two wafers. To enable the contacting of n-in-n structures the oxide has to be opened and metal pads need to be structured. Although the topology of the back-side is uneven, this does not pose severe constraints since the requirements on these contacting pads are rather relaxed.

VTT Process

The process used at VTT [176] is equivalent to the MPI-HLL thinning process up to the fourth step. After finishing the implantations of the front-side, trenches are etched using Deep Reactive Ion Etching (DRIE) [177] at the structure borders. The DRIE process is an iterative anisotropic etching process illustrated in Figure 5.2. In a first step photo resist is applied to the whole wafer surface, but for the region in which the trench should be etched. Then alternatively the silicon is etched with SF_6 and the created hole is passivated with C_4F_8. This allows to achieve straight side-walls, and high aspect ratios. The such revealed sides of the structures are then implanted with the same dopant as the back-side—e. g. in the n-in-p case boron. After finishing these steps the sensors are annealed and the aluminium layer for contacting is applied. Eventually the handle wafer is removed.

5.1.2 SOI1 Production

In the SOI1 production eight p-bulk FZ 6-inch-wafers were processed using the MPI-HLL thinning process to a final active thickness d_{active} of 75 μm and 150 μm. The specific resistivity of these wafers is $\rho \geq 2\,\text{k}\Omega\text{cm}$. The layout of the wafer, shown in Figure 5.3, incorporates ten FE-I2/3 compatible structures (orange) as well as 34 strip sensors, of which half have a

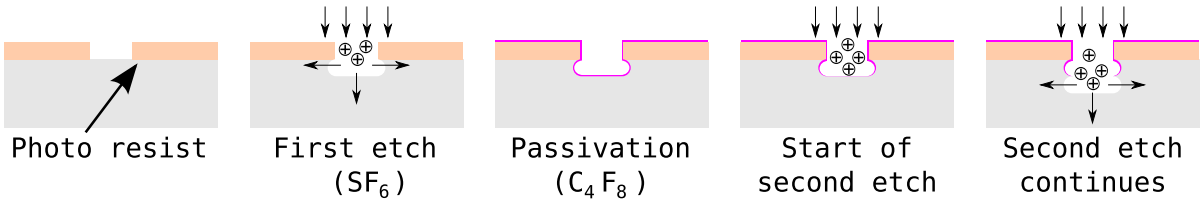

Figure 5.2: Schematics of the DRIE process [84].

pitch of 80 μm (blue) and half a pitch of 50 μm (green). The other structures, i. e. an ATLAS multi-chip module compatible structure as well as the diodes are not used in this thesis and thus not described in the following. A discussion of the electrical characteristics of all structures within the SOI1 production can be found in [84]. The full depletion voltages V_{fd} were found there to be (30 ± 5) V for the sensors with $d_{\text{active}} = 75\,\mu$m and (105 ± 5) V for sensors with $d_{\text{active}} = 150\,\mu$m. This allows for an overdepletion $V_{\text{bd}}/V_{\text{fd}}$ of 3.7 ± 1.0 up to 15 ± 2 for the pixel devices, corresponding to a yield of $79/80 \approx 98.8\,\%$. The leakage currents were determined to be below 10 nA/cm^2.

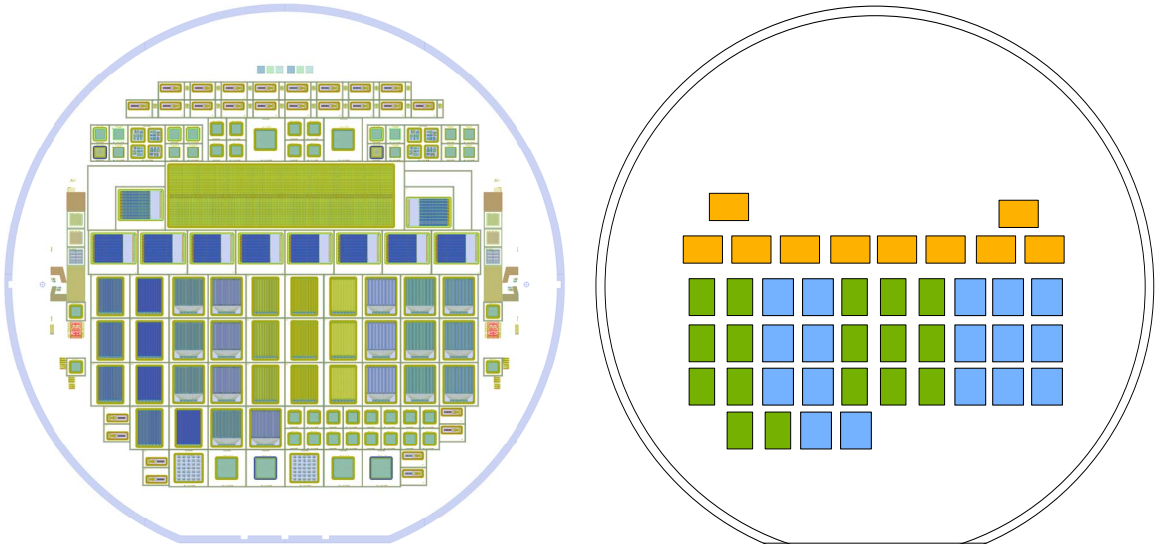

(a) (b)

Figure 5.3: (a) Wafer layout of the SOI1 production. In (b) the used structures are highlighted. FE-I2/3 compatible pixel structures are indicated in orange. Strip structures with 50 μm (80 μm) pitch are indicated in green (blue).

5.1.3 SOI2 Production

The focus of the SOI2 production was to supply FE-I4 compatible sensors with $d_{\text{active}} = 150\,\mu$m. Thus, five remaining, unprocessed wafers of the SOI1 production were processed employing the MPI-HLL thinning process. The wafer layout is shown in Figure 5.4 and contains eight sensors which are designed to be interconnected to a single FE-I4 read-out chip, called Single Chip Sensor (SCS), and seven sensors designed to be interconnected to two FE-I4 read-out chips,

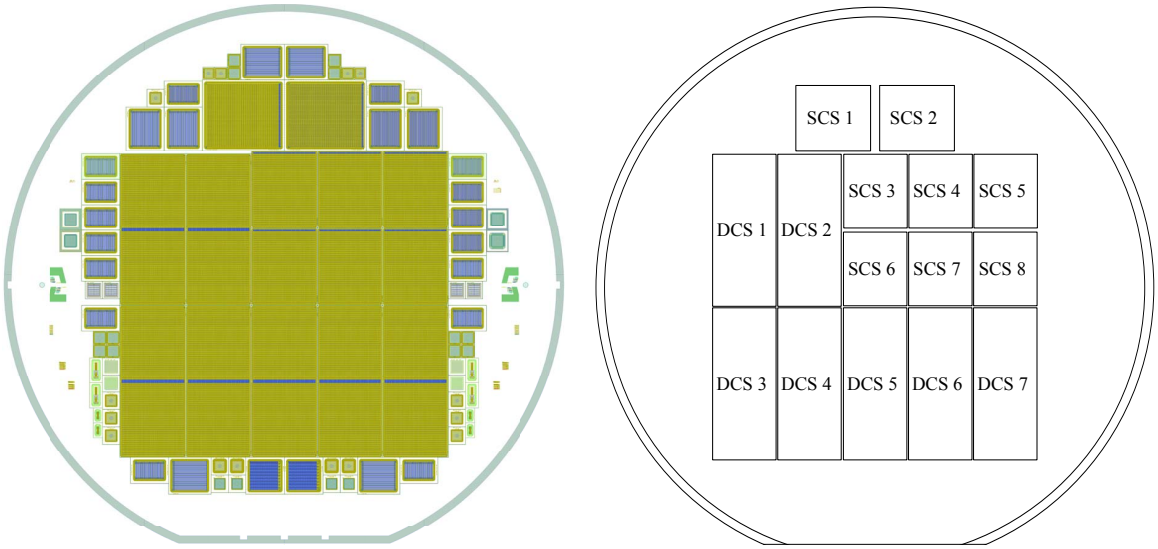

(a) (b)

Figure 5.4: (a) Wafer layout of the SOI2 production. In (b) the FE-I4 compatible structures are indicated.

called Double Chip Sensor (DCS). Since the reduced guard ring scheme performed well in the CiS (see Section 4) as well as in the SOI1 production (see below), the majority of the structures were designed with a reduced guard ring scheme containing twelve guard rings resulting in a distance between the last pixel implantation and the sensor edge of $d_{\text{edge}} = 465\,\mu\text{m}$. Only SCS1 and SCS2 were designed with the full, 19 guard ring scheme, resulting in an inactive edge of $d_{\text{edge}} = 1055\,\mu\text{m}$. For the SCSs, the design of the active area matches the design of the FE-I4 compatible sensors in the CiS production as described in Section 4.1—namely 26880 pixel cells are arranged in 80 columns and 336 rows. The central 78 columns are equipped with $250\,\mu\text{m} \times 50\,\mu\text{m}$ wide normal pixels. The last and the first column house the long pixels measuring $450\,\mu\text{m} \times 50\,\mu\text{m}$. Since for the SOI1 as well as for the CiS production better performance before irradiation was observed for homogeneous p-spray (see [84] and Section 4.2.1) the whole production was carried out using homogeneous p-spray for the inter pixel isolation.

This production was affected by a phosphorus contamination in the oxidation step during the processing, which caused the failure, i. e. a breakdown voltage $\leq 5\,\text{V}$, of all structures included in the production. In a subsequent repair by additional implantations, on three wafers eleven out of 30 reduced guard ring SCSs were cured, i. e. $V_{\text{bd}} > V_{\text{fd}}$. For these cured wafers a $3\,\mu\text{m}$ thick BCB layer and the UBM were applied at IZM. The IV characteristics of all SCSs after this post-processing are summarised in Figure 5.5. The leakage currents of the cured SCSs are with one exception below 50 nA, i. e. below about $13\,\text{nA/cm}^2$ before their breakdown and thus comparable to the ones of the SOI1 production. The breakdown voltages exceed the full depletion voltage of $V_{\text{fd}} = (105 \pm 5)\,\text{V}$ for seven of the structures by a factor of 2.5–4. For the other four devices the breakdown occurs close above V_{fd}, which complicates investigations before irradiation. Due to the shift of the breakdown towards higher voltages after irradiation, the issue is confined to the pre-irradiation characterization.

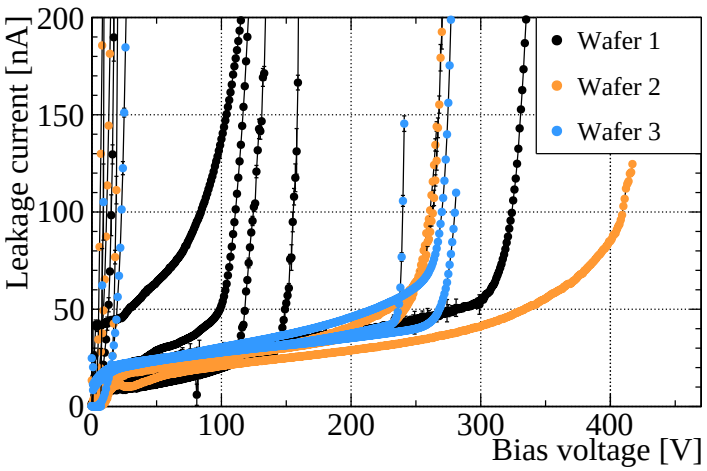

Figure 5.5: IV characteristics of all SCSs included in the SOI2 production after BCB and UBM deposition.

5.1.4 VTT Production

Within a multi project wafer production at VTT p-bulk FZ 6-inch wafers with a thickness d of 100 μm and 200 μm and a resistivity of 10 kΩcm were produced. For this production, the p-spray process used at MPI-HLL was transferred to VTT and applied to the MPP structures. Four different edge designs were included in the production. In the first design, see Figure 5.6(a), an optimised guard ring scheme and safety margin is implemented, which was based on the experience with the CiS (cf. Section 4.1) and SOI productions (see below). It incorporates eleven guard rings as well as a bias ring and $d_{\text{edge}} = 460\,\mu m$. For the second design, see Figure 5.6(b), the number of guard rings is reduced to one and a dedicated bias ring in conjunction with the punch-through structures, ensures the testability of the sensors before interconnection and grounding after interconnection. In this design $d_{\text{edge}} = 125\,\mu m$. In the third design, see Figure 5.6(c), only the bias ring is included in the design, but no dedicated guard ring. As in the second design $d_{\text{edge}} = 125\,\mu m$. The most aggressive design, see Figure 5.6(d), is the fourth design, which only exhibits one floating guard ring, but no bias ring and a d_{edge} of only 50 μm. Here, no testing before interconnection is feasible. Consequently, also the punch through biasing structures on the per pixel level are omitted and hence the lower hit efficiency after high irradiation levels in this region, as e. g. observed in the CiS production, is not expected for these structures. But, if due to a connection failure, one pixel cell remains unconnected, it is not automatically grounded via the biasing grid, but only through the neighbouring pixel cell implantations via the punch-through mechanism despite the non-existence of specialised punch-through structures. This might lead to unwanted field configurations and should be studied in the future. While the first two designs were implemented for FE-I3 and FE-I4 read-out chip compatible structures, the last design, was only implemented for FE-I3 read-out chip compatible structures.

The active area of the sensors resembles the layout in the CiS and SOI productions in terms of pixel types and dimensions, but for the long pixels omitted in the design with eleven guard rings.

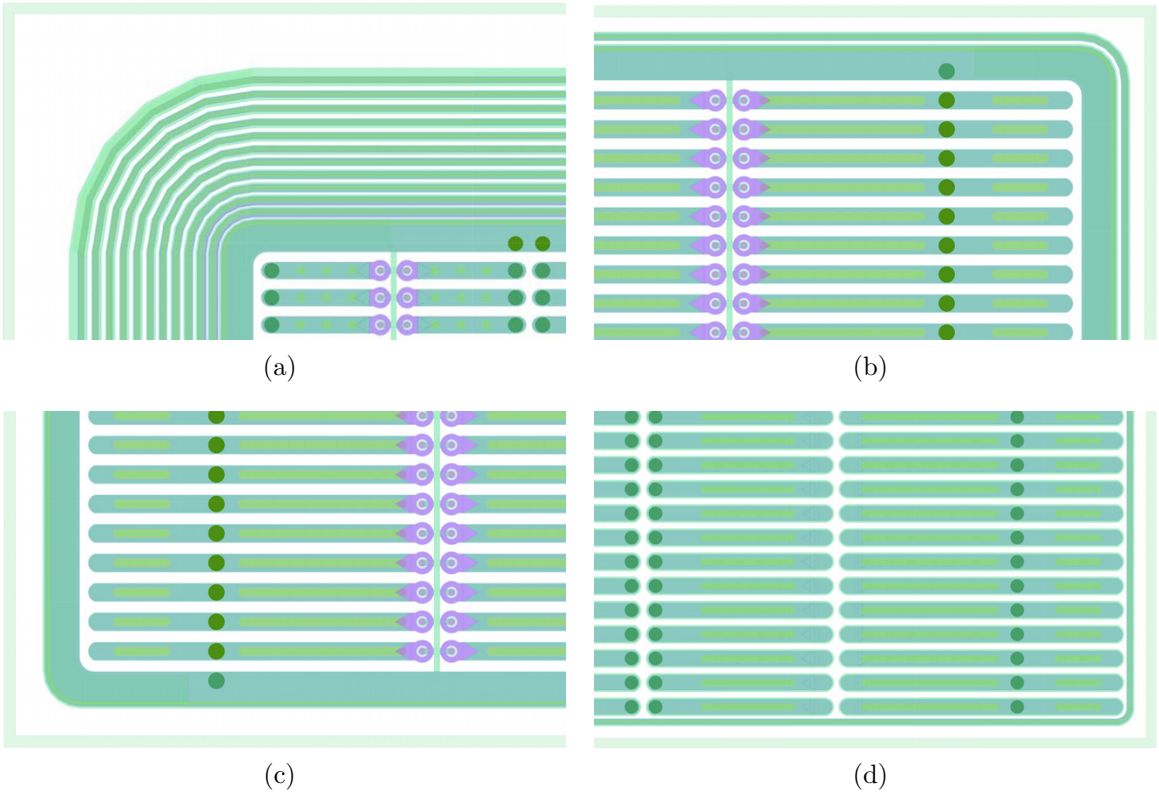

Figure 5.6: Design of edge regions in the VTT production shown to scale. In (a) the version with eleven guard rings and one bias ring is shown, in (b) the one with only one bias and one guard ring, in (c) the one with only one bias ring, and in (d) the one with only one guard ring. Implants and metallization are drawn in green and turquoise. Punch through structures are depicted in violet. The dark green points indicate the future position of the UBM pads for read-out chip interconnection.

At the moment only structures of the $d = 100\,\mu$m production are available. Because of the production on a Multi Project Wafer (MPW), the structures were only delivered after interconnection and thus could not be tested before interconnection. VTT reported leakage currents below 100 nA for all FE-I4 and FE-I3 compatible sensors. The breakdown voltages exceed 80 V for all structures, while V_{fd} is quoted with 9 V.

5.2 Charge Collection of Strip Sensors

In contrast to pixel sensors, strip sensors can be read out using wire bonds, which allows a cost effective and fast possibility to investigate their performance. In this section the charge collection of thin strip sensors will be discussed for neutron irradiated sensors as a function of depth using the edge-TCT set-up (see Section 3.5) and for proton irradiated sensors in absolute terms employing results obtained with the ALiBaVa set-up (see Section 3.4).

5.2.1 Investigated Structures

Different strip sensors of the SOI1 production were used and are summarised in Table 5.1. For the edge-TCT measurements strip sensors with a pitch of 50 μm were employed as this corresponds to the smaller pitch of the ATLAS pixel structures. Since the beetle chip [124] used in the ALiBaVa set-up is accessed via a pitch adapter of 80 μm pitch, strip sensors with 80 μm pitch were employed here. Also given are the received fluence and the measurement temperature. For the ALiBaVa set-up, the lowest achievable environmental temperature of the used climate chamber was $-46\,^{\circ}$C.

For each thickness the charge collection as a function of the voltage was determined before and after different irradiation steps. The fluences used are summarised in Table 5.1 together with the measurement temperature and the geometric dimensions.

Table 5.1: Overview of the strip structures used for the charge collection measurements with the edge-TCT and the ALiBaVa set-up. Also given are the received fluence and the measurement temperature.

Setup	Thickness [μm]	Pitch [μm]	Irradiation sites	Fluence [$10^{15}\,\mathrm{n_{eq}/cm^2}$]	Measurement temperature [°C]
edge-TCT	75	50	JSI	0	−20
				5	−20
				10	−20
	150			0	−20
				5	−20
				10	−20
ALiBaVa	75	80	KIT	0	−30
				1	−30
				3	−40
				10	−46
	150			0	−30
				1	−30
				3	−44
				5	−46

For reference the IV characteristics of the irradiated sensors are given in Figure 5.7. As expected the sensors with $d_{\mathrm{active}} = 75\,\mu$m exhibit lower leakage currents than the sensors with $d_{\mathrm{active}} = 150\,\mu$m and the leakage current increases with the received fluence. No breakdown was observed in the explored bias voltage range, but for the sensors with $d_{\mathrm{active}} = 75\,\mu$m measured within the edge-TCT set-up. These exhibit a breakdown at 800 V for a fluence of $5 \cdot 10^{15}\,\mathrm{n_{eq}/cm^2}$ and at 825 V for a fluence of $10^{16}\,\mathrm{n_{eq}/cm^2}$.

5.2.2 Induced Current Pulse Shapes

In Figure 5.8 the measured current pulses induced by the infra-red laser ($\lambda = 1064\,$nm) as a function of time are shown for different injection depths y, thicknesses and fluences. Sensors with $d_{\mathrm{active}} = 75\,\mu$m ($d_{\mathrm{active}} = 150\,\mu$m) are shown on the left (right). The received fluence increases from the top to the bottom row, from not irradiated to $10^{16}\,\mathrm{n_{eq}/cm^2}$.

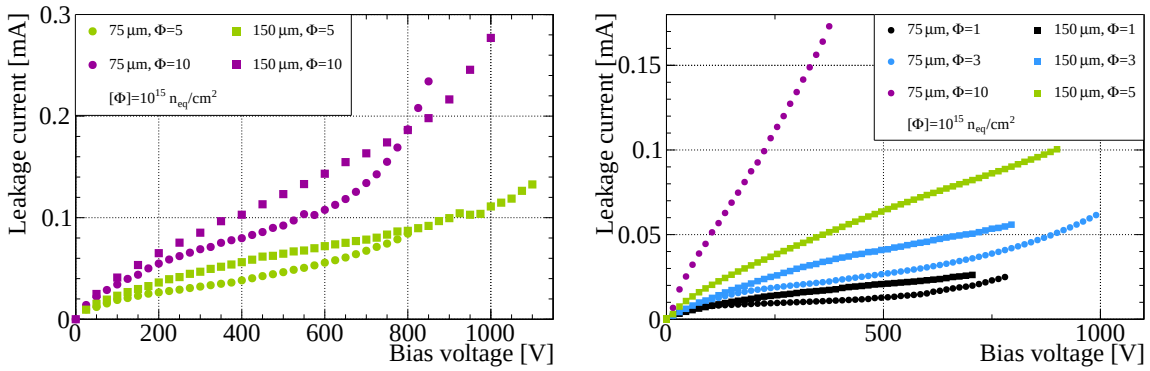

Figure 5.7: IV characteristics of the irradiated strip detectors used within (a) the edge-TCT and (b) the ALiBaVa set-up. All measurements were taken at or scaled to $-20\,^{\circ}\mathrm{C}$, using the prescription given in [105]. The uncertainties are smaller than the symbols.

For the not irradiated sensors bias voltages up to 150 V are investigated. Exemplary shown are the measurements at 10 V, i. e. well below full depletion. The signal is composed of two components. The signal induced by the faster electrons, see Equation 2.8, is maximal after approximately 1 ns, while the signal induced by the slower holes, see Equation 2.9, starts to dominate for times larger than 3 ns, i. e. after the electron signal almost vanished. With increasing injection depth y the signal contribution from electrons becomes longer, while the contribution by holes becomes shorter in time. This reflects dispersion while drifting to the collection electrodes, i. e. for the electrons the n-implants at $y = 0\,\mu$m and for holes the back-side implantation corresponding to $y = 75\,\mu$m or $y = 150\,\mu$m. Comparing the relative signal sizes for different depths between the two different thicknesses it is apparent that for the sensor with $d_{\mathrm{active}} = 75\,\mu$m the signal is non vanishing for all depths, while for the sensor with $d_{\mathrm{active}} = 150\,\mu$m no signals at high injection depths are seen, see Figures 5.8(a) and (b). This reflects the different full depletion voltages of the different sensors. Comparing the absolute signal size for different injection depths within the same sensor, a different behaviour is found for the two thicknesses. While for the 150 μm thick sensor the size of the signal rises towards a depth around 30 μm and subsequently declines again, it is of comparable strength for all depths in the 75 μm case, with the exception of the injection at 5 μm, i. e. very close to the implant. The oscillations overlaying the current pulses stem from impedance mismatching within the measurement instrumentation, whose contribution vanishes after integration in time over the pulse [108].

For the irradiated sensors, exemplary measurements are depicted for the same injection depths but for a bias voltage of 100 V. Two effects emerge after irradiation. First, the contribution of the holes diminishes, i. e. the relative signal heights for $t > 5$ ns with respect to the height at about 1 ns is much smaller than in Figures 5.8(a) and (b). This is seen more clearly in Figure 5.8(c) and Figure 5.8(f), where the impedance mismatch is less pronounced. This shows that indeed holes are more likely trapped. Second, the total time needed until the signal vanishes is expected to shorten. On the one hand this reflects the trapping of the holes but also electrons. On the other hand it indicates that the mean free path of the charge carriers is reduced as predicted [104]. Due to the influence of the impedance mismatch this point cannot

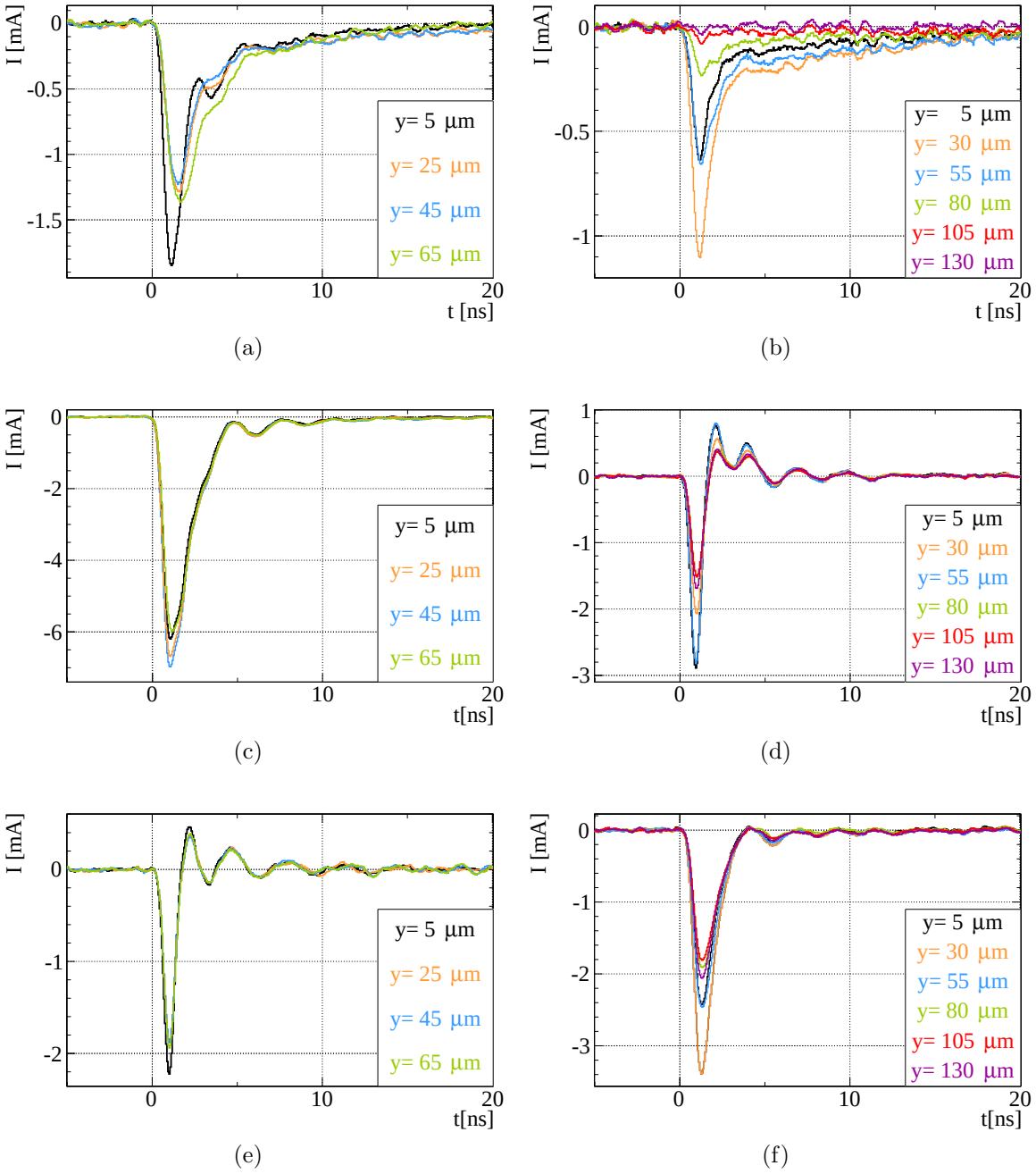

Figure 5.8: Current pulse induced by the infra-red laser ($\lambda = 1064\,\text{nm}$) for different depths in the sensor. Shown on the left (right) are the sensors with $d_{\text{active}} = 75\,\mu\text{m}$ ($d_{\text{active}} = 150\,\mu\text{m}$). The first row is for the not irradiated structures, in the second (third) row the structures irradiated to a fluence of $5 \cdot 10^{15}\,\text{n}_{\text{eq}}/\text{cm}^2$ ($10^{16}\,\text{n}_{\text{eq}}/\text{cm}^2$) are shown. The given y positions have a fully correlated uncertainty of about $1\,\mu\text{m}$. The absolute scale of the signal, is not comparable among different structures, cf. Section 3.5.3.

be proven, but when comparing the endpoint of the current pulses in Figures 5.8(c) and (f), shorter times are found for the thicker sensor, irradiated to $10^{16}\,\mathrm{n_{eq}/cm^2}$, than for the thinner sensor, irradiated to $5 \cdot 10^{15}\,\mathrm{n_{eq}/cm^2}$, in agreement with expectations.

5.2.3 Charge Collection Profile

The normalised charge as a function of the injection depth y for various voltages obtained from integration over all pulses at all depths and at the respective voltage is depicted in Figure 5.9. All measurements are normalised to the mean value of the active part at 150 V before, and at 800 V after irradiation. The ordering for thickness and fluence is the same as for the current pulses depicted in Figure 5.8. The red dotted lines indicate the active volume of the sensors determined from the onset of the signal. An excellent agreement is found with the active thickness of the sensors expected from the production.

Before irradiation, the depletion of the sensor starting from the front-side manifests in the higher charge collection in the region directly under the electrodes compared to the lower charge collection at the back-side. For the sensors with $d_{\mathrm{active}} = 150\,\mu\mathrm{m}$, Figure 5.9(b), at a bias voltage of 5 V (first red line) the charge is collected up to a depth of approximately $y = 80\,\mu\mathrm{m}$, with a higher efficiency in the first $40\,\mu\mathrm{m}$ below the electrodes formed by the n-implants. The full volume starts to contribute at a bias voltage of about 35 V and becomes fully efficient at around 75 V. Afterwards only little CCE is gained up to V_{fd} of approximately $\approx 80\,\mathrm{V}$. The spike at the back-side, which is also present for the sensor with $d_{\mathrm{active}} = 75\,\mu\mathrm{m}$, originates from optical reflections of the laser on the transition from the active wafer to the handle wafer. The handle wafer does not contribute any signal as it is expected due to its electrical isolation.

For the sensors with $d_{\mathrm{active}} = 75\,\mu\mathrm{m}$ already at 5 V the full volume of the detector contributes as discussed in the preceding section, which indicates that the electric field is altered by the small electrode distance. Deviations for electric fields for thin sensors are as well observed in simulations by other RD50 groups [178]. The sensor becomes fully efficient between 15 V and 20 V i. e. roughly at one fourth of the voltage than the sensors with $d_{\mathrm{active}} = 150\,\mu\mathrm{m}$ and thus its behaviour agrees well with what would be expected from the quadratic dependence of V_{fd} on the thickness, cf. Equation 2.4.

The flatness of the charge collection profile as a function of the injection depth y is also found after irradiation (see 2nd and 3rd row) for the sensor with $d_{\mathrm{active}} = 75\,\mu\mathrm{m}$. For the thicker sensor the depletion from the front-side is again visible. While for the fluence of $5 \cdot 10^{15}\,\mathrm{n_{eq}/cm^2}$ the sensors at both thicknesses exhibit an instability for bias voltages between 350 V and 700 V this is not the case at the highest probed fluence.

5.2.4 Charge Collection Efficiency

As a figure of merit and to allow for later comparisons to the pixel assemblies the relative collected charge is given in the following for strip sensors; first, for edge-TCT and then for ALiBaVa measurements.

Edge-TCT Results

The CCE before and the relative collected charge after irradiation derived from the edge-TCT measurement is summarised in Figure 5.10. In Figure 5.10(a) the CCE for the not irradiated sensors is calculated using the mean collected charge $\langle Q \rangle$ at a bias voltage of 150 V, i. e. the operation point of the ATLAS pixel assemblies, as reference. The given uncertainties correspond

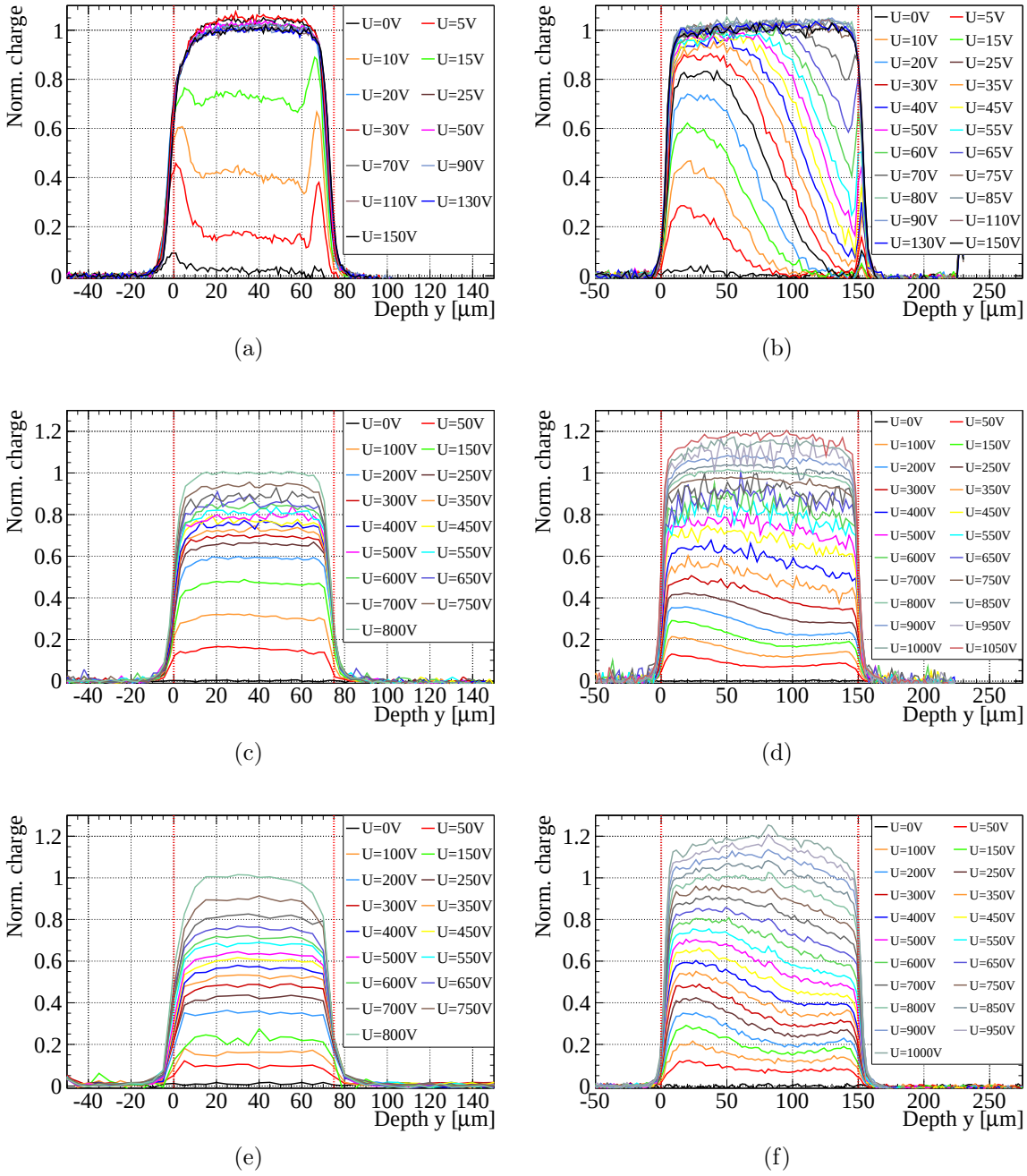

Figure 5.9: Dependence of the collected charge on the depth within the sensor for different bias voltages. Sensors with $d_{\text{active}} = 75\,\mu\text{m}$ ($d_{\text{active}} = 150\,\mu\text{m}$) are shown on the left (right) side. The first row is for not irradiated structures, in the second (third) row the structures irradiated to a fluence of $5 \cdot 10^{15}\,\text{n}_{\text{eq}}/\text{cm}^2$ ($10^{16}\,\text{n}_{\text{eq}}/\text{cm}^2$) are shown. For better visibility no uncertainties are shown. For a discussion of those please refer to Section 3.5. The red dotted lines indicate the boundaries of the active volume of the sensors.

to the 5 % systematic uncertainty introduced in Section 3.5.3. For the voltages, where an instability was observed in the charge collection profiles the uncertainty was increased to 10 %. Both sensors exhibit a rising CCE while depleting. The full CCE is achieved for the sensor with $d_{\text{active}} = 75\,\mu\text{m}$ at $(21.0 \pm 0.5)\,\text{V}$ and for the sensor with $d_{\text{active}} = 150\,\mu\text{m}$ at $(82 \pm 0.8)\,\text{V}$. These values and their uncertainties are determined by intersecting two linear functions, describing the rising and constant part of the CCE. The factor of roughly four between the two voltages agrees well with the expectation from the relation of the thickness of the sensors, cf. Equation 2.4.

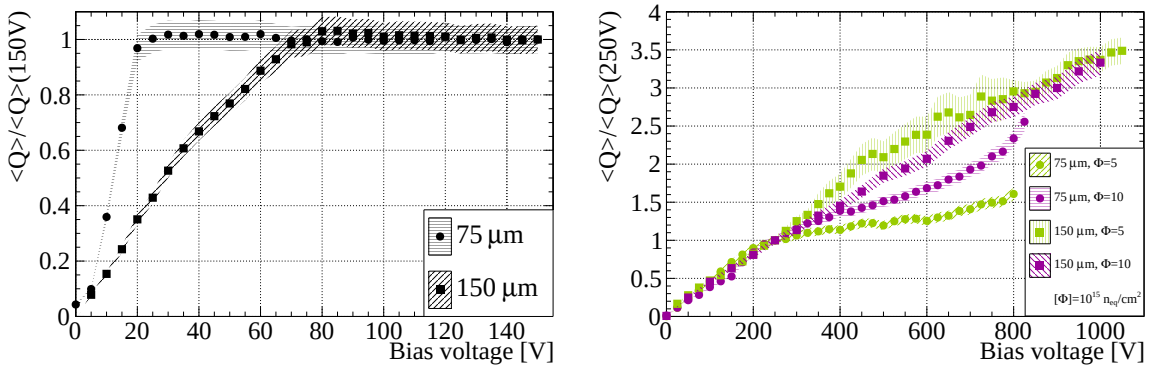

(a) (b)

Figure 5.10: CCE and relative collected charge as a function of the applied bias voltage as determined with the edge-TCT set-up (a) before and (b) after irradiation to a fluence of $5 \cdot 10^{15}\,\text{n}_{\text{eq}}/\text{cm}^2$ and $10^{16}\,\text{n}_{\text{eq}}/\text{cm}^2$. As reference for the not irradiated measurements, the mean charge $\langle Q \rangle$ at 150 V is used; for the irradiated ones the one at 250 V. The uncertainties are systematic and are discussed in Section 3.5.

After irradiation the mean collected charge $\langle Q \rangle$ at a bias voltage of 250 V is used as reference for the relative collected charge calculation. Up to this voltage the evolution of the relative collected charges is nearly linear and independent of the active thickness as well as of the received fluence. While for the sensors with $d_{\text{active}} = 150\,\mu\text{m}$ the linear behaviour continues up to the highest applied voltages of 1000 V or 1100 V respectively, the sensors with $d_{\text{active}} = 75\,\mu\text{m}$ change slope around 400 V. For both sensors with $d_{\text{active}} = 75\,\mu\text{m}$, the measurement had to be stopped at 800 V or 825 V due to a breakdown. Up to this voltage no pronounced rise of the CCE was found for the sensor irradiated to a fluence of $5 \cdot 10^{15}\,\text{n}_{\text{eq}}/\text{cm}^2$. For the sensor irradiated to a fluence of $10^{16}\,\text{n}_{\text{eq}}/\text{cm}^2$ the slope of the CCE increases at around 700 V, which is also reflected in the corresponding IV characteristics, see Figure 5.7(a). This correspondence indicates that the sensor might be operated in a charge multiplication regime. Measurements of these sensors after several annealing steps [179] up to 40960 min at 60 °C indicate that the multiplication regime becomes more pronounced, while the overall stability, i. e. the absence of larger fluctuations as seen for example in Figures 5.9(c) and (d), of the sensor improves.

ALiBaVa Results

Strip detectors from the SOI1 production were also measured with the ALiBaVa set-up. The CCE is calculated normalizing the MPV of the collected charge after irradiation to the corresponding MPV above full depletion before irradiation measured at the same temperature. The resulting

CCEs as a function of the applied bias voltage are summarised in Figure 5.11. The measurements for three different fluences are shown separately for the sensors with $d_{\text{active}} = 75\,\mu\text{m}$ and $d_{\text{active}} = 150\,\mu\text{m}$. The fluences $10^{15}\,\text{n}_{\text{eq}}/\text{cm}^2$ and $3 \cdot 10^{15}\,\text{n}_{\text{eq}}/\text{cm}^2$ were explored for both active thicknesses. Additionally, for $d_{\text{active}} = 75\,\mu\text{m}$ a sensor irradiated to a fluence of $10^{16}\,\text{n}_{\text{eq}}/\text{cm}^2$ was investigated, whereas for the sensors with $d_{\text{active}} = 150\,\mu\text{m}$ the highest fluence investigated is $5 \cdot 10^{15}\,\text{n}_{\text{eq}}/\text{cm}^2$.

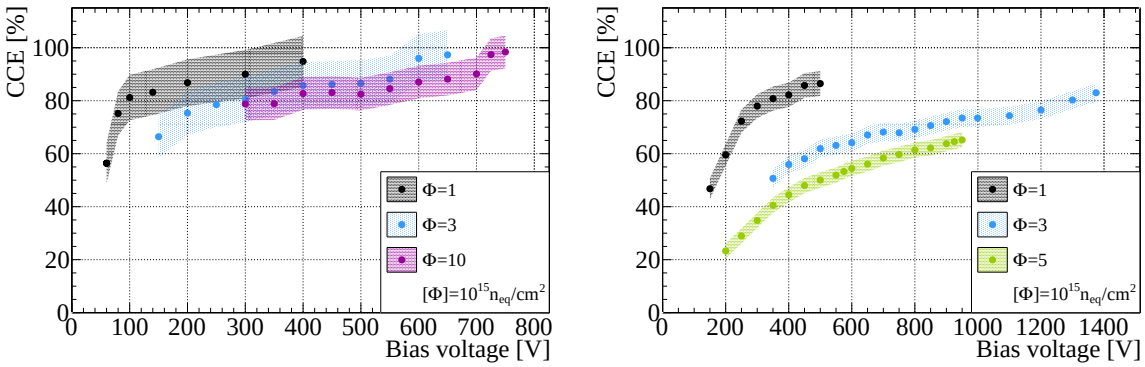

(a) (b)

Figure 5.11: CCE after irradiation determined with the ALiBaVa set-up for the sensors with (a) $d_{\text{active}} = 75\,\mu\text{m}$ and with (b) $d_{\text{active}} = 150\,\mu\text{m}$. The collected charge before irradiation was used as reference. The measurements at a fluence of $10^{15}\,\text{n}_{\text{eq}}/\text{cm}^2$ for both thickness as well as the measurement at a fluence of $3 \cdot 10^{15}\,\text{n}_{\text{eq}}/\text{cm}^2$ for the sensors with $d_{\text{active}} = 75\,\mu\text{m}$ are taken from [84]. The uncertainties are systematic and are discussed in Section 3.4.

Above a certain voltage all sensors exhibit a plateau, i. e. a bias voltage range for which the CCE does not or only slowly increases. This corresponds to a full or almost full depletion of the sensors. While, in the case of the sensors with $d_{\text{active}} = 75\,\mu\text{m}$ these plateaus correspond to CCE values above 80 % and little dependence on the fluence is visible, for the sensors with $d_{\text{active}} = 150\,\mu\text{m}$ the CCE saturation value clearly scales with fluence. When comparing the CCE between the two thicknesses at the same bias voltage and received fluence, the values are always higher for the thinner sensors. This trend is also seen when comparing to the results found for the pixel sensors with $d = 285\,\mu\text{m}$, discussed in Chapter 4. For example the CCE at 500 V and a received fluence of $3 \cdot 10^{15}\,\text{n}_{\text{eq}}/\text{cm}^2$ is around 85 % for the sensors with $d_{\text{active}} = 75\,\mu\text{m}$, around 64 % for the sensors with $d_{\text{active}} = 150\,\mu\text{m}$, and only around 30 % for the sensors with $d = 285\,\mu\text{m}$. These results indicate clearly that employment of thinner sensors is beneficial after high irradiation levels, given their reduced contribution to the material budget and the resulting decrease in occupancy, if it is possible to employ a read-out electronic able to cope with signals around (4–6) ke. The FE-I4 read-out chip for example already fulfils this requirement.

5.3 Properties of Thin Pixel Sensors

The properties of thin pixel sensors were investigated in the laboratory as well as in beam tests for assemblies employing sensors with $d_{\text{active}} = 75\,\mu\text{m}$ from the SOI1 production and for sensors

with $d_{\text{active}} = 150\,\mu\text{m}$ from the SOI2 production. For the assemblies using sensors with active edges and $d = 100\,\mu\text{m}$ from the VTT production, a basic characterization before irradiation was conducted in the laboratory. The thinnest sensors were interconnected to FE-I2 read-out chips using the SLID interconnection by EMFT. The SLID interconnection will be discussed in detail in Chapter 6. The thickest detectors were interconnected to FE-I4 read-out chips using the SnAg solder bump-bonding technique by IZM. The assemblies with active edges were interconnected to FE-I3 and FE-I4 read-out chips by VTT using the SnPb solder bump-bonding technique by VTT. Here, the UBM was applied by IZM for the FE-I3 read-out chips and for the FE-I4 read-out chips. All the active-edge sensors underwent the UBM preparation at VTT.

In Table 5.2 an overview of the available assemblies is given. Hereafter the assemblies employing sensors with $d_{\text{active}} = 75\,\mu\text{m}$ will be referred to as "SLID assemblies", the assemblies employing sensors with $d = 100\,\mu\text{m}$ as "active edge assemblies", and the assemblies with $d_{\text{active}} = 150\,\mu\text{m}$ sensors will be called "SOI2 assemblies". When comparing to results obtained with assemblies employing sensors with $d = 285\,\mu\text{m}$ from the CiS production discussed in the preceding chapter, these assemblies will be referred to as "CiS assemblies".

Table 5.2: Overview of the available thin pixel assemblies and their geometric properties.

Type	Read-out chip	Multiplicity	(Active) thickness [μm]	Edge distance [μm]
SLID Assemblies	FE-I2	7	75	900–1000
Active Edge Assemblies	FE-I3	1	100	125
	FE-I3	1		50
	FE-I4	1		125
SOI2 Assemblies	FE-I4	9	150	475

In this section first the IV characteristics before and after irradiation will be discussed together with the irradiation programme. In Section 5.3.2 the results of the assembly tuning are summarised, with a focus on the achievable threshold and its operability. Subsequently, the charge collection performance (Section 5.3.3), the spatial resolution (Section 5.3.4), and the hit efficiency (Section 5.3.5) will be discussed

All laboratory measurements were conducted in a climate chamber where the environmental temperature was kept at 20 °C for the not irradiated assemblies and at −50 °C for the irradiated assemblies. For the beam test measurements dry-ice cooling was used (cf. Section 3.7).

5.3.1 IV Characteristics and Irradiation Programme

As basic functionality test, the IV characteristics of all seven SLID, six SOI2, as well as the active edge assemblies were measured and are summarised in Figure 5.12. Three additional SOI2 assemblies were sent from IZM directly for irradiation at LANSCE and thus could not be measured before irradiation. All IV characteristics were taken with the front-end chip powered but not configured. At an over-depletion of about 10 V—i. e. at 30 V for the SLID, at 20 V for the active edge, and at 110 V for the SOI2 assemblies—the leakage currents are below 100 nA and thus far below the operational limit of 300 μA [70].

For the SLID assemblies the breakdown voltage lies for one assembly at 100 V, for additional four assemblies at or above 140 V. Additional two structres were measured only up to a bias voltage of 55 V, and no breakdown was observed. For the structures measured up to the

breakdown voltage, V_b, this corresponds to a good over-depletion ratio $V_b/V_{fd} \geq 3$. In the case of the active edge assemblies the over-depletion ratio even exceeds 18 with breakdown voltages around 130 V. The breakdown voltages of three SOI2 assemblies exceed 150 V corresponding to an over-depletion ratio of $V_b/V_{fd} \geq 1.5$. For the other three assemblies lower breakdown voltages are found, of which two come close to the full depletion voltage. The low ratio before irradiation is caused by the contamination in the production discussed in Section 5.1.3.

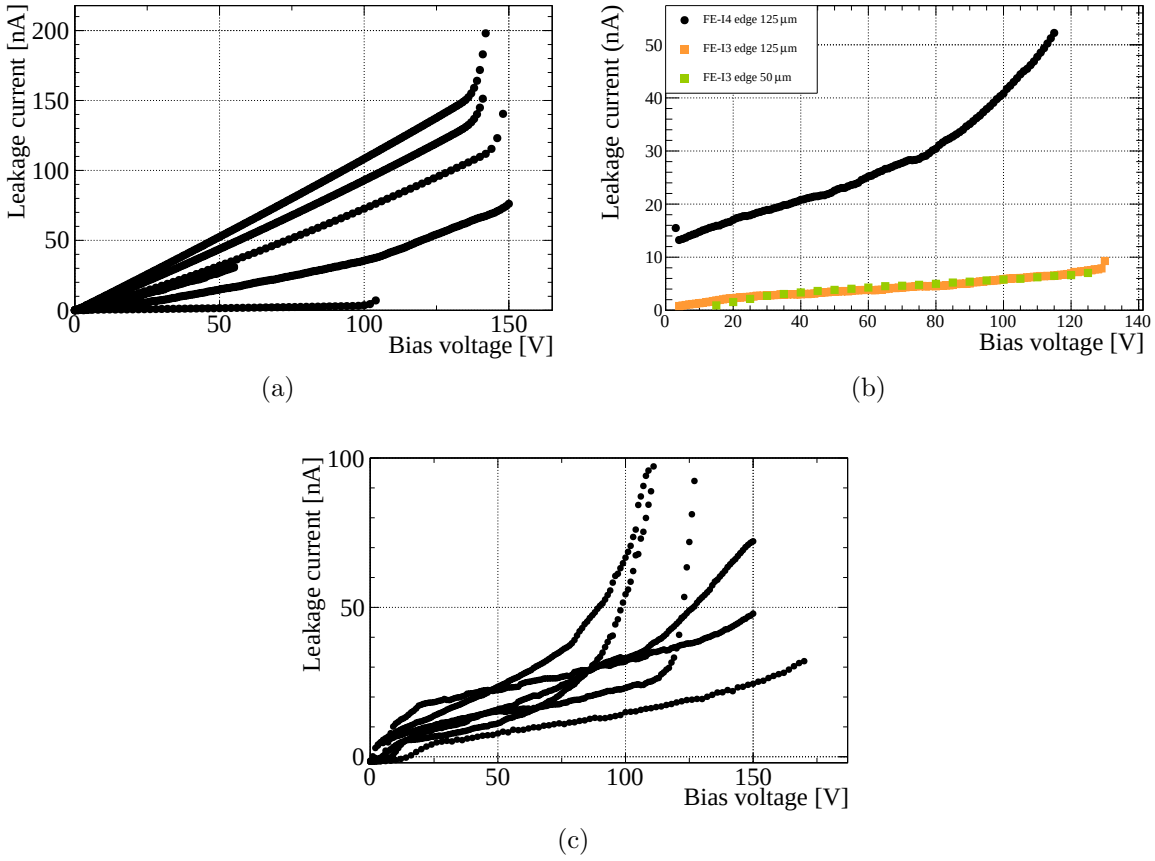

Figure 5.12: IV characteristics before irradiation for (a) the SLID, (b) the active edge, and (c) the FE-I4 assemblies. In (a) the two structures measured up to 55 V are indistinguishable. The statistical uncertainties are smaller than the symbols.

Subsequently, the assemblies were irradiated at KIT, JSI and LANSCE (see Section 3.3). The full irradiation programme is summarised in Table 5.3. For the SLID assemblies the range from $(0.6\text{–}10)\cdot10^{15}\,n_{eq}/cm^2$ was covered, mainly with reactor neutron irradiations. For the SOI2 assemblies two fluence points were probed. Due to high activation of tantalum contained in traces in the FE-I4 read-out chip, irradiations with reactor neutrons could not yet be explored.

In Figure 5.13 the leakage currents as a function of the applied bias voltage are summarised for the irradiated assemblies. All measurements were taken at an ambient temperature of $-50\,°C$ with the read-out chip powered but not configured, compare Section 4.3.2. As expected, the breakdown voltage of the irradiated sensors shifts to higher values and exceeds 500 V for all assemblies. Furthermore, the leakage currents are in agreement with expectations, showing increasing leakage currents with increasing fluences. The increase of leakage current

Table 5.3: Overview of the received fluences for the irradiated SLID and SOI2 assemblies and their respective irradiation sites. Assemblies tested in beam tests are indicated in the beam test column.

Type	Fluence [10^{15} n_{eq}/cm^2]	Irradiation site	Beam test
SLID	0.6	KIT	yes
SLID	0.6+0.4	KIT	no
SLID	2	JSI	yes
SLID	2	JSI	no
SLID	2+3	JSI	no
SLID	5	JSI	yes
SLID	5+5	JSI	no
SOI2	2	KIT	yes
SOI2	4	LANSCE	yes
SOI2	4	LANSCE	no
SOI2	4	LANSCE	no

with thickness, which is expected since leakage current is mainly originated by defects due to radiation in the sensor bulk, is visible as well. For the SOI2 assemblies irradiated to the same fluence of $4 \cdot 10^{15}$ n_{eq}/cm^2 a good agreement for the measurements is found. One of the assemblies exhibits a lower leakage current (light green points) since it was annealed for additional four days due to handling. Annealing effects are also visible when comparing the SLID assembly irradiated directly to a fluence of $5 \cdot 10^{15}$ with the assembly irradiated in two steps, since for irradiations at JSI annealing of about 1.5 d is unavoidable due to handling after each irradiation step. The latter assembly could not be investigated further, since the FE-I2 read-out chip failed after the second irradiation and remounting onto the SCC. In total all leakage currents are found to be $\leq 6\,\mu$A and thus again far below the operational limit.

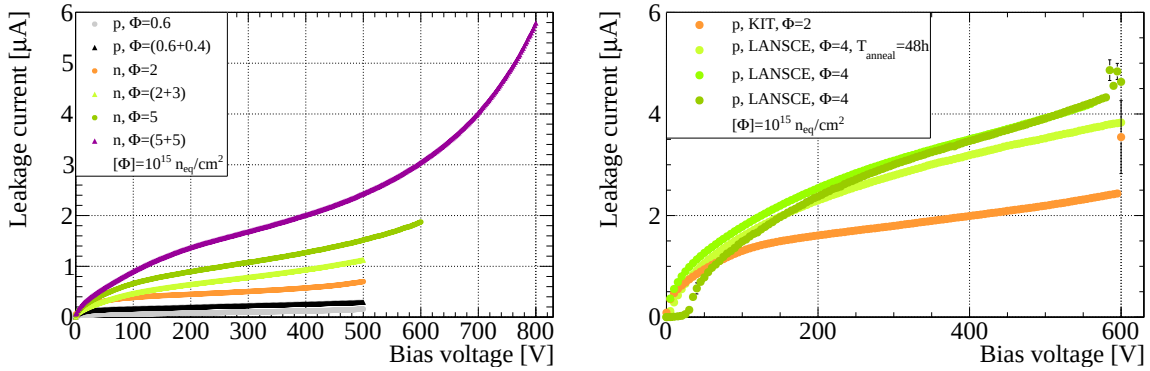

(a) (b)

Figure 5.13: IV characteristics for the irradiated (a) SLID and (b) SOI2 assemblies. All measurements are taken at an environmental temperature of −50 °C. The statistical uncertainties are mostly smaller than the symbols.

Assuming that all irradiated SLID assemblies are fully depleted well below 450 V, it was verified that the damage factors calculated according to Equation 2.11 are about $6 \cdot 10^{-17}$ A/cm, i. e. in agreement with theory predictions for the different target fluences and received period of annealing, see Figure 2.5(a). Although, this cross-check is not possible for the thicker sensors, due to their higher depletion voltages, it can be assumed that the received fluences are accurate to the same level also in their case.

5.3.2 Assembly Tuning

The expected MPV for the charge induced by β-electrons of the ^{90}Sr decay chain, cf. Equations 2.5 and 2.6, is about 4.9 ke for the sensors with $d_{\text{active}} = 75\,\mu$m, 6.6 ke for the sensors with $d = 100\,\mu$m, and 10.8 ke for the sensors with $d_{\text{active}} = 150\,\mu$m, cf. Figure 2.2(b). Therefore, the tuning is focussed to reach lower thresholds than for the CiS assemblies with an MPV of 22.8 ke. As discussed above, the threshold of the FE-I2/3 read-out chip can typically not be tuned below (2.5–3) ke, while for the FE-I4 read-out chips thresholds as low as approximately 1 ke are possible, as will be shown in this section.

SLID Assemblies

Rather than aiming at a common mean threshold the tuning programme for the SLID assemblies was directed towards lowering the threshold as far as possible for each individual assembly. An additional complication for the SLID assemblies is imposed by a fraction of not connected pixel cells in some of the assemblies, see Section 6.1.3, since in the tuning, two very different states of the read-out chip, have to be accommodated in adjacent regions.

A typical achieved tuned threshold and noise distribution for a SLID assembly is shown in Figure 5.14. The target threshold of 2800 e was reached for about 90 % of the pixel cells with a standard deviation of 0.06 ke. The corresponding noise is 0.16 ke with a standard deviation of 0.03 ke over the assembly and thus not significantly different from the noise found for the CiS assemblies.

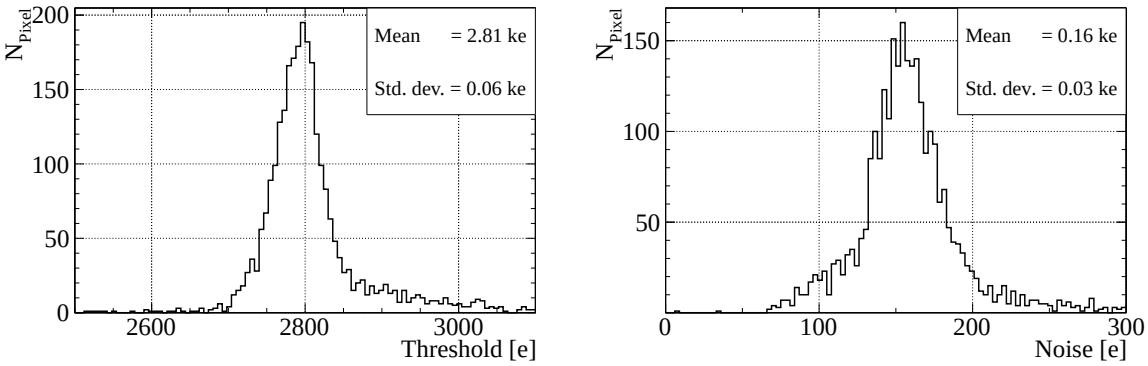

(a) (b)

Figure 5.14: (a) Threshold and (b) noise distribution for a SLID assembly.

In Fig. 5.15 the results of the tuning with the lowest achieved threshold and corresponding noise among all SLID assemblies before and after irradiation is depicted. It was achieved for the SLID assembly irradiated to a fluence of $10^{16}\,\text{n}_{\text{eq}}/\text{cm}^2$. The mean threshold, see. Fig. 5.15(a),

was tuned as low as 2.32 ke with a standard deviation of 0.54 ke over the assembly. The corresponding noise is 0.20 ke with a standard deviation of 0.05 ke over the assembly. The long tail of the distributions is mainly caused by some pixel cells which could not be tuned to such low thresholds. The pixel-by-pixel correlation of threshold and noise shown in Figure 5.15(c) demonstrates that the outliers in both distribution coincide. Since this is a known issue of the FE-I2/3 read-out chip, and the focus in this chapter is on the properties of thin sensors, these outlier pixel cells are disregarded in the following. For the shown tuning the threshold thus lies at (2.07 ± 0.07) ke and the corresponding noise is (0.18 ± 0.02) ke

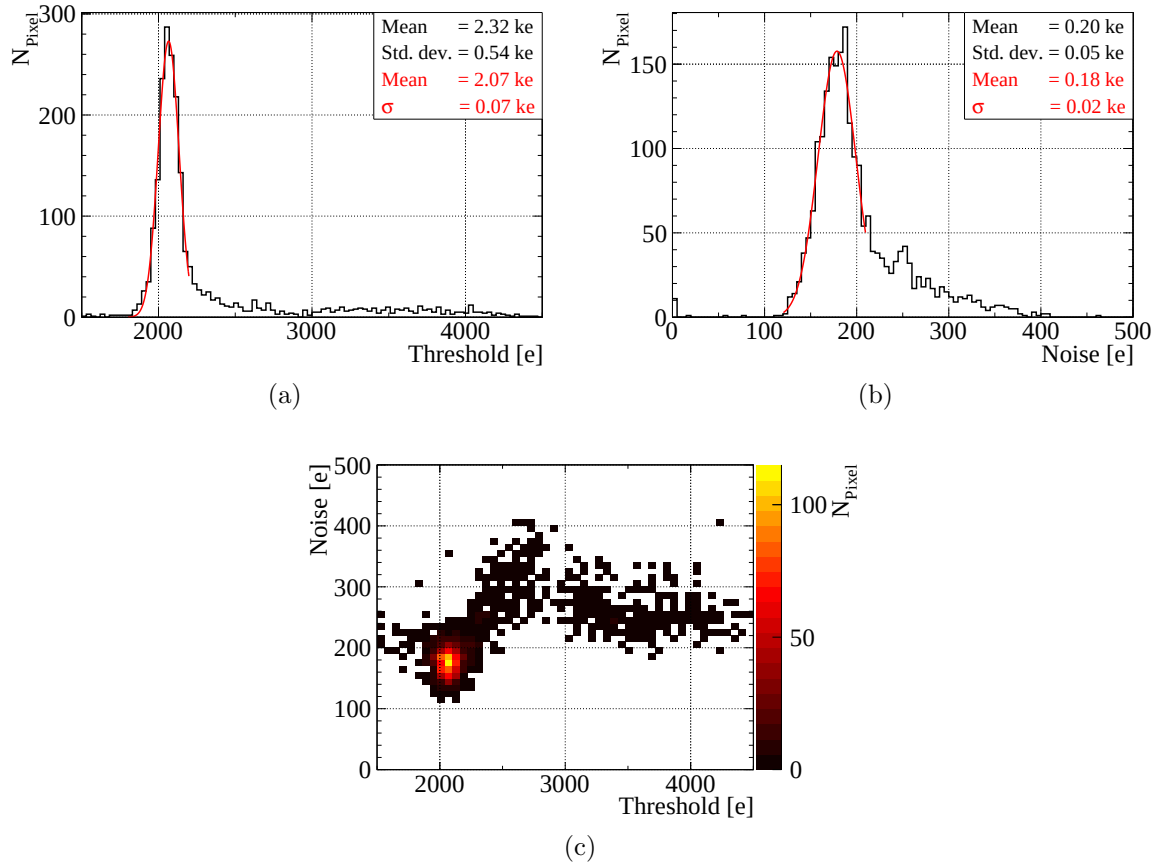

Figure 5.15: (a) Threshold and (b) noise distribution for normal pixel cells in the SLID assembly irradiated to $10^{16}\,n_{eq}/cm^2$. In 5.15(c) the pixel-by-pixel correlation of threshold and noise values is given.

An overview of the threshold tuning and corresponding noise values of all SLID assemblies before and after irradiation is given in Figure 5.16, where the lowest achieved thresholds and their corresponding noise figures are given for each assembly. The uncertainties shown correspond to the standard deviation of the threshold, and the noise respectively. Over all assemblies the average noise is (0.21 ± 0.01) ke. The slightly increased value, with respect to the CiS assemblies, is due to the lower threshold target values on the one hand and the influence of the not connected pixel cells on the other hand. The effect of the not connected pixel cells is especially pronounced in the assemblies with the highest number of not connected cells, number 6 (open squares) and 7 (open circles). Nonetheless, an excellent threshold to noise ratio

exceeding 10 (red dotted line) in all but one case is achieved for assemblies before as well as after irradiation.

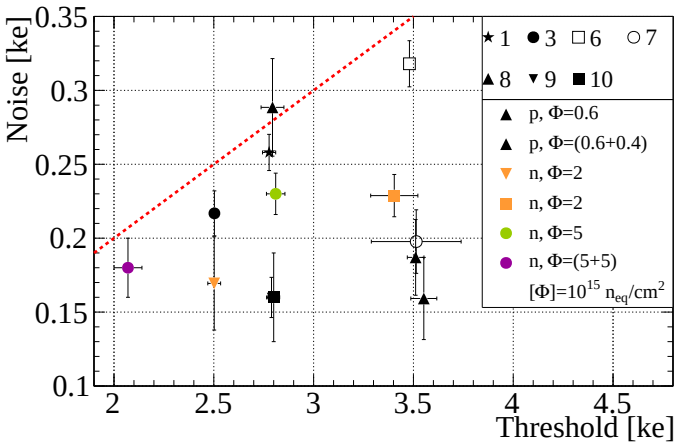

Figure 5.16: Best achieved mean thresholds and their respective noise values for the SLID assemblies before and after irradiation. The symbol style denotes the assembly and the colour the received fluence. Irradiations with protons (neutrons) are indicated by p (n). The uncertainties indicate the standard deviations of the respective distributions. Before irradiation the environment temperature is kept at 20 °C, afterwards at −50 °C. The red dotted line indicates a threshold to noise ratio of ten.

FE-I4 Assemblies

The tuning programme for the SOI2 assemblies has three facets. First, all not irradiated assemblies were tuned to a threshold of 1600 e and a ToT of 10 at a reference charge of 15 ke to allow for a consistent set of measurements in the laboratory and at beam tests. In a second round the possibility to further lower the threshold and the effect on the noise occupancy was investigated for some assemblies. Eventually, the irradiated assemblies where tuned to a threshold of 1400 e and to a ToT to reference charge relation optimal for the expected MPV of the collected charge.

The tuned performance is homogeneous over all SOI2 assemblies. A typical tuning is depicted in Figure 5.17. All active 25536 pixel cells[1] are tuned to the threshold of (1.60 ± 0.03) ke. Only a few outliers are observed towards higher column numbers. The average noise level in this assembly is (0.120 ± 0.008) ke. The influence of the two different injection capacitance implementations in the FE-I4A (cf. Section 3.6.1) is clearly visible in the respective columns (e. g. column 44–50) by the different noise figures.

In the second step the threshold was subsequently lowered and the noise occupancy of the assembly was investigated by sending random triggers. As shown in Figure 5.18(a) and Figure 5.18(b) lowering the threshold does not deteriorate the tuning homogeneity considerably. Still the standard deviation of the distribution is only 0.03 ke and the electronic noise did not change significantly. The other figure of merit, the noise occupancy, is depicted in Figure 5.18(c),

[1] The first as well as the last columns are deactivated due to their special design explained in Section 3.6.1.

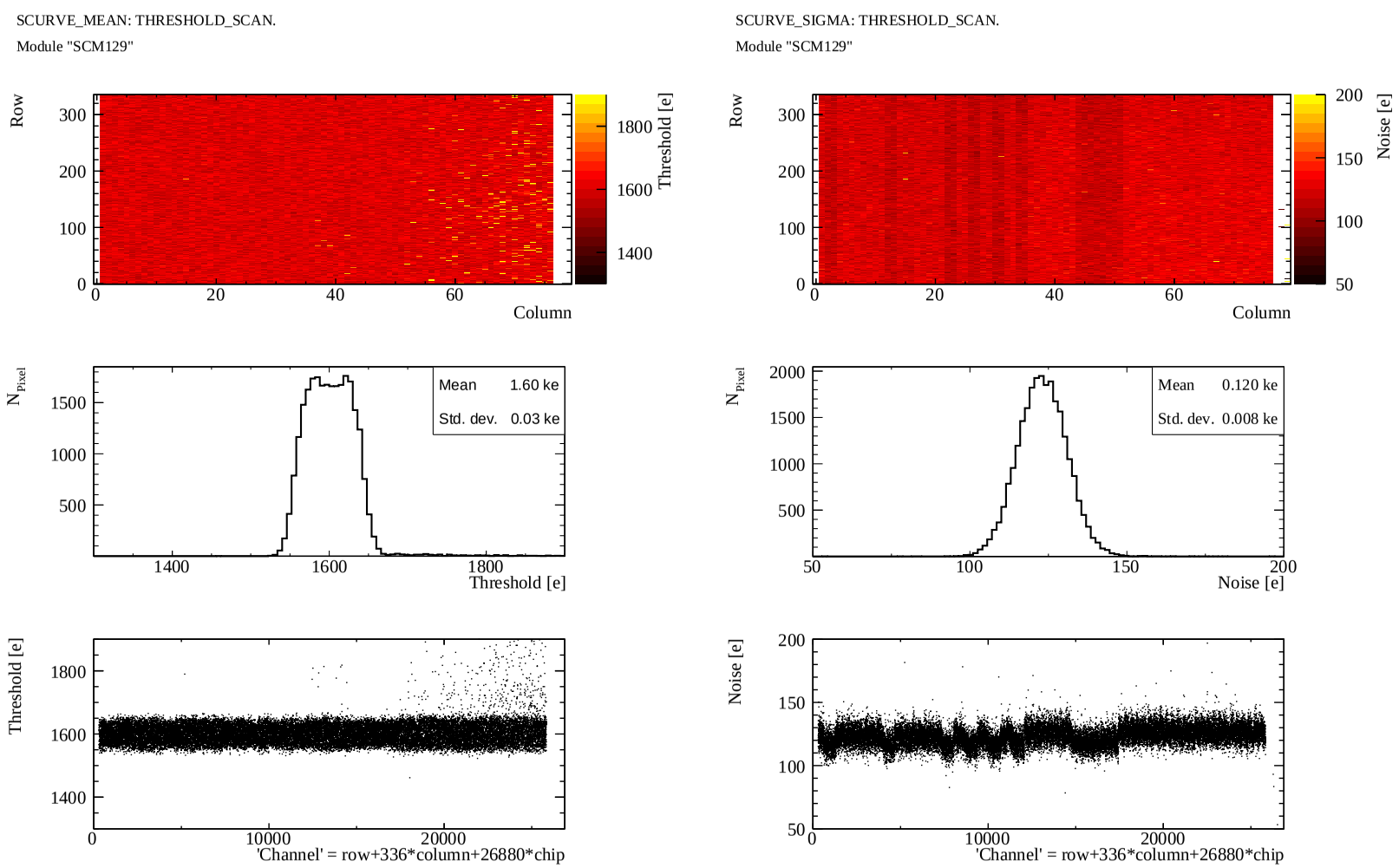

(a) (b)

Figure 5.17: (a) Threshold and (b) noise distribution for an SOI2 assembly using the FE-I4A read-out chip. The representations are the same as in Figure 4.6 The different injection capacitances for the FE-I4A are visible in the uppermost representation of the noise. The first as well as the last three rows were masked.

where the given uncertainties are calculated following [168]. Down to a threshold of 1.2 ke the noise occupancy is lower than 10^{-12}. At lower values the noise occupancy rises up to $4 \cdot 10^{-9}$ at a threshold of 0.65 ke. By masking only one pixel cell this can be lowered to 10^{-10}. This high purity is also visible in a source scan taken with a threshold of 0.8 ke, shown in Figure 5.18(d), where outside of the source spot no noisy pixel is appreciable. These measurements indicate that FE-I4 read-out chip based assemblies employing thin sensors fulfil the noise occupancy requirements of 10^{-8} for the phase II tracker upgrade [180] down to very low thresholds. Of course final statements can only be done when a larger statistics, especially with assemblies employing the FE-I4B and sensors from different vendors, is available.

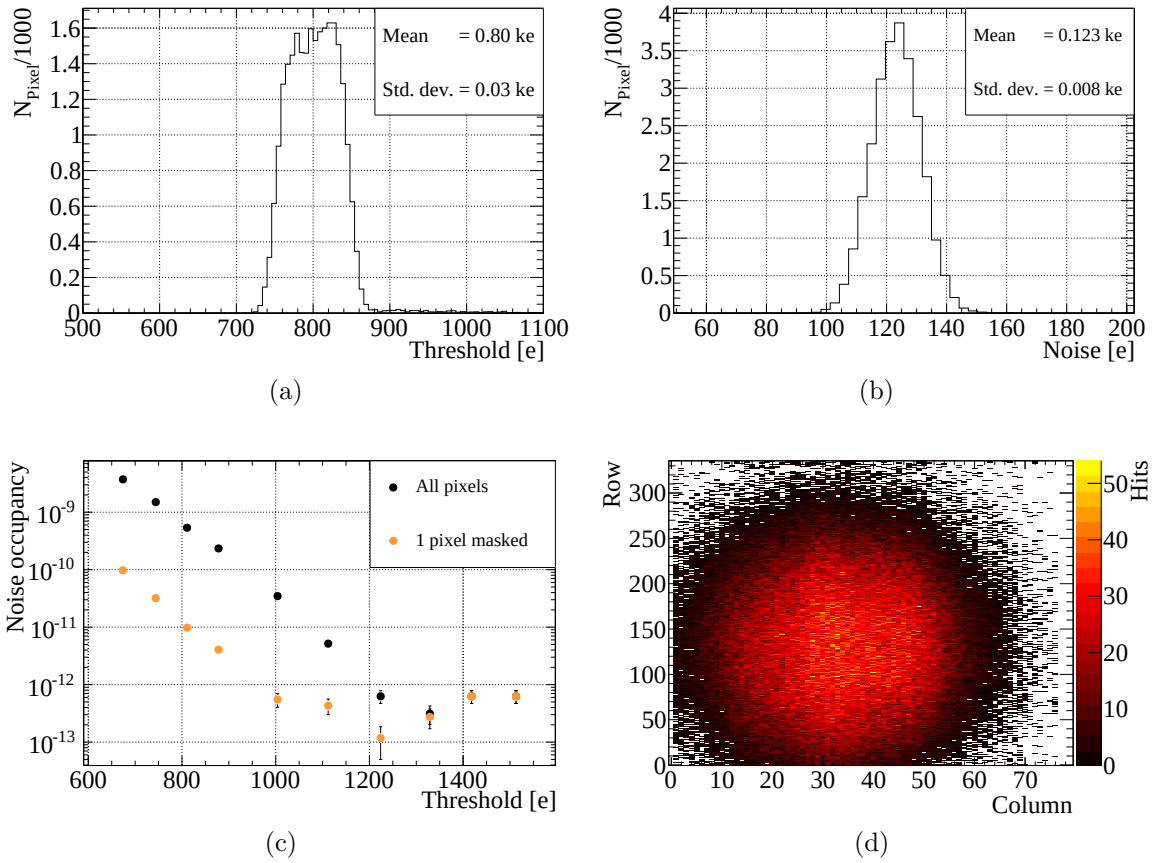

Figure 5.18: Low threshold tuning and noise occupancy for an SOI2 assembly. The distributions for (a) the threshold and (c) the noise of a tuning to a target threshold of 800 e is shown. (c) Noise occupancy versus threshold for all pixel cells (black point) and with one noisy pixel cell masked (orange points). The uncertainties are calculated according to [168]. (d) Hit map for a ^{90}Sr source measurement using the threshold tuning at 800 e.

The overall tuning performance did not change for the SOI2 assemblies up to a fluence of $4 \cdot 10^{15}\,\mathrm{n_{eq}/cm^2}$. This excellent performance and especially the possibility of operating with thresholds as low as 1.2 ke without significant rise of the noise occupancy, favours the usage of the FE-I4 read-out chip when employing thin sensors.

Active Edge Assemblies

For the active edge assemblies a threshold of 2500 e was targeted for in the case of the FE-I3 assemblies and a threshold of 1600 e in the case of the FE-I4 assemblies. A typical tuning is shown for both assembly types in Figure 5.19. In the upper row the tuning distributions for the FE-I3 assembly with $d_{\text{edge}} = 125\,\mu$m is shown. The threshold distribution, see Figure 5.19(a), has a standard deviation of 0.03 ke and exhibits no pronounced tails. To assess the influence of the decreased edge distance the noise distribution is shown in Figure 5.19(b) for the normal (black histogram) as well as for the long pixels (orange histogram). Comparing the noise found for the long pixels, with the results found for the CiS assemblies discussed in Chapter 4, no significant difference is observed if the overall scale uncertainty of 7.3 %, stemming from the injection capacitances (cf. Section 3.6.3) is taken into account. This statement is also valid for the assembly with a d_{edge} of only 50 μm, which exhibits a noise of $(191 \pm 14(\text{syst.}) \pm 7(\text{stat.}))$ e for normal pixels and of $(225 \pm 16(\text{syst.}) \pm 8(\text{stat.}))$ e for long pixels.

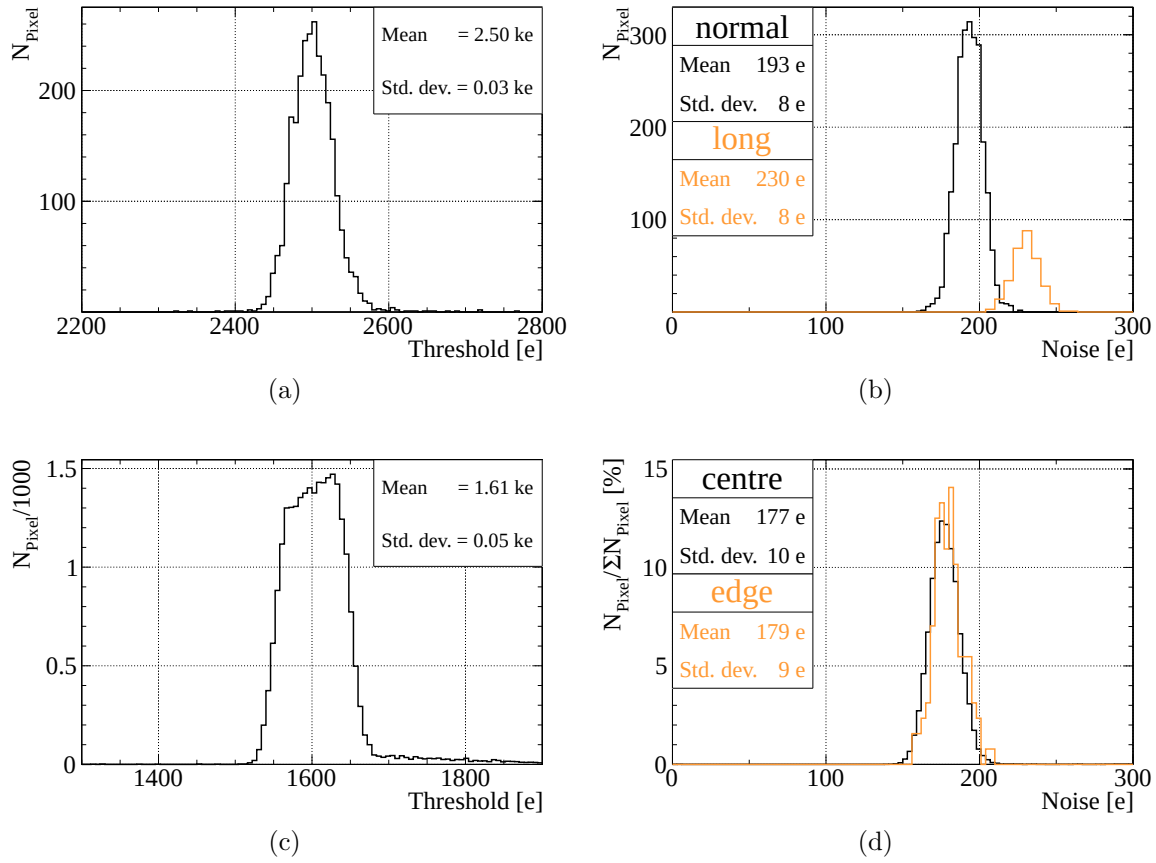

Figure 5.19: Threshold (left) and noise (right) distributions for an FE-I3 (up) and an FE-I4 (down) active edge assembly with an edge distance of 125 μm. In the case of the FE-I3 assemblies the edge pixel cell exhibit a different geometry than the centre pixel cell, while for the FE-I4 assemblies the geometries are identical.

In the lower row of Figure 5.19 the results of the tuning for the FE-I4 assembly with a d_{edge} of 125 μm are shown. The standard deviation of the threshold distribution is slightly larger than

for standard assemblies, but still negligibly small. Since the long pixels are not accessible when employing the FE-I4A read-out chip, for reliable investigations the first and last pixel row is used for investigations of the reduced edge distance influences. In Figure 5.19(d) the normalised distribution of the centre (black histogram) and the edge pixels (orange histogram) are depicted simultaneously. No significant difference is observed. Nonetheless, the overall noise is found to be higher than for the assemblies with standard edge design and $d_{\text{active}} = 150\,\mu\text{m}$. This is most likely caused by the reduced thickness, evoking a higher capacitance, which increases the noise. Anyhow, the threshold to noise ratio is about nine and thus excellent for operation.

5.3.3 Charge Collection and Sharing

As discussed in Chapter 2 and outlined in Section 5.2 with strip devices, thin sensors show higher charge collection efficiencies after irradiation, since trapping and full depletion voltages are reduced. In this section these findings will be confronted to thin pixel sensors and their validity in this context is investigated. Measurements using radioactive sources and beam tests before and after irradiation will be covered. Within uncertainties no significant difference in charge collection was found between the assemblies of the same class.

To investigate the charge collection, measurements using ^{241}Am and ^{90}Sr sources were conducted. While, in the first (photons) case the internal trigger logic was used; in the latter (β-electrons) case the external trigger was employed. Additionally, beam test measurements allow for an analysis of the charge collection profile within and the charge sharing between pixel cells.

SLID Assemblies

In Figure 5.20 the ^{241}Am γ-source spectra obtained with a SLID assembly biased at different bias voltages between 5 V and 55 V are depicted. Each histogram is normalised to its bin with the highest content. For a high resolution reference spectrum taken with a high purity Germanium detector please refer to Figure 4.8(b). At 55 V the prominent 59 keV γ-line is measured at $(14.4 \pm 0.5(\text{fit}) \pm 1.1(\text{syst.}))$ ke (Gaussian fit not shown), which is in good agreement with the expected peak position, when taking the calibration bias of the FE-I3 read-out chip into account. The former uncertainty denotes the fit uncertainty and the latter uncertainty the systematic uncertainties stemming from the ToT to charge calibration discussed in Section 3.6.3. The second prominent line in the spectrum at 26 keV is expected at 7.2 ke. Due to the charge resolution it merges with the lines below, such that only the upper edge is appreciable between 6 ke and 7.5 ke. Since all MIP induced charges will be below 6 ke in this chapter, no correction for the ToT to charge calibration will be applied in this case.

At lower bias voltages a fraction of the sensor volume does not contribute to charge collection and thus the full charge is only collected for events where the photo-electric process occurred in an already depleted region. In the not yet depleted part, only the fraction of the charges diffusing into the depleted volume can be measured. This leads to a broadening of the peaks and to a less defined spectrum. Due to the low thickness of the sensor this only strongly affects the measurements below 15 V, which is in good agreement with the corresponding edge-TCT measurements, see Figure 5.9.

A charge distribution of a ^{90}Sr measurement with a SLID assembly biased at 55 V is shown in Figure 5.21(a). The threshold in this measurement was tuned to 3.0 ke and is indicated by the dotted red line. Entries below threshold are explained by the fact, that the threshold is the 50 % efficiency point. A convolution of a Landau distribution with a Gaussian describes

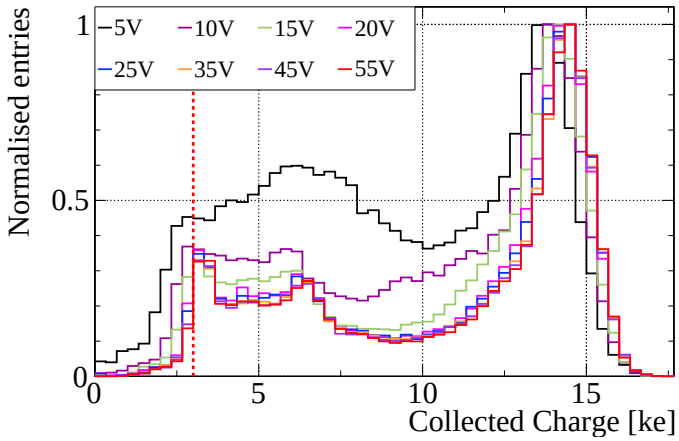

Figure 5.20: Evolution of an ^{241}Am source energy spectrum with applied bias voltage for a SLID assembly. The threshold of 3.0 ke is indicated by the dotted red line.

well the measurement. The resulting MPVs of the collected charge as a function of the bias voltage are summarised in Figure 5.21(b). The fully correlated uncertainty band is evoked by the calibration uncertainty. For a discussion please refer to Section 3.6.3. Since the MPV of the collected charge is close to the threshold, the uncertainties arising from the fit are larger than for assemblies employing thicker sensors. They are indicted by the uncertainty bars. Full charge collection is reached at a bias voltage of (21 ± 0.7) V as determined by the intersection of two linear functions describing the different parts of the charge collection measurement. This agrees well with the edge-TCT measurements. In the shown assembly the charge saturates at $(4.6 \pm 0.4(\text{fit}) \pm 0.3(\text{syst.}))$ ke and thus is in good agreement with the expectations for a sensor with $d_{\text{active}} = 75\,\mu m$, cf. Figure 2.2(b).

Aiming for HL-LHC environments, a high CCE at high irradiation levels is of utmost importance. The measured values of this parameter are summarised for all irradiated SLID assemblies as a function of the applied bias voltage and different received fluences (colour) in Figure 5.22(a). Since the uncertainties stemming from charge calibration before and after irradiation are highly correlated they almost completely cancel, when investigating the ratio. As a conservative estimate a 5 % uncertainty is assigned to the ratio. As expected from the strip measurements in the preceding section, a saturation is found up to the highest fluences. The onset of the saturation increases with fluence, but lies for all fluences at comparable low voltages, i. e. below 500 V. These low bias voltages in combination with the fact that all assemblies saturate within uncertainties to a CCE of 100 % up to a received fluence of $5 \cdot 10^{15}\,\text{n}_{\text{eq}}/\text{cm}^2$ and to 90 % at a received fluence of $10^{16}\,\text{n}_{\text{eq}}/\text{cm}^2$, allows to operate them in a restricted bias voltage range over the life-time of an experiment. This leads to looser requirements on the read-out electronics.

For comparison in Figure 5.22(b) the results obtained from edge-TCT measurements are depicted together with the results obtained with the SLID assemblies for the two highest received fluences. Here the edge-TCT measurement was renormalised globally to achieve comparable scales. For the measurement at $5 \cdot 10^{15}\,\text{n}_{\text{eq}}/\text{cm}^2$ an excellent agreement is found over the entire measurement range. At the higher fluence slight deviations at low and high applied bias voltages are observed, which are most likely caused by the different annealing history of the structures,

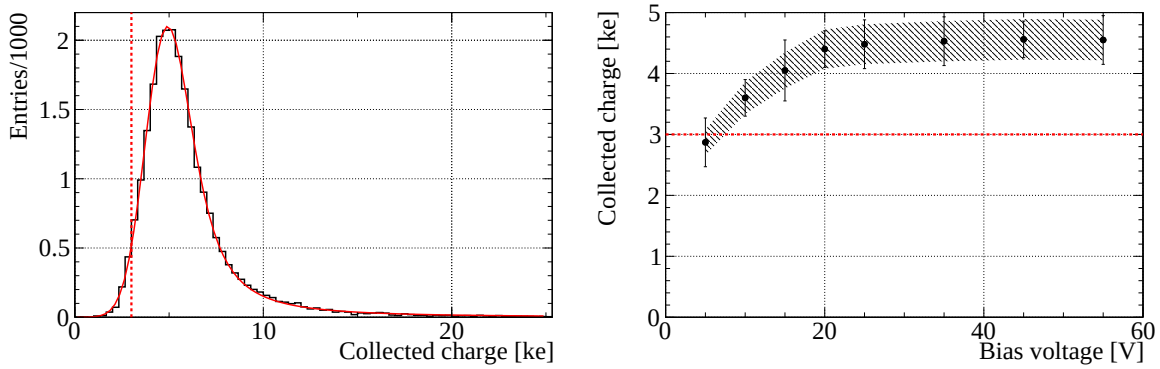

(a) (b)

Figure 5.21: (a) Distribution of collected charge induced by a ^{90}Sr source for a SLID assembly biased at 55 V. In red the fit function, a Landau distribution convoluted with a Gaussian is shown. The resulting MPV of the collected charges as a function of the bias voltage is shown in (b). The uncertainty bars account for the fitting uncertainty and the band for the fully correlated systematic uncertainty. The dotted red line indicates the threshold.

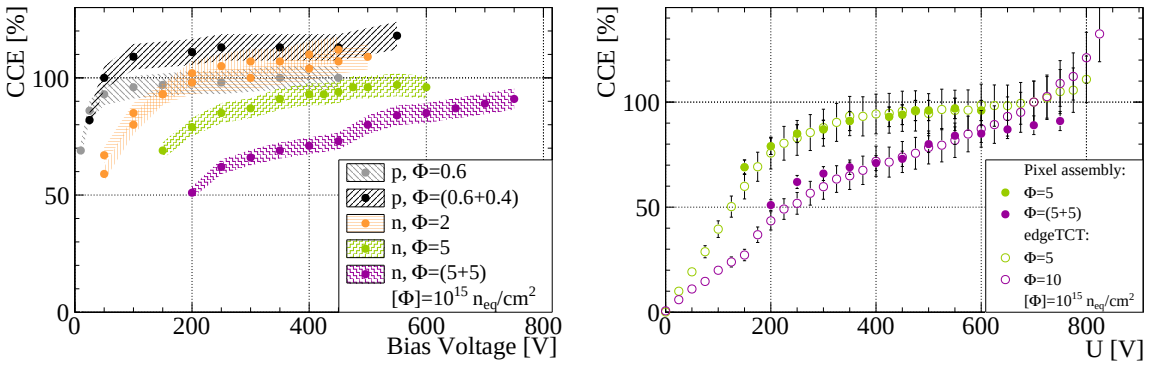

(a) (b)

Figure 5.22: (a) CCE with respect to the charge collected by the respective assembly before irradiation as a function of the applied bias voltage for irradiated SLID assemblies. Proton (Neutron) irradiated samples are denoted with p (n) in the legend. The uncertainty band accounts for the overall time-over-threshold to charge calibration. (b) Comparison of the MPV of the collected charges obtained with SLID assemblies (full symbols) to the edge-TCT measurements (open symbols). For a better visibility the fully correlated uncertainty bands are drawn as simple bars.

stemming from the two step irradiation for the SLID assembly. However, considering the use of a single scaling factor over the whole range a good agreement is achieved.

As a consequence of the low absolute collected charge for the SLID assemblies, the probability that charges are shared between adjacent pixel cells is very low, as depicted in Figure 5.23, where the charge sharing probability P(Share) (cf. Section 3.7.3) is given as a function of the bias

voltage for different received fluences (colour) and incidence angles φ (closed/open symbols). Already before irradiation the P(Share) is below 4 % if perpendicular impinging particles are considered. Even, if the assembly is tilted in φ by 15°, P(Share) stays below 10 %. Mirroring

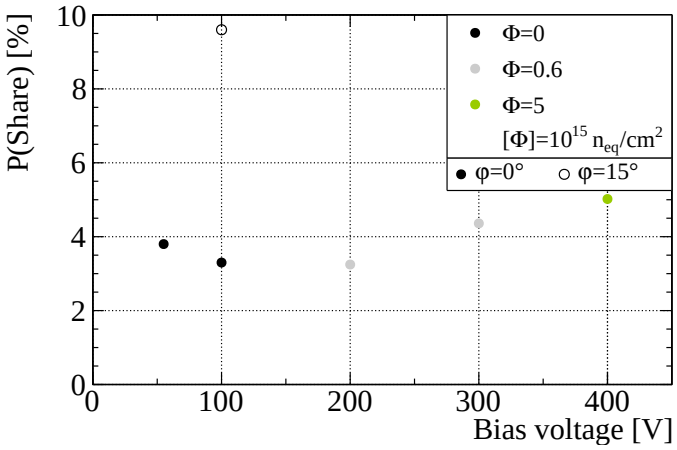

Figure 5.23: Charge sharing probability P(Share) for the SLID assemblies as a function of the bias voltage. The received fluence (colour), and the incidence angle φ (closed/open symbols) are indicated. The uncertainties calculated according to [168] are smaller than the symbols.

the high CCE after irradiation, P(Share) rises to about the same level after irradiation. The low overall charge sharing eventually leads to a lower detector occupancy, which is beneficial in high luminosity environments. Furthermore, it makes two trajectories that are close in space easier distinguishable. On the other hand the low dynamic range of the sharing probability before and after irradiation is favourable for a stable operation within the experiment.

SOI2 Assemblies

Since no reliable ToT to charge calibration is available for the FE-I4A read-out chip, the discussion for these assemblies will be based mostly on the ToT, which, around the tuning point, is linearly proportional to the charge. For comparison the MPV of the ToT will be converted into charges, which is justified given the large assigned uncertainty of 20 %, see Section 3.6.3.

In Figure 5.24 the evolution of an ^{241}Am source spectrum measured in ToT with increasing applied bias voltage is shown. The 59 keV line is measured at (9.2 ± 0.9) ToT (Gaussian fit not shown), where the uncertainty arises from the fit uncertainty. In the underlying tuning the central value corresponds to $(13.8 \pm 2.8(\text{syst.}) \pm 1.4(\text{stat.}))$ ke, where a 20 % uncertainty is used as a conservative estimate of the FE-I4A calibration uncertainty at the tuned value. The low energy-part of the spectrum is affected by the non-linearity of the ToT and therefore cannot be analysed quantitatively because of its low resolution. Still, the broadening of the γ-line caused by partial depletion, as discussed for the SLID assemblies, is visible. The similar shape of the spectra measured at an applied bias voltage of 90 V and 100 V indicates that the assembly is fully depleted at this bias voltage. This is also verified by ^{90}Sr measurements at different bias voltages. Two exemplary collected ToT distributions, once well below depletion and once close to full depletion, are shown in Figure 5.25(a). Both distributions are normalised to the bin with the maximum content. The last bin—ToT=15—is the overflow bin. A Landau

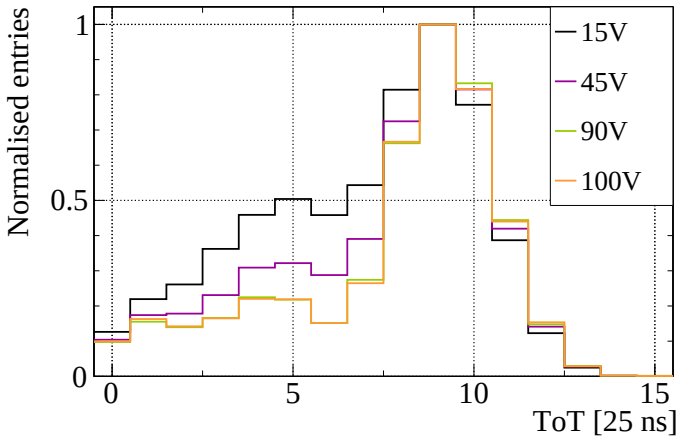

Figure 5.24: Evolution of an ^{241}Am source energy spectrum with applied bias voltage for an SOI2 assembly.

distribution convoluted with a Gaussian still describes the distributions well, but given the lower resolution on ToT of the FE-I4 the statistical uncertainties on the fit rise with respect to those for the FE-I2/3 assemblies. The obtained MPVs from the different Landau fits are shown as a function of the applied bias voltage in Figure 5.25(b). A saturation at a ToT of about (7.8 ± 0.8) ToT, derived from constant fit to the last three data points is found, which corresponds to $(12 \pm 0.8(\text{fit}) \pm 2.4(\text{syst.}))$ ke and thus agrees well with the expected collected charge for a sensor with $d_{\text{active}} = 150\,\mu$m. Full depletion as determined from two linear functions describing the data is reached at (67 ± 7) V.

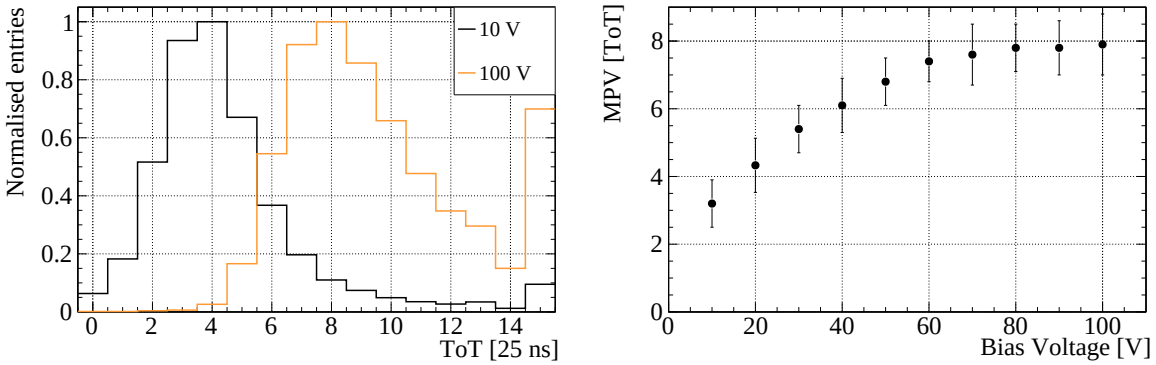

(a) (b)

Figure 5.25: (a) Distribution of the measured ToT at 10 V and at 100 V normalised to the bin with maximum content. (b) Evolution of MPV of the measured ToT with applied bias voltage for an SOI2 assembly. The uncertainties denote the fit uncertainties.

The MPV of the measured ToT as a function of the applied bias voltage after irradiation is depicted in Figure 5.26. Here tunings with a one-to-one correspondence between the ToT and the charge at the MPV of the ToT were employed. Thus the observed saturation at (8.1 ± 0.4) ToT and (7.5±0.4) ToT for the assemblies with received fluences of $2{\cdot}10^{15}$ n_{eq}/cm^2 and $4{\cdot}10^{15}$ n_{eq}/cm^2

corresponds to $(8.1 \pm 0.4(\text{stat.}) \pm 1.6(\text{syst.}))$ ke and $(7.5 \pm 0.4(\text{stat.}) \pm 1.5(\text{syst.}))$ ke. At the higher received fluence the saturation is reached between 300 V and 500 V.

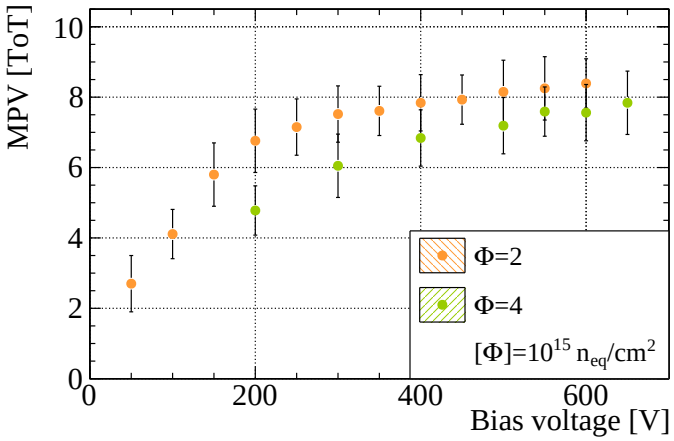

Figure 5.26: Evolution of MPV in TOT with applied bias voltage for the irradiated SOI2 assemblies. The uncertainties denote the fit uncertainties.

The position resolved charge collection was determined in beam test measurements at the CERN SPS. Exemplary, in Figure 5.27(a) the result for the assembly irradiated to a fluence of $4 \cdot 10^{15}\,\text{n}_{\text{eq}}/\text{cm}^2$ and biased at 500 V is shown. The same characteristics as for the FE-I3 based assemblies are found, namely a fully efficient charge collection behaviour in the central part of the pixel cell, and a diminished charge collection efficiency in the corners and the punch through region. Anyhow, this only poses a challenge for perpendicular impinging particles as outlined in Chapter 4.

In Figure 5.28(a) P(Share) as a function of the impact point predicted by the beam telescope for an SOI2 assembly irradiated to a fluence of $4 \cdot 10^{15}\,\text{n}_{\text{eq}}/\text{cm}^2$ and biased at 500 V is shown. As for the CiS assemblies the charge sharing probability is highest along the pixel cell borders. Mainly caused by the higher collected charge to threshold ratio it is about 21 % for the thinner assembly employing the FE-I4 read-out chip, while it is only about 5 % in the FE-I3 assembly with a received fluence of $5 \cdot 10^{15}\,\text{n}_{\text{eq}}/\text{cm}^2$. As in the the CiS assemblies the P(Share), cf. Figure 4.12, is diminished on the side of the bias dot, i. e. at x-positions around 200 μm, as a result of the reduced charge collection efficiency in this region.

Active Edge Assemblies

In the case of the active edge assemblies it is especially important to analyse the performance of the edge pixels in terms of charge collection. Since no beam test data is available yet for these assemblies, the charge collected by the pixel cells located along the edges is compared to the charge collected by the central pixel cells. While for the FE-I3 read-out chip based assemblies the entire frame is used for this analysis, for the FE-I4 read-out chip based assemblies only the first and last row is used, due to the special character of the first and last column. The distributions of collected charges or measured ToTs are shown in Figure 5.29. All distributions are well described by a Landau distribution convoluted with a Gaussian. For the FE-I3 read-out chip based assembly with a $d_{\text{edge}} = 125\,\mu$m an MPV of the collected charge of $(5.2 \pm 0.2(\text{stat.}) \pm 0.4(\text{syst.}))$ ke is determined for the central pixel cells identical to the edge pixels. For the more aggressive design

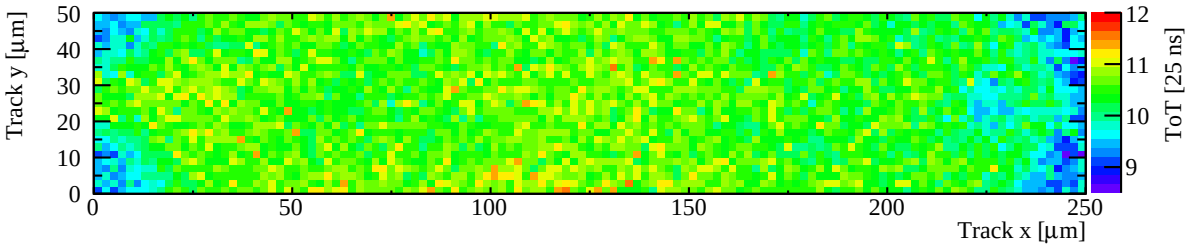

(a)

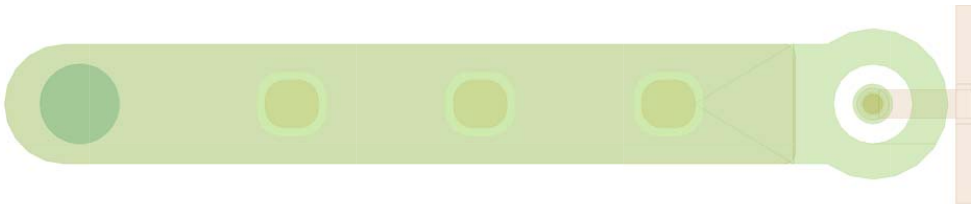

(b)

Figure 5.27: (a) Mean collected ToT as a function of the impact point predicted by the beam telescope for an SOI2 assembly irradiated to a fluence of $4 \cdot 10^{15}\,\mathrm{n_{eq}/cm^2}$ and biased at 500 V. For reference in (b) the geometry of (a) is shown in the design. The mean ToT is systematically higher than the MPV of the collected charge, cf. Section 2.1.3.

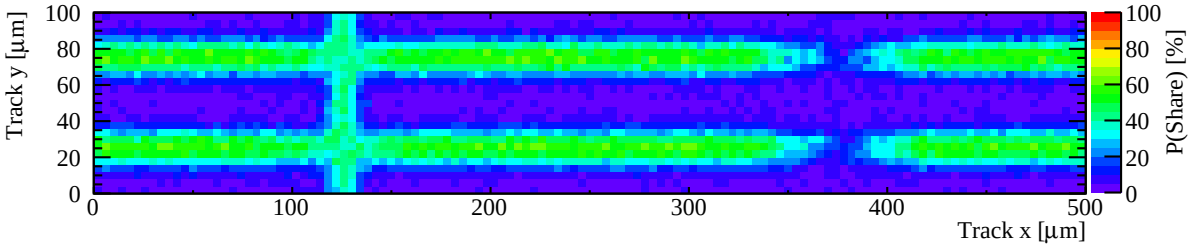

(a)

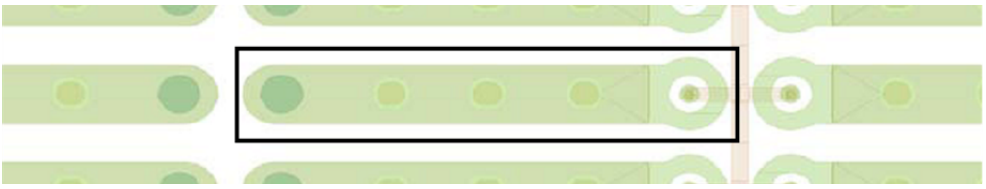

(b)

Figure 5.28: (a) Probability P(Share) for a deposited charge to be shared among neighbouring pixels as a function of the impact point predicted by the beam telescope for an SOI2 assembly irradiated to a fluence of $4 \cdot 10^{15}\,\mathrm{n_{eq}/cm^2}$ and biased at 500 V. For reference in (b) the geometry of (a) is shown in the design. The central pixel cell is indicated by the black frame.

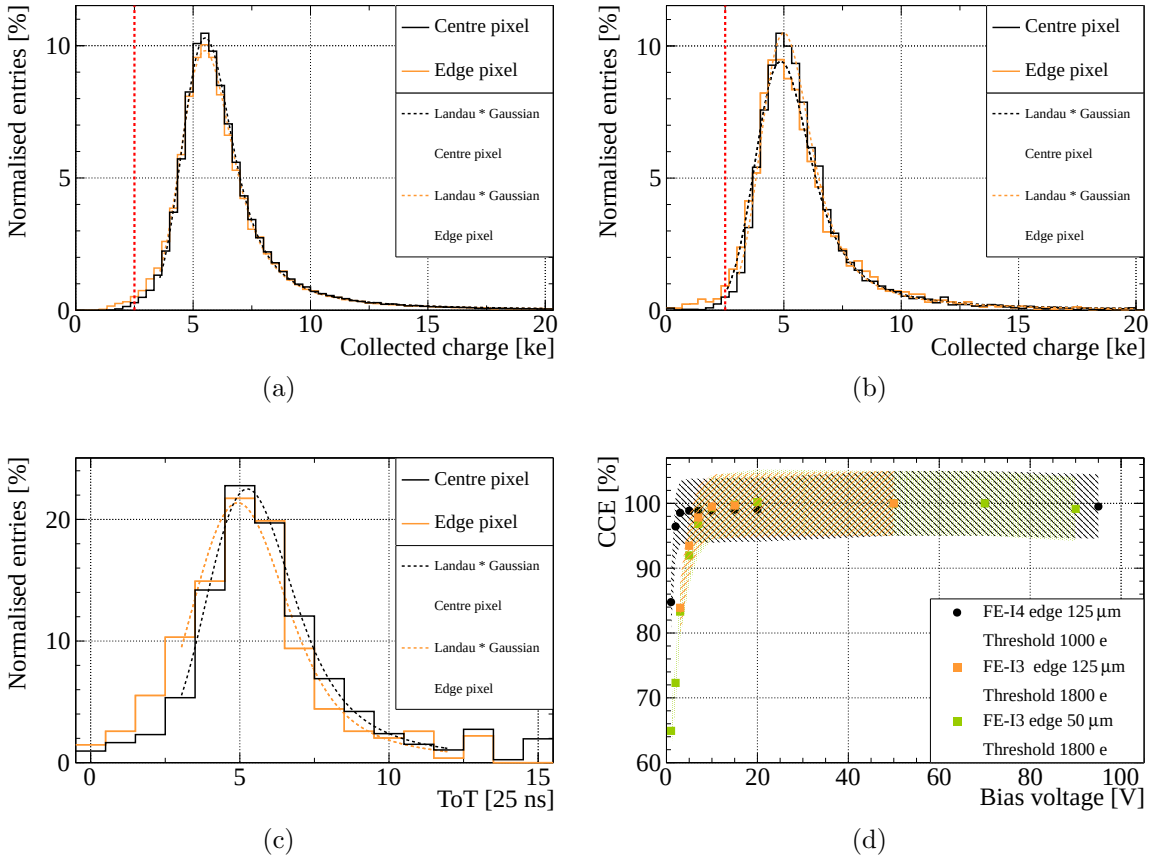

Figure 5.29: Distribution of the collected charge or measured ToT of the assemblies with active edges. In (a) and (b) the results obtained with the FE-I3 read-out chip based assemblies with $d_{\text{edge}} = 125\,\mu\text{m}$ (only bias ring) and $d_{\text{edge}} = 50\,\mu\text{m}$ are shown. Respectively (c) depicts the ToT distributions for the FE-I4 based assembly with $d_{\text{edge}} = 125\,\mu\text{m}$ together with the Landau distribution convoluted with a Gaussian, describing the distribution. (d) summarizes the CCE as a function of the bias voltage. The MPV of the collected charge or measured ToT at a bias voltage of 50 V is used for normalization. The uncertainties reflect the systematic uncertainties discussed in Section 3.6.3.

with only $50\,\mu\text{m}$ edge distance the MPV of the collected charge in the central pixel cells is $(4.7 \pm 0.2(\text{stat.}) \pm 0.3(\text{syst.}))$ ke while it is $(4.5 \pm 0.2(\text{stat.}) \pm 0.3(\text{syst.}))$ ke for the edge pixel cells. In the FE-I4 read-out chip based assembly which uses the less aggressive design with $d_{\text{edge}} = 125\,\mu\text{m}$ no significant shift of the MPV of the collected charge is found. The MPV of the measured ToT is (4.8 ± 0.2) ToT, which corresponds to $(4.8 \pm 0.2(\text{stat.}) \pm 1.0(\text{syst.}))$ ke. Still, comparing the shape of the pair of distributions in all three cases a slight difference is visible. Future beam test measurements will give deeper insight, if this is a significant effect and especially if it influences the hit efficiency in this region.

In Figure 5.29(d) the CCE as a function of the bias voltage is compared for the three devices. All graphs are normalised to their respective MPV at 50 V, to equilibrate the different absolute scales, due to the offset of the calibration capacitances. All assemblies fully collect the charge

already at bias voltages below 10 V which allows for a very low power budget operation and/or high over-depletions.

Comparison of Charge Collection for Different Sensor Thicknesses

The MPV of the collected charge as a function of the applied bias voltage after irradiation are given in Figure 5.30 grouped by comparable fluence for the SLID, SOI2, and CiS assemblies discussed before. For a better comparability the MPVs of the measured ToT for the SOI2 assemblies are converted in ke, which is justified given the conservative systematic uncertainty of 20 %. In Figure 5.30(a) the comparison at a fluence of $2 \cdot 10^{15}\,\mathrm{n_{eq}/cm^2}$ is shown, in Figure 5.30(b) the one at $5 \cdot 10^{15}\,\mathrm{n_{eq}/cm^2}$, where for the SOI2 assembly a similar fluence of $4 \cdot 10^{15}\,\mathrm{n_{eq}/cm^2}$ is used. At a fluence of $10^{16}\,\mathrm{n_{eq}/cm^2}$ no measurements for the SOI2 assemblies is yet available and thus only the data for the SLID and the CiS assemblies are shown in Figure 5.30(c). The

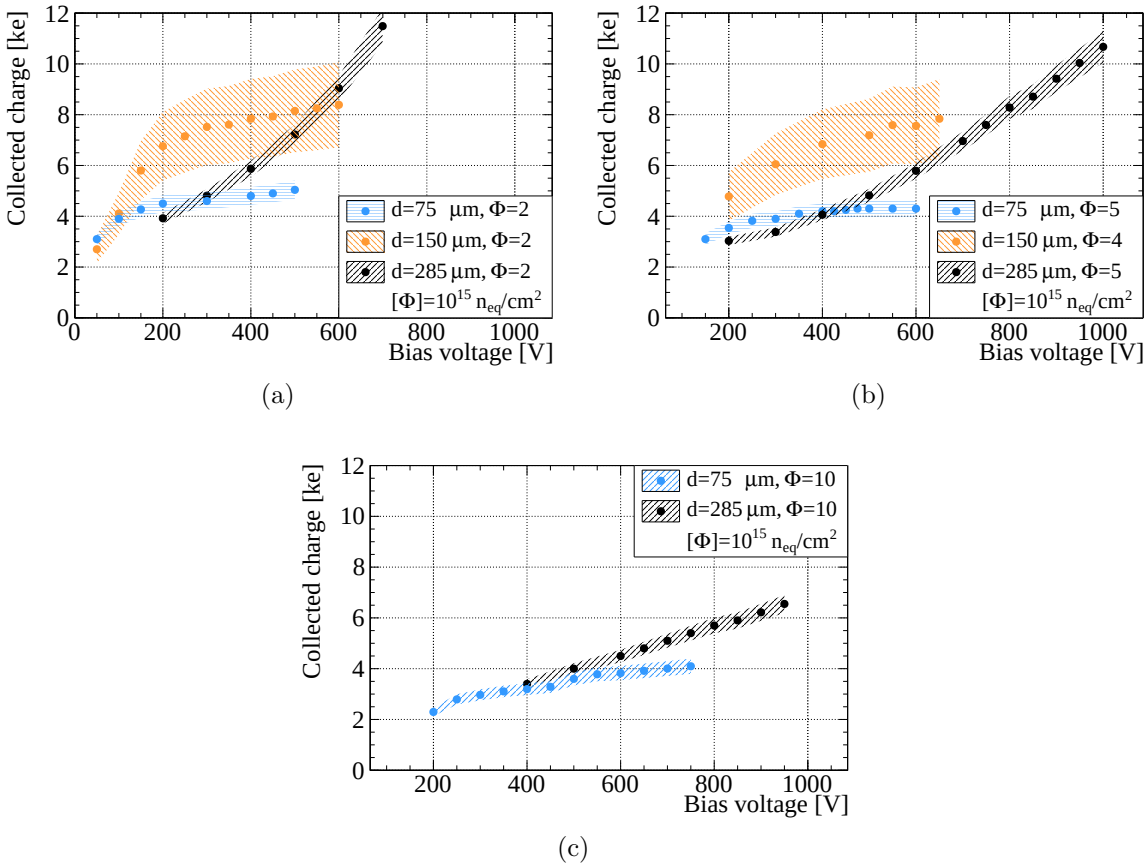

Figure 5.30: Comparison of charges collected with irradiated pixel detectors of different thicknesses and received fluences. In (a) the result for a received fluence of $2 \cdot 10^{15}\,\mathrm{n_{eq}/cm^2}$ is shown. In (b) results for fluences of $4 \cdot 10^{15}\,\mathrm{n_{eq}/cm^2}$ and $5 \cdot 10^{15}\,\mathrm{n_{eq}/cm^2}$ are shown, while (c) summarises the results at $10^{16}\,\mathrm{n_{eq}/cm^2}$. For better comparability all plots share the same scale. For the assignment of the uncertainties please refer to the discussion in this Section and Chapter 4.

data in all figures exhibit similar characteristics. While for the CiS assemblies no saturation is

found up to the highest probed bias voltages, both, the SLID as well as the SOI2 assemblies saturate at bias voltages below 500 V. Comparing the measured MPV for the collected charge to pre-irradiation values an ascending order with decreasing thickness is found, in accordance with theory predictions. While the CiS assemblies barely collect 50 % of their pre-irradiation collected charges, the SOI2 assemblies saturate at a CCE around 60 % to 70 %. Eventually, the SLID assemblies saturate at a CCE of 90 % to 100 %. The saturation, in combination with the high CCE already at low bias voltages for sensors of thinner active thickness, allows for operating the read-out electronics in a similar dynamic range before and after irradiation. The lower applied bias voltages are especially beneficial in terms of power consumption of the assembly and thus helps to reduce the cooling load. In contrast, for the thick sensors as they are used within ATLAS today, high bias voltages are needed to achieve the same collected charge, as in thinner sensors.

5.3.4 Spatial Resolution

For thinner sensors the spatial resolution is expected to differ from the one observed in thick sensors given the different cluster size abundances. When comparing the resolution on events with a specific cluster size between different thicknesses no difference is expected. On the other hand, lower cluster sizes lead to a reduced occupancy in high occupancy environments. These effects will be discussed in this section.

While the cluster size can be reliably determined for trajectories perpendicular to the assembly, the resolution, which is assessed via the cluster residuals demands for a high spatial resolution and especially the lowest possible contribution from multiple scattering within the beam test. Thus the latter analysis is more precise for beam tests at the CERN SPS than at DESY, and the determination of the tracking resolution was omitted for the DESY beam test periods.

Cluster Sizes

The lower charge sharing probability reported above is also reflected in the smaller abundances of higher multiplicity clusters. In Figure 5.31 a summary on the cluster sizes as a function of the bias voltage for different received fluences (colour), directions (symbol style), and incidence angles φ (closed/open symbols) is given, where the uncertainties calculated according to [168] are smaller than the symbols. For the SLID assemblies in the direction of the short pixel pitch y only about 5 % of two-hit clusters are observed for perpendicular incidence. If the assemblies are tilted by $\varphi = 15°$ about 10 % of the clusters in y are composed by two hits. As expected from the charge collection efficiency measurements, no difference is found before and after irradiations, provided that the applied bias voltage is around or above the value corresponding to the charge saturation.

In the case of the SOI2 assemblies a small difference between the pre- and post-irradiation values is still appreciable in y, which is most likely caused by a small, not recognised, tilt in φ. While the percentage of two-hit clusters in y is slightly lower than for the CiS assemblies (cf. Figure 4.13), the reduced pitch in x, when compared to the FE-I3 assemblies, equilibrates the effect of the thinner bulk and leads to a comparable fraction of two-hit clusters in this direction. The slight rise of the collected charge with applied bias voltage for the assembly irradiated to a fluence of $4 \cdot 10^{15}\,\mathrm{n_{eq}/cm^2}$ is also reflected in the cluster sizes, which slightly change their ratio between 400 V and 500 V, towards higher multiplicity clusters.

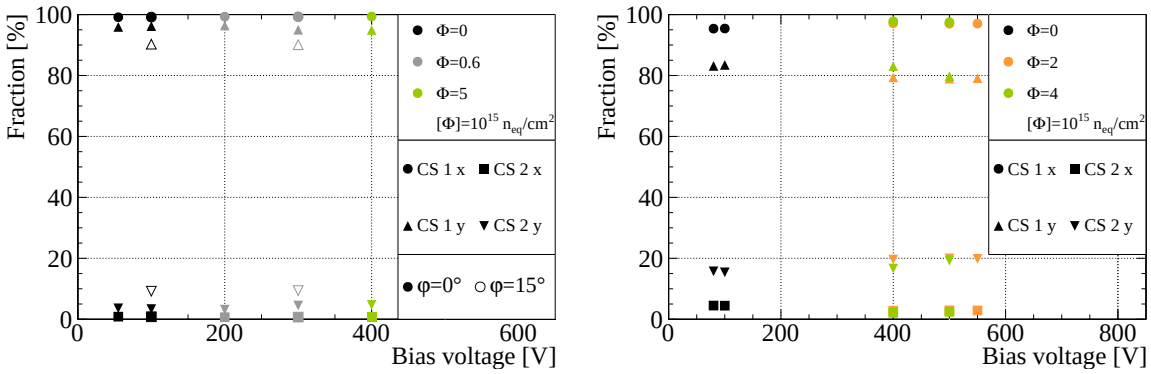

(a) (b)

Figure 5.31: Summary on the cluster size fractions as a function of the bias voltage for thin sensors before and after irradiation. In (a) the results for the SLID assemblies and in (b) the results for the SOI2 assemblies are given. Uncertainties calculated according to [168] are smaller than the symbols. The colours represent the received fluences and the marker type the cluster size as well as its directions. Filled (open) markers stand for measurement at perpendicular ($\varphi = 15°$) incidence.

Cluster Residuals

In the case of the SLID assemblies no significant difference for the single-hit cluster residuals to the CiS assemblies is present, as expected from the identical pixel cell geometry. For the SOI2 assemblies the pixel cell measures 250 μm in x and thus a resolution of 72 μm is expected for single-hit clusters. The residual distributions for single- and two-hit clusters are shown in Figure 5.32 for the assembly irradiated to a fluence of $4 \cdot 10^{15}\,\mathrm{n_{eq}/cm^2}$ operated at a bias voltage of 500 V. The experimental values in this case are found to be $(70.4 \pm 2)\,\mu$m in x and $(14.6 \pm 2)\,\mu$m in y, where the uncertainty accounts for the tracking resolution and alignment of the telescope (cf. Section 3.7.2). The statistical uncertainty is less than 0.1 μm. Thus, also with the reduced pitch, theoretical predictions are confirmed.

Since for the two-hit cluster residuals solely the region between adjacent pixel cells, as well as the collected charge to threshold ratio is decisive, the width σ of the core Gaussian (cf. Section 3.7.3) is expected to match the width of CiS assemblies. Indeed no significant difference is found for the SOI2 assemblies. But, given the higher charge collection efficiency after irradiation, the widths obtained after irradiation, see Figure 5.32(c) and Figure 5.32(d), are not degraded with respect to before irradiation as it was observed for the CiS assemblies, see Figure 4.26. Also the percentage of clusters for which the η correction did not yield an improved resolution, i. e. the entries not described by the core Gaussian does not increase significantly. This allows for a stable operation within an experiment, without the need for adaptations to the reconstruction algorithms to account for degrading detectors. For the SLID assemblies the low statistics of two-hit clusters does not allow for a determination of the resolution in the two-hit cluster case.

5.3.5 Hit Efficiency

Besides the resolution, the tracking efficiency of the pixel detector is the key figure of merit. For a high tracking efficiency, a high hit efficiency of the pixel assemblies is mandatory. The latter

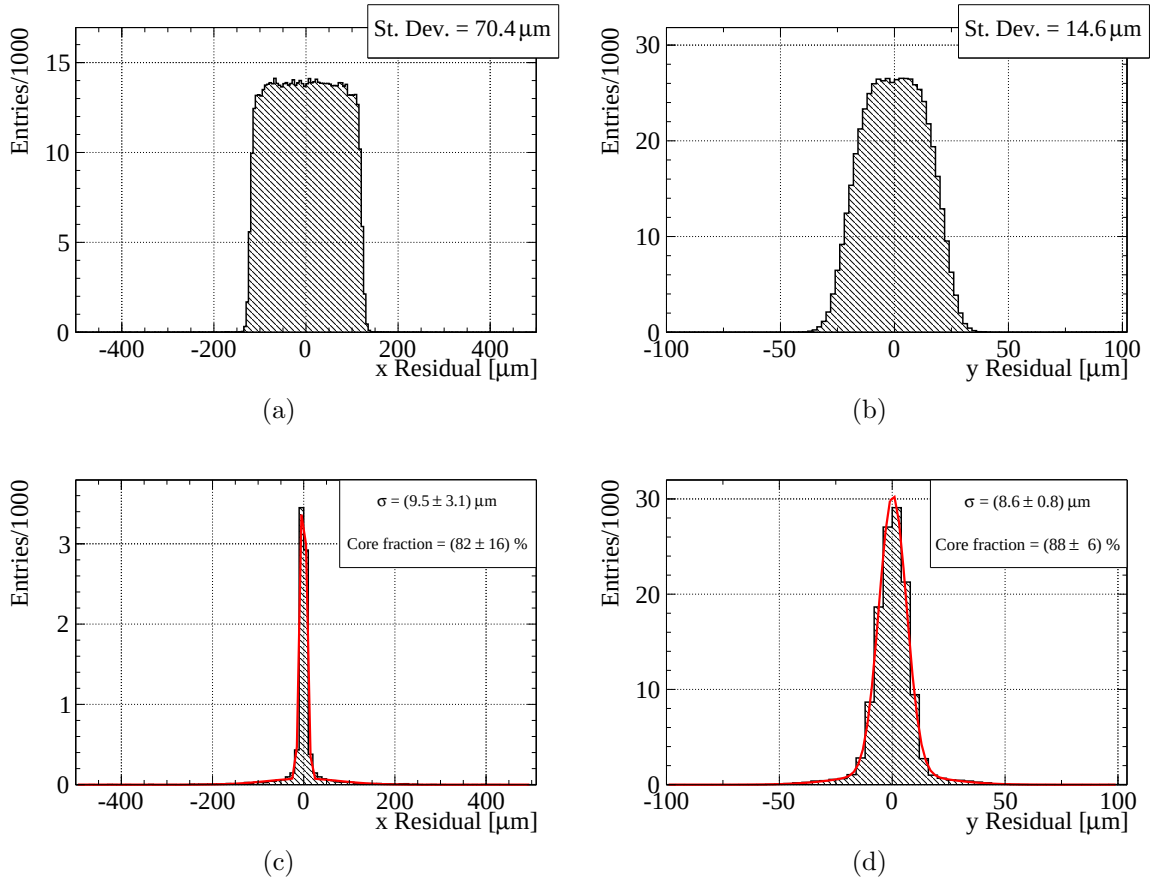

Figure 5.32: Residual distributions for an SOI2 assembly irradiated to a fluence of $4{\cdot}10^{15}\,\mathrm{n_{eq}/cm^2}$ and biased at 500 V. Shown are single- (top) and two-hit (bottom) clusters for the long pixel coordinate x (left) and for the short pixel coordinate y (right).

is mainly driven by the ratio between collected charge and threshold. So for thinner sensors the lowest possible threshold is desirable as discussed before. This criterion is especially challenging for the SLID assemblies since the difference between the mean threshold and the MPV of the collected charge is so small that part of the distribution lies below threshold as shown for example in Figure 5.21(a). Since the threshold corresponds to an efficiency of 50 % for the electronic circuits of the pixel cell this diminishes the overall hit efficiency considerably. In Figure 5.33 the mean hit efficiency as a function of the impact point predicted by the beam telescope is depicted for a SLID assembly before and after irradiation to a fluence of $6 \cdot 10^{14}\,\mathrm{n_{eq}/cm^2}$. The thresholds were tuned to 2800 e and 3300 e respectively. The impact of the different thresholds is most pronounced in the corner regions, where the higher threshold leads to a loss of hit efficiency due to the sharing among several pixels. The overall hit efficiencies are found to be (98.1 ± 0.3) % and (94.8 ± 0.3) % respectively. If just the central region (indicated by the box) is considered the hit efficiencies rise to (98.5 ± 0.3) % and (95.8 ± 0.3) % respectively. An overview of the measured hit efficiencies as a function of the bias voltage for different received fluences (colour), incidence angles φ (closed/open symbols), and tuned thresholds (symbol style) for the SLID assemblies is given in Figure 5.34(a).

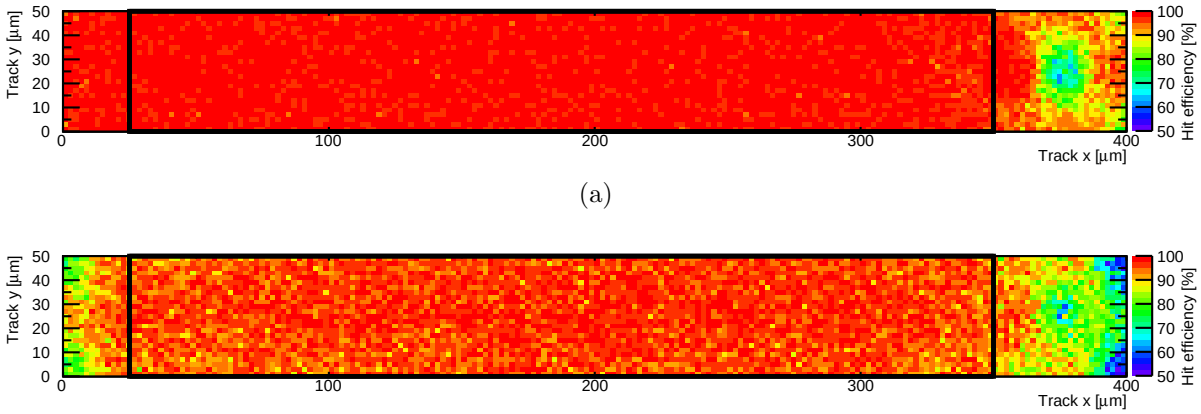

(a)

(b)

Figure 5.33: Map of mean hit efficiency as a function of the impact point predicted by the beam telescope for SLID assemblies (a) before and (b) after irradiation to a received fluence of $6 \cdot 10^{14}\,\mathrm{n_{eq}/cm^2}$.

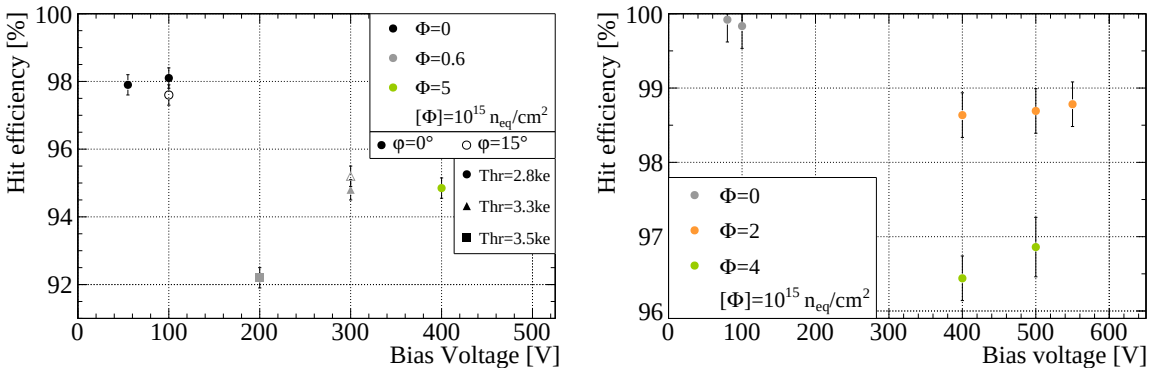

(a) (b)

Figure 5.34: Mean hit efficiency as a function of the bias voltage for different received fluences (colour), incidence angles φ (open closed symbols), and thresholds (symbol style) in (a) the SLID assemblies and (b) the SOI2 assemblies. The uncertainties are purely systematic due to the reference plane.

Using the FE-I4 read-out chip, lower thresholds can be exploited and thus higher hit efficiencies are achievable. For not irradiated assemblies a hit efficiency above 99.8 % is measured with a homogeneous behaviour over the pixel. After irradiation hit efficiency losses are observed in the corner regions as well as in the bias dot region. An exemplary measurement is depicted in Figure 5.35 for the assembly irradiated to a fluence of $4 \cdot 10^{15}\,\mathrm{n_{eq}/cm^2}$ and operated at $V_{\mathrm{bias}} = 500\,\mathrm{V}$. Given the larger fraction of the assembly area occupied by these deficient areas, their impact is bigger than for the FE-I3 based assemblies. Nonetheless, this effect is only expected at perpendicular incidence angle, which only occur in the centre-most region of the tracking system. Thus the hit efficiencies quoted in Figure 5.34(b) have to be considered as lower limits.

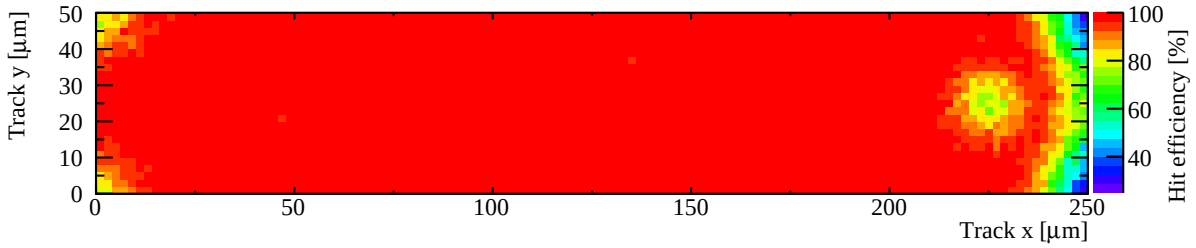

Figure 5.35: Map of the mean hit efficiency as a function of the impact point predicted by the beam telescope for an SOI2 assembly irradiated to a fluence of $4 \cdot 10^{15}\,\mathrm{n_{eq}/cm^2}$ and biased at 500 V.

5.4 Conclusions and Outlook

The properties before and after irradiation for thin planar silicon sensors were discussed in this chapter. Their thicknesses range from $d_{\mathrm{active}} = 75\,\mu\mathrm{m}$ to $d_{\mathrm{active}} = 150\,\mu\mathrm{m}$, and the findings were compared to thick sensors with $d = 285\,\mu\mathrm{m}$. The assemblies employing the $d_{\mathrm{active}} = 75\,\mu\mathrm{m}$ sensors are among the thinnest pixel assemblies ever built and characterised.

It was found that for strip as well as for pixel sensors, the CCE is always higher for thinner sensors, when comparing the same voltage and fluence. Especially for the thinnest sensors even at the highest probed fluence of $10^{16}\,\mathrm{n_{eq}/cm^2}$ a CCE above 90 % at a moderate bias voltage of 750 V was measured. The charge collection measurements were confronted with edge-TCT measurements allowing for insight in the charge collection profile of the sensor. While for the $d_{\mathrm{active}} = 150\,\mu\mathrm{m}$ sensors the expected profile, reflecting a depletion from the front-side was found, for the sensors with $d_{\mathrm{active}} = 75\,\mu\mathrm{m}$ a flat profile was observed, which is currently also found in simulations by other groups within RD50.

Motivated by the dependence of the hit efficiency on the collected charge to threshold ratio, the possibilities of low threshold operation for the FE-I4A read-out chip were explored, and tuning was found to be feasible down to a threshold of about 1.2 ke. In addition, it was shown that the threshold ranges offered by the FE-I2/3 read-out chip are not sufficient to operate thin sensors in a high energy physics experiment environment. Anyhow, only the use of the FE-I4 read-out chip and successors is planned for future applications within ATLAS. When designing these successor read-out chips for ATLAS, CMS, and other high energy physics experiments emphasis should be put on aiming at low threshold operability for the use of thin sensors.

Beam test measurements, showed that the average cluster size diminishes as expected with decreasing thickness, which corresponds to a reduced occupancy within the detector. The occupancy is also lowered, due to the smaller absolute charge signal observed, since these correspond to smaller ToT values and thus shorter dead times of the pixel cell. Hit efficiencies were found to be challenged by two factors. First, the mentioned charge to threshold ratio, second, by losses in the bias dot region. Although the latter challenge only exists for perpendicular incidence, within the PPS collaboration several approaches are explored to improve the hit efficiency also in this area. This is especially crucial for the assemblies based on the FE-I4 read-out chip, since here the smaller pixel size increases the fraction of area covered by this structures.

Additionally, first investigations for novel pixel sensors with implanted sides, and extremely small distances between the last pixel implant and the sensor edges were presented. Down to a

edge distance of only 50 μm, within uncertainties the collected charge for the edge pixels was determined to be as high as for central pixels. Also the other important operational parameters: leakage currents, breakdown voltages and noise were found to be compatible with currently used devices, making these devices extremely attractive for future upgrades of ATLAS, provided these results persist after irradiation and are confirmed in beam tests.

6 3D-Integration: SLID and ICV

This chapter is dedicated to investigations towards a fully 3D integrated demonstrator pixel assembly allowing for 4-side-buttability and a maximised active area. As discussed in Chapter 1.4, a 3D-integration demands two key technology parts: An interconnection technology which enables stacking several layers, as well ICVs to route signals through the read-out chip. The first aspect will be discussed in Section 6.1, the latter in Section 6.2.

Parts of the results presented in this chapter, were already published in [172, 181].

6.1 Solid Liquid Interdiffusion

Solid Liquid Inter-Diffusion (SLID) is a class of interconnection techniques, where the formation of the interconnection takes place at temperatures significantly lower than the ones the connections can withstand afterwards. The concept was introduced in the 1960s [182, 183] and is based on binary, ternary, or even higher-order metal systems, where one low-melting metal is coated on a high-melting core. By bringing the temperature of the metal system above the melting point of the low-melting metal and applying high pressure, the high-melting metal dissolves and diffuses into the liquid low-melting metal. This process stops as soon as the liquid phase is separated from the high-melting metal by the solution and diffusion begins to dominate. As soon as the concentration of the high-melting metal is sufficient to increase the melting point of the inter-metallic compound above the heating temperature, the liquid phase solidifies.

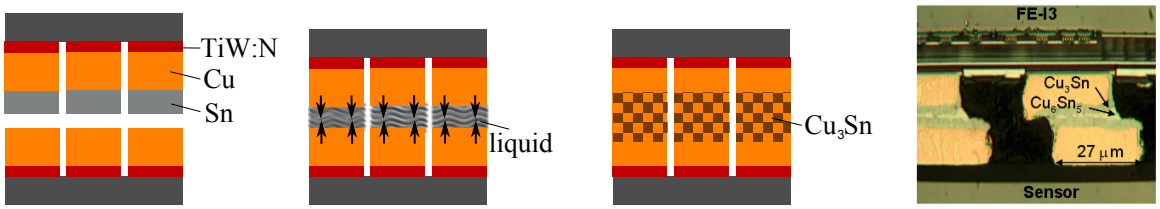

Figure 6.1: (a)–(c) Process flow of the SLID interconnection, adapted from [184]. For an explanation of the individual steps please refer to the text. (d) Cross section of SLID pads in a pixel assembly built from an FE-I2 read-out chip and a dummy sensor (aluminium and silicon oxide only). Photograph taken by [185].

While many different metal systems are known to form SLID bonds, certain constraints apply when using the technique in real applications [184]. For example, the melting point of the low-melting metal should be below 400 °C, which is the maximum temperature most ASICs can withstand. In this thesis, the SLID process as developed by the EMFT [185] is used, in which Sn ($T_{\mathrm{melt}} = 231.9\,^{\circ}\mathrm{C}$) is used as the low-melting component and Cu ($T_{\mathrm{melt}} = 1083.0\,^{\circ}\mathrm{C}$) as the high-melting component. Out of these, Cu_3Sn ($T_{\mathrm{melt}} = 676\,^{\circ}\mathrm{C}$) and Cu_6Sn_5 ($T_{\mathrm{melt}} = 415\,^{\circ}\mathrm{C}$)

are formed. The high melting point of the interconnecting alloy allows for subsequent stacking of additional SLID-interconnected layers.

When comparing the process flows of conventional bump bonding techniques and SLID (see Figure 6.2) further advantages and challenges are found. While the first step—a patterned electroplating step needed for the deposition of the Cu and Sn—is similar for both technologies, the so-called reflow step is not needed to form SLID interconnections. In the reflow step, the alloy or metal—e. g. PbSn or In—used instead of Sn in the bump bonding process is melted; the surface tension leads to solder ball formation. Since the diameter of the balls is determined by the initial pad size, all bump-bond connections have to be of equal size to form good connections (compare 3rd connection to the neighbouring ones in Figure 6.2). In contrast, a SLID bond can have an arbitrary shape and size, with the only constraint that its dimensions exceed 5 μm by 5 μm. Additionally, the reduction of one process step is expected to lower the costs once the process is established in industry. In the third step, the so-called pick-and-place, the read-out chip and the sensor are brought together. In the bump-bonding process a built-in self alignment due to the surface tension of the bump-balls is exploited, while the SLID interconnection has to rely on the pick-and-place precision for the placement of the read-out chips on the handle wafer, when the technique is applied in the chip-to-wafer approach. If a high accuracy can be achieved in the pick-and-place procedure, the pitch of the SLID connections can be as low as approximately 20 μm [89], which is not possible for the bump-bonding offered for industrial applications. In the final step, the actual bond is formed by pressing the two layers together. While a non functional bump-bonded assembly with a broken read-out chip or sensor can be separated again for repair by reheating, this is not possible for SLID assemblies.

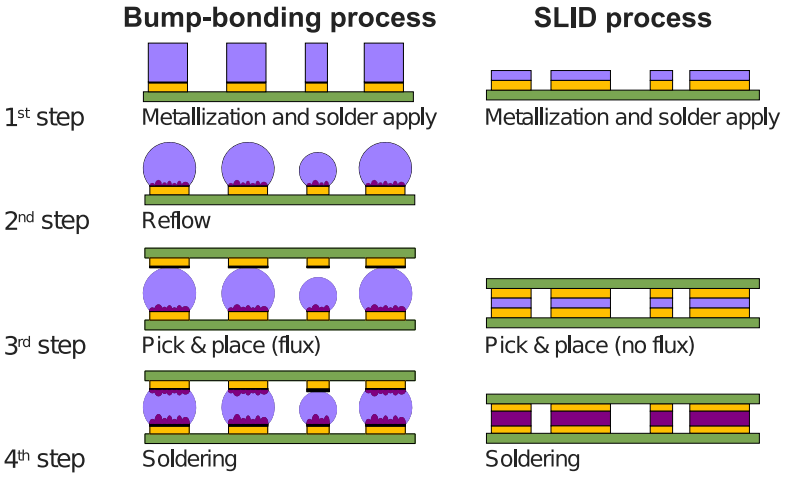

Figure 6.2: Comparison of the process steps for bump bonding (left) and SLID interconnection (right). Adapted from [185]

6.1.1 Alignment

The EMFT SLID process can be carried out in a wafer-to-wafer or chip-to-wafer approach; in the latter case a handle wafer is used. The direct interconnection of one sensor to one read-out chip is a possible development of the technique for the future. Results presented here were obtained with assemblies connected in the chip-to-wafer approach. Due to the high applied pressure in the process, a homogeneous population of the handle wafer is mandatory. Figure 6.3

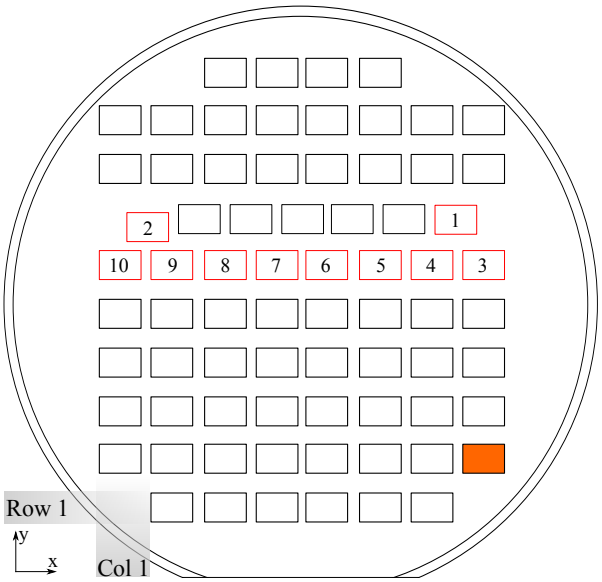

Figure 6.3: Population layout of the handle wafer. Read-out chips corresponding to a SCS in the SOI1 layout are indicated in red. Dummy read-out chips for mechanical stability are drawn in black. The read-out chip indicated in orange is missing. The coordinate systems referred to in the following are indicated.

illustrates the layout of the used handle wafer. FE-I2 read-out chips known to be functional were used for the positions facing the SCSs included in the SOI1 production (compare Figure 5.3). The rest of the handle wafer was populated regularly with electrical non-working read-out chips. The electroplated SLID pad structure is the same for the working and for the dummy read-out chips.

An excellent alignment of the read-out chips on the handle wafer is needed, given the small pitch of 50 μm in the short pixel direction, the SLID pad size of $27 \times 60\,\mu\text{m}^2$, and the minimal

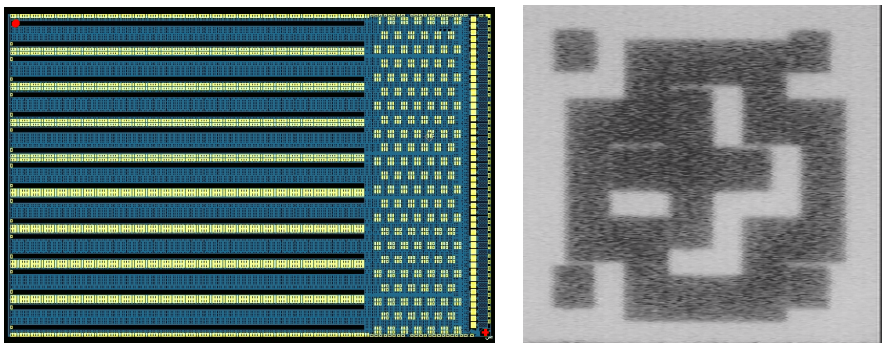

(a) (b)

Figure 6.4: (a) SLID pad distribution over the FE-I2 read-out chip (yellow rectangles). The alignment marks are indicated in red. The pad is in the upper left corner, the cross is in the lower right corner. (b) Infra-red image of the alignment cross after interconnection. The cross has a total dimension of 150 μm in both directions.

needed overlap of 5 μm $\times$5 μm. Additionally, it is important that rotations of the read-out chips are below about 0.5°. These requirements demand cutting-edge pick-and-place technology. To achieve this, a precise pick-and-place machine, DATACON EVO [186], exploiting the precise alignment marks on the read-out chip and sensors is used. In one corner a cross is used, while in the opposite corner a circle is used. Their position is indicated in red in Figure 6.4(a). In Figure 6.4(b), an infra-red picture of the cross alignment marks is depicted for a connected stack. Based on these microscope photographs, the quality of the alignment was determined after interconnection.

Table 6.1 summarises the deviations of the alignment marks from their optimal positions as well as the resulting angles. Although the misalignments are large compared to the specifications given above, due to the small angles, they can mostly be corrected by a global shift of the handle wafer with respect to the sensor wafer by $\Delta x_{\text{global}} = -20\,\mu m$ and $\Delta y_{\text{global}} = -30\,\mu m$. For the assemblies 2, 4, and 5 the misalignment is too large for the pixel assemblies to be functional, even after the global correction.

The residual misalignment after applying the global corrections of all structures is summarised in Table 6.2. In total, six out of ten assemblies were built successfully, i. e. without shorts or open connections caused by misalignment.

In Figure 6.5 two photographs show the SLID pads in the central region of two assemblies. The pictures were taken after the separation of the read-out chip from the sensor by a pull test (see below). The read-out chip SLID pads are still connected to the sensor SLID pads, lying one on top of the other. This implies that the SLID interconnection is more durable than the

Table 6.1: Deviations of alignment marks from their optimal position as well as resulting angle for the populated handle wafer.

Assembly	Cross		Pad		Angle
ID	Δx [μm]	Δy [μm]	Δx [μm]	Δy [μm]	[°]
1	13.78	7.99	50.02	50.40	−0.25
2	−118.91	−9.97	−83.28	33.33	−0.25
3	−3.69	−4.58	49.33	64.30	−0.38
4	64.32	103.01	−21.06	−36.52	0.72
5	−14.44	−28.45	66.90	81.65	−0.61
6	11.17	10.25	42.13	47.73	−0.21
7	4.04	11.61	35.19	49.99	−0.22
8	3.04	4.90	35.18	47.18	−0.23
9	2.29	9.48	37.14	50.48	−0.24
10	3.69	4.58	37.20	53.47	−0.26

Table 6.2: Residual misalignment of the alignment cross after correction for a global offset of the FE-I2 read-out chips.

Assembly	1	2	3	4	5	6	7	8	9	10
Δx [μm]	−6	−139	−23	44	−34	−8	−16	−17	−17	−16
Δy [μm]	−22	−40	−34	73	−58	−19	−18	−25	−21	−25
Tilt [°]	−0.25	−0.25	−0.38	0.72	−0.61	−0.21	−0.21	−0.23	−0.24	−0.26

electroplating. The images testify the good geometrical definition of the processed SLID pads and the level of alignment achieved in the central part of the assemblies, less affected by the read-out chip rotation.

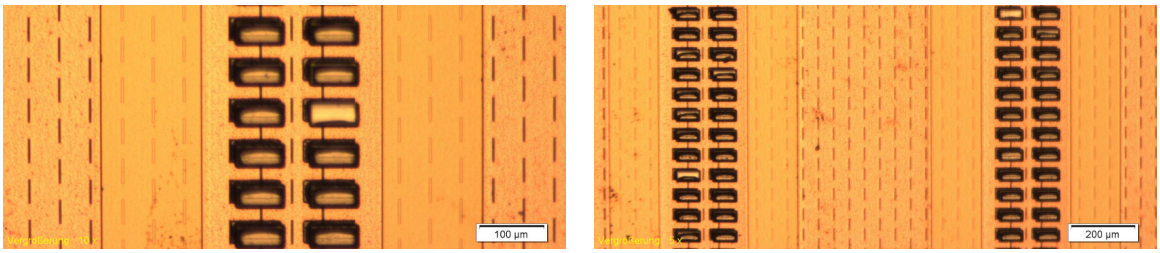

(a) (b)

Figure 6.5: Well aligned SLID stacks in the centre of the structure for a dummy read-out chip separated from the dummy sensor. The SLID connections can be seen. The scale is (a) 100 μm and (b) 200 μm.

To improve the precision of the alignment for future productions, a new pick-and-place machine, Panasonic FCB3 [187], specified to a precision of 3 μm in pick-and-place mode will be employed instead of the machine used in this production, specified for 10 μm in pick-and-place mode [186]. Additionally, the alignment can be improved by exploiting self alignment via evaporative liquid glues while populating the handle wafer. At the moment, this possible change in the method to populate the read-out chips onto the handle wafer is under investigation at EMFT.

6.1.2 Mechanical Strength

A high mechanical strength is desirable for the applied inter-connection technology, as it eases the handling of the device, ensures that bonds do not break accidentally, and that they are stable in time. To determine the mechanical strength, a piece of plexiglas was glued onto each dummy read-out chip (black in Figure 6.3) in the lower half of the handle wafer. Subsequently, weight was hanged onto the plexiglas holder while the sensor wafer was stabilised in its position by a plexiglas support covering the full area except the region around the read-out chip under study. After each increase of weight the strain was relieved using a small hoisting platform to apply the force in a controlled manner. Before adding the next weight the hoisting platform was lifted again. A photograph of the set-up is depicted in Figure 6.6(a). Due to the construction, the minimum weight applied is 0.6 kg.

The distribution of the weight needed to break the connection between sensor and read-out chip is given in Figure 6.6(b). Apart from the first row, no systematic trend over the wafer is appreciable and the weight needed is approximately two kilograms, which corresponds to 0.01 N per SLID connection. This is of the same order of magnitude to what is found for other interconnection technologies [188–192]. With the exception for extreme cases of misalignment, no significant correlation between the misalignment and the connection is found.

In Figure 6.5 photographs of the pulled off read-out chips are shown. In almost all cases, the whole SLID stack is appreciable, indicating that the weakest point of the interconnection is at the electroplated layers—i. e. layers that are similar in other technologies as for example bump bonding.

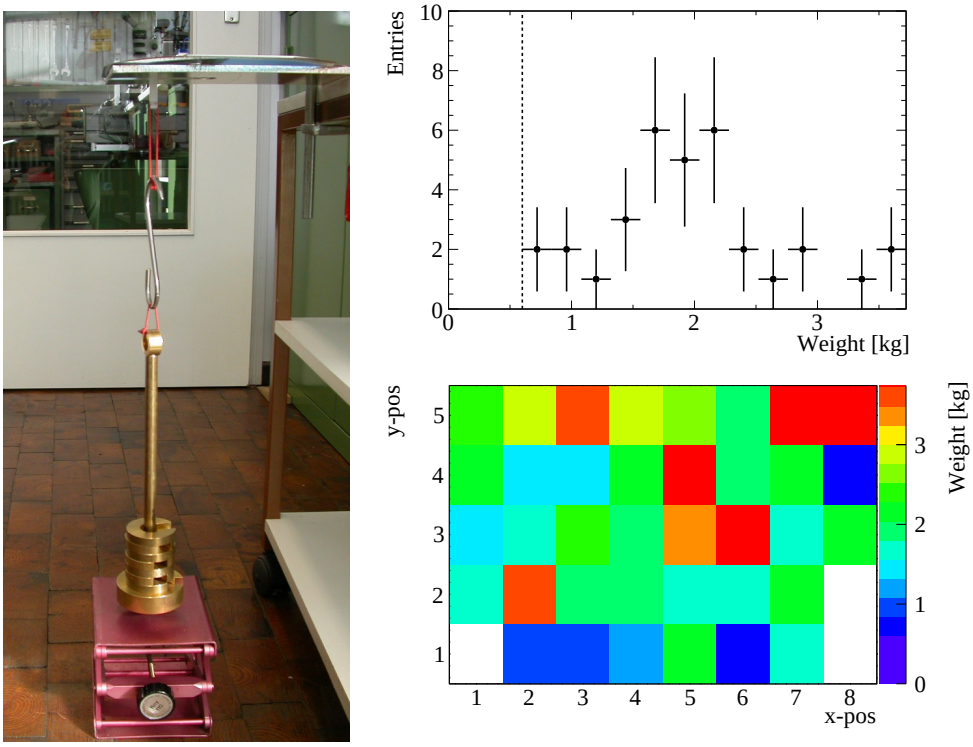

(a) (b)

Figure 6.6: (a) Photograph of the mechanical strength test set-up. (b) Amount of weight at which the read-out chip was separated from the sensor. In the top figure the distribution is shown. The dotted line indicates the minimal weight applied. In the lower figure the position of the read-out chip on the wafer is indicated. The read-out chip at position (8,2) fell off before the test; the positions (1,1) and (8,1) are not populated by design, cf. Figure 6.3.

6.1.3 Interconnection Efficiency

The key parameter for a interconnection technology in pixel modules is the efficiency with which interconnections are formed. Open connections can e. g. be found in a measurement with a radioactive source, where not connected pixel cells exhibit a low hit rate, since they can only contribute via electronic noise, but not via genuine signal. Using high statistics measurements with a ^{90}Sr source, not connected pixel cells were searched for. In Figure 6.7 the distributions of the hit rate per pixel are shown for (a) a fully connected assembly and for (b) an assembly containing not connected pixel cells. At the given statistics, around 150 events are expected per pixel, in the centre of the beam spot. For the upper- and lowermost rows, the trigger efficiency is a bit lower, due to the shielding effect of the ceramics on which the assembly is glued, see Figure 3.12(a). Thus a pixel cell is defined as connected, if it exhibits more than 50 hits. Uncertainties are assessed by varying this threshold by ±10 %. The percentages of connected pixel cells per assembly are summarised in Table 6.3. While assembly 1, 3, and 10 show no pixel-cells that are not connected, assembly 6 exhibits around 30 % of not connected

pixel cells. A geometric overview of the not connected pixel cells is given in Figure 6.7(c), with a visible trend towards the centre of the wafer.

Table 6.3: Percentages of connected pixel cells for the SLID assemblies. For the definition of connected and the uncertainties, please refer to the text. Assemblies 2, 4, and 5 were not built due to misalignment.

Assembly	1	3	6	7	8	9	10
Connected [%]	100	100	$70.1^{+0.3}_{-0.3}$	$66.5^{+0.4}_{-0.4}$	$88.7^{+0.3}_{-0.5}$	$94.5^{+0.1}_{-0.3}$	100

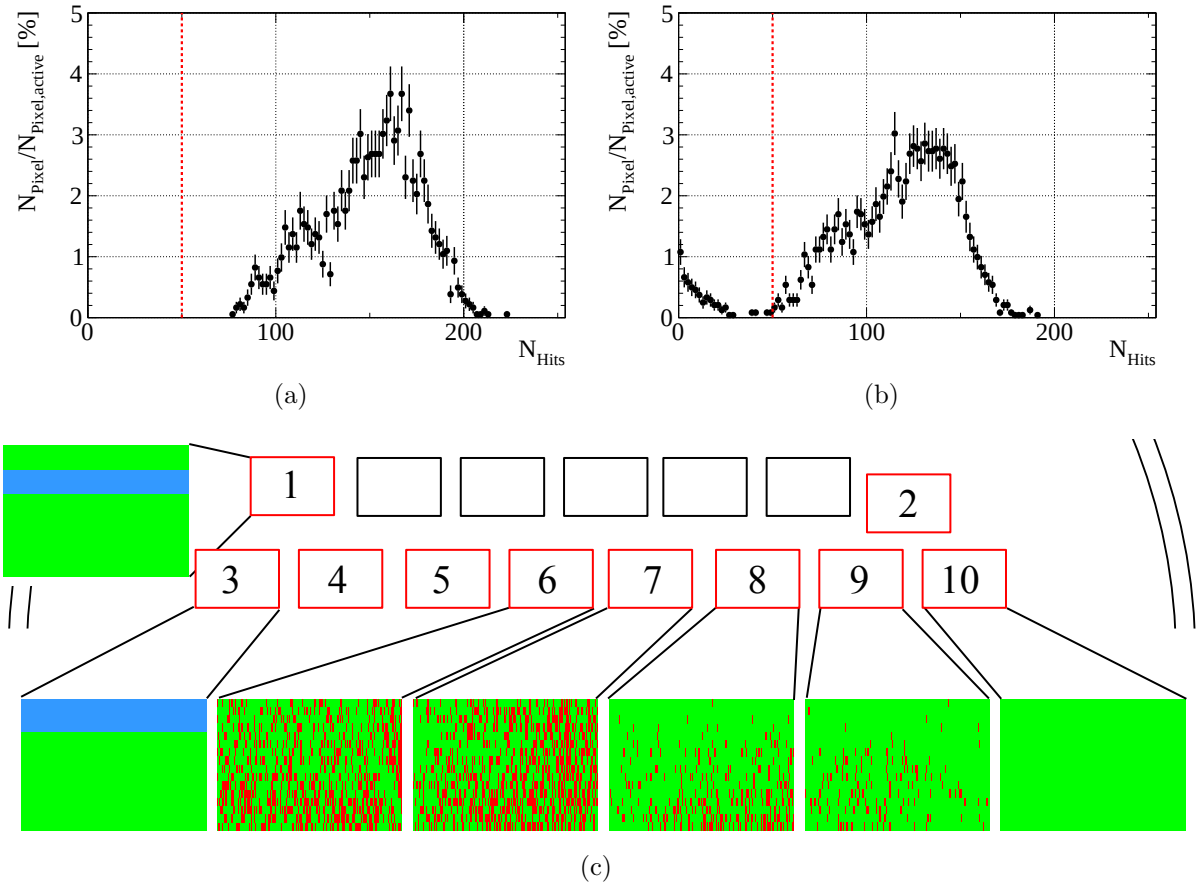

Figure 6.7: Percentages of active pixel as a function of the hit multiplicity seen within 10^6 triggers. While in (a) the ideal case is shown, in (b) not connected pixel cells are present. The red line indicates the threshold for a pixel cell to be called not connected. (c) Geometric distribution of connected (green), not connected (red), and electronically non-functional (blue) pixel cells.

Subsequent optical re-inspections of not yet connected sensor wafers from the same production, reveal that the cause for these not connected pixel cells is an imperfect opening of the BCB passivation layer underneath the SLID pad. Photographs of such not fully opened layers are depicted in Figure 6.8(a) and Figure 6.8(b). For future module assemblies, a removal of residual

BCB in the openings using an SF_6 plasma descum process offered by IZM was investigated. In the following optical inspection all openings were found to be fully opened. Figure 6.8(c) and Figure 6.8(d) are photographs of fully opened contacts.

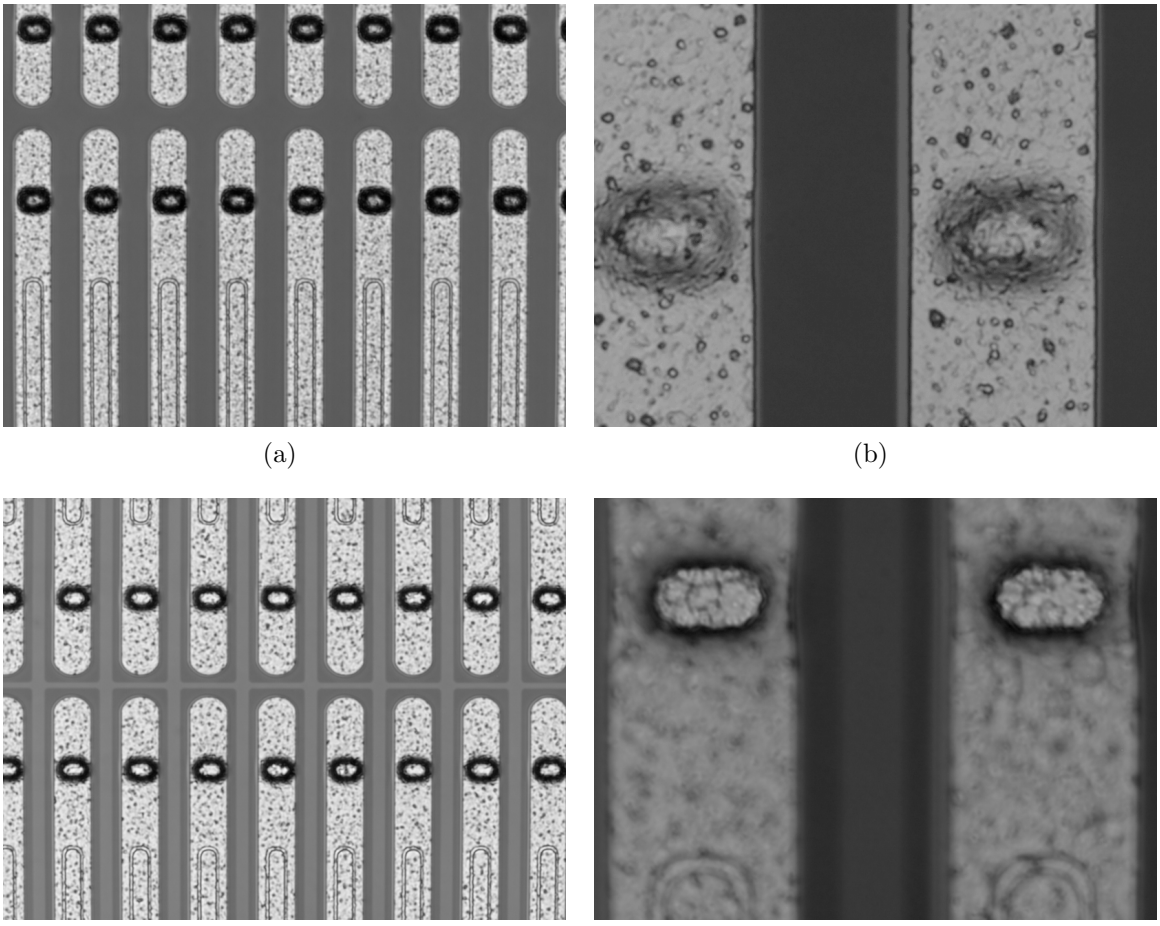

(a) (b)

(c) (d)

Figure 6.8: Photographs of (a)–(b) insufficiently opened BCB passivation layer in the position corresponding to the SLID pads and (c)–(d) opened BCB passivation layer. The horizontal distance between two openings is 50 μm in all figures.

Another crucial factor is the stability of the connections within the experiment, where, in addition to high radiation levels, temperature cycles are present. Within the laboratory and beam test measurements the number of not connected pixel cells did not change with numerous thermal cycles between 20 °C and −50 °C. Furthermore, no changes after irradiation up to a fluence of $10^{16}\,n_{eq}/cm^2$ were observed, also for what regards the noise, as further indication of the stability of the interconnection with fluence. This is a strong indication that SLID interconnections are radiation hard and withstand thermal cycles.

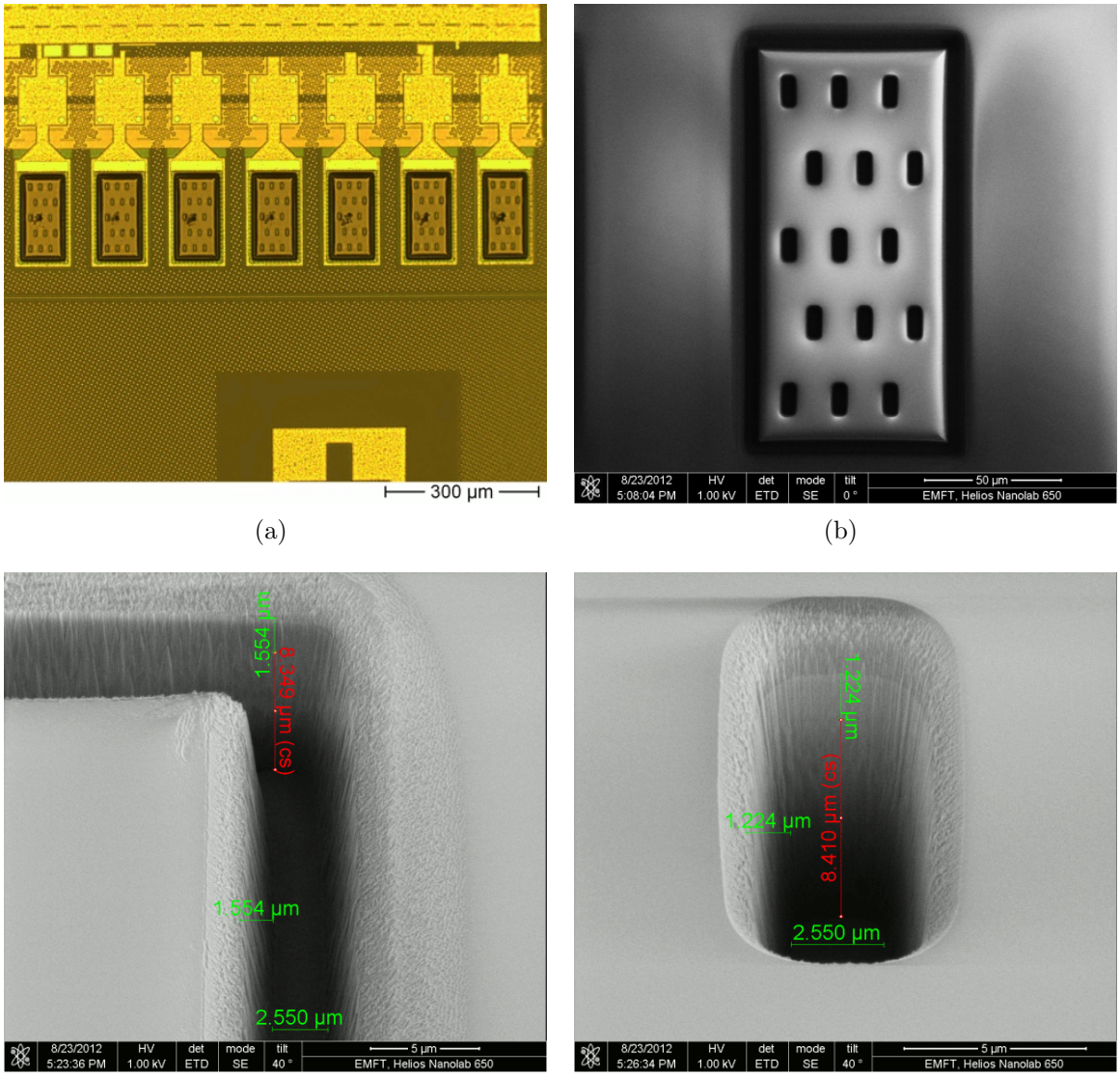

(a) (b)

(c) (d)

Figure 6.9: (a) Distribution of the ICVs over the wire-bonding pad and layout of the encircling trenches. (b–d) Illustrate the result of the first etching step on the covering dielectrics. The achieved depths, including the protecting photo resist layer, are indicated in red; lateral widths, indicated in green, are measured at the bottom of the trench or ICV and as width differences with respect to the surface width. Photographs from [185].

6.2 ICV

To enable 3D-integration and reduce or even remove the read-out chip contribution to the inactive area of the assembly, vertical signal transport to the back-side of the read-out chip is needed. This is permitted by ICVs, which are extending perpendicular through the bulk of the chip to its back-side. For the investigated assembly concept the ICV process of EMFT [193] is

investigated, which is a so-called "via last" approach, i. e. the ICVs are etched into the finished chip. Furthermore, the employed ICV technology offers high aspect ratios up to 10:1, which are important to eventually transfer the process to a pixel-by-pixel level.

The ICVs are achieved in several steps. First, using DRIE [177] (cf. Section 5.1.1) channels reaching to a depth of (50–60) μm are etched through the different read-out chip layers. Subsequently they are first isolated with Chemical Vapour Deposition (CVD) of silicon dioxide and filled with tungsten for signal transport. To expose the ICVs, the read-out chip is thinned starting from the back-side from its initial thickness of several hundred of μm down to about (50–60) μm. Eventually, to ensure connectivity of the read-out chip wire-bondable pads are electroplated on the back-side.

In the R&D programme, FE-I2 read-out chips are employed for the construction of a demonstrator assembly as shown in option B of Figure 1.8. Since this read-out chip was not designed for the usage with ICVs, they are etched on the the wire-bonding pads, since the volume below them is not filled with logic blocks. Several redundant ICVs are etched into each wire-bonding pad as illustrated in Figure 6.9(a). To insulate the volumes of neighbouring wire-bonding pads against each other, an additional encircling trench is etched. The trench as well as the ICVs have a width of about 3 μm. The length of the ICVs is around 10 μm^2.

On the read-out chips planned to be interconnected to thin n-in-p sensors from the SOI1-production (cf. Section 5.1.2) the first etching step was started on the covering dielectrics. The results are depicted in Figures 6.9(b–d). The achieved depth, including the protecting layer of photo-resist, of the first etching step is 8.4 μm for the ICVs and 8.3 μm for the trench, cf. red numbers in Figures 6.9(c) and (d). The lateral width of the ICVs and trench is about 2.6 μm at the bottom, corresponding to a width reduction of about 1.6 μm on each side, cf. green numbers in Figures 6.9(c) and (d). At the moment the etching is completed and the ICVs are filled with tungsten by EMFT. The interconnection of the read-out chips to the sensors is planned for the beginning of 2013.

6.3 Conclusions

In developing a 3D integrated and 4-side-buttable pixel detector for high energy physics experiments an important step was taken—the first production of working assemblies using SLID interconnections instead of conventional bump bonds. It was shown that the mechanical strenght per connection is about 0.01 N/bond. This is comparable with currently used interconnection technologies. The most challenging part within the SLID interconnection process is the alignment of the read-out chips on the handle wafer, which is needed if a selection of read-out chips is required when the sensor and chip placement in the respective wafers do not match or to maximize the number of good read-out chips. The widening availability of modern pick-and-place machines at the moment helps to overcome this limitation. This, together with self-aligning steps, opens the possibility to decrease the minimal possible pixel pitch in the SLID process by over a factor of two compared to conventional bump-bonding. Not connected pixel cells in the produced assemblies are caused by process inhomogeneities in steps prior to the SLID interconnection and thus are not caused by the interconnection technology. An additional SF_6 plasma descum process was found to solve the issue for future productions and thus a very high interconnection efficiency is expected in these productions. Finally, SLID interconnections were found to be robust against thermal cycles and extreme radiation levels that occur in high energy physics experiments at hadron colliders.

The etching of first high-aspect ICVs was started at EMFT, based on an optimised geometry of the encircling isolation trenches and of the individual ICVs. Provided the good results are also achieved for the further etching and post-processing steps, first demonstrator assemblies are expected within the next year.

7 Conclusions and Outlook

A novel pixel assembly concept answering the challenges posed to the pixel parts of the tracking detectors of the LHC experiments by the upgrades planned for the accelerator complex was presented and its performance investigated. It is based on five new technologies, namely n-in-p sensors, thin sensors, slim edges with or without active edges, and 3D-integration incorporating SLID interconnections as well as ICVs. The first four technologies were integrated into dedicated assemblies and their performance was investigated before and after irradiation. In the case of ICVs first etchings were started but ICVs are not yet available within fully operational demonstrator pixel assemblies.

Novel n-in-p pixel assemblies were characterised for the first time. Using assemblies matching the geometric properties and employing the same read-out electronics as the present ATLAS FE-I3 single chip assemblies, it was shown that their performance is equivalent to the currently employed n-in-n assemblies before as well as after irradiation in all aspects relevant for high energy physics experiments, i. e. charge collection, spatial resolution, and hit efficiency. Especially the hit efficiency of $(97.2 \pm 0.3)\,\%$ at a received fluence of $10^{16}\,\mathrm{n_{eq}/cm^2}$ already at a moderate applied bias voltage of 600 V indicates that the planned upgrades for the inner tracking detector of the ATLAS detector are possible with these planar pixel sensors. Further improvements can be expected from lower thresholds available with the new read-out chip generation FE-I4 and design improvements, where the structures and areas identified to be deficient, like the punch-through biasing, are realised differently. Furthermore, it was shown that a BCB passivation layer inhibits destructive electric discharges that represent a potential problem for n-in-p assemblies, up to the typically used voltages of 1 kV. Given the lower production costs, thanks to the single sided processing, this renders n-in-p pixel sensors a good candidate for the upgrades of the tracking detectors at HL-LHC experiments, and they are an excellent candidate for the outer pixel layers of the ATLAS phase II tracking detector upgrade.

If thinner sensors are employed the requirements on high voltage stability are relaxed since they exhibit a much higher CCE already at moderate bias voltages. The CCE and the absolute collected charge was investigated systematically as a function of the thickness, the received fluence, and the applied bias voltage for strip as well as for pixel sensors. It was shown that after an irradiation to a received fluence of $10^{16}\,\mathrm{n_{eq}/cm^2}$, assemblies with a thickness of $d = 285\,\mu\mathrm{m}$ collect about one third of their pre-irradiation collected charges, assemblies with $d_{\mathrm{active}} = 150\,\mu\mathrm{m}$ collect around 60 % to 70 %, and assemblies with $d_{\mathrm{active}} = 75\,\mu\mathrm{m}$ even saturate at a CCE of 90 % to 100 %. For an application within an experiment, in addition to the CCE also the absolute charge has to be taken into account and to be compared to the available threshold of the read-out chip. With the low thresholds possible with the new FE-I4 read-out chip a sensor thickness down to about $100\,\mu\mathrm{m}$ seems feasible, which would lead to a reduction in needed cooling capacity by about 50 % for the sensor part and multiple scattering, leading to an even better spatial resolution of the tracking detector.

Furthermore, the spatial resolution is increased by a decreased distance between the innermost pixel detector layer and the interaction point. Since due to space constraints, no overlapping of individual pixel assemblies in z is possible at small mounting radii, in this thesis different

ways were exploited to reduce the distance between the last pixel implantation and the edge of the sensor from 1.1 mm down to 50 μm, leading to a significantly enlarged active fraction of the sensor. Apart from high energy physics experiments this reduction is especially needed in medical applications. The same performance as for sensors with larger edge distances was found before and after irradiation, for assemblies down to edge distances of 450 μm. For the assemblies with active edges and edge distances down to 50 μm, pre-irradiation measurements indicate an equivalent performance to other investigated assemblies in terms of charge collection. A systematic irradiation programme employing a larger set of assemblies will answer the applicability of the approach after high received fluences.

To complement the increased active sensor area also on the read-out chip side, 3D-integration is foreseen in the assembly concept investigated in this thesis. Here first etching steps on the read-out chips were conducted, which will finally allow to route signals through ICVs to the back-side of the read-out chip making the implementation of the cantilever extruding beyond the sensor area superfluous. Furthermore, the high aspect ratio of the EMFT ICVs opens the possibility to transfer them eventually to a per pixel level. Employing the second component of the 3D-integration concept, the SLID interconnection technique by EMFT, first demonstrator assemblies were built and it was shown, that SLID interconnections have a stability and durability en par with other used interconnection technologies. Furthermore, all pixel cells were interconnected for assemblies where the underlying BCB passivation layer was fully opened in correspondence to the SLID interconnections. An SF_6 plasma descum process will guarantee that in future interconnections the BCB passivation layer is opened sufficiently everywhere. Also at the moment new tools and processes are installed and implemented at EMFT to further improve the alignment precision, which will allow for smaller pitches.

About one decade before the foreseen installation of the phase II tracking detector into the ATLAS experiment, main components of the novel assembly concept, as n-in-p sensors, thin sensors, and SLID interconnections, are already proven to work in an HL-LHC environment. Further alignment improvements will make SLID interconnections also an interesting candidate for the inner layers, where smallest pitch sizes are required. Active edges are shown to work in first demonstrator assemblies, but need to undergo further radiation hardness investigations in the next years to be fully qualified for the HL-LHC. Eventually, ICVs will complete the picture. Nonetheless, all components on their own also deliver huge improvements to the currently used pixel assembly structure and some were already included in the letter of intent of the ATLAS phase II tracking detector.

List of Abbreviations and Acronyms

ADC	Analogue to Digital Converter
ALiBaVa	Analogue Liverpool Barcelona Valencia
ALICE	A Large Ion Collider Experiment
ASIC	Application Specific Integrated Circuit
ATLAS	A Toroidal LHC ApparatuS
BCB	BenzoCycloButene
CAD	Computer Aided Design
CCE	Charge Collection Efficiency
CERN	Conseil Européen pour la Recherche Nucléaire
CiS	CiS Forschungsinstitut für Mikrosensorik und Photovoltaik GmbH
CMOS	Complementary Metal Oxide Semiconductor
CMP	Chemical Mechanical Polishing
cms	centre of mass
CMS	Compact Muon Solenoid
CSC	Cathode Strip Chamber
CVD	Chemical Vapour Deposition
DAC	Digital to Analogue Converter
DCS	Double Chip Sensor
DESY	Deutsches Elektronen-Synchrotron
DRIE	Deep Reactive Ion Etching
DUT	Device Under Test
EMFT	Einrichtung für Modulare Festkörper-Technologien
ENC	Equivalent Noise Charge
EOC	End-Of-Column
FWHM	Full Width Half Maximum
FZ	Float-Zone
HL-LHC	High Luminosity-Large Hadron Collider
IBL	Insertable B-Layer
ICV	Inter-Chip-Via
IP	Interaction Point
IZM	Fraunhofer Institut für Zuverlässigkeit und Mikrointegration
JSI	Jožef Stefan Institute
KIT	Karlsruher Institut für Technologie
LANSCE	Los Alamos National Laboratory spallation neutron sources
LEIR	Low Energy Ion Ring
LHC	Large Hadron Collider
LHCb	Large Hadron Collider beauty
LINAC	LINear ACcelerator
LOI	Letter-Of-Intent
LS	Long Shutdown
MCC	Module Control Chip
MDT	Monitored Drift Tube

MIP	Minimal Ionizing Particle
MPI-HLL	Max-Planck-Institut HalbLeiterLabor
MPP	Max-Planck-Institut für Physik
MPV	Most Probable Value
MPW	Multi Project Wafer
MWPC	Multi-Wire-Proportional Chamber
NIEL	Non-Ionizing Energy Loss
PPE	Poly Phenylene Ether
PS	Proton Synchrotron
RHIC	Relativistic Heavy Ion Collider
RMS	Root Mean Square
RPC	Resistive Plate Chamber
SCC	Single Chip Card
SCS	Single Chip Sensor
SCT	SemiConductor Tracker
SLID	Solid Liquid Inter-Diffusion
SM	Standard Model
SPS	Super Proton Synchrotron
TCT	Transient Current Technique
TGC	Thin Gap Chamber
ToT	Time-over-Threshold
TMAH	TetraMethyl Ammonium Hydroxide
TRT	Transition Radiation Tracker
UBM	Under-Bump-Metallization
UCSC	University of California Santa Cruz
USB	Universal Serial Bus
VME	Versa Module Eurocard
VTT	Valtion Teknillisestä Tutkimuslaitoksesta

List of Figures

List of Tables

Bibliography

[1] L. Evans and P. Bryant, editors, *LHC Machine*, JINST **3** (2008) S08001.

[2] O. Brüning, H. Burkhardt, and S. Myers, *The large hadron collider*, Prog. in Part. Nucl. Phys. **67** (2012) 705 .

[3] *Conseil Européen pour la Recherche Nucléaire (CERN)*, `http://cern.ch`.

[4] R. R. Wilson, *The Tevatron*, Fermilab, (1978), TM-763.

[5] M. Harrison, S. G. Peggs, and T. Roser, *The RHIC accelerator*, Ann. Rev. Nucl. Part. Sci. **52** (2002) 425.

[6] M. Harrison, T. Ludlam, and S. Ozaki, *RHIC project overview*, Nucl. Instr. Meth. **A499** (2003) 235.

[7] *Brookhaven National Laboratory (BNL)*, `http://www.bnl.gov`.

[8] ATLAS Collaboration, *The ATLAS Experiment at the CERN Large Hadron Collider*, JINST **3** (2008) S08003.

[9] CMS Collaboration, *The CMS experiment at the CERN LHC*, JINST **3** (2008) S08004.

[10] ALICE Collaboration, *The ALICE experiment at the CERN LHC*, JINST **3** (2008) S08002.

[11] LHCb Collaboration, *The LHCb Detector at the LHC*, JINST **3** (2008) S08005.

[12] S. Glashow, *Partial Symmetries of Weak Interactions*, Nucl. Phys. **22** (1961) 579.

[13] S. Weinberg, *A Model of Leptons*, Phys. Rev. Lett. **19** (1967) 1264.

[14] A. Salam, *Weak and electromagnetic interactions*, in *Proc. of the 8th Nobel Symposium on 'Elementary particle theory, relativistic groups and analyticity'*, pp. 367–377, 1969.

[15] ATLAS Collaboration, *Observation of a new particle in the search for the Standard Model Higgs boson with the ATLAS detector at the LHC*, Phys. Lett. **B716** (2012) 1.

[16] CMS Collaboration, *Observation of a new boson at a mass of 125 GeV with the CMS experiment at the LHC*, Phys. Lett. **B716** (2012) 30.

[17] F. Englert et al., *Broken Symmetry and the Mass of Gauge Vector Mesons*, Phys. Rev. Lett. **13** (1964) 321.

[18] P. W. Higgs, *Broken Symmetries, massless particles and gauge fields*, Phys. Lett. **12** (1964) 132.

[19] P. W. Higgs, *Broken Symmetries and the Masses of Gauge Bosons*, Phys. Rev. Lett. **13** (1964) 508.

[20] G. Guralnik, C. Hagen, and T. Kibble, *Global Conservation Laws and Massless Particles*, Phys. Rev. Lett. **13** (1964) 585.

[21] P. W. Higgs, *Spontaneous Symmetry Breakdown without Massless Bosons*, Phys. Rev. **145** (1966) 1156.

[22] T. W. B. Kibble, *Symmetry Breaking in Non-Abelian Gauge Theories*, Phys. Rev. **155** (1967) 1554.

[23] ATLAS Collaboration, *Physics at a High-Luminosity LHC with ATLAS*, CERN, (2012), ATL-PHYS-PUB-2012-001.

[24] S. Weinberg, *Implications of Dynamical Symmetry Breaking*, Phys. Rev. **D13** (1976) 974.

[25] E. Gildener, *Gauge Symmetry Hierarchies*, Phys. Rev. **D14** (1976) 1667.

[26] S. Weinberg, *Implications of Dynamical Symmetry Breaking: An Addendum*, Phys. Rev. **D19** (1979) 1277.

[27] L. Susskind, *Dynamics of Spontaneous Symmetry Breaking in the Weinberg-Salam Theory*, Phys. Rev. **D20** (1979) 2619.

[28] S. Dimopoulos, S. Raby, and F. Wilczek, *Proton Decay in Supersymmetric Models*, Phys. Lett. **B112** (1982) 133.

[29] H. Miyazawa, *Baryon Number Changing Currents*, Prog. Th. Phys. **36** (1966) 1266.

[30] P. Ramond, *Dual Theory for Free Fermions*, Phys. Rev. **D3** (1971) 2415.

[31] Y. Golfand and E. Likhtman, *Extension of the Algebra of Poincare Group Generators and Violation of P Invariance*, JETP Lett. **13** (1971) 323.

[32] A. Neveu and J. Schwarz, *Factorizable dual model of pions*, Nucl. Phys. **B31** (1971) 86.

[33] A. Neveu and J. Schwarz, *Quark Model of Dual Pions*, Phys. Rev. **D4** (1971) 1109.

[34] J.-L. Gervais and B. Sakita, *Field theory interpretation of supergauges in dual models*, Nucl. Phys. **B34** (1971) 632.

[35] D. Volkov and V. Akulov, *Is the Neutrino a Goldstone Particle?*, Phys. Lett. **B46** (1973) 109.

[36] J. Wess and B. Zumino, *A Lagrangian Model Invariant Under Supergauge Transformations*, Phys. Lett. **B49** (1974) 52.

[37] J. Wess and B. Zumino, *Supergauge Transformations in Four-Dimensions*, Nucl. Phys. **B70** (1974) 39.

[38] G. R. Farrar and P. Fayet, *Phenomenology of the Production, Decay, and Detection of New Hadronic States Associated with Supersymmetry*, Phys. Lett. **B76** (1978) 575.

[39] S. Dimopoulos and H. Georgi, *Softly Broken Supersymmetry and SU(5)*, Nucl. Phys. **B193** (1981) 150.

[40] N. Sakai and T. Yanagida, *Proton Decay in a Class of Supersymmetric Grand Unified Models*, Nucl. Phys. **B197** (1982) 533.

[41] S. Weinberg, *Supersymmetry at Ordinary Energies. 1. Masses and Conservation Laws*, Phys. Rev. **D26** (1982) 287.

[42] K. Schindl, *The Injector Chain for the LHC*, CERN, (1999), CERN-PS-99-018-DI.

[43] O. S. Brüning et al., *LHC Design Report*, CERN, (2004).

[44] C. Lefèvre, *The CERN accelerator complex*, CERN, (2008), CERN-DI-0812015.

[45] M. Reiser, *Theory and Design of Charged Particle Beams*, Wiley-VCH, 2nd edition, (2008), ISBN 978-3-527-40741-5.

[46] E. Courant et al., *Theory of the Alternating-Gradient Synchrotron*, Ann. Phys. **3** (1958) 1.

[47] TOTEM Collaboration, *First measurement of the total proton-proton cross section at the LHC energy of* $\sqrt{s} = 7\,TeV$, Europhys. Lett. **96** (2011) 21002.

[48] CERN, *LHC Performance and Statistics*, `http://lhc-statistics.web.cern.ch/LHC-Statistics/index.php?act=3`.

[49] ATLAS Collaboration, *Luminosity Public Results*, `https://twiki.cern.ch/twiki/bin/view/AtlasPublic/LuminosityPublicResults`.

[50] L. Rossi and O. Brüning, *High Luminosity Large Hadron Collider A description for the European Strategy Preparatory Group*, CERN, (2012), CERN-ATS-2012-236.

[51] L. Arnaudon et al., *Linac4 Technical Design Report*, CERN, (2006), CERN-AB-2006-084.

[52] K. Oide et al., *Beam-beam collision scheme for storage-ring colliders*, Phys. Rev. **A40** (1989) 315.

[53] K. Akai et al., *RF systems for the KEK B-Factory*, Nucl. Instr. Meth. **A499** (2003) 45.

[54] J. Pequenao, *Computer generated image of the whole ATLAS detector*, CERN, (2008), CERN-GE-0803012.

[55] J. Pequenao, *Computer generated image of the ATLAS inner detector*, CERN, (2008), CERN-GE-0803014.

[56] ATLAS Collaboration, *ATLAS Inner Detector: Technical Design Report 1*, CERN, (1997), CERN-LHCC-97-016.

[57] ATLAS Collaboration, *ATLAS Inner Detector: Technical Design Report 2*, CERN, (1997), CERN-LHCC-97-017.

[58] ATLAS Collaboration, *ATLAS Magnet System : Technical Design Report*, CERN, (1997), CERN-LHCC-97-018.

[59] ATLAS Collaboration, *ATLAS Central Solenoid : Technical Design Report*, CERN, (1997), CERN-LHCC-97-021.

[60] ATLAS Collaboration, *ATLAS Muon Spectrometer : Technical Design Report*, CERN, (1997), CERN-LHCC-97-022.

[61] J. P. Badiou et al., *ATLAS barrel toroid : Technical Design Report*, CERN, (1997), CERN-LHCC-97-019.

[62] ATLAS Collaboration, *ATLAS End-Cap Toroids : Technical Design Report*, CERN, (1997), CERN-LHCC-97-020.

[63] G. Charpak et al., *The use of multiwire proportional counters to select and localize charged particles*, Nucl. Instr. Meth. **62** (1968) 262.

[64] ATLAS Collaboration, *ATLAS Calorimeter Performance : Technical Design Report*, CERN, (1996), CERN-LHCC-96-040.

[65] ATLAS Collaboration, *ATLAS Liquid-Argon Calorimeter : Technical Design Report*, CERN, (1996), CERN-LHCC-96-041.

[66] ATLAS Collaboration, *ATLAS Tile Calorimeter : Technical Design Report*, CERN, (1996), CERN-LHCC-96-042.

[67] J. Abdallah et al., *The Production and Qualification of Scintillator Tiles for the ATLAS Hadronic Calorimeter*, CERN, (2007), ATL-TILECAL-PUB-2007-010.

[68] ATLAS Collaboration, *ATLAS High-Level Trigger, Data-Acquisition and Controls : Technical Design Report*, CERN, (2003), CERN-LHCC-2003-022.

[69] N. Wermes and G. Hallewel, *ATLAS pixel detector: Technical Design Report*, CERN, (1998), ATLAS-TDR-011.

[70] G. Aad et al., *ATLAS pixel detector electronics and sensors*, JINST **3** (2008) P07007.

[71] I. Peric et al., *The FEI3 readout chip for the ATLAS pixel detector*, Nucl. Instr. Meth. **A565** (2006) 178.

[72] R. Beccherle et al., *MCC: the Module Controller Chip for the ATLAS Pixel Detector*, Nucl. Instr. Meth. **A492** (2002) 117.

[73] D. Dobos, Commissioning Perspectives for the ATLAS Pixel Detector, PhD thesis, Universität Dortmund, (2007), CERN-THESIS-2008-022.

[74] M. Capeans et al., *ATLAS Insertable B-Layer Technical Design Report*, CERN, (2010), CERN-LHCC-2010-013.

[75] S. Parker et al., *3D - A proposed new architecture for solid-state radiation detectors*, Nucl. Instr. Meth. **A395** (1997) 328.

[76] M. Garcia-Sciveres et al., *The FE-I4 pixel readout integrated circuit*, Nucl. Instr. Meth. **A636** (2011) S155.

[77] ATLAS Collaboration, *Letter of Intent for the Phase-I Upgrade of the ATLAS Experiment*, CERN, (2011), CERN-LHCC-2011-012.

[78] Y. Giomataris et al., *MICROMEGAS: a high-granularity position-sensitive gaseous detector for high particle-flux environments*, Nucl. Instr. Meth. **A376** (1996) 29.

[79] ATLAS Colaboration, *Letter of Intent for the Phase-II Upgrade of the ATLAS Experiment*, CERN, (2013), ATL-COM-UPGRADE-2012-040, (in preparation).

[80] M. Moll, *RD50 Status Report 2009/2010 - Radiation hard semiconductor devices for very high luminosity colliders*, CERN, (2012), CERN-LHCC-2012-010.

[81] Y.-S. Tsai, *Pair production and bremsstrahlung of charged leptons*, Rev. Mod. Phys. **46** (1974) 815.

[82] R. Sternheimer, M. Berger, and S. Seltzer, *Density effect for the ionization loss of charged particles in various substances*, Atomic Data and Nucl. Data Tab. **30** (1984) 261.

[83] L. Andricek et al., *Processing of Ultra-Thin Silicon Sensors for Future e^+e^- Linear Collider Experiments*, IEEE Trans. Nucl. Sci. **51** (2004) 1117.

[84] M. Beimforde, Development of thin sensors and a novel interconnection technology for the upgrade of the atlas pixel system, PhD thesis, Technische Universität München, (2010), MPP-2010-115.

[85] ATLAS IBL Collaboration, *Prototype ATLAS IBL modules using the FE-I4A front-end readout chip*, KINST **7** (2012) P11010.

[86] P. Garrou, C. Bower, and P. Ramm, editors, *Handbook of 3D Integration*, volume 1, Wiley-VCH, (2008), ISBN 978-3-527-32034-9.

[87] P. Garrou, C. Bower, and P. Ramm, editors, *Handbook of 3D Integration*, volume 2, Wiley-VCH, (2008), ISBN 978-3-527-32034-9.

[88] A. Klumpp et al., *Vertical System Integration by Using Inter-Chip Vias and Solid-Liquid Interdiffusion Bonding*, Jpn. J. Appl. Phys. **43** (2004) L829.

[89] H. Huebner et al., *Face-to-Face Chip Integration with Full Metal Interface*, in B. Melnick et al., editors, *Advanced Metallization Conference*, volume XVIII of *Conference Proceedings ULSI*, p. 53, Mat. Res. Soc., 2002.

[90] L. Rossi et al., *Pixel Detectors - From Fundamentals to Applications*, Springer-Verlag, (2006), ISBN 3-540-28332-3.

[91] S. M. Sze and K. K. Ng, *Physics of semiconductor devices*, Wiley-Interscience, 3rd edition, (2007), ISBN 0-47114323-5.

[92] G. Lutz, *Semiconductor Radiation Detectors*, Springer-Verlag, (1999), ISBN 3-540-64859-3.

[93] M. A. Green, *Intrinsic concentration, effective densities of states, and effective mass in silicon*, J. Appl. Phys. **67** (1990) 2944.

[94] H. Bethe, *Zur Theorie des Durchgangs schneller Korpuskularstrahlen durch Materie*, A. Phys. **397** (1930) 325.

[95] F. Bloch, *Bremsvermögen von Atomen mit mehreren Elektronen*, Z. Phys. **A81** (1933) 363.

[96] C. Leroy and P.-G. Rancoita, *Silicon Solid State Devices and Radiation Detection*, World Scientific Publishing Co. Pte. Ltd., Singapore, (2012), ISBN 978-981-4390-04-0.

[97] H. Bichsel, D. E. Groom, and S. R. Klein, *Passage of Particles through matter*, J. Phys. **G37** (2010) 285.

[98] H. Bichsel, *Straggling in thin silicon detectors*, Rev. Mod. Phys. **60** (1988) 663.

[99] M.-M. Bé et al., *Table of radionuclides - Volume 3: A =3 to 244*, Bureau International des Poids et Measures, (2006), Monographie BIPM-5.

[100] C. D. Clark, P. J. Dean, and P. V. Harris, *Intrinsic Edge Absorption in Diamond*, Proc. Royal Soc. London **A 277** (1964) 312.

[101] R. Wunstorf, Systematische Untersuchungen zur Strahlenresistenz von Silizium-Detektoren für die Verwendung in Hochenergiephysik-Experimenten, PhD thesis, Universität Hamburg, (1992).

[102] A. Vasilescu, *The NIEL scaling hypothesis applied to neutron spectra of irradiation facilities and in the ATLAS and CMS SCT*, CERN, (1999), ROSE RD-48 internal Note, ROSE/TN/97-2.

[103] S. Gibson, *Radiation damage to currently running LHC silicon detecors*, Proc. Sci. (2012), (in preparation).

[104] G. Kramberger et al., *Effective trapping time of electrons and holes in different silicon materials irradiated with neutrons, protons and pions*, Nucl. Instr. Meth. **A481** (2002) 297.

[105] M. Moll, Radiation Damage in Silicon Particle Detectors, PhD thesis, Universität Hamburg, (1999).

[106] G. Casse et al., *Enhanced efficiency of segmented silicon detectors of different thicknesses after proton irradiations up to* $1 \times 10^{16}\,\mathrm{n_{eq}/cm^2}$, Nucl. Instr. Meth. **A624** (2010) 401.

[107] I. Mandić et al., *Annealing effects in n^+-p strip detectors irradiated with high neutron fluences*, Nucl. Instr. Meth. **A629** (2011) 101.

[108] M. Milovanović et al., *Effects of accelerated long term annealing in highly irradiated n^+-p strip detector examined by Edge-TCT*, JINST **7** (2012) P06007.

[109] G. Kramberger et al., *Determination of effective trapping times for electrons and holes in irradiated silicon*, Nucl. Instr. Meth. **A476** (2002) 645.

[110] G. Kramberger et al., *Investigation of Irradiated Silicon Detectors by Edge-TCT*, IEEE Trans. Nucl. Sci. **57** (2010) 2294.

[111] V. Eremin et al., *Avalanche effect in Si heavily irradiated detectors: Physical model and perspectives for application*, Nucl. Instr. Meth. **A658** (2011) 145.

[112] R. H. Richter et al., *Strip detector design for ATLAS and HERA-B using two-dimensional device simulation*, Nucl. Instr. Meth. **A377** (1996) 412.

[113] T. Wittig, Design and Quality Control of Planar ATLAS IBL Sensors Based on Slim Edge Studies, PhD thesis, TU Dortmund, (2013), (in preparation).

[114] M. Benoit, Étude des détecteurs planaires pixels durcis aux radiations pour la mise à jour du d'etecteur de vertex d'ATLAS, PhD thesis, Université Paris Sud - Paris XI, (2011), LAL-11-118.

[115] T. Rohe et al., *Planar sensors for the upgrade of the CMS pixel detector*, Nucl. Instr. Meth. **A650** (2011) 136.

[116] Hamamatsu Photonics K.K., *Emission Microscope Phemos Series*, 2011.

[117] L. Snoj, G. Žerovnik, and A. Trkov, *Computational analysis of irradiation facilities at the JSI TRIGA reactor*, Appl. Rad. Iso. **70** (2012) 483.

[118] G. Lindström et al., *Radiation hard silicon detectors—developments by the RD48 (ROSE) collaboration*, Nucl. Instr. Meth. **A466** (2001) 308.

[119] P. Lisowski et al., *Los Alamos National Laboratory spallation neutron sources*, Nucl. Sci. and Eng. **106** (1990) 208.

[120] A. Dierlamm, Untersuchungen zur Strahlenhärte von Siliziumsensoren, PhD thesis, Universität Karlsruhe, (2003), IEKP-KA/2003-23.

[121] A. Furgeri, Qualitätskontrolle und Bestrahlungsstudien an CMS Siliziumstreifensensoren, PhD thesis, Universität Karlsruhe, (2006), IEKP-KA/2005-1.

[122] R. Marco Hernández, Design Of A Readout System For Microstrip Silicon Sensors, Master thesis, Universitat de València, (2008).

[123] R. Marco Hernández, *A Portable Readout System for Microstrip Silicon Sensors (ALIBAVA)*, IEEE Trans. Nucl. Sci. **56** (2009) 1.

[124] S. Löchner and M. Schmelling, *The Beetle Reference Manual - chip version 1.3, 1.4 and 1.5*, CERN, (2006), LHCb-2005-105.

[125] Hamamatsu, *Photosensor Modules H5773/H5783/H6779/H6780 Series*, 2e edition, 2007.

[126] J. Härkönen et al., *Radiation Detector, Pitch Adapter, And Method For Producing A Pitch Adapter*, International Patent WO/2012/007634, (2012).

[127] M. A. Green, *Self-consistent optical parameters of intrinsic silicon at 300 K including temperature coefficients*, Solar Energy Mat. and Solar Cells **92** (2008) 1305.

[128] Picosecond Pulse Labs, *Model 5531 High Voltage Bias Tee Product Specification*, 2009, SPEC-4040035, Rev. 3.

[129] MITEQ Inc., *AM-1039 Datasheet*, 2010, MITEQ-AM-1309-1583433-H1610.

[130] HB Electronic Components, *Thermoelectric Cooler TEC1-12705 Datasheet.*

[131] M. Backhaus et al., *Development of a versatile and modular test system for ATLAS hybrid pixel detectors*, Nucl. Instr. Meth. **A650** (2011) 37.

[132] L. Blanquart et al., *FE-I2: a front-end readout chip designed in a commercial 0.25-μm process for the ATLAS pixel detector at LHC*, IEEE Trans. Nucl. Sci. **51** (2004) 1358.

[133] T. Stockmanns, Multi-Chip-Modul-Entwicklung für den ATLAS-Pixeldetektor, PhD thesis, Universität Bonn, (2004).

[134] F. Wanlass and C. Sah, *Nanowatt logic using field-effect metal-oxide semiconductor triodes*, in *Solid-State Circuits Conference*, volume VI of *Digest of Technical Papers*, pp. 32–33, IEEE International, 1963.

[135] F. M. Wanlass, *Low stand-by power complementary field effect circuitry*, US Patent 3356858, (1967).

[136] D. Dobos, Production accompanying testing of the ATLAS Pixel module, Diploma thesis, Universität Dortmund, (2004), CERN-THESIS-2007-016.

[137] G. Aad, Mise en service du détecteur à pixels de l'expérience ATLAS auprès du LHC et étude du canal $t\bar{t}H, H \to b\bar{b}$ pour la recherche du boson de Higgs, PhD thesis, Université de la Méditerranée Aix-Marseille II, (2009), CERN-THESIS-2010-015.

[138] FE-I4 Collaboration, *The FE-I4A Integrated Circuit Guide*, 2011, Version 11.6 (unpublished).

[139] J. Große-Knetter et al., *USBpix - USB based readout system for ATLAS FE-I3 and FE-I4*, `http://icwiki.physik.uni-bonn.de/twiki/bin/view/Systems/UsbPix`.

[140] K. Einsweiler, *ATLAS On-detector Electronics Architecture*, LBNL, (2003), Draft 3, (unpublished).

[141] M. Backhaus, *Characterization of new hybrid pixel module concepts for the ATLAS Insertable B-Layer upgrade*, JINST **7** (2012) C01050.

[142] J. Jansen, Development of an FPGA-based FE-I3 pixel readout system and characterization of novel 3D and planar pixel detectors, Diploma thesis, Universität Bonn — Physikalisches Institut, (2010), BONN–IB–2010-08.

[143] J. Große-Knetter, Vertex Measurement at a Hadron Collider – The ATLAS Pixel Detector, Habilitation thesis, Universität Bonn, (2008), BONN-IR-2008-04.

[144] J. Weingarten et al., *Planar Pixel Sensors for the ATLAS Upgrade: Beam Tests results*, JINST **7** (2012) P10028.

[145] A. Bulgheroni, *Results from the EUDET telescope with high resolution planes*, Nucl. Instr. Meth. **A623** (2010) 399.

[146] C. Hu-Guo, *A ten thousand frames per second readout MAPS for the EUDET beam telescope*, CERN, (2009), CERN-2009-008.

[147] J. Behr, Jets at High Q^2 at HERA and Test Beam Measurements with EUDET Pixel Telescope, PhD thesis, Universität Hamburg, (2010), DESY-THESIS-2010-038.

[148] DIN, *Industrielle Platin-Widerstandsthermometer und Platin-Temperatursensoren*, (2009), DIN EN 60751.

[149] G. Troska, Development and operation of a testbeam setup for qualification studies of ATLAS pixel sensors, PhD thesis, TU Dortmund, (2012).

[150] J. Große-Knetter et al., *The TurboDAQ*, `http://physik2.uni-goettingen.de/~jgrosse/TurboDAQ`.

[151] R. Turchetta, *Spatial resolution of silicon microstrip detectors*, Nucl. Instr. Meth. **A335** (1993) 44.

[152] E. Belau et al., *Charge collection in silicon strip detectors*, Nucl. Instr. Meth. **214** (1983) 253.

[153] P. Weigell et al., *Characterization and performance of silicon n-in-p pixel detectors for the ATLAS upgrades*, Nucl. Instr. Meth. **A658** (2011) 36.

[154] C. Gallrapp et al., *Performance of novel silicon n-in-p planar pixel sensors*, Nucl. Instr. Meth. **A679** (2012) 29.

[155] P. Weigell, *Recent Results of the ATLAS Upgrade Planar Pixel Sensors R&D Project*, (submitted to Nucl. Instr. Meth **A**), arXiv:1210.7661.

[156] R. A. Kirchhoff, *Polymers derived from poly(arylcyclobutenes)*, US Patent 4540763, (1985).

[157] The Dow Chemical Company, *Processing Procedures for CYCLOTENE 3000 Series Dry Etch Resins*, The Dow Chemical Company, (2008).

[158] A. Küchler, *Hochspannungstechnik*, Springer-Verlag, (2009), ISBN 978-3-540-78413-5.

[159] T. Fritzsch et al., *Cost effective flip chip assembly and interconnection technologies for large area pixel sensor applications*, Nucl. Instr. Meth. **A650** (2011) 189.

[160] V. Fadeyev et al., *Scribe-Cleave-Passivate (SCP) Slim Edge Technology for Silicon Sensors*, (submitted to Nucl. Instr. Meth **A**).

[161] M. Backhaus, Development of an USB-based test system for the FE-I3 readout chips of the ATLAS pixel detector and Noise Occupancy Studies, Diploma thesis, Universität Bonn, (2009), BONN-IB-2009-14.

[162] I. Perić, Design and realization of integrated circuits for the readout of pixel sensors in high-energy physics and biomedicinal imaging, PhD thesis, Universität Bonn, (2004), CERN-THESIS-2004-055.

[163] R. Gehrke et al., *Radioactinide additions to the electronic Gamma-ray Spectrum Catalogue*, J. Rad. Nucl. Chem. **248** (2001) 417.

[164] γ-ray spectrometry center, *Gamma-Ray spectrum catalogue*, Idaho National Engineering & Environmental Laboratory, (2001).

[165] G. Audi and A. Wapstra, *Masses, Q-values and nucleon separation energies – The 1995 update to the atomic mass evaluation*, Nucl. Phys. **A595** (1995) 409.

[166] D. Münstermann, *R&D on Planar Pixel Sensor Technology for the ATLAS Inner Detector Upgrade*, CERN, (2008), ATU-RD-MN-0019.

[167] R. Nagai et al., *Evaluation of novel KEK/HPK n-in-p pixel sensors for ATLAS Upgrade with testbeam*, Nucl. Instr. Meth. **A699** (2013) 78–83.

[168] M. Paterno, *Calculating Efficiencies and Their Uncertainties*, Fermilab, (2004), FERMILAB-TM-2286-CD.

[169] A. Rummler, Radiation hardness of n^+-in-n planar silicon pixel detectors for future ATLAS upgrades, PhD thesis, TU Dortmund, (2013), (in preparation).

[170] S. Altenheiner et al., *Radiation hardness studies of n^+-in-n planar pixel sensors for the ATLAS upgrades*, Nucl. Instr. Meth. **A658** (2011) 25.

[171] P. Weigell et al., *Characterization of Thin Pixel Sensor Modules Interconnected with SLID Technology Irradiated to a Fluence of $2{\cdot}10^{15}$ n_{eq}/cm^2*, JINST **6** (2011) C12049.

[172] A. Macchiolo et al., *Thin n-in-p pixel sensors and the SLID-ICV vertical integration technology for the ATLAS upgrade at the HL-LHC*, (submitted to Nucl. Instr. Meth **A**), arXiv:1210.7933.

[173] U. Gösele et al., *Semiconductor wafer bonding*, Annu. Rev. Mater. Sci. **28** (1998) 215.

[174] R. W. P. Anton Nenadic, *Method of chemical-mechanical polishing an electronic component substrate and polishing slubry therefor*, US Patent 5084071, (1992).

[175] O. Tabata et al., *Anisotropic etching of silicon in TMAH solutions*, Sensors and Actuators A: Physical **34** (1992) 51.

[176] S. Eränen et al., *3D processing on 6 in. high resistive SOI wafers: Fabrication of edgeless strip and pixel detectors*, Nucl. Instr. Meth. **A607** (2009) 85.

[177] F. Lärmer, *Verfahren zum anisotropen Ätzen von Silizium*, DE Patent 4241045 C1, (1994).

[178] E. Verbitskaya, *Operational conditions for enhancement of collected charge via avalanche multiplication in n-on-p strip detectors*, in *20th RD50 Workshop (Bari)*, 2012.

[179] M. Milovanović, Electric field and charge multiplication in radiation damaged silicon detectors, PhD thesis, Univerza v Ljubljani, (2013), (in preperation).

[180] A. Clark, M. Elsing, and P. Wells, *Performance Specifications of the Tracker Phase II Upgrade*, CERN, (2012), ATL-UPGRADE-PUB-2012-003.

[181] A. Macchiolo et al., *Performance of n-in-p pixel detectors irradiated at fluences up to $5x10^{15}$ n_{eq}/cm^2 for the future ATLAS upgrades*, Ph. Proc. **37** (2012) 1024–1031.

[182] L. Bernstein and H. Batrtholomew, *Applications of Solid-Liquid Inderdiffusion (SLID) Bonding in integrated-Circuit Fabrication*, Trans. Met. Soc. AIME **236** (1966) 405.

[183] L. Bernstein, *Semiconductor Brazing by the Solid-Liquid-Inter-Diffusion (SLID) Process*, in *ECS Meeting, San Francisco*, pp. 319–325, 1965, Abstract No. 133.

[184] A. Klumpp, *Bonding with Intermetallic Compounds*, in P. Garrou, C. Bower, and P. Ramm, editors, *Handbook of 3D Integration: Technology and Applications of 3D Integrated Circuits*, pp. 261–269, Wiley-VCH, 2008.

[185] *Fraunhofer-Einrichtung für Modulare Festkörper-Technologien*, `http://www.emft.fraunhofer.de`.

[186] Datacon, *Multichip Die Bonder 2200 evo*, 2010.

[187] Panasonic, *Panasonic FCB3 Microelectronics Bonder*, 2008.

[188] T. C. Go, *Bonding of aligned conductive bumps on adjacent surfaces*, United Sattes Patent 4912545, (1990).

[189] C. Broennimann et al., *Development of an Indium bump bond process for silicon pixel detectors at PSI*, Nucl. Instr. Meth. **A565** (2006) 303.

[190] J. Eldring, E. Zakel, and H. Reichl, *Flip Chip Attach of Silicon and GaAs Fine Pitch Devices as well as Inner Lead TAB Attach Using Ball-bump Technology*, Microelectron. Int. **11** (1994) 20.

[191] C. Broennimann et al., *The PILATUS 1M detector*, J. Synch. Rad. **13** (2006) 120.

[192] L. K. Cheah et al., *Gold to gold thermosonic flip-chip bonding*, SPIE proc. series **4428** (2001) 165.

[193] A. Klumpp, P. Ramm, and R. Wieland, *3D-integration of silicon devices: A key technology for sophisticated products*, in *Design, Automation Test in Europe Conference Exhibition*, pp. 1678 –1683, 2010.

Danksagungen

Die letzten Zeilen sind jenen gewidmet, die mir halfen und mich unterstützten, diese Dissertation zu schreiben.

Herrn Professor Siegfried Bethke möchte ich zuerst für die Möglichkeit danken, die Dissertation am Max-Planck-Institut für Physik durchzuführen. Danken möchte ich Ihnen für die konstruktiven Rückmeldungen während der Advisory Panels und bei anderen Gelegenheiten.

Entscheidend zum Erfolg der Arbeit beigetragen, haben die vielen guten Ratschläge, Ideen und die richtigen Fragen, gepaart mit der akribischen Durchsicht des Manuskripts durch Richard Nisius. Ich glaube wenige Doktoranden können sich so glücklich schätzen, einen Betreuer zu haben dessen Tür immer offen ist, wenn Hilfe benötigt wird, der Hilfe aber nicht aufdrängt.

Ad Anna Macchiolo va un ringraziamento speciale. Senza la sua esperienza e la sua supervisione di aspetti sia scentifici che umani del progetto, molti risultati non sarebbero stati ottenuti. Senza di lei molte delle precedenti pagine bianche sarebbero state ancora meno piene e molte delle gialle sarebbro rimaste vuote, cosa che avrebbe allungato considerevolmente i tempi di consegna di questa tesi. Spero che molti altri studenti dopo di me abbiano la fortuna di lavorare con Te e mi auguro di poter rimanere in contatto anche in futuro.

Auch ohne den anderen *Giganten*, auf dessen Schultern ich stand, Michael Beimforde, wäre die Ernte magerer ausgefallen. Danke, dass Du zusammen mit Anna, Richard und der Expertise vom HLL die Grundsteine gelegt hast, auf denen diese Arbeit mit aufbaut. Darüber hinaus freue ich mich schon auf den nächsten Klettersteig mit Dir und Vivi.

Kein Buch, kein Paper, kann einen so tiefen und alles übersehenden Einblick in die Welt der Halbleiterphysik vermitteln, wie ein Gespräch mit Rainer Richter. Kein Effekt den Du nicht kennst oder zumindest erklären kannst. Danke für die viele Zeit und aufschlussreichen Erklärungen.

Nicht vergessen werden dürfen Gabriele Compostella, Giorgio Cortiana, Tobias Göttfert, Petra Haeffner, Roland Härtel, Andreas Maier, Sophio Pataraia, Anja Reiter, Jochen Schieck und Silke Zollinger, die neben den schon Genannten wesentlich zum guten Klima in der sehr kollegialen und allzeit hilfsbereiten ATLAS SCT-Gruppe und am MPP beigetragen haben. Entscheidend beigetragen zum guten Klima haben natürlich auch die üblichen Verdächtigen um 16 Uhr im Raum 339. Vielen Dank für die vielen kurzweiligen Momente.

Die Arbeit am MPP wäre ungleich schwerer ohne die fleißigen Helfer aus den Werkstätten Günther Tratzl, Carina Schlammer und Christoph Knust, die immer Verständnis für kurzfristigste Änderungen oder Bondwünsche hatten.

Warm thanks go to the whole PPS beam test crew which enabled many of the measurements presented in this thesis. First of all to Jens Weingarten and Marco Bomben, who are herding us cats. Von den vielen helfenden Händen während der Beam Tests möchte ich besonders Silke Altenheiner und André Rummler hervorheben, die stets das richtige Werkzeug im Koffer hatten und immer zur Seite sprangen, wenn Hilfe gebraucht wurde. After the beam tests the central reconstruction by Mathieu Benoit, Matthias George, Igor Rubinsky and Stefano Terzo cannot be thanked for enough. Obviously my summer student Michael Ellenburg was a great help during and after the beam test.

Děkuji André Rummlerovi nejen za pomoc při ozařovacím testu. Bez něj by nebyla možná některá srovnání s n-in-n moduly. Díky Andrému jsem věděl, že téměř bez ohledu na to, kam pojedu, vždy potkám někoho známého.

Marko Milovanoviću želim da ti se zahvalim za kolaboraciju tokom edge-TCT merenja, za mnogo korisnih diskusija i za fenomenalno vreme provedeno zajedno u Srbiji! Ermöglicht wurden die edge-TCT Messungen von Gregor Kramberger; hierfür und für die vielen interssanten und aufschlussreichen Diskussionen möchte ich Dir herzlich danken.

Wenn mal wieder ein Labor am CERN gebraucht, ein Abend zu füllen oder auch nur Zeit für einen Kaffee war, stand Christian Gallrapp stets parat. Danke dafür and thanks to you and Alessandro La Rosa for insisting on writing the paper.

Without the help of Alexander Dierlamm, Igor Mandić, Vladimir Cindro, Sally Seidel, and Maurice Glaser the irradiations of the different sensors would not have been possible. For this, but also for the many interesting discussions at RD50 meetings or in Ljubljana, I want to thank you.

I want to thank and mention at this point also the official entities, which besides the Max Planck Society funded part of the sensor productions and the irradiations. This work has been partially performed in the framework of the CERN RD50 Collaboration. Part of the irradiation were supported by the Initiative and Networking Fund of the Helmholtz Association, contract HA-101 ("Physics at the Terascale"). Another part of the irradiations and the beam test measurements leading to these results has received funding from the European Commission under the FP7 Research Infrastructures project AIDA, grant agreement no. 262025.

Abschließend sei meiner Familie gedankt; meinen Eltern, die mir ein Studium ermöglicht haben und mir stets den nötigen Rückhalt gaben, wenn ich ihn brauchte. Mein Dank an Eva ist schwer in Worte zu fassen. Zuerst möchte ich für das viele Verständnis danken, wenn ich wieder einmal im Flieger oder der Bahn nach irgendwo saß und erst Wochen später nach Hause kam. Aber wie bereits gesagt, es lässt sich eigentlich nicht in Worte fassen, daher einfach nur DANKE und auf viele weitere gemeinsame Jahre.

Philipp Weigell, München im Dezember 2012